A COLLAGEN-HYALURONAN INFUSED 3D-PRINTED POLYMERIC SCAFFOLD FOR PARTIAL MENISCUS REGENERATION

By

SALIM AMIN GHODBANE

A dissertation submitted to the

School of Graduate Studies

Rutgers, The State University of New Jersey

In Partial Fulfillment of the Requirements

For the Degree of

Doctor of Philosophy

Graduate Program in Biomedical Engineering

Written under the direction of

Michael G Dunn

And approved by

_____

_____

_____

_____

New Brunswick, New Jersey

May, 2018

ABSTRACT OF THE DISSERTATION

A Collagen-Hyaluronan Infused 3D-Printed Polymeric Scaffold for Partial Meniscus Regeneration

by SALIM AMIN GHODBANE

Dissertation Director:
Michael G Dunn, Ph.D.

The menisci are semilunar fibrocartilaginous disks, which serve several purposes within the tibiofemoral joint including shock absorption, force transmission, load distribution, joint stability, and lubrication. Partial meniscectomy is the gold standard for treatment of meniscal lesions and represents the most common orthopaedic surgical procedure with cost upwards of $4 billion per annum. This provides short term symptomatic relief but is known to increase the risk of osteoarthritis as a result of increased stresses on the articular surfaces with a well-documented link between meniscectomy volume and osteoarthritis. This has led to great interest in the regeneration of meniscal tissue. An ideal meniscus scaffold would be of an appropriate geometry to fit into the replacement site, facilitate cell attachment, infiltration, and distribution, and possess appropriate mechanical properties to stimulate the regeneration of meniscal tissue and protect the surrounding bone surfaces.   3D printing is a method of manufacturing in which materials are deposited onto one another in layers to produce three-dimensional structures. This method allows for the fabrication of complex and interconnected architectures needed to mimic the geometry of the native meniscus.   The objective of this study was to develop an acellular, biomechanically functional scaffold for partial meniscus regeneration. The central hypothesis was a collagen-infused 3D-printed polymeric scaffold could be fabricated and implanted to 1) mimic the mechanical properties of the native meniscus, 2) be successfully fixed to the remaining native meniscal rim, 3) increase the contact area and reduce peak stresses relative to partial meniscectomy, 4) encourage cell infiltration, extracellular matrix production, and organized tissue deposition, 5) integrate robustly to the surrounding native meniscal tissue, and 6) protect the articular surfaces to prevent or delay degenerative changes. We tested our hypothesis through the pursuit of the following specific aims:

Aim 1: Determine the physical, mechanical, and enzymatic differences among bovine, porcine, and ovine derived collagen scaffolds.
1. Swelling Properties
2. Tensile Testing
3. Confined Compression
4. Unconfined compression
5. Pore Structure Analysis
6. Enzymatic Stability

Aim 2: Biomechanical characterization of a collagen-hyaluronan infused 3D-printed polymeric scaffold and assessment of suture retention properties and ability to restore joint contact mechanics.

1. Poly(DTD DD) Degradation Assay
2. Scaffold Confined Compression Creep
3. Scaffold Circumferential Tensile Testing
4. Scaffold Single Suture Pull-out Testing
5. Scaffold Fixation Strength Testing
6. *In Situ* Contact Stress Distribution Analysis

Aim 3: Functional in Vivo Evaluation of Partial Meniscus Scaffold in an Ovine Model
1. Gross Analysis
2. Histology of the Synovium
3. Histology of the Scaffold
4. Immunofluorescence of the Scaffold
5. Biochemical Analysis of the Scaffold
6. Histology of the Articular Cartilage

Aim 4: Enhancement of Scaffold Mechanical Properties via Molecular Orientation during 3D printing

1. Thermal Degradation Assessment of poly(DTD DD)
2. Rheological Characterization of poly(DTD DD) and PLLA
3. Optimization of Molecular Orientation in poly(DTD DD)
4. Transition to Other Polymers: PLLA
5. Printing and Mechanical Characterization of Meniscus Scaffold

Acknowledgements

I would like to first, and foremost, thank my family. I'd like to thank my parents, Samir and Rachida Ghodbane, for their never ending support and love. My dad always helped me keep things in perspective with his favorite quote about graduate school "it's 99% perspiration, 1% exhilaration." Although I think he greatly underestimates the proportion of perspiration, the message stuck with me. I'd like to thank my mother for always helping me out during my toughest times and never, ever asking anything in return. I'd like to thank my brother, Mehdi, warning me about what I was getting into and for always being my best friend. I'd like to thank my sister-in-law for putting up with all of the complaining Mehdi and I did for hours on end and for always being a great person.

I would like to acknowledge my committee members. I would like to thank Dr. Murat Guvendiren for his aid with the early development of the 3D printing process and coordinating the acquisition of the 3D Bioplotter. I'd like to thank Dr. Joseph Freeman for his outside opinion and his laidback confidence that the project would always be a success.

I'd especially like to thank my advisors Dr. Michael Dunn and Dr. Charles Gatt for their continued support throughout the project. They provided me the keys I needed to succeed but also gave me the creative freedom that I desired to really run with this project. They were also very supportive of my career goals allowing me to pursue an internship alongside my PhD. This was an excellent environment for me to succeed and I hope that I exceeded their expectations.

Table of Contents

Table of Figures

List of Tables

1 Background

1.1 The Meniscus

The human knee joint is a complex organ with the ability to bear large loads while simultaneously allowing for flexion and extension about its transverse axis. The knee joint consists of four bones, the tibia, femur, patella, and fibula, connected by a system of ligaments and tendons (Figure 1). At the center of this array of ligaments and tendons are two menisci, the medial and lateral menisci. The menisci are soft tissue extensions of the tibia which act to cushion the interaction between the incongruous surfaces of the tibial plateau and femoral condyles[122]. Once thought to be a vestigial organ, the menisci work to protect the articular cartilage of the knee by transmitting loads through the joint, distributing high peak stresses on the femoral condyles and the tibial plateau, absorbing shock, and provide lubrication[10]. With increasing scientific evidence supporting its importance, deficiency of meniscus has been identified as a significant precursor of osteoarthritis[102].
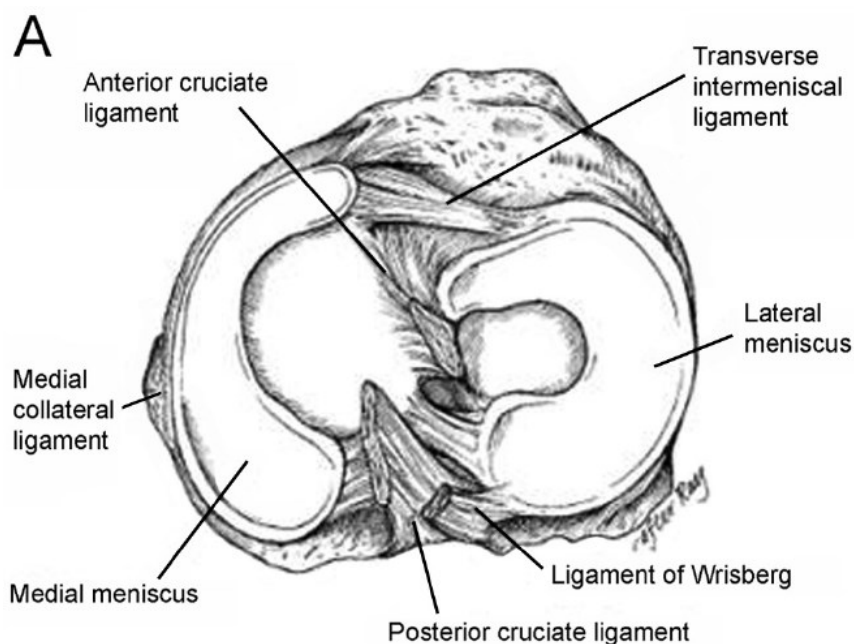
Figure 1 Anatomy of the knee joint as viewed from above[41].

1.2   Medial Meniscus: Gross Anatomy

The medial meniscus is a semilunar fibrocartilage structure with a concave proximal surface and a flat distal surface [26]. The peripheral border of the meniscus is thick, convex, and attaches to the joint capsule throughout its circumference. The inner margin of the meniscus is free from attachment. The medial meniscus has its anterior attachment anterior to the anterior cruciate ligament in the anterior intercondylar fossa with posterior fibers merging with the transverse ligament. The posterior attachment of the medial meniscus is firmly attached to the posterior intercondylar fossa of the tibia. This attachment is flanked by the attachments of lateral meniscus and the posterior cruciate ligament[19].

1.3   Meniscus: Biochemistry, Ultrastructure, and Biomechanics

1.3.1   Meniscus Composition

The meniscus is composed of fibrocartilaginous tissue, with properties of both ligament and cartilage. Ligamentous tissue is characterized by excellent tensile properties and cartilaginous tissue by excellent compressive and shear properties. Therefore, fibrocartilage has the ability to support all three loading types. The biomechanical functions of the meniscus stem from its composition and geometry.

The meniscus' composition is primarily water (60-70%), type I collagen (15-25% wet weight), and proteoglycans (1-2% wet weight)[91]. There are several other minor components (cumulative <5%) including hyaluronan, collagens type I, V, VI, IX, and XI, matrix glycoproteins, elastin, and decorin[91].

1.3.2   Collagens

Collagen represents the most abundant protein in the mammalian organism with at least 28 collagens that have been described[110]. The unifying feature of the collagen family is a triple helical structural motif that impart the protein its plasticity and flexibility on the molecular

level correlating to its tremendous tensile mechanics at the macroscopic level. Collagens can be divided into 4 groups: fibrillar, beaded filaments, anchoring fibrils, and networks[110].

Fibrillar collagen molecules join together to form hierarchical polymeric networks beginning with fibrils that form into fibrils, and finally fibrils into fibers. The structure is further stabilized via intra- and inter-molecular crosslinks. Collagens I, II, X, and XI are the fibrillar collagens whose primary functions are to provide tensile properties in meniscal tissue.   Type I collagen is the most abundant collagen in the body[43]. Type II collagen is present primarily in articular cartilage and fibrocartilage[91].

1.3.3   Proteoglycans

Although proteoglycans account for only 1-2% of the wet weight of fibrocartilage, they have a significant effect on the tissue's viscoelastic properties in compression. Proteoglycans are polypeptides covalently attached glycosaminoglycans (GAGs). GAGs possess an array of negative charges in the form of carboxyl or sulfate groups[19]. Aggrecan is the primary proteoglycan in fibrocartilage, composed of about 100 chains of the GAG chondroitin sulfate and, to a lesser extent, keratin sulfate.

Aggrecan molecules can attach non-covalently to lone strands of hyaluronan to form larger proteoglycan aggregates (Figure 2). The tremendous size of these aggregates entraps them within the collagen meshwork and sodium cations in free solution must diffuse into the tissue to associate with the highly negative charge in an effort to establish electro-neutrality (an effect known as Donnan Osmotic Pressure)[85]. Consequently, water must follow due to the large osmotic potential and the tissue will swell until constrained by the tensile stress of the collagen fibrils. The tissue is pressurized as a result of this hydrostatic pressure[19], and has a much greater ability to support large compressive loads.
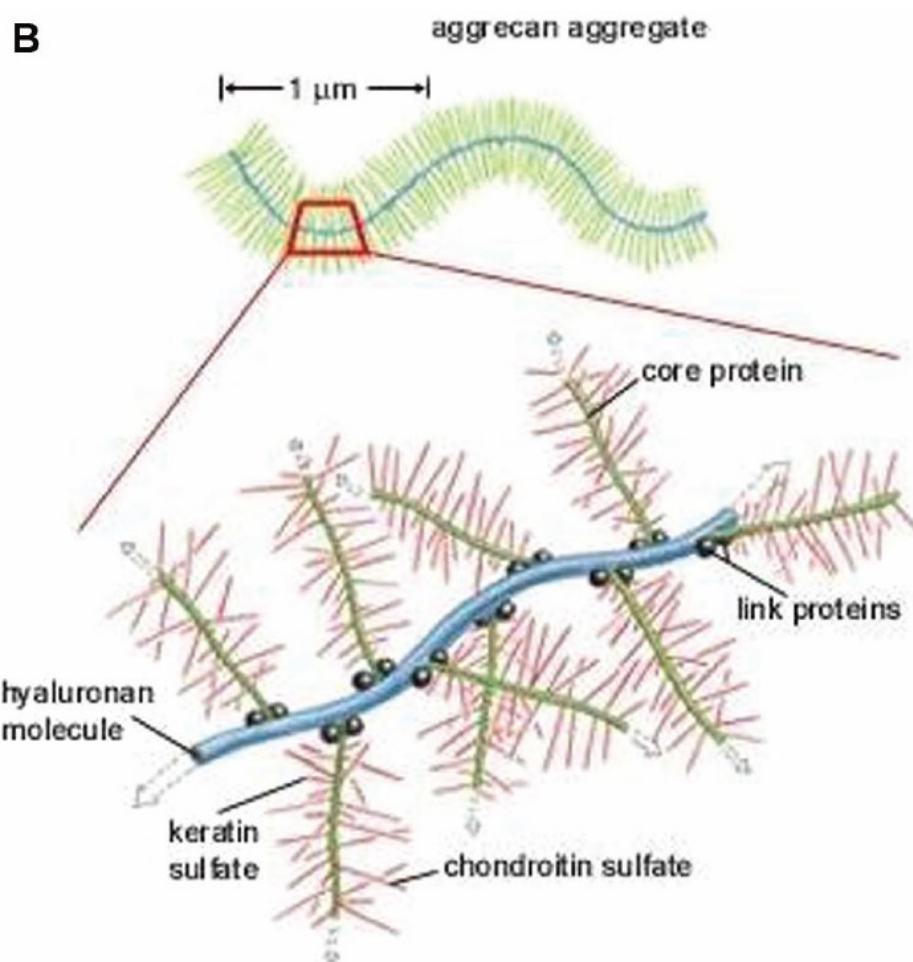
Figure 2 Schematic of an aggrecan aggregate with associated GAG molecules [41].

1.3.4 Minor Components' Functions

The minor components are each important in regards to specific functions in the

organization of the ultrastructure of the meniscus. The matrix glycoproteins stabilize

proteoglycan-hyaluronic acid aggregates[19]. Decorin is a small proteoglycan which binds to type I

and II collagen and plays a role in the regulation of fibril diameter. Adhesive glycoproteins, like

fibronectin and thrombospondin, can bind to together matrix macromolecules and cell surfaces

to play a role in supramolecular organization of the extracellular[19].

1.3.5   Meniscal Cell Types

The menisci have spatial distribution of different cell types, whose primary function are synthesizing and maintaining the extracellular matrix. In the superficial layers and inner third of the meniscus are the fibrochondrocytes, fusiform cells that are chondrocytic in nature. These cells have an intermediate phenotype as they are similar in appearance to chondrocytes but produce and maintain a fibrous matrix.   In the remainder of the meniscus are fibrocytes, ovoid or polygonal cells. These cells are found in the middle third of the meniscus. Fibroblasts represent the subset of fibrocytes that are active and located only in the outer third[26]. This heterogeneous cell population adds another dimension of complexity when attempting to tissue engineer this tissue with cell seeded scaffolds.

1.3.6   Ultrastructure

1.3.6.1   Collagen Organization

The primary function of collagen is to tolerate tensile loads. The arrangement of the collagen fibers within the meniscus relates directly to its biomechanical tensile properties. On the superficial, articulating layers, 35 nm diameter collagen fibers are arranged in a random mesh-like woven matrix (Figure 3)[91]. Below the superficial network, 120 nm diameter fibrils lie together in large lamellar bundles. On the tibial side, these bundles run radially, however, on the femoral side, this is only true in the anterior and posterior regions. In the central region, the bundles intersect to form a rhomboid fiber network. Interestingly, the bundles intersect in such a way that the resultant force between the acute angles of the rhomboids run parallel to the internal circumference[40, 107]. In the deep layer of the meniscus, fibrils with a diameter of 120 nm form bundles of various thicknesses which run primarily circumferentially. In the interior and central thirds, these circumferential bundles are interwoven radially by narrow fiber

structures[41, 91]. At half the height of the meniscus' cross-section, thick radial fibers are present

which connect to the loose connective tissue of the joint capsule[107].
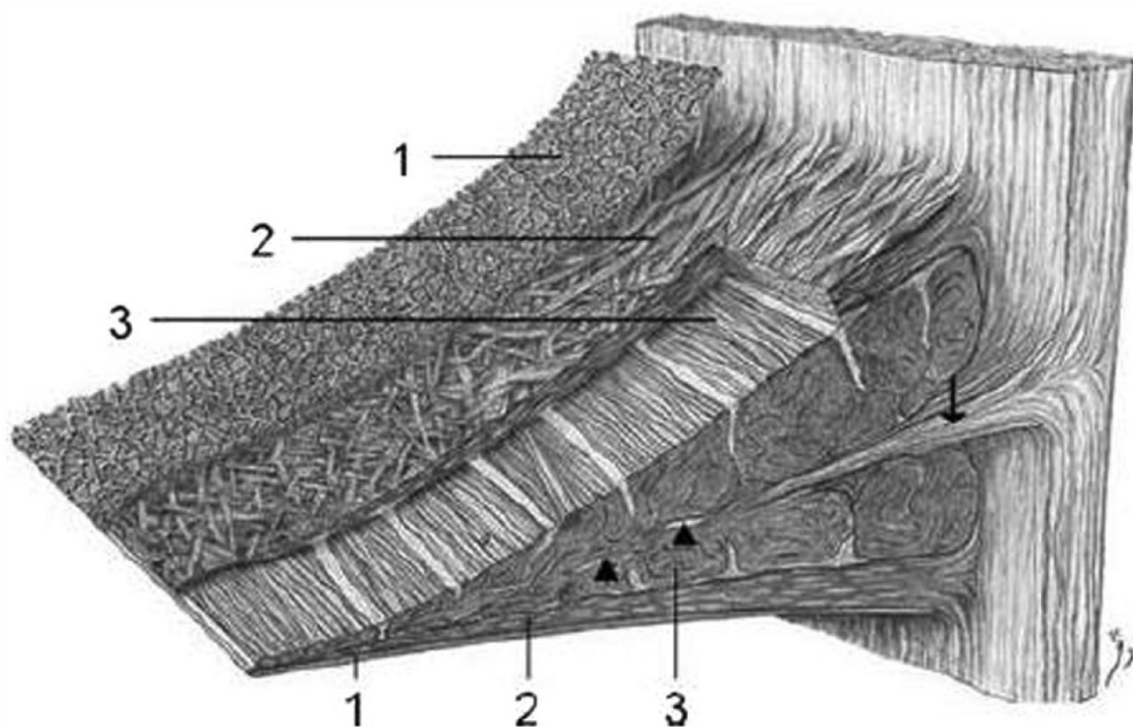
Figure 3 Schematic diagram of collagen fiber ultrastructure and organization in the meniscus. 1 represents the superficial network; 2 the lamellar layer; 3 central main layer, and the arrows represent the radial interwoven fibers[41].

1.3.6.2 Neurological and Vasculature Anatomy

The meniscus is relatively avascular with a limited blood supply in its outer 10-30%. This

area is relatively well vascularized, which allows for meniscal healing in this portion. The

remaining portion of the meniscus receives nourishment via diffusion or mechanical pumping of

the synovial fluid and has a poorer healing potential. Nerve fibers penetrate the capsule and

follow the vasculature to the periphery and the anterior and posterior horns, where the nerve

fibers are most concentrated. The central third of the meniscus is innervated, but to a lesser

degree than the outer third[41]. As a result, the vascularized portion is referred to as the red-red

zone, the central third is the red-white zone, and the inner third is the white-white zone.

1.4   Meniscus Biomechanics

Although the meniscus was once thought to be an embryonic remnant, it is now known that it performs essential biomechanical functions[41]. Specifically, the lateral meniscus carries as high as 70% of the lateral load and the medial meniscus as much as 50% of the medial load of the joint[138]. Since the femur and tibia contact at one point on each side, without a meniscus to disperse the load across the joint, the forces transmitted would be large and concentrated. These peak stresses that are experienced following meniscectomy can ultimately lead to premature osteoarthritis, as shown by the direct correlation between extent of meniscectomy and the increased onset of osteoarthritis[36, 37].

The unique biomechanics of the meniscus are a result of its gross anatomy and ultrastructure. The concave proximal articulating surface conforms well to the curvature of the femoral condyles and, therefore, effectively redistributes transmitted loads by maintaining maximal congruency[122]. In addition, the compressive force transmitted to the tibial from the femur is always less than the compressive force applied by the femur[41]. This is a direct consequence of the curvature of the femoral condyles and the meniscus.

When an axial load is applied, there is both an axial component and a radial (tangential to the tibial plateau) component. The radial component works to extrude the meniscus outward; however, this is prevented by the attachments of he meniscus to the tibia. As a result, a hoop stress is generated within the tissue and resisted by the high circumferential tensile stiffness provided by the circumferential collagen fibers of the tissue. This tensile stress is transmitted to the tibia. Essentially, a portion of the axial compressive forces are transmitted to the meniscus in the form of circumferential tensile loads.

The meniscus must also have the ability to bear the axial component (which is not converted into tensile loads) and absorb shock. In this case, meniscal tissue is analogous to articular cartilage. Cartilaginous tissues exhibit biphasic viscoelastic properties in compression

[92]. Developed by V.C. Mow, the prevailing theory describes the time-dependent response of a material with two phases: a porous-permeable solid matrix and interstitial fluid flowing within the matrix [92]. Cartilaginous tissues have very low value of permeability and, as a result, high diffusive drag coefficients. When loaded in compression, the interstitial fluid is forced out of the solid matrix and a frictional drag force develops. Even at very low fluid flow speed, very large drag forces and hydraulic pressures are exerted on the solid phase. These drag forces can bear the majority of the load that would otherwise cause significant compaction of the solid matrix. Therefore, this drag force and associated hydraulic pressures are the major mechanisms for load support in cartilaginous tissues[91].

1.5   Meniscus: Injuries and Healing

1.5.1   Classification of Tears

Meniscal tears can cause pain, swelling, clicking, catching, giving way, or locking of the knee. They are typically classified according to their orientation: vertical longitudinal, vertical radial, horizontal, oblique, or complex (Figure 4) [90].

Vertical longitudinal tears occur between and tangential to the circumferential collagen fibers. These tears are typically asymptomatic considering these mechanically essential circumferential fibers are not disrupted. However, more extensive vertical longitudinal tears can eventually allow the inner portion to twist within the joint and become a bucket handle tear. This is a highly unstable tear associated with mechanical symptoms, like knee locking[90]. Vertical radial tears disrupt the circumferential collagen fibers and adversely affect the ability of the meniscus to support load[77]. Horizontal tears divide the meniscus into upper and lower portions and are typically asymptomatic. Extensive horizontal tears and oblique tears may give

rise to a flap. Flaps are mechanically unstable and lead to mechanical symptoms. Complex tears

are two or more tear types that coexist.

The location of a tear is usually classified as red-red, red-white, or white-white zone

according to the vascular supply and healing prognosis[57]. The red-red zone is fully vascular with

an excellent healing prognosis. The red-white zone has some vascularity running along its

periphery with good healing potential. The white-white zone is completely avascular and no

healing occurs.
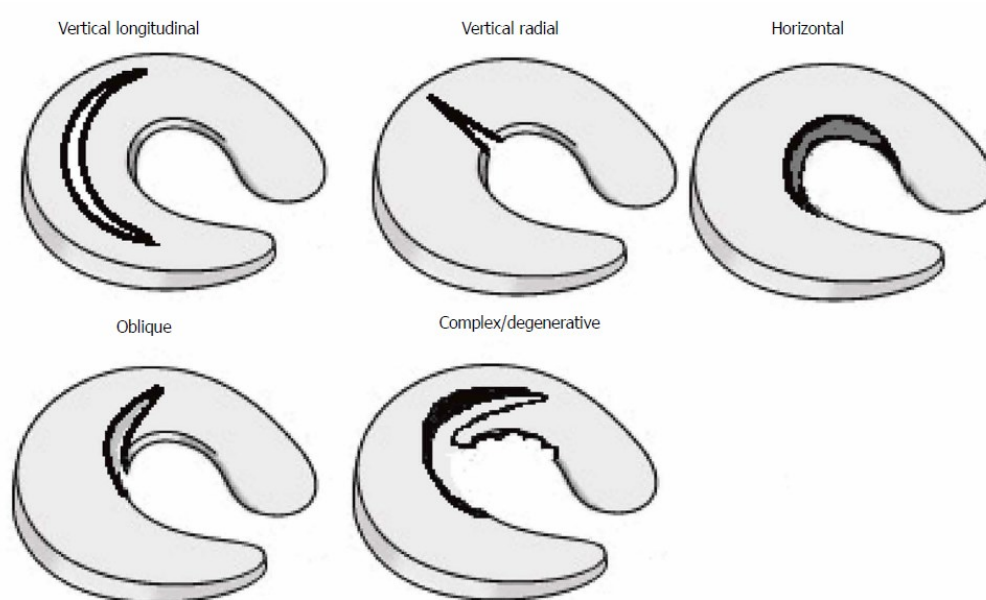
Figure 4 Meniscal tear classifications[90]

1.5.2   Epidemiology

Meniscal injuries account for about 6% of all acute knee injuries[95]. Tears in the medial

meniscus account for the majority of meniscal lesions, reported to be approximately 73-77 of

cases[54, 117]. The mean age of patients with meniscal lesions who underwent operation was 34[97, 117]. The majority of tears occur in the central or posterior portion of the meniscus[95, 97], with 76%

of tears occurring in these regions[117]. Longitudinal tears are the most common tear

representing 34% of all tears[54, 97, 117]. This is followed closely by bucket-handle tears at 30%,

then all other tear types occur at much lower frequencies[54].

1.5.3 Meniscal Healing and Treatment Options

Tear pattern, location, vascularity, and pain are important factors to determine a course

of action. The first decision once a meniscal tear is diagnosed is whether to treat surgically or

without intervention. Not all tears cause clinical symptoms and as long as the peripheral

circumferential fibers are left intact the meniscus will still perform its biomechanical function[34].

Tears that might be left alone are stable tears less than 5 mm vertical, oblique, and radial

tears[34]. One study showed that after an average of 4.3 years only 12% of patients required

surgical treatment[144] . Common treatment protocols include exercise and physical training to

improve knee function and reduce joint pain[90].
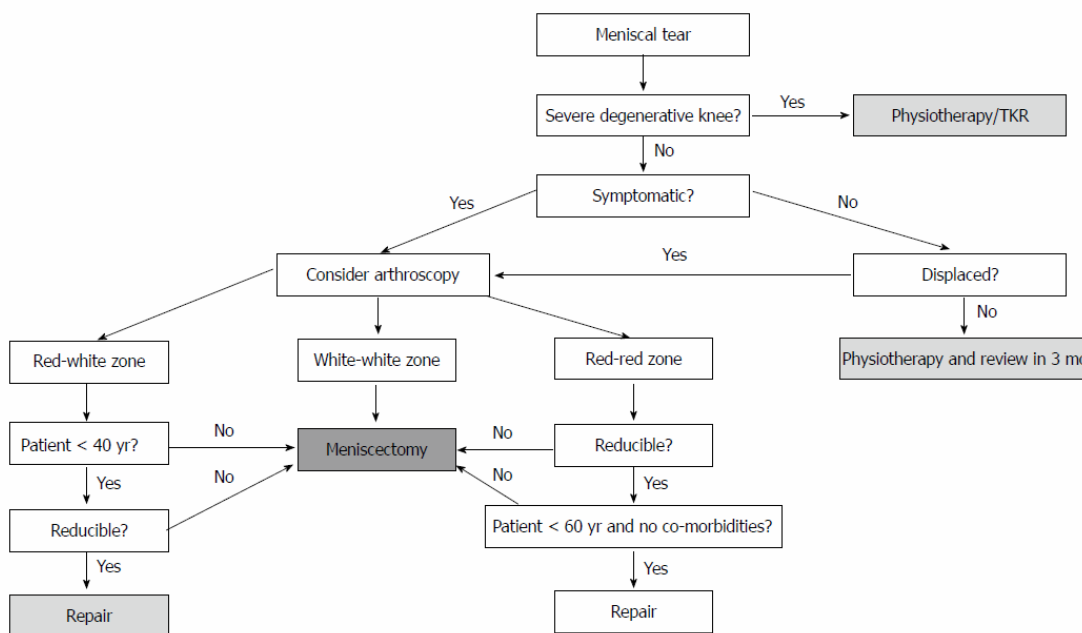
Figure 5 Meniscal tear treatment decision tree[90].

Once surgical intervention is deemed necessary, the choice is between arthroscopic

repair and meniscectomy, whether be it partial or total. The location of the tear becomes

crucial when considering this decision. Tears that are suitable for repair include traumatic tears

in the red-red zone (within 3 mm of the meniscosynovial junction) that are greater than 7 mm in

length and have not sustained major structural damage. Some tears are questionably repairable

if the tear is in the red-white zone (3-5 mm from the meniscosynovial junction) and a large

portion of the meniscal body has been damaged[34].

If the tear is unsuitable for repair, then the only choice left is to excise the damaged

tissue. If the peripheral rim is intact, then the meniscus is a candidate for partial meniscectomy.

If the peripheral rim has been disrupted, then the only choice is total meniscectomy.

1.5.4   Meniscal Repair Techniques

Arthroscopic repair first requires the use of posteromedial and posterolateral incisions.

There are two basic types of arthroscopic repair: inside-out and outside-in. The inside-out

technique remains the gold standard[48], in which the sutures are placed under arthroscopic

control using a cannula system from the ipsilateral portal in a vertical mattress suture in the

desired area of the meniscus. The suture is passed through the meniscal body and capsule using

a needle. Then the suture is captured under direct vision through the posterior incision, and the

sutures are tied over the capsule. The number of sutures depends on the amount of damaged

tissue and the sutures can be placed both on the superior and inferior sides of the meniscus.
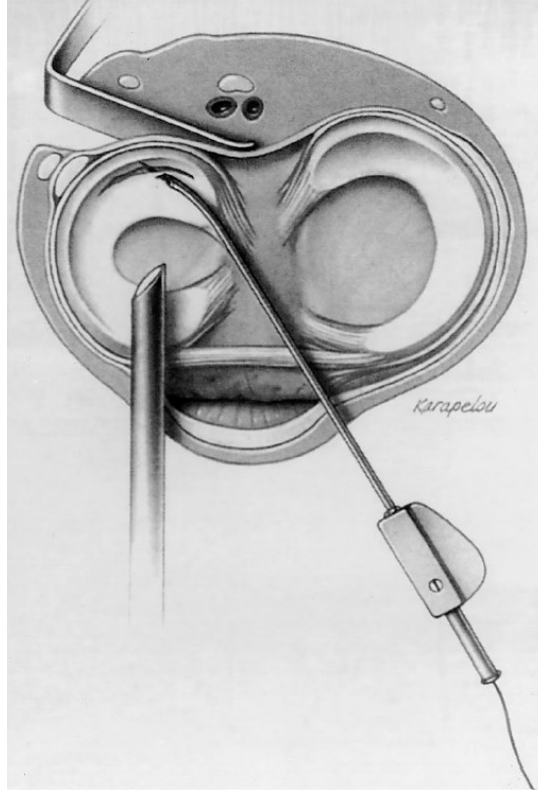
Figure 6 The inside-out technique [84].

The outside-in technique begins with a spinal needle passed through the capsular bed, across the tear and through the meniscus body under arthroscopic control. The repair suture is passed through the spinal needle and retrieved within the joint. Using Johnson's technique, a second spinal needle is inserted at a nearby site and the suture is brought back out through the capsule and tied over the capsule[34]. Using Warren, Morgan, and Cassells' technique, the suture is grasped inside the joint, pulled through the anterior portal, a knot is tied on the end of the suture, and the suture is pulled back into the joint and pulled against the meniscal body. The other end of the suture is tied with adjacent sutures together over the capsular bed[34].
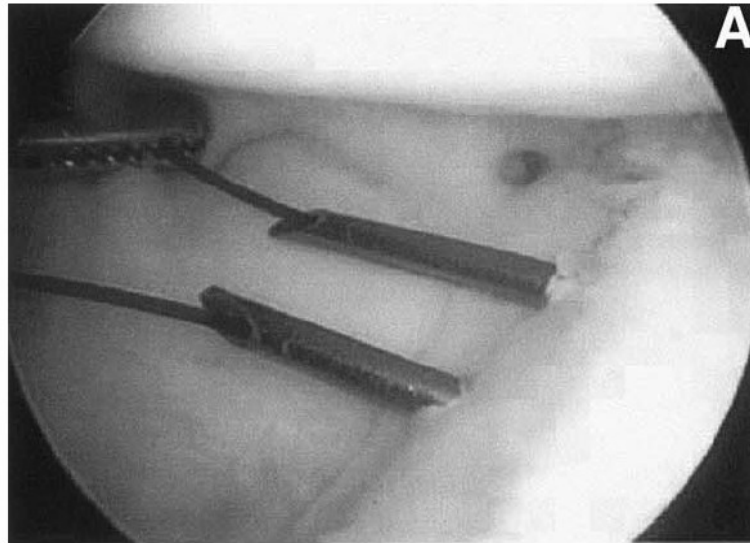
Figure 7 Arthroscopic view of the outside-in repair technique [120].

Second generation meniscal repair devices have allowed for the development of all-inside techniques. These devices are suture based devices consisting of an anchor component and a sliding knot[90]. However, these devices are not without drawbacks including increased cost, retained polymer fragments, chondral injury, and a high rate of pullout during insertion[89]. These devices have been found to have success rates of 83% at a mean 30 month follow-up[12]. However, more long-term data is needed to make any conclusions.

Several studies have attempted to establish the optimum repair technique. Grant et al. performed a systematic review of 19 studies investigating different repair techniques. No difference in clinical failure rate or subjective outcome measures was found between inside-out and all-inside meniscus repair[48]. Nepple et al. performed another systematic review of 13 studies comparing inside-out and all-inside techniques with a minimum 5-year follow-up. The failure rate of inside-out meniscal repair ranged from 0% to 26.9% with a pooled failure rate of 22.3% and the failure rate of all-inside meniscal repair ranged from 4% to 28.6% with a pooled failure rate of 24.3%. Therefore, no significant difference between techniques could be concluded.

1.6 Total versus Partial Meniscectomy

1.6.1 Clinical Outcomes

The menisci are treated in over a million surgeries annually in the United States [81].

However, the importance of menisci was not always known. Originally, it was believed that the

menisci served no functional purpose and they were often excised through open total

meniscectomy. Fairbank was the first to report adverse outcomes after total meniscectomy.

Specifically, after total medial meniscectomy, radiological findings indicated that 43% of patients

had formed an anteroposterior ridge projecting downward from the margin of the femoral

condyle, 32% had narrowing of the joint space on the side of the operation, and 18% had

flattening of the marginal half of the femoral articular surface. These changes could be seen as

soon as 5 months after the operation and progressed with time[38]. In addition, Roos et al. found

that knees that underwent total meniscectomy had a relative risk of 14 to develop osteoarthritis

compared to the opposite non-operated knee[117].

As a result, more recently there has been a shift toward preserving as much meniscus as

possible with partial meniscectomy. Arthroscopic partial meniscectomy is the most common

orthopedic procedure performed in the United States and the gold standard for the treatment

of meniscal tears[29]. Approximately 700,000 arthroscopic partial meniscectomies are performed

annually, with annual direct medical costs over $4 billion[123]. The purpose of this procedure is to

remove torn meniscal fragments and trimming the meniscus back to a stable rim. The major

advantage of this procedure is that the peripheral rim of the meniscus is preserved and the rim

is responsible for the majority of the biomechanical function of the meniscus[57].

Short term clinical results of partial meniscectomy are excellent. Northmore-Ball et al.

found 90% of patients had either good or excellent satisfaction following arthroscopic partial

meniscectomy compared to only 68% of those who had undergone arthroscopic total

meniscectomy at a 4.3 year mean follow-up time[97]. At 15 year follow-up, it was found that 88%

had good or excellent results in ACL stable knees[21].

However, it is obvious when analyzing long term results of partial meniscectomy that

the procedure only delays and does not prevent the onset of osteoarthritis. Jaureguito et al.

performed a retrospective study of 47 arthroscopic partial lateral meniscectomies with a mean

follow-up of 8 years and observed knees graded as excellent or good decreased from 92% to68%

from the time of maximal improvement to the follow-up time[56]. Additionally, they found that

although 85% of patients returned to preinjury levels after the procedure, only 48% maintained

this level at follow-up. The results seem to be worse for athletes whose knee joints are

subjected to higher loads. Jorgensen et al. studied 147 athletes with isolated meniscal injury at

4.5 and 14.5 year follow-ups. The frequency of complaints increased from 53% to 67%, knee

instability increased from 10% to 36%, and radiologic signs of degeneration rose from 40% to

89%[58] .

1.7   Joint Contact Mechanics

The clinical outcomes can easily be explained by biomechanical studies of partial and

total meniscectomies. Lee et al. performed an excellent study using human cadaveric knees that

were tested under an 1800 N load with an intact meniscus, 50% radial width partial

meniscectomy, 75% radial width partial meniscectomy, segmental meniscectomy, and total

meniscectomy (Figure 8).   A direct correlation was observed between amount of tissue

removed, increase in contact stress, and decrease in contact area[70]. Segmental meniscectomy,

in which the peripheral rim was completely disrupted, produced an almost identical outcome as

total meniscectomy. This demonstrates that it is the peripheral rim that is responsible for the

majority of the biomechanical function of the meniscus.
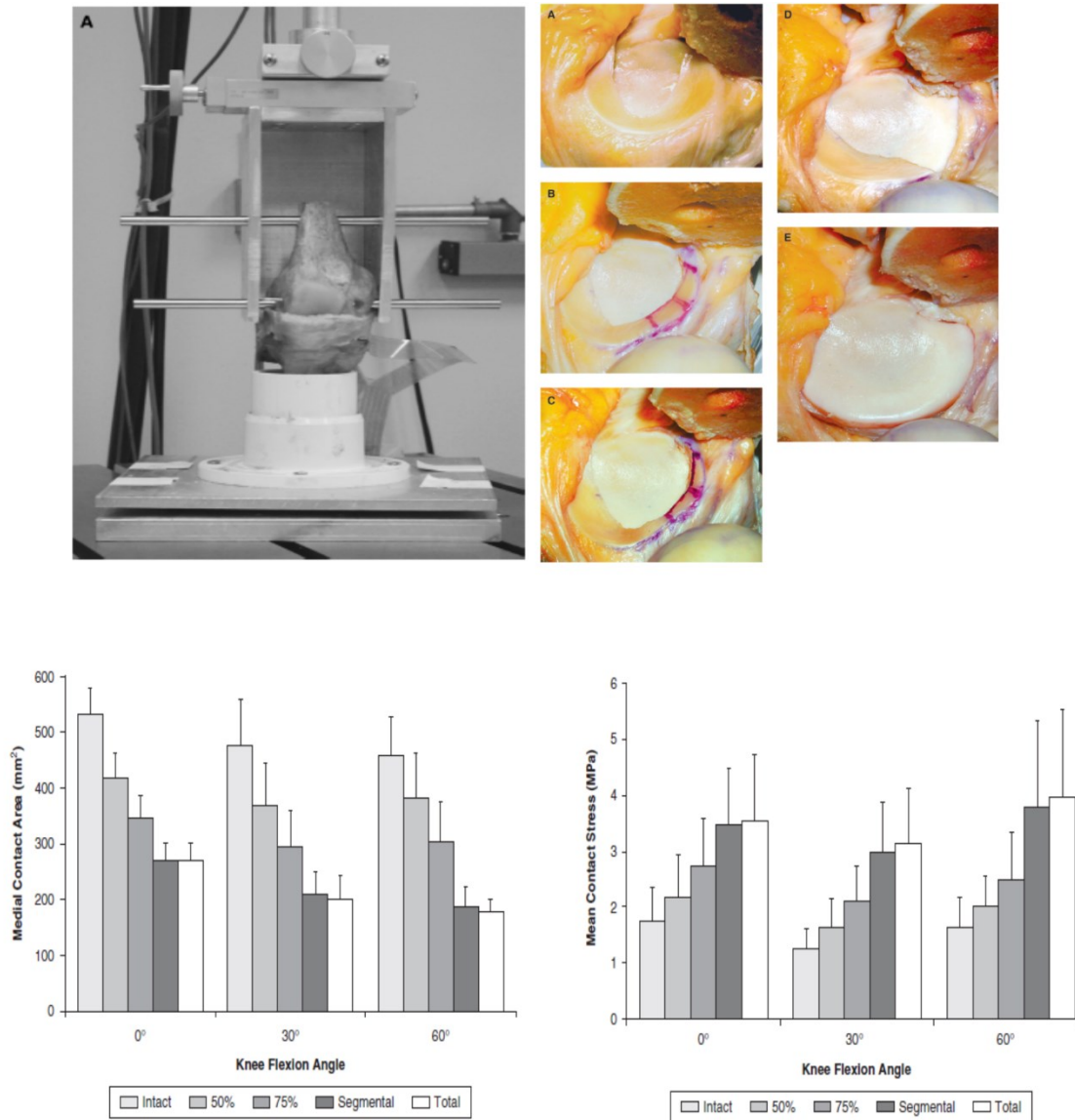
Figure 8 (Top-left) Knee specimen uniaxial compression setup. (Top-right) The five posterior medial meniscetomy conditions: intact medial meniscus (A), 50% radial width medial meniscectomy (B), 75% radial width medial meniscectomy (C), segmental medial meniscectomy (D), and total medial meniscectomy (E). (Bottom left) Medial contact areas for the posterior medial meniscectomy conditions at 0, 30 and 60 degrees flexion. (Bottom right) Medial mean contact stress for the posterior medial meniscectomy conditions [70].

Bedi et al. performed a similar study in which the meniscus was tested intact, radially teared involving 30% of the meniscal width, 60% of the width, 90% of the width, treated with an inside-out repair with horizontal mattress sutures, and a partial meniscectomy[14]. They witnessed a similar trend as Lee et al. except they observed little change between intact, 30%,

and 60% meniscal width radial tears (Figure 9 and Figure 10). There was a significant increase in peak contact pressure from 60% to 90% meniscal width further demonstrating the importance of the peripheral rim of the meniscus. Interestingly, there was no change after performing an inside-out repair and partial meniscectomy had higher peak pressure and less contact area than all other conditions. Additionally, the highest peak pressures were found in the posterocentral region of the meniscus, the region which has the highest occurrences of meniscal lesions [54]. These observations support that the hypothesis that partial meniscectomy adversely affect the biomechanics of the knee.
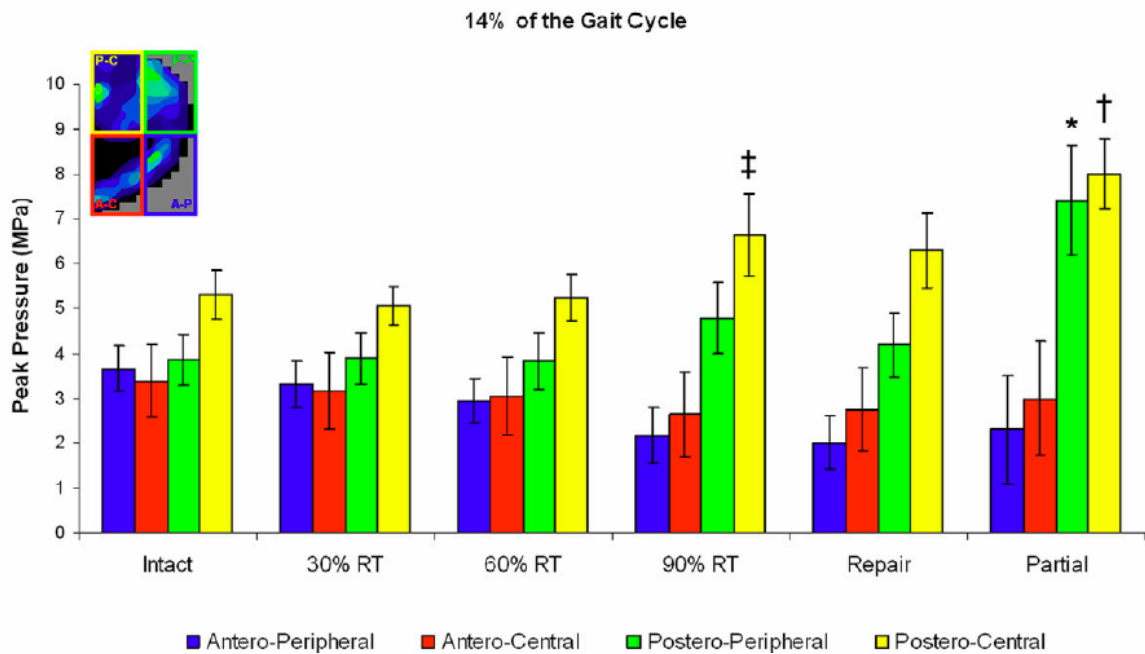
Figure 9 Peak contact stress in each region of the human native meniscus[14].

Fig. 4-B
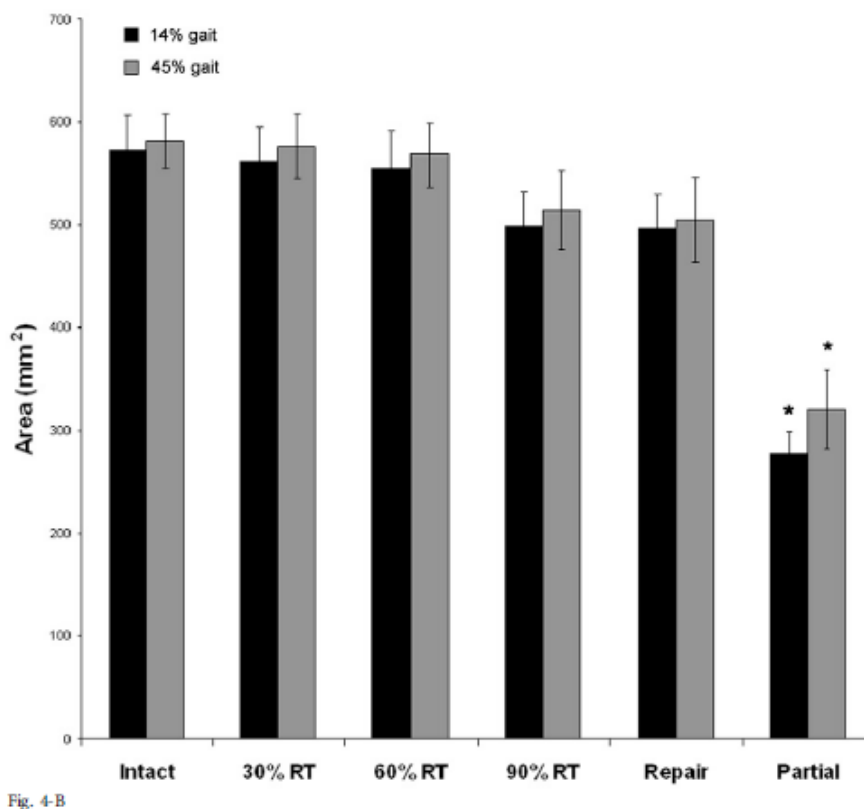
Figure 10 Contact area of the human meniscus when intact, 30% radial tear, 60% radial tear, 90% radial tear, repaired, and partial meniscectomized at 14% and 45% gait[14].

1.8   Meniscal Replacement

1.8.1   Allografts

In an attempt to damaged menisci, allograft transplantation has been investigated as an option. The concept rests on the idea that the dense extracellular matrix could be immediately functional, infiltrated by host cells, and then remodeled *in situ*. It has been shown that allografts possess the appropriate mechanical properties, especially regarding circumferential tensile strength[115]. In fact, this treatment has shown clinical significant improvements in terms of pain, swelling, and function over meniscectomy controls [115].

However, allograft fixation has been a major challenge. Three techniques for fixation are available: suture, bone plug, and bone trough (Figure 11)[3]. In suture fixation, the graft is cut at the posterior and anterior horns, a suture is attached to the horns then pulled through bone

tunnels and tied over a cancellous screw[22]. For bone plug fixation, the allograft is harvested

with bone plugs of the sites of attachment of the meniscus. These bone plugs are then fit into

bone tunnels drilled during implantation[2]. Bone trough fixation is the most difficult method of

fixation. In this method, the allograft is harvested with a bone block that contains both the

anterior and posterior sites of attachment. During implantation, a trough is removed from the

tibial plateau and the bone block is fit into the trough. Although most complex, this method

provides the best fixation of the three methods[71].
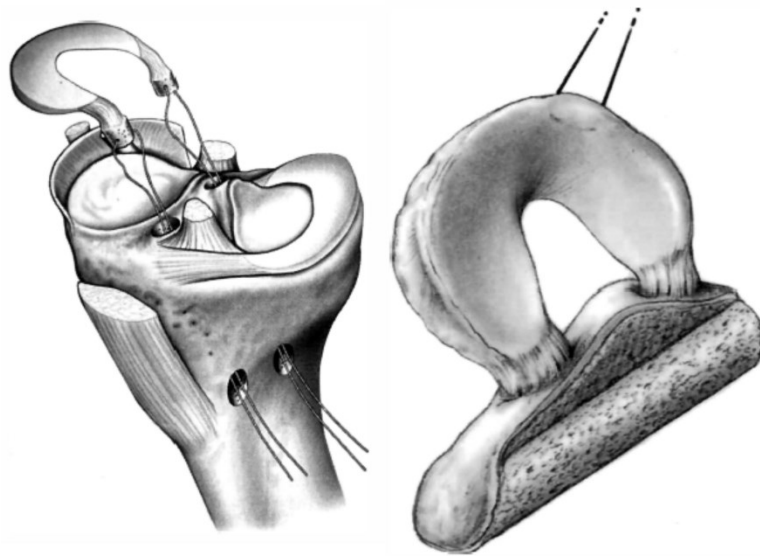
Figure 11 Allograft fixation strategies: bone plug (left) and bone block (right) [115].

Although initial mechanics are excellent, allografts suffer from significant issues. First,

the risk of disease transmission and immune response must be considered[140]. In addition,

allografts may be too dense for a robust host cell infiltration[98]. The grafts must be size matched

as well or else issues with stability and load transmission may result[115, 121]. Finally, the supply of

meniscal allografts is quite limited because healthy allografts can only be harvested from young

donors who did not experience orthopaedic trauma. These significant limitations provide

motivation for the development of engineered meniscal replacements.

1.8.2   Tissue Engineering Strategies

In an attempt to address the disadvantages of allografts, there have been several attempts to develop synthetic meniscal replacements. Early work experimented with non-resorbable replacements composed of Dacron, Teflon, polyvinyl alcohol hydrogel, and carbon fiber composites[65, 125, 137, 147]. Due to excellent time zero mechanical properties, the initial results improved function but long-term deformation and wear released debris particles caused an immunological response[88]. The success of a non-resorbable implant seems improbable since the implant must survive over time in the harsh environment of the joint.

Resorbable tissue engineered scaffolds have become a heavily researched field in the treatment of meniscal injury. The success of a meniscus scaffold relies on the ability to meet the following criteria[7]:

1) Induce cellular ingrowth and promote new fibrocartilage formation

2) Have a porous structure to allow for cellular ingrowth and diffusion of nutrients

3) Be biodegradable with a degradation profile that mirrors neo-tissue formation and remodeling

4) Have initial mechanical properties that allow the implant to withstand normal loads in the joint without losing structural integrity until neo-tissue can assume load-bearing

These scaffolds have been developed utilizing both synthetic and natural materials.

Therefore, researchers have investigated the possibility of meniscal regeneration either with biological (including collagen[82], hyaluronan[68], and silk fibroin[50]) or synthetic materials (polycaprolactone (PCL)[68, 69], polylactic acid[106], poly vinyl alcohol[65], polyglycolic acid[61], and polyurethane[78]). Manufacturing methods have included electrospinning, 3D printing, and fiber based technologies. Composite implants have increased in popularity because no single material has successfully replicated the complex anisotropy of the native meniscus.

Among the tissue engineered solutions undergoing clinical trials are the collagen meniscus scaffold (CMI) and Actifit, a porous polyurethane scaffold. However, the efficacy of these homogenous scaffolds remains unclear in the clinical data [55] and their mechanicals are well inferior of those of the natives[118]. Actifit (Orteq Ltd), a porous polyurethane, has been commercialized in Europe for partial meniscus replacement (Figure 12). Interestingly, the literature does not support the ability of this implant to be a load sharing device. In the first generation device, Tienen et al. utilized a highly porous estane polyurethane sponge that had initial compressive properties below that of the native meniscus[133] and tensile properties have never been published. The device allowed for tissue ingrowth but the compressive properties remained significantly less than native tissue. This prompted the authors to study a poly(caprolactone) polyurethane copolymer which stimulated less of a tissue reaction than the estane polyurethane[134]. However, even at 2-year follow-up this implant had an inferior compressive modulus, scaffold fragmentation with no evidence of mass degradation, and the implant did not prevent cartilage degradation[145].

Figure 12 Lateral (left) and medial (right) Actifit products [31].

The success of Actifit as a partial meniscus implant is clouded by inconclusive results. In an ovine model, there was found to be no significant differences between Actifit and a partial meniscectomy at 1 year[79]. The degradation of polyurethane also may hinder the formation of neo-fibrocartilaginous tissue[134]. In a human, proof of concept clinical trial, the implant was

shown to provide relief of symptoms and allowed for tissue ingrowth up to 12 months[141] but has

exhibited poor survivorship[139].

The Collagen Meniscus Implant has been commercialized by Ivy Sports Medicine (Figure

13). Collagen provides a substrate for neo-tissue ingrowth but degrades far too quickly to act as

a scaffold. Therefore, the collagen is heavily cross-linked to increase its mechanical strength and

slow degradation. The final formulation included collagen, hyaluronic acid, and chondroitin

sulfate. In the literature, this implant had strong preliminary results in canines but there have

been issues associated with the toxic byproducts of glutaraldehyde crosslinking and the

mechanical properties of the implant are well below that of native meniscal tissue[20, 118, 129].
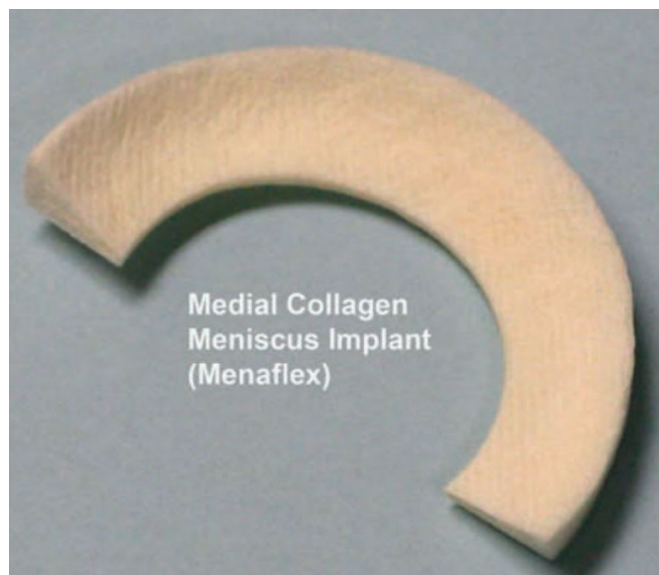
Figure 13 Collagen Meniscus Implant from Ivy Sports Medicine[116].

1.9   Three Dimensional (3D) Printing

3D printing is an additive manufacturing technique that has gained recent attention in

the tissue engineering field. printing forms three-dimensional objects by depositing material in

layers onto each previous layer, according to a Computer Aided Design (CAD) model. This has

been developed as an alternative to conventional scaffold manufacturing methods including

fiber-bonding, solvent casting, particulate leaching, membrane lamination, melt molding,

thermally induced phase separation, and gas foaming. None of these scaffolds give researchers

the ability to build a scaffold with a completely interconnected pore network with large

interconnection channels, a highly regular scaffold morphology, and unprecedented

reproducibility [149].

3D printing methods can be classified in 4 groups: extrusion-based methods, particle

fusion-based methods, light induced methods, and inkjet printing methods. Typically, thermal,

extrusion based methods are utilized for making polymeric tissue engineering scaffolds. In this

method, a polymeric material is heated to the molten state, and pneumatically extruded

through a nozzle as the print head translate according to the coordinates of the CAD file. The

nozzle diameter practically ranges from 200 to 400 μm and the diameters of the extruded fibers

are approximately on the same range.

Although 3D printing has several advantages, it is not free of limitations. First, the flow

rate is a function of the nozzle diameter, the extrusion pressure, and the viscosity of the

polymer. Greater flow rates can allow for faster print times, allowing for more complex scaffold

designs. The flow rate increases with increasing nozzle diameter but this corresponds to a large

fiber diameter as well. The extrusion pressure should be maximized but is typically limited by

the 3D printer rating. The viscosity of the polymer is the most significant factor governing flow

rate. High molecular weight polymers, which are necessary for long term resorbable implants,

are very viscous. The viscosity decreases with increased temperature but this can lead to

thermal degradation leading to polymer chain scission and decreased scaffold mechanics[46].

Finally, 3D printing does not allow for molecular orientation of the printed polymer fibers unlike

draw polymer fibers used in fiber based technologies.

Lee et al. recently published a study of a 3D printed PCL scaffold for partial meniscus

tissue engineering (Figure 14). The scaffold utilized PLA/PGA microspheres which released

connective tissue growth factor (CTGF) and transforming growth factor-β3 (TGF- β3) at two

separate rates[69]. This method produced good tissue ingrowth and mechanics at 12 weeks.

However, the scaffold is very complex utilizing several materials and growth factors. Although

this solution produces good results, it may be more complicated than necessary and represents

a difficult regulatory pathway to market.

Figure 14 Lee et al. FDM printed PGA/PLA microspheres, PCL meniscus scaffold [69].

1.10 Partial Meniscus Scaffold Requirements

A partial meniscus scaffold must satisfy several requirements for success. First, there is

an anatomic requirement, the device must be of the appropriate geometric size and shape to

replace the complex geometry of the native meniscus. Next, there is the biological requirement

in which the device must be porous enough to allow for cell attachment, infiltration, and

distribution, and for the transport of nutrients and signals. In addition, there is the mechanical

requirement in which the device must possess appropriate mechanical properties to provide the

correct mechanical loading environment for infiltrating cells and support the imposed loads, and

protect the underlying articular surfaces to prevent the onset of osteoarthritis. Finally, there is

the clinical requirements which are the most significant differentiators from that of total

meniscus devices. The device must be able to be cut to fit each unique defect geometry and it must be able to be fixed to the remaining meniscal rim to allow for mechanical function and robust tissue integration.

2 Preliminary Work

2.1 Design Criteria

An analysis of the literature shows that the critical design criteria for a successful partial meniscus scaffold are pore size, tensile stiffness, and aggregate modulus. The optimal pore sizes range from 150-500 µm, a conclusion derived from several studies that observed various biomaterials with macroscopic pores in this range promoted better fibrocartilaginous tissue growth. Klompmaker et al. tested fibrocartilage tissue ingrowth into scaffolds with varying pores sizes in wedge-shaped defects in the meniscus of rabbits. Tissue ingrowth was present in all pores with sizes greater than 150 µm and up to 500 µm and 30% less tissue ingrowth into scaffolds with smaller pore sizes[64]. Baker et al. performed an *in vitro* study on the effect of nano-fibrous alignment on the development of fibrocartilage from meniscal fibrochondrocytes and mesenchymal stem cells[9]. The fiber aligned scaffolds had a tensile modulus of about 12 MPa compared to the non-aligned scaffolds, which possessed a tensile modulus of about 5.0 MPa. The fiber aligned scaffolds contained comparable amounts of ECM but the aligned fiber scaffolds had a seven-fold larger increase in mechanical properties relative to the non-aligned scaffolds, suggesting fiber aligned scaffolds with a tensile modulus of at least 12 MPa should promote fibrocartilaginous ingrowth.   De Groot et al. studied the effect of compressive modulus on fibrocartilage formation and observed a modulus of at least 150 kPa showed 80-100% ingrowth compared to 100 kPa scaffolds which only yielded 50-70% ingrowth[33].

Table 1 Design Criteria for a partial meniscus scaffold

Parameter	Range	Citations
Minimum Fiber Spacing	150 µm	33, 35, 63, 64, 141, 146
Circumferential Tensile Stiffness	101.9-143.5 N/mm^2	[104] (95% confidence interval of native stiffness)
Aggregate Modulus	>150 kPa	33

2.2   Native Meniscus Dimensions

Five native ovine medial menisci were dimensioned using image processing techniques

in ImageJ. This following parameters were measured: the anteroposterior length, meniscal

width, medial-lateral length, and inner and outer radii of curvatures. The average dimensions

can be seen in Figure 15. In addition, anterior and posterior histological slices from previous

studies were utilized to estimate the cross-sectional geometry of the meniscus. However, these

values were utilized as relatively numbers in case of processing artifact (Figure 16 and Figure

17). The dimensions of the meniscus scaffold were based upon these values.
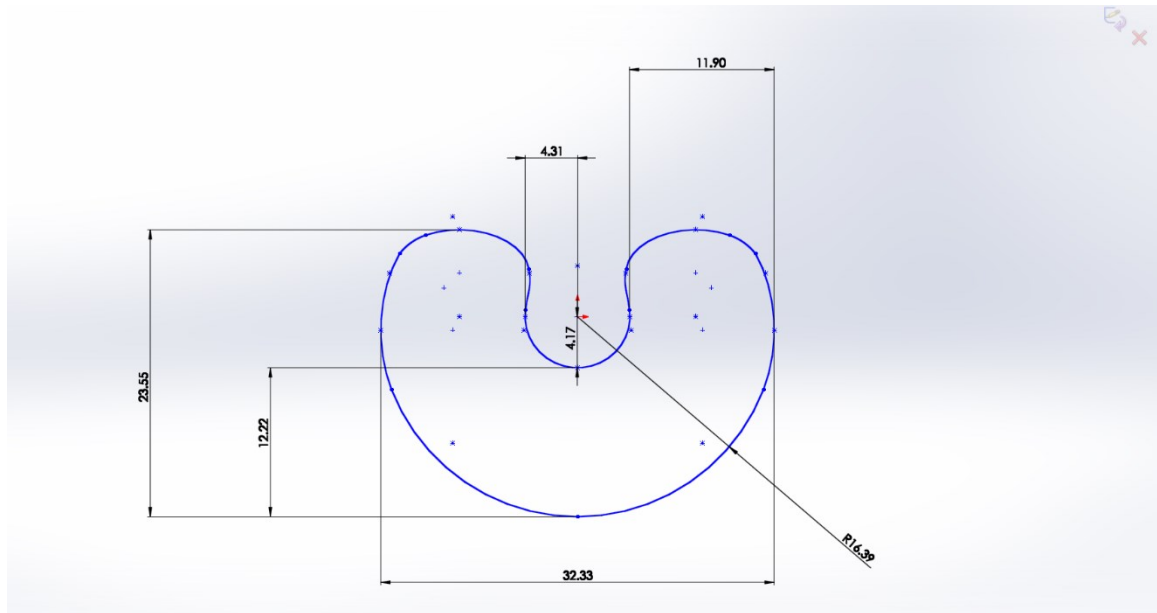
Figure 15 Native ovine meniscus dimensions.
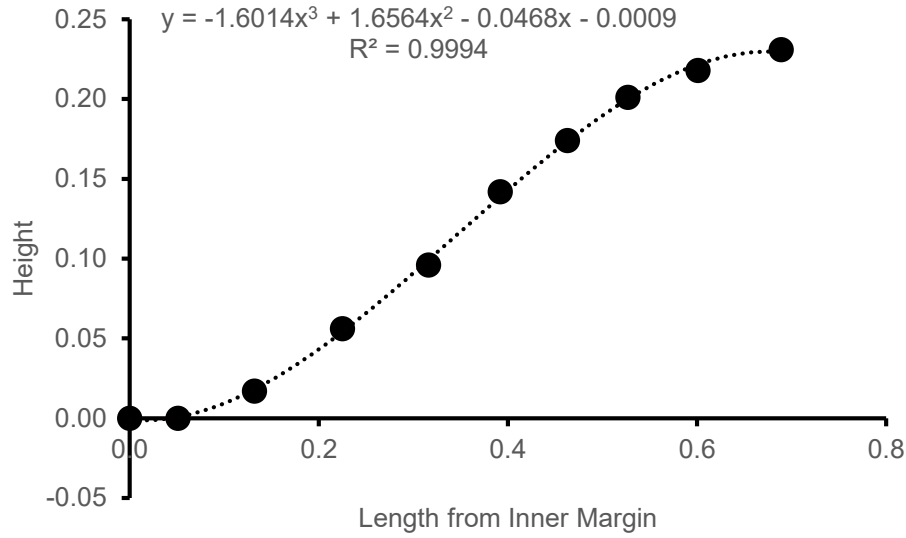
Figure 16 Relative native meniscus cross-sectional height at the posterior region as a function of distance from the inner margin.
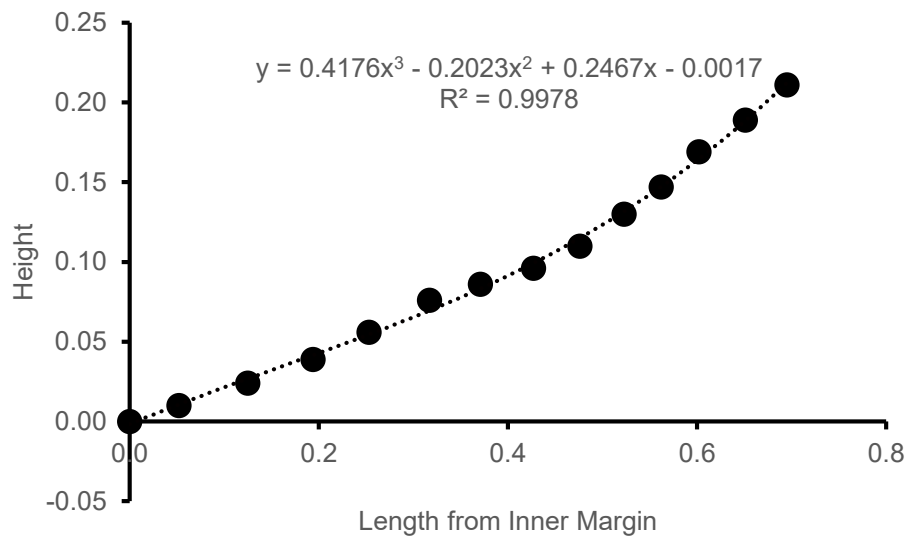
Figure 17 Relative native meniscus cross-sectional height at the anterior region as a function of distance from the inner margin.

2.3 Printing Designs

The design of the polymer network has passed through numerous design iterations. The first design possessed successive, repeating layers of radial and circumferential fibers with a step-wise reduction in the number and length of fibers, resulting in the concave surface

characteristic of the meniscus (Figure 18). This design matched the curvature of the peripheral rim very closely.
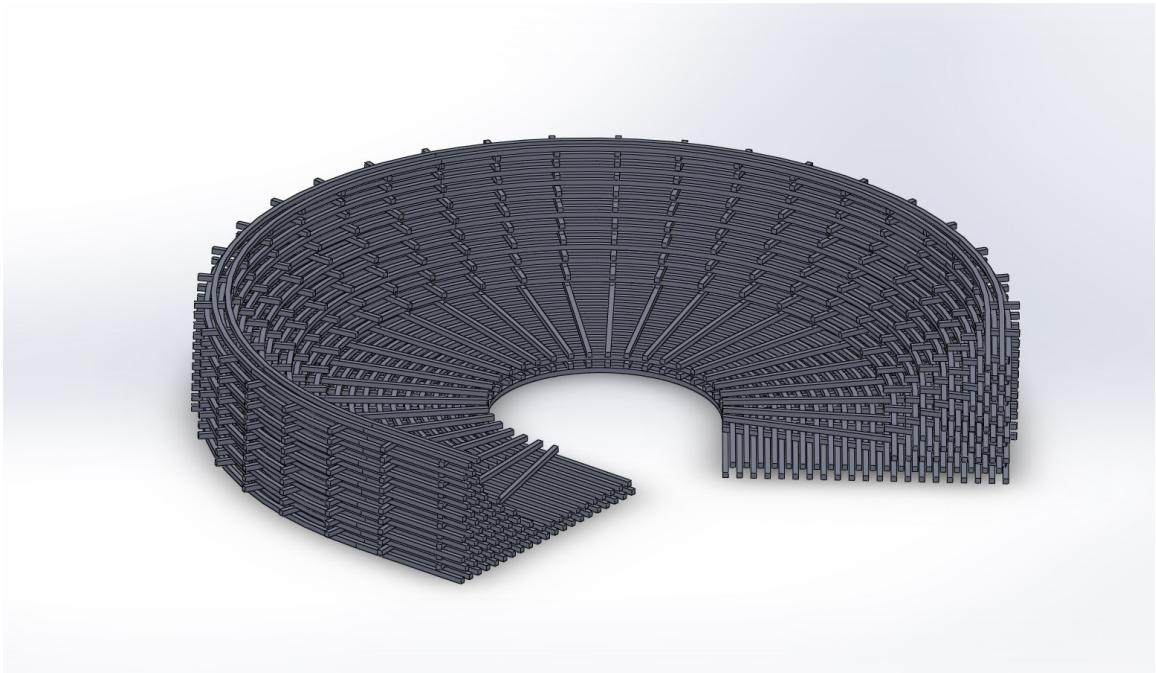
Figure 18 First generation partial meniscus scaffold 3D CAD drawing.

The second design greatly increased the number of fibers present within the scaffold when initial mechanical estimates suggested the scaffold would be significantly less stiff than the native meniscus and the body of the meniscus was reduced to only 80% of the native meniscal width, considering the indication for a partial meniscus scaffold requires an intact peripheral rim which represents approximately 20% of the width (Figure 19). In addition, flaps that extend the scaffold to capsule, above and below the meniscus, were added to provide a mechanism to fix the scaffold to the capsule.
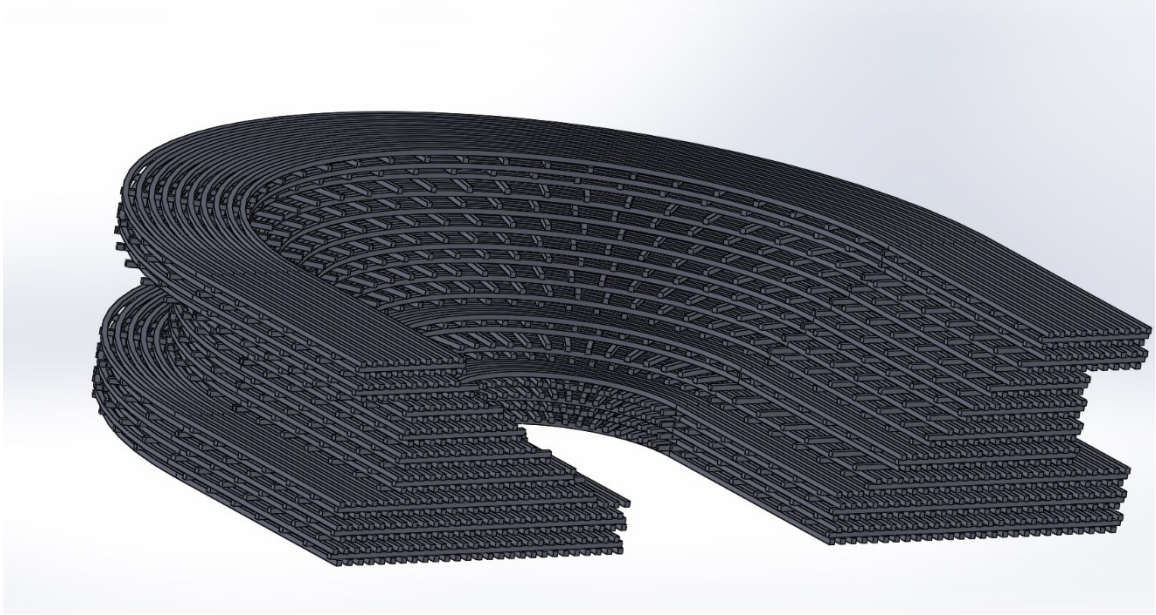
Figure 19 Second generation partial meniscus scaffold 3D CAD drawing.

In the third design iteration, the radius of curvature of the scaffold was returned to more closely match the that of the peripheral rim to allow for a better fit during implantation, according to clinician recommendation (Figure 20). The upper flap was also eliminated because the implantation was deemed unfeasible.
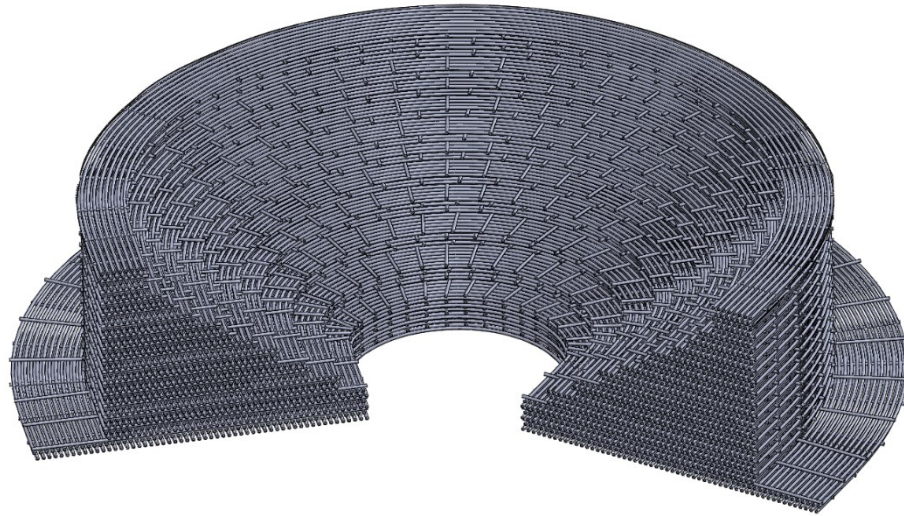
Figure 20 Third generation partial meniscus scaffold 3D CAD drawing.

In the final design iteration, the peripheral contour was changed to a smooth elliptical contour and the flaps were eliminated. Although the idea of utilizing a flap to provide a substrate for cells to infiltrate from the synovium is promising, the implantation of a device with flaps proved to be difficult in the smaller ovine model. The height of the implanted was oversized by about 10% when it was observed that the scaffold would deform to match the contour of the native meniscus when loaded in the ovine stifle joint.
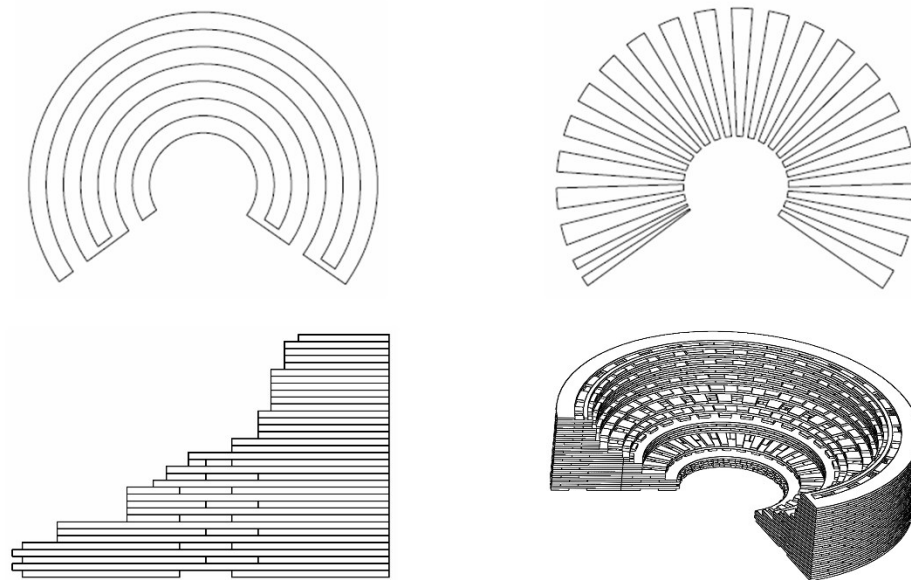
Figure 21 Final generation CAD design. (Top-left) Circumferential layer, (top-right) radial layer, (bottom-left) Cross-sectional view, and (bottom-right) 3D view.

2.4   Fused Deposition Modeling: Filament Fed 3D Printing

A significant amount of effort was completed in attempting to develop a filament fed 3D printing process for poly(DTD DD). The goal of these experiments was to determine the minimum fiber diameter that can be achieved using a Type A Machines Series 1 printer, a consumer level printer, located at the New Jersey Center for Biomaterials. The printer is controlled by the computer language, GCODE, which is written by a slicing program, Slic3r. All experiments were performed with a 0.35 mm nozzle. The main advantage of filament based 3D printing technologies is the polymer is exposed to high temperatures for only a very short period of time and, therefore, thermal degradation is minimized.

The printing process is controlled by multiple parameters that control the 3D printing process including extrusion temperature, print-head speed, layer height, extrusion multiplier, etc. Print head speed indicates the speed at which the nozzle is moving in the XY plane. Temperature is the hot end temperature of the extruder. Extrusion multiplier is a post script augmentation that scales the extrusion amount calculated by the program Slic3r. Layer height is the distance in which the nozzle is raised in the Z direction; this parameter is crucial for producing fibers in a three dimensional lattice.

Poly(DTD DD) proved to be difficult to print using a FDM printer. Although FDM possesses the advantage of minimal residence time of the polymer in the molten state, the difficulty lies in the low compressive modulus of the material, the relatively gradual thermal transition from solid to the melt, and its tendency to buckle in filament form. A 1.75 mm filament is fed by a rotating gear that holds onto the filament using a spring loaded pinch wheel. The filament then travels about 1 cm unconstrained to an aluminum block with a cylindrical hole passing through it. Next, the filament enters a 2 mm diameter Teflon tube for about 1 cm and then finally a 26 mm brass barrel. The brass barrel has a hot end attached which contains a

heating element and a thermistor. The glass transition temperature of poly(DTD DD) is about

60°C.

Using the standard extruder setup, at temperatures less than 155°C negligible extrusion

occurred and at temperatures greater than 155°C, the poly(DTD DD) filament would buckle in

the span between the feeding gear and the aluminum block.

2.4.1 3D Printer Modifications

In an attempt to avoid buckling, modifications were made to the Series 1 print.   The

first alteration to the extruder extended a Teflon tube to support the entire length of the

filament from the feeding gear to the nozzle (Figure 22) and solved the buckling issue by

supporting the filament. However, the filament would thermally expand upon entry into the

this led to the filament expanding immediately upon entry into the barrel of the extruder. As a

result, the filament would clog within the barrel.
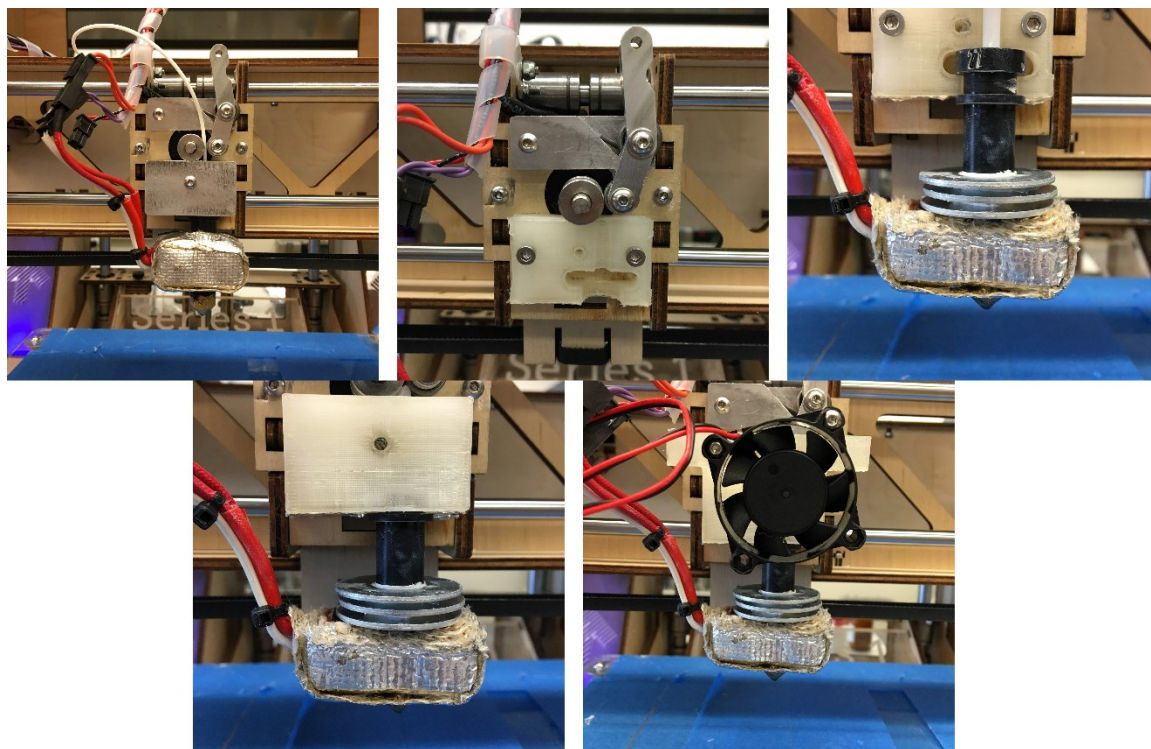
Figure 22. Summary of 3D Printer Modifications. (Top-left) Original extruder, (top-middle) with 3D printed block, (top-right) with modified barrel and heat sink, (bottom-left) with 3D printed block cover, and (bottom-right) with fan.

To resolve this new issue, the brass barrel was drilled out to about 1 cm from the end of the barrel and the Teflon tube was extended into the drilled hole. The Teflon was expected to insulate the fiber for the majority of its path through the extruder and provide a sharp thermal transition to allow for the filament to remain stiff while in the Teflon tube and then quickly become viscous enough to flow for extrusion. However, the barrel still became clogged after a few minutes of printing.   The Teflon tube is most likely slowly increasing in temperature until the poly(DTD DD) can expand and clog the tube.

Finally, a heat sink was fabricated using a stack of alternating large and small diameter washers just above the hot end. This was expected to maintain a sharp thermal transition between the feeding unit and the extruder. However, similar issues were experienced. Therefore, FDM extrusion of poly(DTD DD) through a 0.35 mm nozzle under these conditions were not feasible.

2.5 Pneumatic Extrusion Based 3D Printing with the 3D Bioplotter

When it was determined that FDM printing was not possible, the 3D Bioplotter, a

pneumatic extrusion based 3D printer with capabilities to handle temperatures up to 250°C and

pressures up to 9 bar was investigated as an alternative manufacturing method (Figure 23).

Air Pressure

Stainless
Steel
Cartridge

Head Speed

Molten
Polymer

Needle Tip
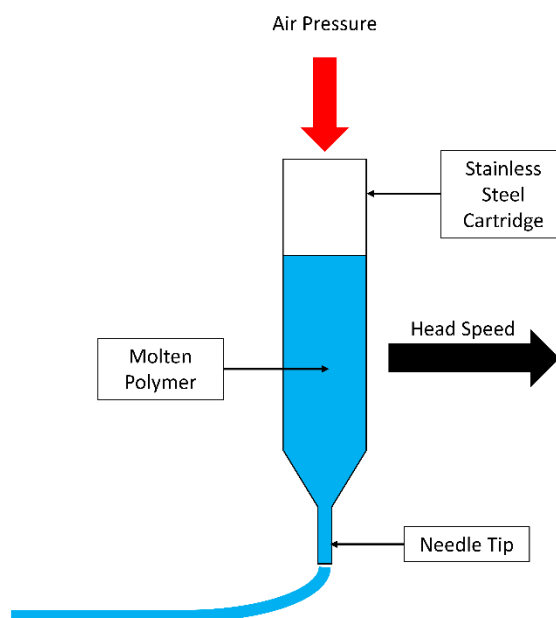
Figure 23 Schematic of 3D Bioplotter extruder.

Initial experiments with PCL were performed at 6.4 bar due to compressor limitations.

At 6.4 bar, the maximum rates at speeds at which the 3D Bioplotter could be printed are listed

in Table 1. However, significant discoloration was noticed for temperatures at 173°C in short

time frames so it was determined that lower temperatures are more desirable.

Table 2 Maximum achievable print speeds as a function of needle inner diameter and polymer temperature.

	Maximum Achievable Speed (mm/s)			
Needle	140°C	150°C	160°C	173°C
200 µm	0.3	-	-	0.5
300 µm	-	-	-	2.1
400 µm	2.1	3	-	-

Initial experiments were also performed to determine the limitations on fiber spacing that would still allow for reproducible printing. It was determined that the fibers could be defined as close as 400 μm and as far as 1500 μm. Spacing lower than this would lead to fiber fusing and, therefore, no longer a uniform porous structure. Larger spacing would lead to fiber disruptions due to a lack of support.

2.6   Optimal Design of PCL Scaffolds

The density of the fibers in PCL scaffolds was varied to optimize the aggregate modulus of the scaffolds to that of the native ovine meniscus (1-1.2 MPa)[104]. With the goal to maximize the circumferential tensile properties of the scaffold, the circumferential fibers were placed 400 μm apart. The radial fiber density was varied from 400 μm to 1500 μm. The scaffolds were printed at 155°C, 6.4 bar, and 2.1 mm/s. The scaffolds were tested in confined compression creep and analyzed according to Mow's biphasic theory.

There was no significant change in aggregate modulus over the entire achievable fiber density and the modulus was approximately three times greater than the native meniscus (Figure 24). Therefore, the circumferential fiber density had to be decreased as well.
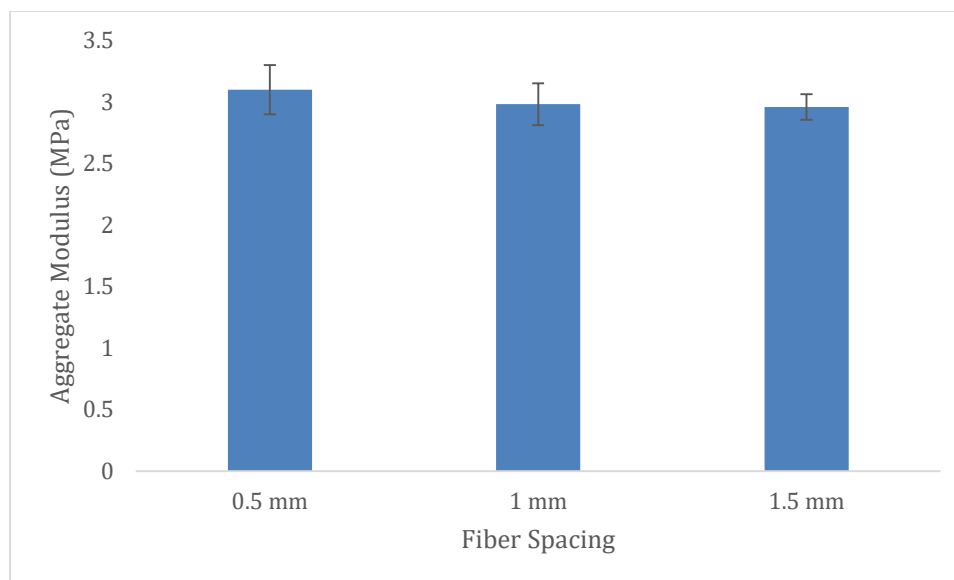
Figure 24 Aggregate modulus of scaffolds with circumferential fibers spaced 0.5 mm apart and varying radial fiber spacing.

Next, the radial fiber spacing was held constant at 1500 µm, the circumferential fiber spacing was varied from 400 µm to 1200 µm to achieve an aggregate modulus of approximately 1-1.2 MPa. The scaffolds were printed at 155°C, 6.4 bar, and 2.1 mm/s. The aggregate modulus could be effectively varied from 3 MPa to 0.3 MPa by modulating the circumferential fiber spacing (Figure 25), demonstrates that it is the densest layer that is responsible for the time-dependent compressive properties of the scaffold.
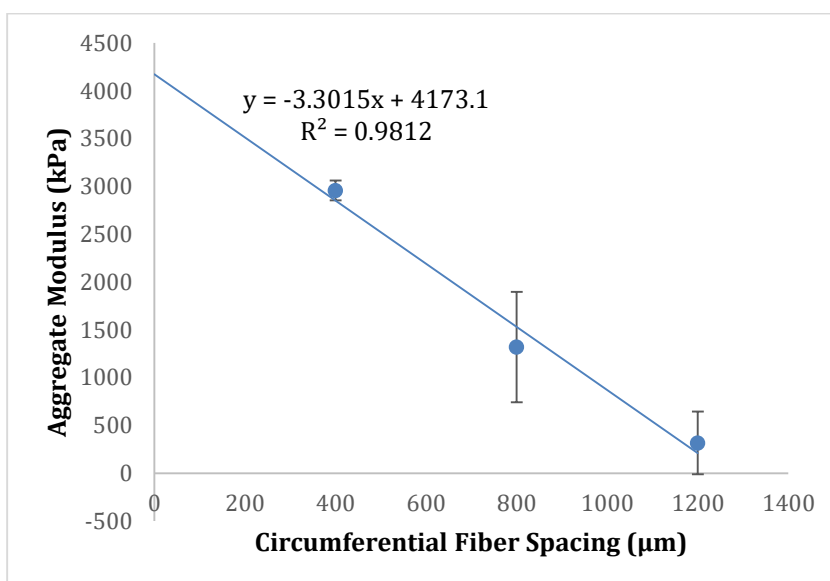
Figure 25 Aggregate modulus of scaffold as a function of circumferential fiber spacing with 1500 µm radial fiber spacing.

2.7   Poly(DTD DD) Thermal Degradation Rates

The polymer was found to be stable for at least 2 hours at all test temperatures tested

(Figure 26). At 150°C and 160°C, the molecular weight decreased by 35% and 33% at 4 hours,

and by 52% and 57% d at 6 hours, respectively. These results lead us to conclude that poly(DTD

DD) should be printed at 140°C, but can be printed at higher temperature, provided the printing

is complete in less than 2 hours to avoid significant polymer thermal degradation.
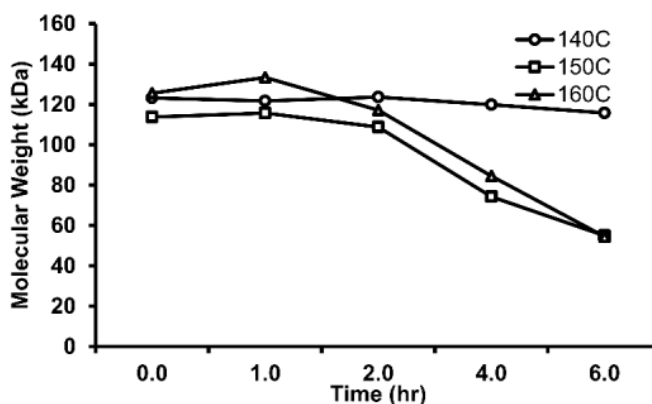
Figure 26 Thermal Degradation of poly(DTD DD) at 140, 150, and 160⁩C as measured via GPC.

2.8   Determination of Poly(DTD DD) Extrusion Temperature

Poly(DTD DD) was tested at 140°C, 150°C, and 160°C and 9 bar to determine which

temperatures could be successfully printed in a 3D Bioplotter. The two acceptance criteria were

ability to stick to the underlying layers and the qualitative rate of flow.   160°C was found to be

the minimum acceptable temperature for high quality printing (Table 3).

Table 3 Printing qualities of Poly(DTD DD) at varying temperatures.

Temperature	Sticking	Flow
140°C	---	-
150°C	-	+
160°C	+	+++

2.9   Optimal Design of Poly(DTD DD) Scaffolds

Design optimization was performed again with poly(DTD DD). The designs tested possessed radial fiber spacing of 1500 µm and varying circumferential spacing to determine the design with the optimal aggregate modulus. The scaffolds were printed at 160°C, 9 bar, and 1.6 mm/s. The aggregate modulus of scaffolds with a circumferential spacing of 1000-1200 µm was higher than those of native values (Figure 27). However, the 1200 µm design resulted in the scaffold with the properties most similar to the native ovine meniscus, suggesting the optimal design tested was a scaffold with radial spacing of 1500 µm and circumferential spacing of 1200 µm.
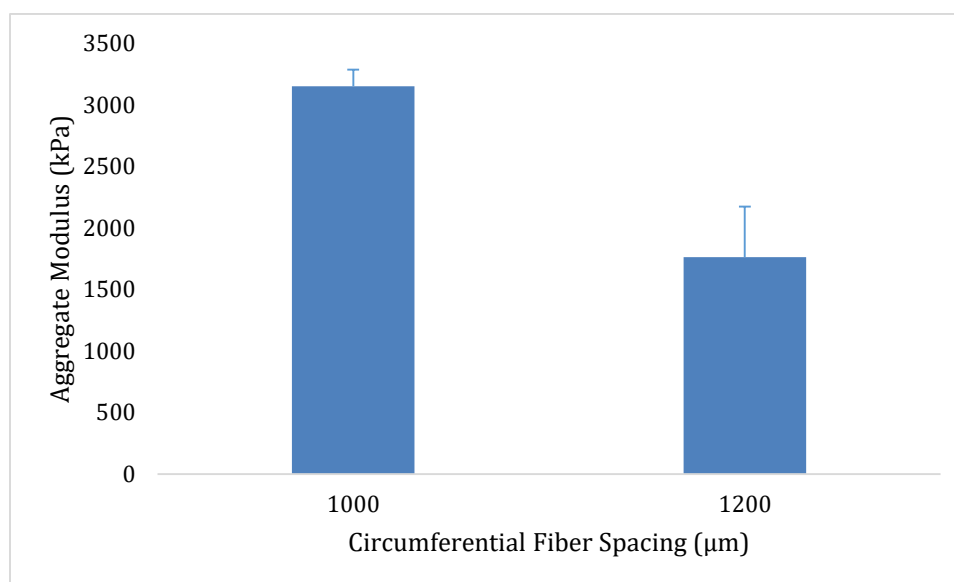
Figure 27 Aggregate modulus of Poly(DTD DD) scaffolds with 1000-1200 µm circumferential spacing and 1500 µm radial spacing.

2.10 Effect of Print Speed on Compressive Properties of Poly(DTD DD) Scaffolds

Optimization of printing speed was performed to further approach the aggregate modulus of the native ovine meniscus. Poly(DTD DD) scaffolds with radial fiber spacing of 1500 µm and circumferential fiber spacing of 1200 µm were printed at 1.2 mm/s, 1.6 mm/s, and 1.7 mm/s to assess the effect of printing speed on the compressive properties of the scaffolds. The scaffolds were printed at 160°C and 9 bar.

The aggregate modulus and permeability of the scaffolds were affected by print speed (one-way ANOVA, $p<0.01$, Figure 28). These results suggest the optimal printing speed for a 3D printed poly(DTD DD) meniscal scaffold is 160°C, 9 bar, and 1.2 mm/s.
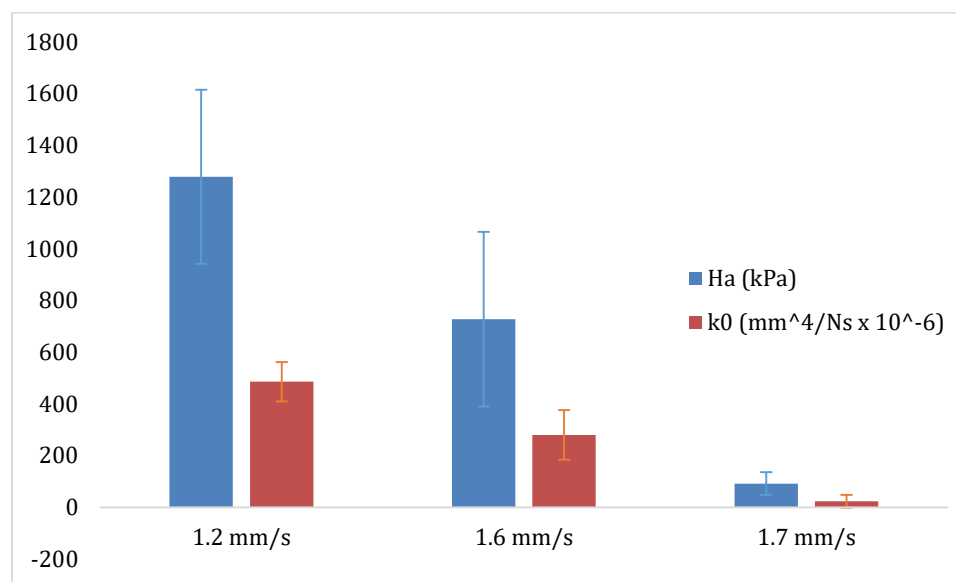
Figure 28 Effect of printing speed on Poly(DTD DD) Scaffold Compressive Mechanics

2.11 Centrifugal Collagen Method

A novel method of infusing the polymer reinforcement with collagen was necessary to be developed. In the previous state-of-the-art, collagen is simply injected utilizing a syringe. However, due to the highly connected structure of the partial meniscus polymer reinforcement, a syringe could not be inserted into the body of the scaffold without damaging the reinforcement. As a result, a centrifugal casting method was developed.

This process begins with a scaffold being placed in a negative mold and the collagen dispersion is placed atop. The scaffold is centrifuged at 650g for 30 minutes so the collagen completely fills any void space within the fibers and the scaffold is subsequently lyophilized. The collagen is then crosslinked using a EDC/NHS solution and the scaffold is lyophilized once more. Other methods were studied such as placing the scaffold on an oscillating shaker for 30 minutes but due to the high viscosity of the collagen dispersion this proved to be ineffective but the centrifugal method was highly effective (Figure 29 and Figure 30).
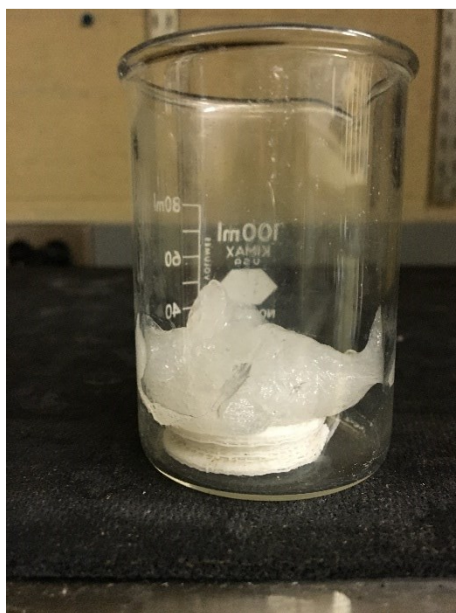
Figure 29 A partial meniscus scaffold covered with a viscous collagen dispersion after 30 minutes on a shaker at moderate speed.
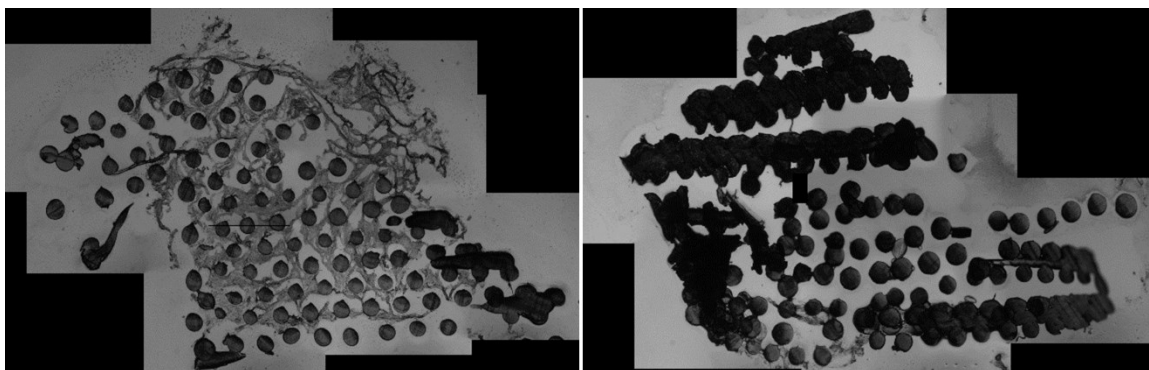
Figure 30 (Left) Cross-section of partial meniscus scaffold prepared using centrifugal casting method. (Right) Cross-section of scaffold prepared using shaker at moderate speed. Dark circles represent polymer cross-section. Light gray depicts collagen sponge.

3   Approach, Hypothesis, Aims

The goal of this thesis is to develop a hybrid poly(DTD DD) collagen-hyaluronan scaffold

for partial meniscus regeneration.

3.1   Rationale

In meniscal tissue engineering, the anisotropic architecture and mechanics of the native

tissue must be one of the first considerations when developing a meniscal replacement device

for the following reasons:

1) To be a truly functional tissue engineered scaffold, the construct must support the

   physiological loads imparted onto it,

2) The mechanical loading of the scaffold will impart the proper mechano-transduction

   signals to promote the infiltrating cells to differentiate into the correct phenotype,

   and

3) The infiltrating cells will produce aligned tissue growth in the axis of greatest

   mechanical properties.

Previous studies have revealed that scaffold alignment and physiological mechanical

stimulation are sufficient to drive MSC differentiation without the need for additional chemical

stimuli[4, 49, 130, 131]. The mechanical environment is essential for guiding the differentiation of

progenitor cells[74] and maintaining the phenotype and functionality of cells[25, 109]. Baker et al.

tested non-aligned and aligned nano-fibrous scaffolds seeded with meniscal fibrochondrocytes

or mesenchymal stem cells (MSCs) *in vitro* and observed that although the cells produced a

similar total amount of ECM, the aligned constructs experienced a significantly larger increase in

mechanical properties compared to the non-aligned constructs in the axis of alignment [9, 135].

Interestingly, the MSCs on the aligned scaffold exhibited more fibro-chondrocytic qualities, as

demonstrated by an increase in GAG production as compared to non-aligned scaffolds.

However, most devices in the literature are composed of isotropic materials and all possess inferior compressive and/or tensile properties relative to the native meniscus. For example, the tensile stiffness of both Actifit and CMI were 33% and 55%, respectively, of that of the native human meniscus (Figure 31)[118] and the compressive behavior was significantly inferior as well (Figure 32)[118]. Therefore, there is a need for a partial meniscus scaffold that is biomechanically functional with an anisotropic architecture which could potentially promote superior tissue ingrowth than previous devices.
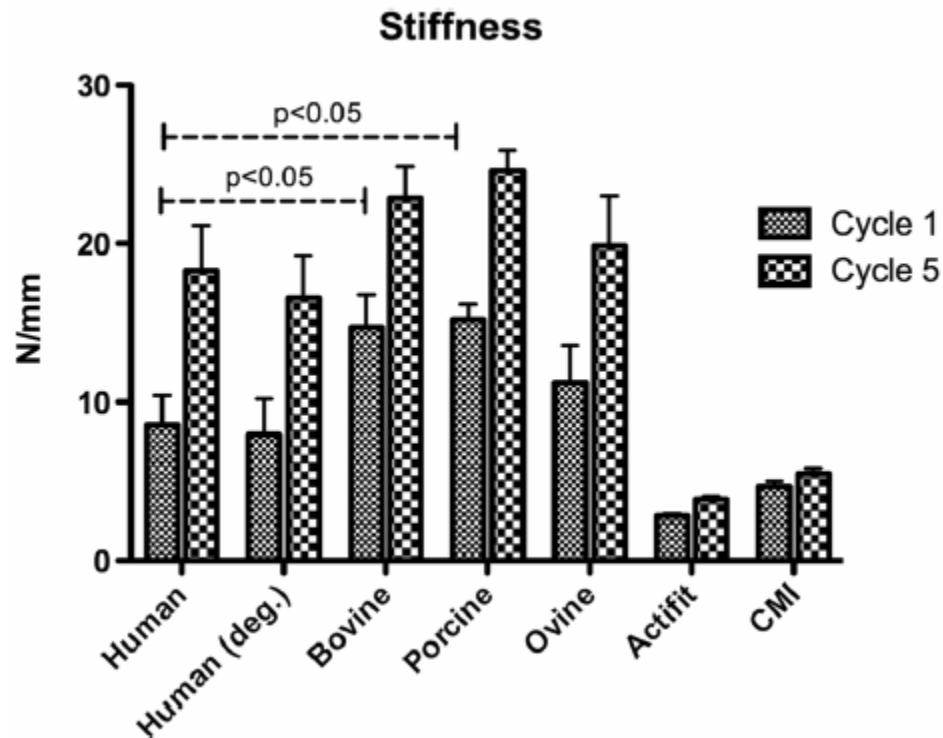
Figure 31 Tensile stiffness for rectangular specimens of various species native meniscus and two artificial meniscal constructs: Actifit and the Collagen Meniscus Implant at cycles 1 and 5[118].
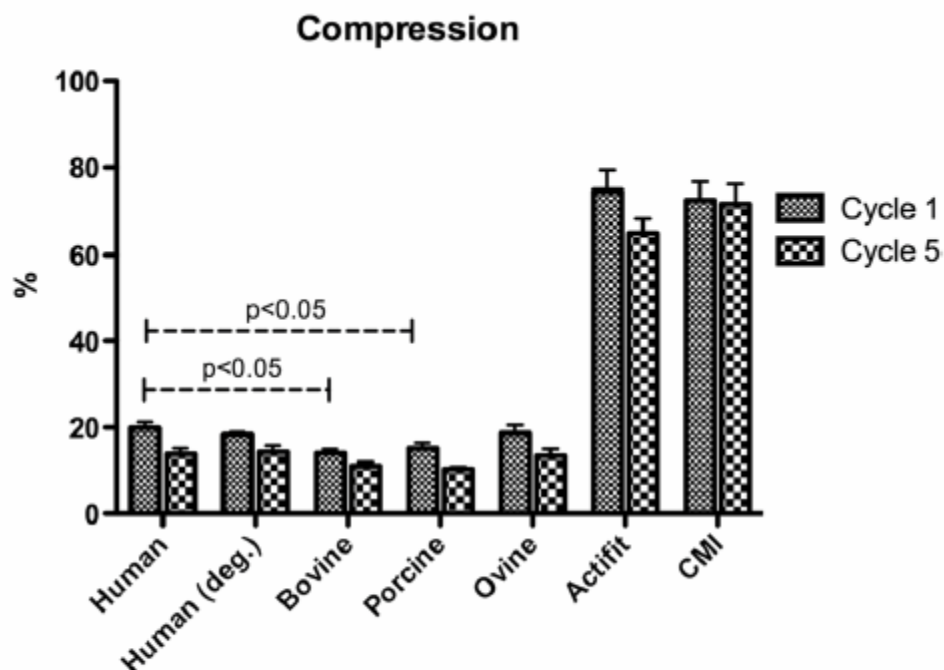
Figure 32 Compressive strain percent at 7 N for rectangular specimens of various species native meniscus and two artificial meniscal constructs: Actifit and the Collagen Meniscus Implant, at cycles 1 and 5[118].

3.2   Approach

The work described in this dissertation was based off a total meniscus scaffold which

first developed by Eric Balint and then modified by Aaron Merriam and Jay Patel in the

Orthopaedic Research Laboratories at Robert Wood Johnson Medical School. This patented

technology consists of a polymer reinforced collagen-hyaluronan sponge[44] . The polymer fibers

are hand woven in a pattern that mimics the semi-lunar wedge shape of the native meniscus.

The fibers provide circumferential tensile strength to the scaffold and the collagen sponge fills

the bulk of the scaffold providing compressive strength and a biological substrate for cells to

attach, infiltrate, and remodel[10]. The implant degrades over time and host cells remodel the

scaffold into a functional, load-bearing tissue.
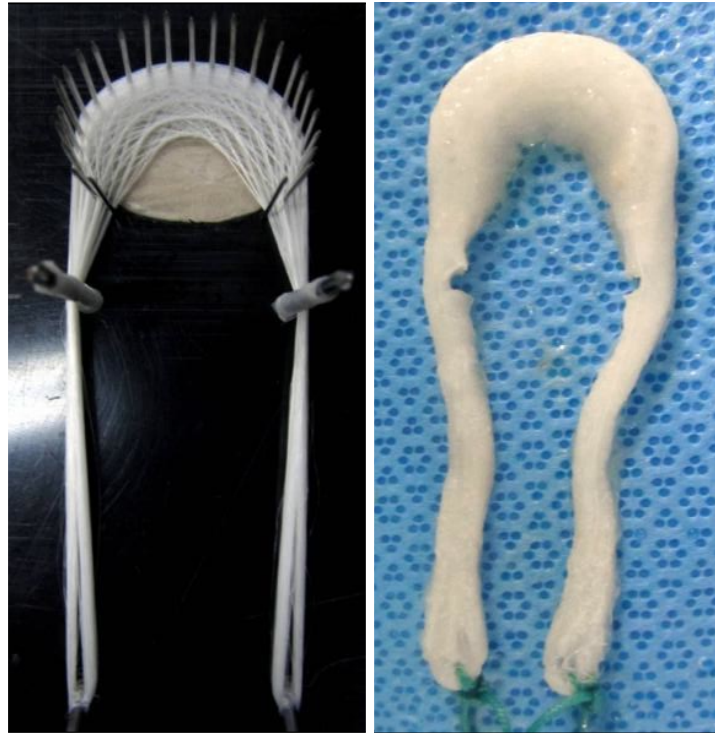
Figure 33 The orthopaedic research laboratory's previous total meniscus implant.

The scaffold is composed of poly(desaminotyrosyl-tyrosine dodecyl ester dodecanoate) (or poly(DTD DD)) (Figure 34), has been demonstrated to successfully endure mechanical loading, be biocompatible, tissue inductive and conductive, and chondroprotective up to 2 years[87, 104]. However, a poly(L-lactide) version of the total meniscus scaffold was tested and demonstrated excellent initial mechanics but the scaffold deteriorated over time *in vivo* and caused an osteophyte to quickly develop[106]. Therefore, poly(DTD DD) is a necessary choice for the development of a partial meniscus scaffold.
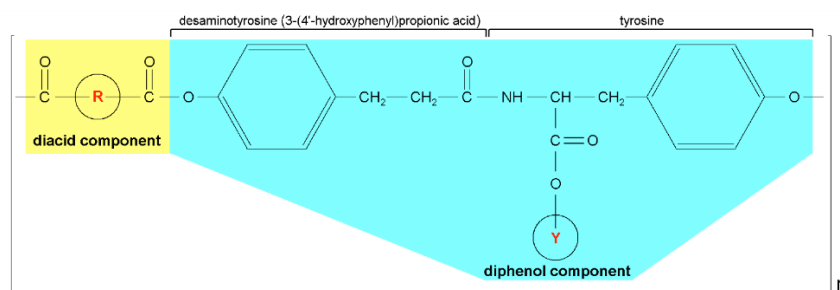
Figure 34 Poly(desaminotyrosyl-tyrosine dodecyl ester dodecanoate) (12,10) (poly(DTD DD)) [11].

This design has demonstrated a great deal of promise for meniscal tissue engineering; however, the design does not lend itself to use for partial meniscus defects. Due to the single fiber design, this implant cannot be resized or cut to specific defect geometries while retaining its mechanical integrity. In addition, the initial compressive mechanics of the implant are inferior to the native mechanics. A partial meniscus device must match the compressive properties of the native tissue (Figure 35). If the scaffold is too stiff, the scaffold will cause a stress concentration underneath it and if the scaffold is too soft, it will not be loaded properly. Therefore, the total meniscus device would not act as a load sharing device.
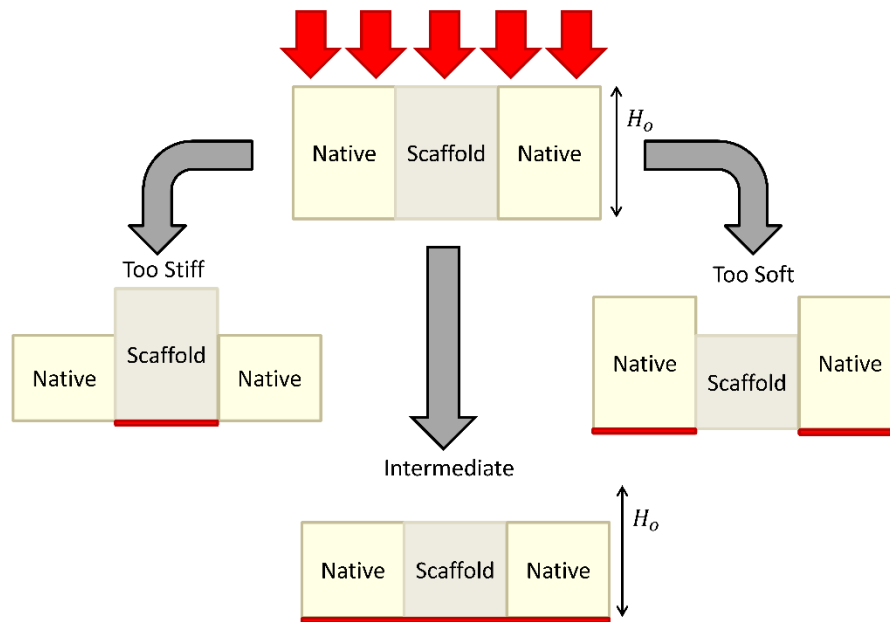
Figure 35 Schematics of scaffolds loaded with native tissue with varying compressive stiffness.

Therefore, the objective of this study was to develop an acellular scaffold for partial meniscus regeneration utilizing an entirely new manufacturing method, thermal extrusion based 3D printing, to fabricate poly(DTD DD) in an interconnected architecture that will allow for the scaffold to be trimmed to each individual's specific defect geometry with the ability to share physiological loads with the host tissue.

3.3 Hypothesis

We hypothesized that a collagen-hyaluronan infused 3D-printed polymeric scaffold could be fabricated and implanted to:

1) mimic the mechanical properties of the native meniscus

2) be successfully sutured to the remaining native meniscal rim

3) increase the contact area and reduce peak stresses relative to partial meniscectomy

4) encourage cell infiltration, extracellular matrix production, and organized tissue deposition,

5) integrate robustly to the surrounding native meniscal tissue, and

6) protect the articular surfaces to prevent or delay degenerative changes in the underlying cartilage.

3.4 Specific Aims

3.4.1 Aim 1: Determine the physical, mechanical, and enzymatic differences among bovine, porcine, and ovine derived collagen scaffolds.

Cattle is one of the most commonly utilized sources of collagenous materials in the medical industry due to abundance and accessibility. However, these materials may potentially transmit bovine spongiform encephalopathy. Therefore, we investigated porcine and ovine derived collagen as potential alternative sources for our tissue engineering implants.

We hypothesized that 1-ethyl-3-(3-dimethyl aminopropyl) carbodiimide (EDC)/ N-hydroxysuccinimide (NHS) cross-linked collagenous sponge-like scaffolds isolated from porcine and ovine tendons possess comparable mechanical and enzymatic properties as those derived from bovine tendons. The collagen sponges was evaluated using the following *in vitro* assays:

1. Swelling Properties

2. Tensile Testing

3. Confined Compression

4. Unconfined compression

5. Pore Structure Analysis

6. Enzymatic Stability

3.4.2 Aim 2: Biomechanical characterization of a collagen-hyaluronan infused 3D-printed polymeric scaffold and assessment of suture retention properties and ability to restore joint contact mechanics.

There are several mechanical properties which contribute to a device's ability to distribute loads in the knee joint. The scaffold must possess sufficient mechanical properties to support the tissue until the ingrown tissue is strong enough to carry the imposed loads itself. The scaffold must be adequately fixed to the remaining meniscal tissue. Therefore, in this aim, we characterized the axial compressive, circumferential tensile, and suture retention properties of our scaffold. Once our scaffold demonstrated the proper mechanics, we tested the ability of our scaffold to protect the underlying articular cartilage from high contact stresses in an ovine cadaveric model.

Our objective was to assess if the optimized partial meniscus scaffold could 1) degrade at a rate that allows for the gradual transfer of loads to the regenerating tissue, 2) match the axial compressive properties and 3) circumferential tensile properties of the native ovine meniscus, 4) possess adequate suture retention properties, and 5) restore functional contact mechanics of the ovine stifle joint relative to 80% meniscectomy.

Experimental Studies:

1. Poly(DTD DD) Degradation Assay

2. Scaffold Confined Compression Creep

3. Scaffold Circumferential Tensile Testing

4. Scaffold Single Suture Pull-out Testing

5. Scaffold Fixation Mechanics

6. *In situ* Contact Stress Distribution Analysis

3.4.3 Aim 3: Functional in Vivo Evaluation of Partial Meniscus Scaffold in an Ovine

Model

The purpose of this study was to assess the performance of the scaffold *in vivo*. We hypothesized that the scaffold would promote neo-fibrocartilaginous tissue and integrate well with the remain native tissue without adversely affecting the surrounding articular cartilage.

Experimental Studies:

1. Gross Analysis

2. Histology of the Synovium

3. Histology of the Scaffold

4. Immunofluorescence of the Scaffold

5. Biochemical Analysis of the Scaffold

6. Histology of the Articular Cartilage

3.4.4 Aim 4: Enhancement of Scaffold Mechanical Properties via Molecular

Orientation during 3D printing

The purpose of this aim was to enhance the circumferential tensile mechanics of the scaffold by introducing molecular orientation in the scaffold fibers by optimizing the 3D printing parameters. Highly oriented polymer fibers can be produced by drawing a melt-spun fiber but this orientation is missing when 3D printed. We achieved molecular orientation comparable to drawn fibers by 3D printing with a critical combination of print speed, nozzle diameter, the extrusion pressure and polymer melt and platform temperature that allowed for the drawing process to occur before the polymer has had sufficient time to cool into a solid. The method was illustrated with poly(DTD DD). Poly(L, lactic acid), PLLA, was also processed under similar

conditions to determine if these results could be generalized to other materials. Finally, we

assessed the tensile mechanics of the scaffold fabricated under two conditions, one lacking and

one possessing molecular orientation, to determine if this phenomenon would translate to

improved mechanical performance.

1. Thermal Degradation Assessment of poly(DTD DD)

2. Rheological Characterization of poly(DTD DD) and PLLA

3. Optimization of Molecular Orientation in poly(DTD DD)

4. Transition to Other Polymers: PLLA

5. Printing and Mechanical Characterization of Meniscus Scaffold

4   Specific Aim 1

Our lab has previously used industrial collagen of bovine origin. However, these

materials may carry the risk of transmitting bovine spongiform encephalopathy (or Mad Cow

Disease) and transmissible spongiform encephalopathy[62]. Therefore, there is a need for

alternative, safer sources of collagen from non-bovine sources.

Other studies of collagen derived from bovine tendon and skin, porcine skin, avian skin

and feet, equine tendon, sharkskin, frog skin, jellyfish, ovine skin, fish scale, and rat-tail sources

have been performed[5, 75, 96, 101, 103, 114, 126]. However, these studies cannot be directly compared

due to critical differences in collagen concentration, swelling pH, EDC/NHS concentrations and

crosslinking duration, and freezing rates.

Marine derived collagens have low denaturation temperatures and enzymatic

resistance[72, 75]. Dermal collagen has inferior mechanical properties when compared to tendon

collagen[86].   Therefore, mammalian tendon appears to be the optimal source for insoluble

collagen. Beef, pork, and lamb are the three highest consumed mammalian meats per capita in

the United States, providing a logical sources for collagens [1]. The tendons can be harvested with

minimal meat wasted.

A direct comparative study on the properties of bovine, porcine, and ovine tendon

derived collagenous tissue engineering scaffolds was performed to assess the differences of the

physical, mechanical, and enzymatic properties of three-dimensional collagenous scaffolds

isolated from bovine, ovine, and porcine tendons and cross-linked using EDC and NHS.

4.1   Study Design

1 % (w/v) collagen sponges were evaluated (to reduce materials needed) from bovine,

porcine, and ovine sources. Subsequently, 2% (w/v) collagen with 1.25%(w/w) hyaluronic acid

was tested between the previously used bovine collagen and isolated porcine collagen to see if any differences would be observed.

Isolated collagen was ground into a powder using a Wiley mill. Collagen was dispersed in dilute HCl acid (pH=2.35), degassed under high vacuum, and injected into a perforated polystyrene mold. The dispersion was frozen in a dry ice-ethanol bath for 30 minutes and lyophilized until completion.

Scaffolds were then cross-linked in a 10 mM EDC and 5 mM NHS solution for 5 hours under minimal compression to maintain a uniform thickness. The scaffolds were rinsed 3 times in DI water for 10 minutes and soaked in a 100 mM sodium phosphate solution for 2 hours to remove any residual byproducts from the reaction. The scaffolds were then rinsed in DI water overnight, frozen in a dry ice-ethanol bath for 30 minutes, and lyophilized until completion.

4.2   Collagen Isolation
Methods

Fresh frozen animal tendons were purchased from a local meat supplier (Farm to Pharm, Warren, NJ). Ovine extensor tendons were obtained from 8-10 month lambs. Bovine and porcine Achilles tendons were obtained from 4-8 week old and 3 month old animals, respectively. These age ranges represent similar, skeletally immature points in the life cycle of the respective animals. Extensor tendons were used because harvesting the Achilles tendon would interfere with meat harvesting.

Tendons were thawed, dissected, and removed from any other debris. The tendons were cut into 1 cm pieces, lyophilized, and shredded. The shredded tendons were treated to numerous subsequent 24 hour treatments: 6 treatments of 0.211 M sodium phosphate, 2 treatments of 0.48 M NaCl, 2 treatments of 0.225 M citrate buffer (pH 3.7), and 2 treatments of 0.175 M acetic acid (Figure 36). When changing solutions, the tendinous tissue was centrifuged at 800g for 15 minutes, the supernatant was aspirated, 500 mL of ultrapure DI water water

added, centrifuged at 800 g for 15 minutes, filled with fresh solution, placed on an oscillator for ten minutes, and returned to 4°F. The tissue was subjected to 4 treatments of ultrapure distilled water, frozen, and lyophilized until completion.   The yield of this procedure was defined as the ratio of the mass of lyophilized collagen to the mass of the initial lyophilized tendon.
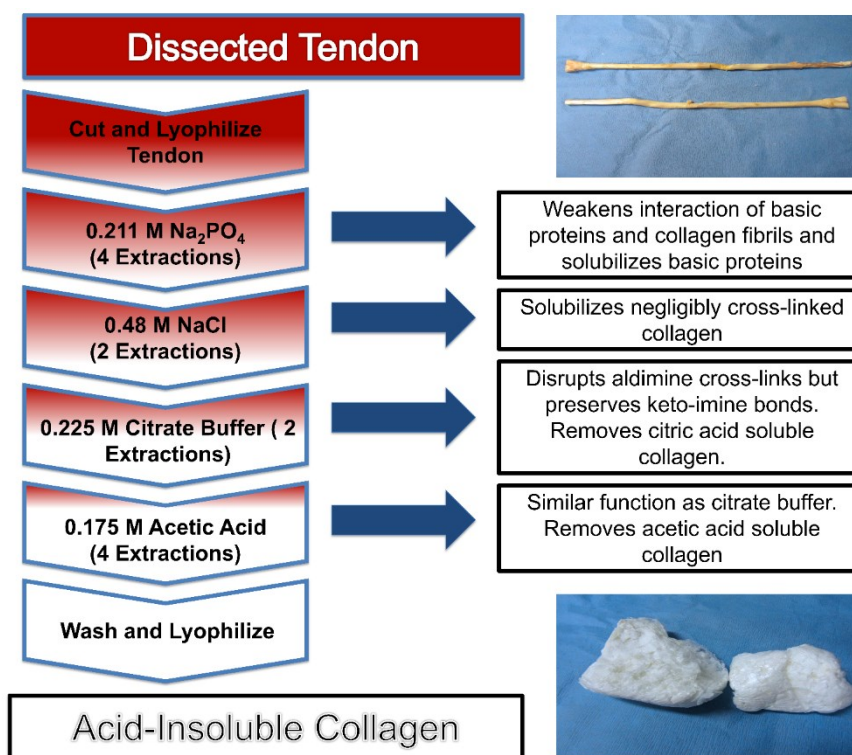
Figure 36 Collagen Isolation Process Flow Chart.

Results

The isolation procedure produced similar yields of yield of 74.3%, 75.1%, and 80.0% for bovine, porcine, and ovine collagen, respectively. All Collagens were bright white in appearance with no significant differences in gross morphology or texture.

4.3   Tensile Testing and Swelling Ratio
Methods

Uniaxial tensile tests were performed on collagen scaffolds dogbones with an initial gage length of 56 mm (Figure 37). A 1.5 cm strip was cut from the sponge, a custom jig with two parallel faces was used to cut the central region with a scalpel, and a 6 mm biopsy punch

was utilized to taper the ends. The samples were weighed before hydration and then placed in

phosphate buffered solution (PBS) at room temperature overnight.

Figure 37 Collagen Scaffold Dogbones.

The samples were blotted with filter paper and weighed once more. Swelling ratio was

calculated as the mass of the hydrated scaffold to that of the dried scaffold. Sample thickness

was measured three times and averaged using a Z-Mike Model 1202B. Samples were imaged

and the width of the gauge length was measured in MATLAB.

Samples were gripped using cryogenic clamps (Bose ElectroForce, Eden Prairie, MN) and

strained at a rate of 14 mm/min until failure with an Instron 5569 (Instron, Norwood, MA) with a

100 N load cell. Samples that did not fail midsubstance were omitted. The tensile modulus,

ultimate strain, ultimate stress, and toughness were calculated for each sample.

Results

Bovine, porcine, and ovine collagen scaffolds were tested in a hydrated state in uniaxial

tension. No significant differences in the tensile modulus were detected for any source (Figure

39). Ovine scaffolds had greater ultimate strain, stress, and toughness than both bovine and

porcine scaffolds (Figure 38 and Figure 39). In addition, porcine scaffolds demonstrated a

greater ultimate strain than bovine scaffolds (p=0.001). The collagen scaffolds were compared

macroscopically with respect to their ability to retain water. No significant differences in

swelling ratio were observed between species (Figure 40).
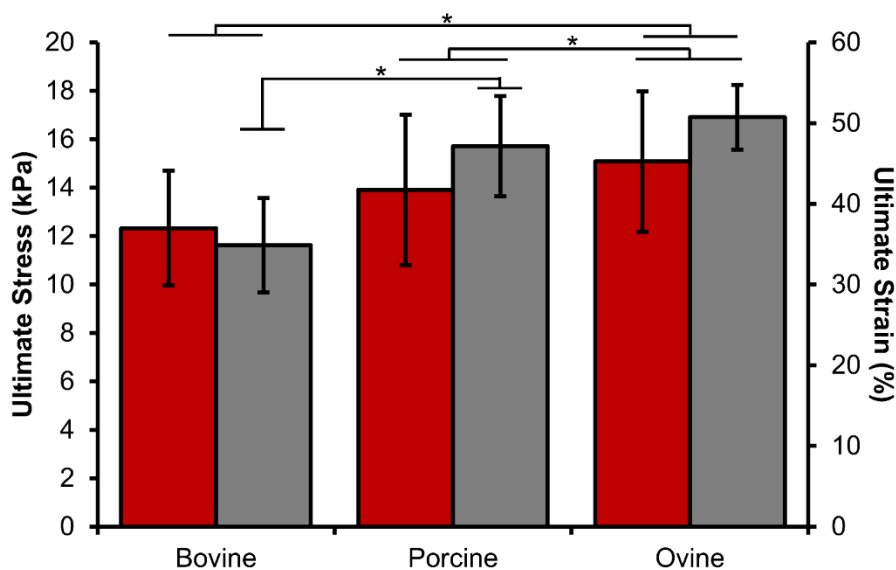
Figure 38 Ultimate Strain and Ultimate Stress of 1% isolated bovine collagen (n=12), 1% isolated porcine collagen (n=9), and 1% isolated ovine collagen (n=14). Values represent mean±S.D. Statistical significance, as depicted by an asterisk, was determined by a one-way ANOVA with post-hoc Tukey's test.
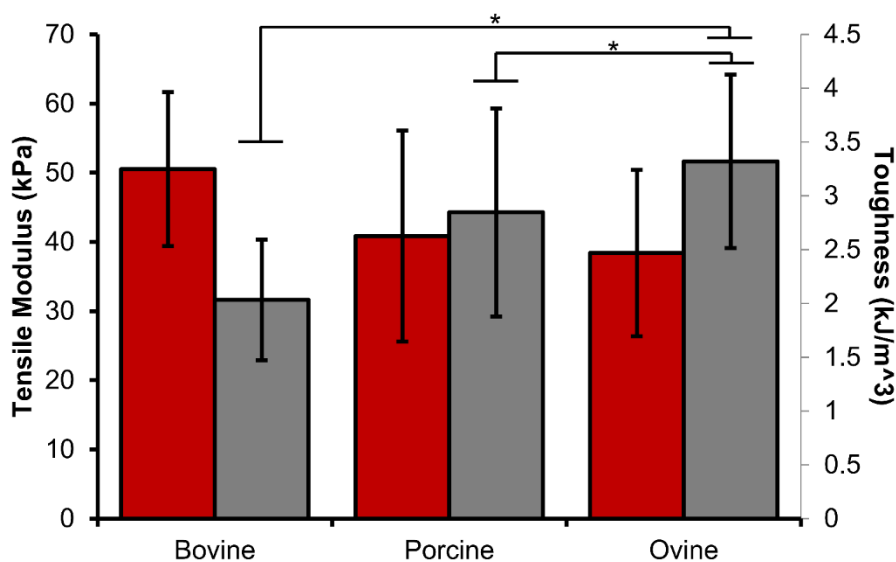
Figure 39 Tensile modulus and toughness of 1% isolated bovine collagen (n=12), 1% isolated porcine collagen (n=9), and 1% isolated ovine collagen (n=14). Values represent mean±S.D. Statistical significance, as depicted by an asterisk, was determined by a one-way ANOVA with post-hoc Tukey's test.
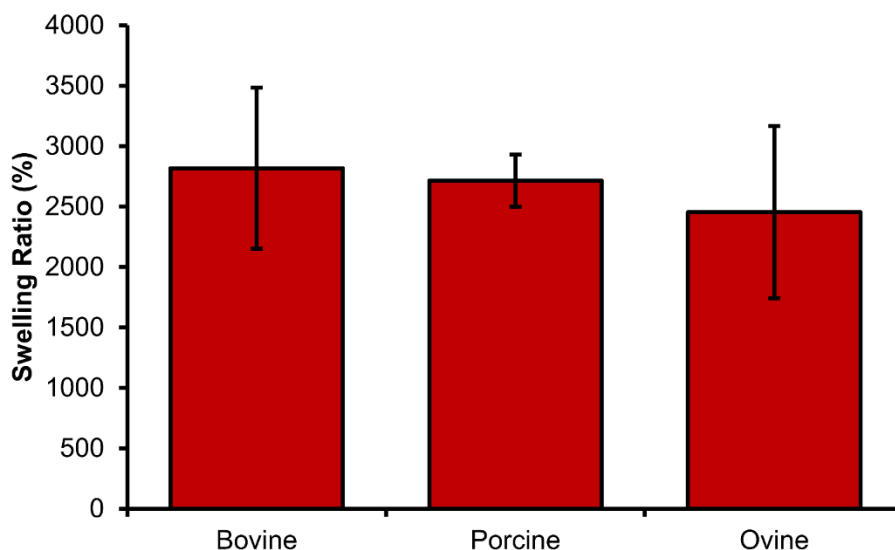
Figure 40 Swelling ratio of 1% isolated bovine collagen (n=19), 1% isolated porcine collagen (n=14), and 1% isolated ovine collagen (n=14). There were not any statistically significant differences observed (p =0.22). Values shown represent mean±S.D.

4.4 Confined Compression

Methods

Four-millimeter diameter plugs of the scaffolds were taken and trimmed to a height of approximately 5 mm. The samples were hydrated in PBS and loaded into a custom-made jig described by Armstrong and Mow[6]. The samples were tested in compressive creep using an Instron 5542 so a smooth, rapid load of 0.1 N was applied to the sample and held for 3600 seconds. The aggregate modulus and permeability was calculated, according to Mow's biphasic theory, using a custom MATLAB script[92].
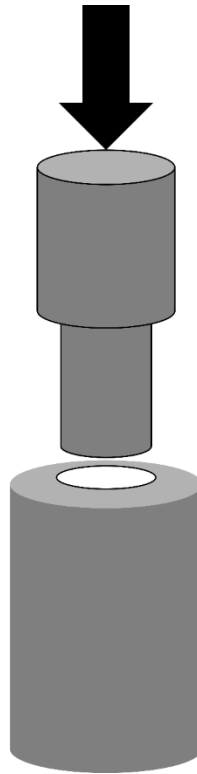
Figure 41 Schematic of confined compression setup. A 4 mm plunger applies a smooth and rapid 1 N load to a sample within a 4 mm chamber, which is impermeable on the sides but permeable on the bottom to allow for fluid flow.

Results

Bovine, porcine, and ovine collagen scaffolds were tested in confined compression to determine their aggregate moduli and permeabilities. High levels of variability and no significant differences were observed in either of the material properties (Figure 42). Although, the ovine aggregate modulus mean was greater than bovine and porcine moduli. The bovine permeability mean was greater than porcine and ovine permeabilities.
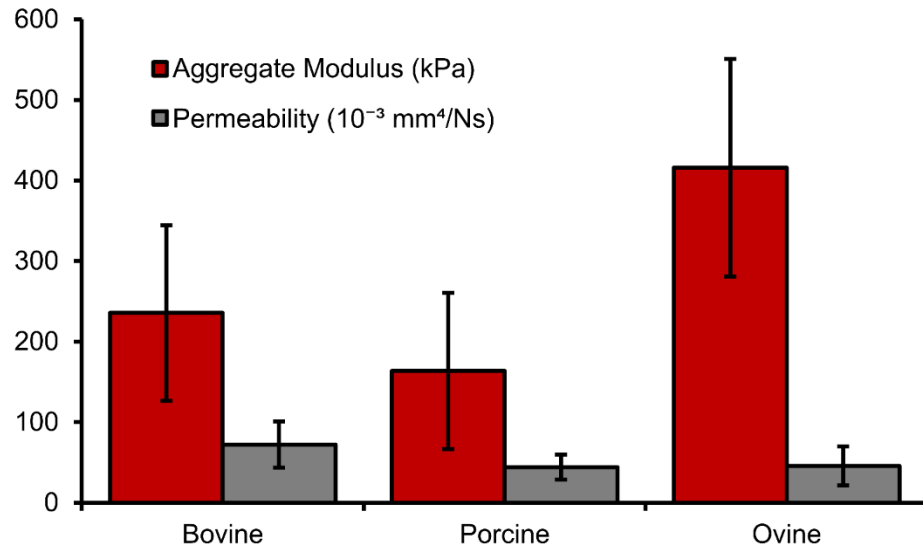
Figure 42 Aggregate modulus and permeability of 1% isolated bovine collagen (n=7) 1% isolated porcine collagen (n=8), and 1% isolated ovine collagen (n=8). No statistical differences were found between groups (one-way ANOVA, p=0.23).

4.5   Unconfined Compression
Methods

Unidirectional, unconfined compression was performed on 10 mm diameter cylindrical

samples with a height of 9 mm. The samples were bonded to a metallic disc using a

cyanoacrylate to prevent undesired movement and then hydrated in PBS. Samples were

compressed at a rate of 0.01 mm/s to a maximum of 75% strain using an Instron 5542. The

samples were immersed in PBS throughout the test. The compressive modulus was defined as

the best linear fit between 2% and 5% strain and compressive strength at 20%, 40%, and 75%

calculated using a custom MATLAB script[45, 53, 60].

Results

Hydrated collagenous scaffolds from bovine, porcine, and ovine sources were tested in

unconfined compression and submerged in PBS throughout. All scaffolds performed similarly in

compression with no significant differences regarding the compressive modulus and

compressive strength at 20%, 40%, and 75% strain (Figure 43). However, there were small

trends of increased compressive performance for bovine derived scaffolds for all compressive

material properties.
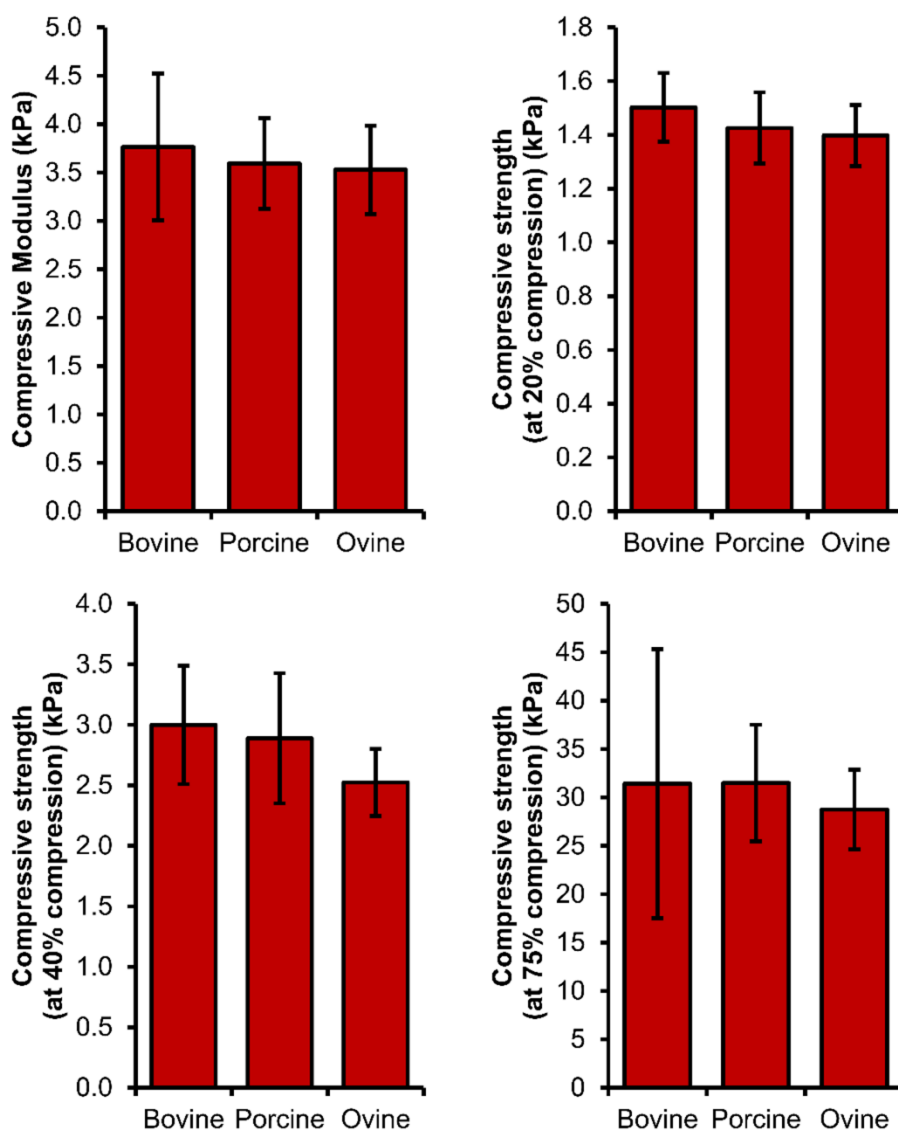
Figure 43 Compressive moduli and compressive strength at 20%, 40%, and 75% strain of 1% isolated bovine collagen (n=7), 1% isolated porcine collagen (n=8), and 1% isolated ovine collagen (n=8). No statistically significant differences were observed (one-way ANOVA for compressive modulus and one-way ANOVA on ranks for compressive strengths).

4.6 Pore Structure Analysis
Methods

Dry scaffolds were sectioned to image the interior of the material. The samples were

sputter coated in gold (Balzers SCD 004) and 60x magnification images were taken at random

locations using an Amray 1830I Scanning Electron Microscope. Fifteen images per source were

converted to binary using an adaptive thresholding algorithm. The images were analyzed using

a mean linear intercept MATLAB script, adapted from Freyman[42, 99].   This determined a best-fit

ellipse representing the average pore size of each image. Next, the ellipse major and minor axes

were multiplied by 1.5 to account for the effect of pores not cut sectioned through their

maximum cross-section[47]. The mean intercept length was defined as the average of the

corrected major and minor axes for each image. The average pore size was calculated from the

average of the mean intercept lengths of all images analyzed[99].

Results

Scanning electron microscopy (SEM) was used to quantitatively compare the pore

structure of the scaffolds to determine if there are any differences across species. Visual

inspection revealed no obvious differences for pore structure between species (Figure 44).   All

groups displayed no alignment in scaffold strut architecture. The mean pore size of scaffolds

derived from bovine, porcine, and ovine tendons were quite similar. Although no significant

differences, the ovine mean pore size value (73.05 μm ± 10.79) was somewhat less than bovine

(85.84 μm ± 9.51) and porcine (87.32 μm ± 10.69) values (Figure 45).
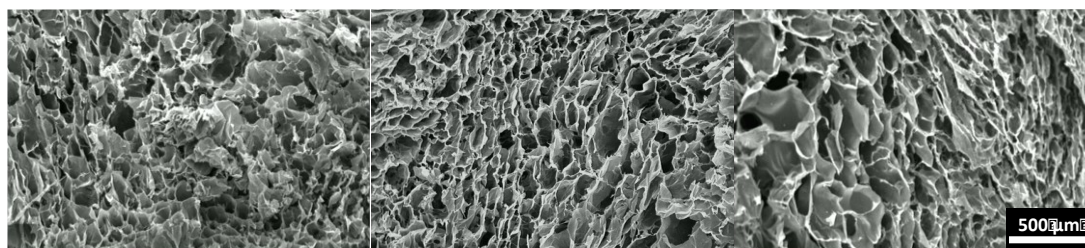
Figure 44 Representative SEM images of 1% isolated bovine (left), 1% isolated porcine (center), and 1% isolated ovine (right).
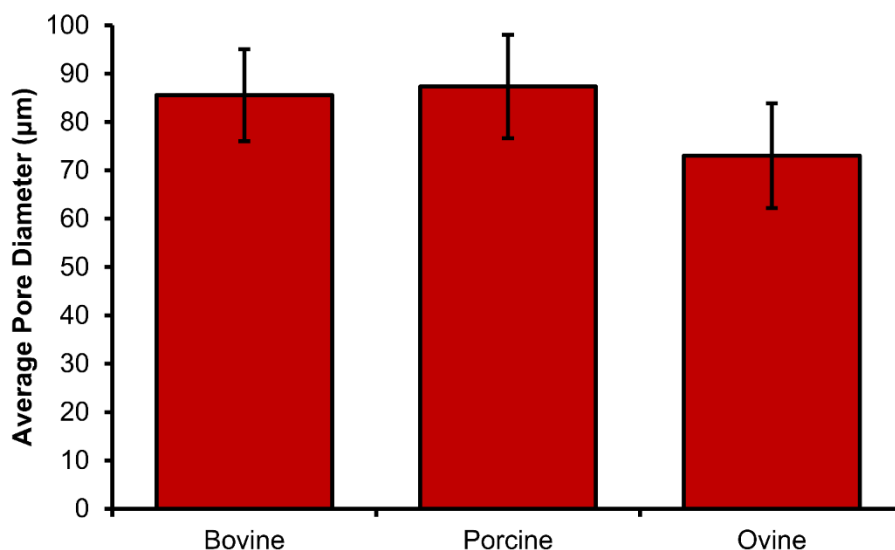
Figure 45 Average pore diameter of 1% isolated bovine (left), 1% isolated porcine (center), and 1% isolated ovine (right) determine through a mean linear intercept algorithm. No statistically significant differences were observed, according to a one-way ANOVA.

4.7   Enzymatic Stability
Methods

Enzymatic stability of the scaffolds was tested via an *in vitro* collagenase resistance

assay. Non-crosslinked scaffolds were used in order to avoid masking any differences in the

enzymatic stability between animal sources. For each source, 8 squares were cut with a mass of

2.0 mg ± 5%. All samples were incubated for 1 hour beforehand and the enzyme solutions were

incubated separately, both at 37°C. The samples were evaluated at 37°C using the following four

conditions. A sample was incubated in 2 mL tris buffer to act as a control. A sample was

incubated in 2 mL of 8000 U/mL trypsin. Trypsin solubility is commonly used to assess the

extent of denaturation of collagenous materials[100]. A sample was first immersed in boiling water

to induce heat denaturation for 2 minutes and subsequently incubated in 2 mL of 8000 U/mL

trypsin. 5 samples were incubated in 2 mL of 500 U/mL bacterial collagenase, from Clostridium

histolyticum. Samples were assessed every 5 minutes using a semi-quantitative scale from 0 to

5, with 0 representing complete dissolution and 5 indicating completely intact.

Results

The enzymatic stability of collagen scaffolds was tested in vitro using collagenase. All control and untreated samples incubated in trypsin demonstrated either minor or no degradation (≥4 on the semi-quantitative scale). All boiled samples incubated in trypsin were completely solubilized within less than 1 hour.

For experimental samples, ovine scaffolds (170 min ± 9) resisted degradation significantly longer than bovine samples (110 min ± 11) and bovine samples endured significantly longer than porcine samples (87 min ± 17) (Figure 47). The semi-quantitative assessment of the samples revealed an initial steady rate of degradation with a diminished rate as the samples approach complete dissolution (Figure 46).
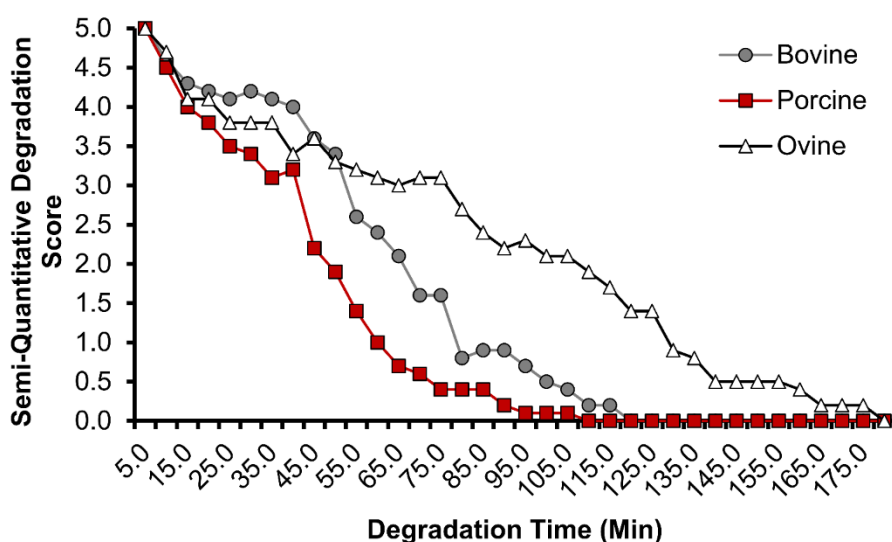
Figure 46 Semi-quantitative assessment of degradation 1% isolated bovine collagen (n=5), 1% isolated porcine collagen (n=5), and 1% isolated ovine collagen (n=5). Values represent mean at each time point.
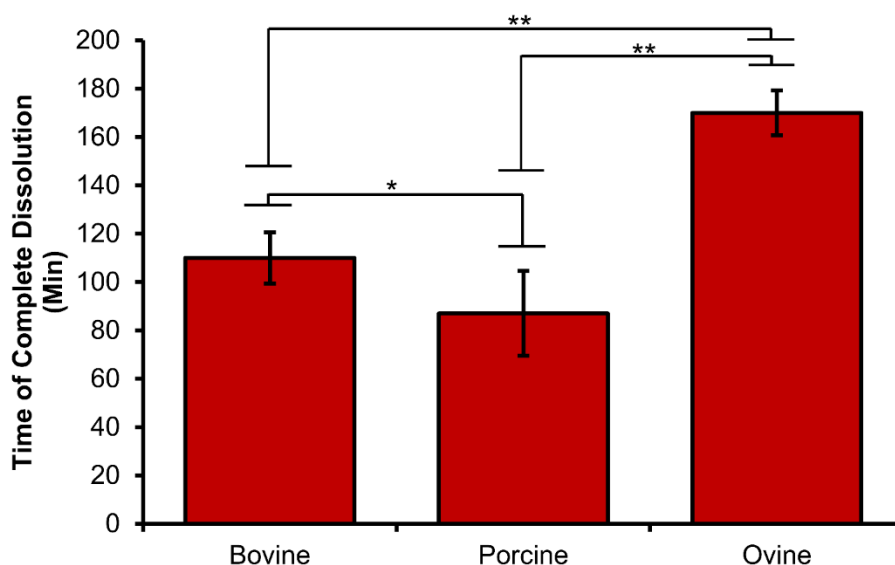
Figure 47 Time to dissolution of 1% isolated bovine collagen (n=5), 1% isolated porcine collagen (n=5), and 1% isolated ovine collagen (n=5). Values represent mean±S.D. Statistical significance, as depicted by an asterisk, was determined with a one-way ANOVA with post-hoc Tukey's test.

4.8   2% (w/v) collagen with 1.25%(w/w) hyaluronic acid

Our lab has had significant interest in utilizing porcine derived collagen instead of bovine

derived collagen. But to ensure that the similarities found in the 1% collagen assays. These

tests were repeated with 2% (w/v) collagen with 1.25%(w/w) hyaluronic acid sponges to see if

the trends observed with 1% collagen are the same when the concentration is increased and

hyaluronic acid was added. In order to test against our current standard, 2% purchased bovine

collagen with 1.25% hyaluronic acid was compared to 2% porcine collagen with 1.25%

hyaluronic acid, isolated according to the procedure above.

4.8.1   Swelling Results

As the concentration of collagen increased from 1% to 2%, the swelling ratio decreased

for both porcine and bovine collagens. Interestingly, 2% collagen demonstrated the opposite

trend as 1% collagen between groups. 1% purchased bovine collagen had a significantly greater

swelling ratio than porcine (p=0.0001) but at 2% (w/v) porcine had a significantly greater

swelling ratio (p=0.02) (Figure 48).
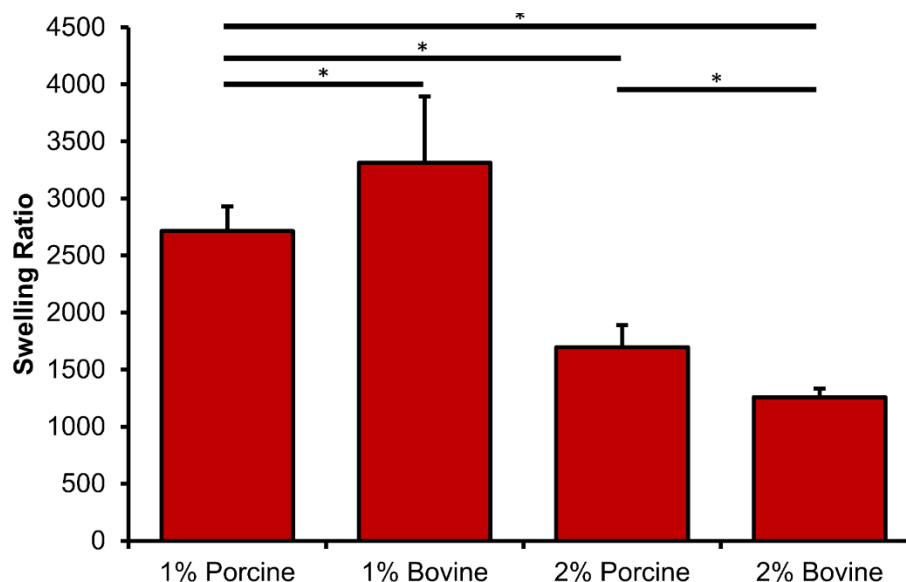
Figure 48 Swelling ratio of 1% isolated porcine collagen (n=13), 2% isolated porcine collagen (n=11), 1% purchased bovine collagen (n=12), and 2% purchased bovine collagen (n=12). All groups were statistically significantly different, according to a 1-way ANOVA with post-hoc Tukey's test (p<0.02). Values shown represent mean±S.D.

4.8.2   Tensile Results

As the concentration of collagen increased from 1% to 2%, the tensile properties

became more brittle as demonstrated by an increase in elastic modulus and a decrease in

ultimate stain and toughness (Figure 49). The trends between the 1% collagen groups were very

similar to those found between the 2% groups. The ultimate strain was statistically different

between all groups (p=0).   The ultimate stress was not significantly different, except 2% bovine

collagen was greater than 2% porcine (p=0.04). Toughness was only found to be different

between 1% porcine and 2% bovine collagen (p=0.002). The elastic modulus was significantly

different between 1% bovine, 2% porcine, and 2% bovine collagen groups (p=0). It is important

to note that the elastic modulus of 2% bovine collagen was 143% than that of 2% porcine

collagen and the ultimate strain of 2% bovine collagen was 81% less than that of 2% porcine
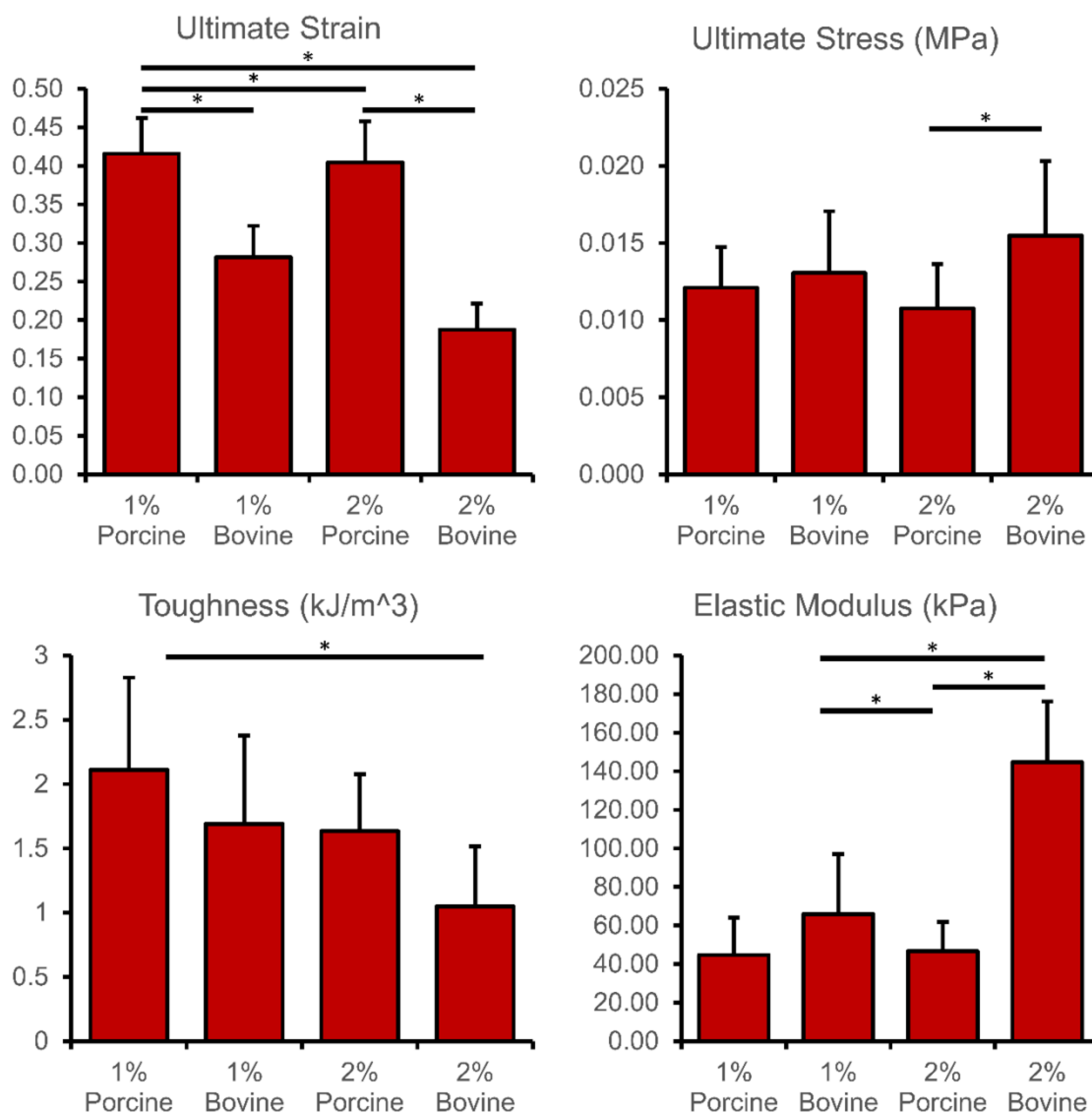
collagen.

Figure 49 Ultimate Strain, Ultimate Stress, Toughness, and Elastic Modulus of 1% isolated porcine collagen (n=9), 2% isolated porcine collagen (n=9), 1% purchased bovine collagen (n=10), and 2% purchased bovine collagen (n=10). Values represent mean±S.D. and statistical significance was determined by a one-way ANOVA with post-hoc Tukey's test.

4.8.3 Confined Compression Results

Although there were several difference found among the tensile properties of collagens,

there were no significant differences found between 2% porcine and 2% purchased bovine

collagens (Figure 50). The aggregate modulus was found to be about 160 kPa and the

permeability was calculated to be about 4.1e-4 mm⁴/Ns. The aggregate modulus has been

shown to promote fibrochondrogenic ingrowth[33].

Biphasic Properties
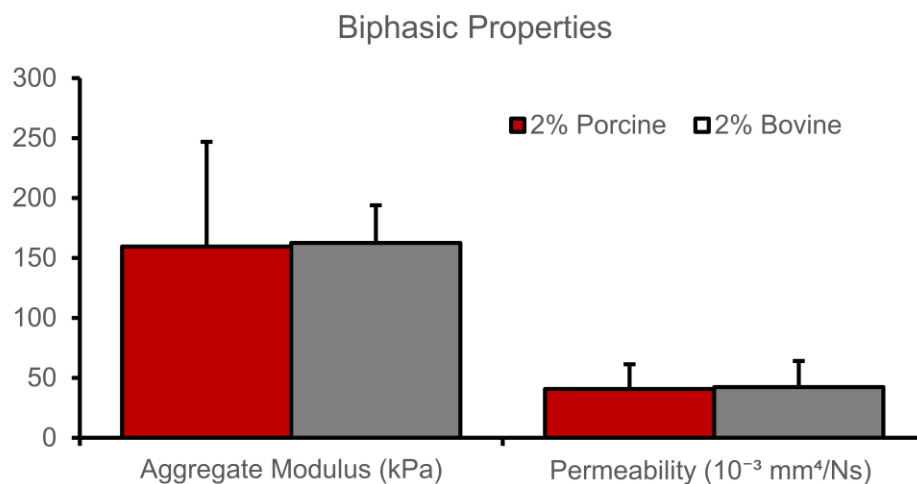
Figure 50 Aggregate modulus and permeability of 2% porcine (n=5) and 2% purchased bovine collagen (n=5). No statistical differences were found between groups (two sample t-test assuming unequal variances).

4.8.4 Enzymatic Stability Results

The enzymatic stability increased with increasing concentration of collagen (Figure 51 and Figure 52). 2% purchased bovine collagen was 125%, 120%, and 96% greater than 1% porcine, 1% bovine, and 2% porcine collagen, respectively.
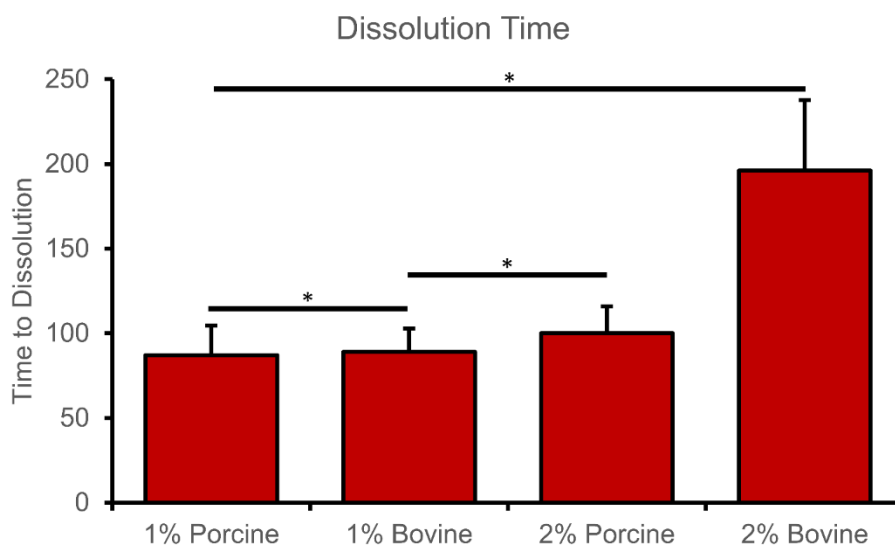
Dissolution Time

Figure 51 Time to dissolution of 1% isolated porcine collagen (n=5), 2% isolated porcine collagen (n=5), 1% purchased bovine collagen (n=5), and 2% purchased bovine collagen (n=5). Values represent mean±S.D. Statistical significance was determined with a one-way ANOVA with post-hoc Tukey's test.
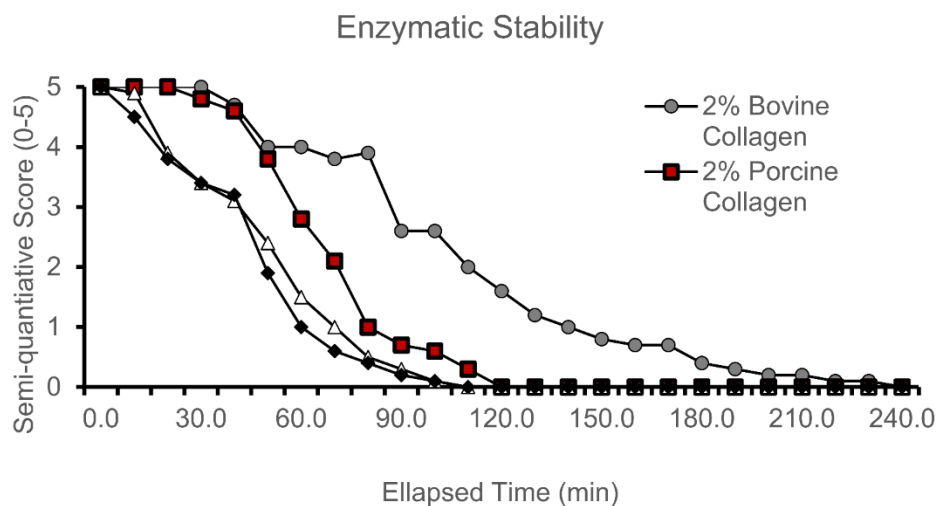
Figure 52 Semi-quantitative assessment of degradation of 1% isolated porcine collagen (n=5), 2% isolated porcine collagen (n=5), 1% purchased bovine collagen (n=5), and 2% purchased bovine collagen (n=5). Values represent mean.

4.9 Aim 1 Discussion

The overall purpose of this aim was to assess porcine and ovine sources of collagen as alternative for bovine collagen, which has previously been utilized in our lab. The preliminary study was performed using 1% collagen and demonstrated that isolated porcine and ovine derived collagen was comparable to isolated bovine collagen. However, in the 2% study which assessed differences between 2% porcine collagen that was isolated using our own protocol and 2% bovine that was purchased from a commercial supplier, significant differences arose. Since there were no large differences resulting from changes in the source species, the differences are most likely due to differences in the processing of the tendinous tissue. The differences may be a result of the repetitive centrifuging necessary during the isolation process required to change daily solutions. A future study should investigate the use of dialysis tubing to hold the soaking tissue and allow for simple solution changes that do not require the harsh centrifugal forces used in this study.

5   Specific Aim 2

The purpose of this aim is to characterize the mechanical and degradation properties of the scaffold. Time zero mechanics are essential to create a scaffold that can tolerate the large loads imposed in the knee joint. For a truly load sharing partial meniscus device, the compressive properties must be comparable to the native meniscus. In addition, scaffolds with compressive moduli which more closely match that of the native meniscus induce the fibrochondrogenic phenotype [32]. Circumferential tensile mechanics are also integral to the load sharing properties of a meniscal replacement device and are important for proper mechanical signaling to infiltrating cells.

The degradation profile of the polymer over time can give an estimate as to the mechanical profile over time. Ideally, the scaffold mechanics will decrease at the rate which allows for the gradual transition of mechanical loads to the neo-tissue until finally the new tissue bears all of the loads.

Fixation mechanics were assessed through a single suture pull-out test and a whole construct fixation test to validate the implantation of the device. Finally, the chondroprotective ability of the scaffold was tested functionally in an *in situ* contact stress study.   This was performed in an ovine cadaveric model using a pressure sensor located between the meniscus and the tibial plateau. This was performed to determine if the partial meniscus scaffold could return the contact mechanics of the knee joint back to pre-meniscectomy levels.

We hypothesized the optimized partial meniscus scaffold could 1) degrade at a rate that allows for the gradual transfer of loads to the regenerating tissue, 2) match the axial compressive properties and 3) circumferential tensile properties of the native ovine meniscus, 4) possess adequate suture retention properties, and 5) restore functional contact mechanics of the ovine stifle joint relative to 80% meniscectomy.

5.1 Scaffold Fabrication

Poly(DTD DD) was 3D printed at 160 **°C** and 1.2 mm/s on a 3D Bioplotter (EnvisionTEC) at the New Jersey Center for Biomaterials.   Sodium hyaluronate (0.25 g/L; molecular weight 1.5-2.2 MDa, Acros Organic) was dissolved in dilute hydrochloric acid (pH 2.35). Achilles bovine tendon collagen (Worthington Biochemical Corporation) was ground into particles of less than 425µm and swollen in an acidic solution (20 g/L).

Collagen was filled into the voids of the scaffold using the centrifugal technique. The dispersion was frozen via ethanol-dry ice bath for 30 minutes, and lyophilized at -50°C and 0.05 mbar (FreeZone 1 Liter, Labconco). Scaffolds were cross-linked with 10 mM, 1-ethyl-3-(3-dimethaylaminopropyl)carbodiimide hydrochloride (EDC) and 5 mM N-hydroxysuccinimide (NHS) for 6 hours. Scaffolds were rinsed three times for 10 minutes in DI water, one time for 3 hours in 100 mM sodium phosphate, and rinsed for 24 hours in DI water. Scaffolds were frozen, lyophilized, and sterilized with 25kGy of gamma irradiation at Sterigenics (Figure 53).
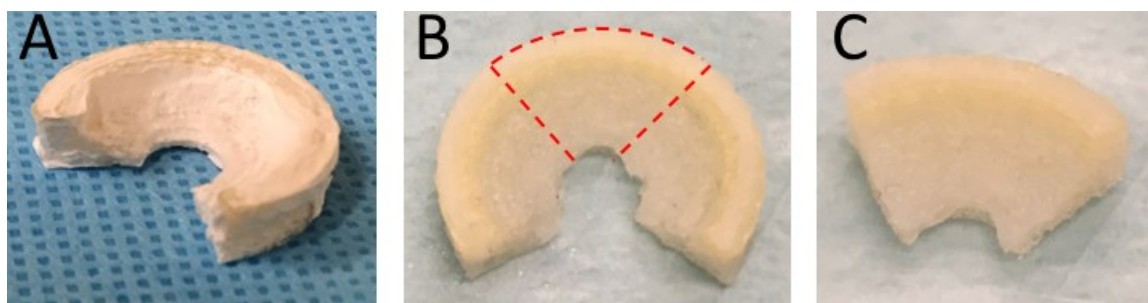
Figure 53 (A) Sterilized partial meniscus scaffold, (B) hydrated scaffold with red dotted lines indicating cutting lines, and (C) resulting cut scaffold for 80% native tissue replacement.

5.2 Poly(DTD DD) Degradation Assay
Rationale

The purpose of this study was to test the effect of degradation on the mechanics of poly(DTD DD) single fibers as it experiences *in vitro* degradation. Specifically, the changes in elastic modulus, yield stress, and ultimate stress of poly(DTD DD) single fibers were studied over

a 32 week period. In addition, 3D printed strips of poly(DTD DD) were tested in order to

determine the effect of 3D printing on the degradation of Poly(DTD DD) as well.

Methods

Poly(DTD DD) fibers were extruded at the NJ Center for Biomaterials by Sanjeeva

Murthy. The fibers were cut into 100mm strands and initial fiber diameters were measured in

triplicate using a Z-Mike. Fibers were placed into 15 mL conical tubes and soaked with 10mL of

phosphate-buffered solution (PBS). Tubes were then placed into an incubator at 37°C (Water

Jacketed Incubator 3250, Forma Scientific) for t = 1 day, 1, 2, 4, 8, 16, 32, and 52 weeks (n=8

fibers per time point).

At each time point, fibers were dried superficially with Kim wipes and taped at each end

for gripping with a 50mm gauge length, and final fiber diameters were measured in triplicate.

Percent thickness change was calculated from fiber diameter data. Fibers were tested at a rate

of 30mm/min (Instron 5542, Norwood MA). Load and deformation were measured, and the

elastic modulus was calculated from the greatest slope in the elastic region of the curve. Yield

stress was calculated using a 0.2% offset strain line. Comparisons were made using a two-tailed,

Student's t-test relative to the day 1 control (α=0.05).

For 3D printed Poly(DTD DD) strips, poly(DTD DD) was printed at 1.2 mm/s at 160°C and

8.9 bar on the platform. The thickness could not be measured due to the elliptical cross-section

of this printing method. As a result, only relative changes could be assessed over time. The

strips were tested in the same manner as the poly(DTD DD) fibers. A regression analysis was

performed in Microsoft Excel and a student's t-test was used to determine if there was a

statistically significant difference in the slope of the regression lines.

Results

The poly(DTD DD) fiber results can be seen in Figure 54, Figure 55, and Figure 56.

Interestingly, the elastic modulus increased 46% over 16 weeks but then drastically decreased

between 16 and 32 weeks. The earlier time points had varying changes to the elastic modulus with the relative changes of 7%, 30%, 27%, and 33% at the 1, 2, 4, and 8-week time points, respectively. This data demonstrates that the poly(DTD DD) becomes more brittle over time.

Conversely, the ultimate stress decreased over the duration of the study. There were no differences until 4 weeks at which point the ultimate stress decreased 16%. At 8, 16, and 32 weeks, the ultimate stress decreased 40%, 61%, and 98% relative to the control. The yield stress demonstrated no significant differences throughout the assay except at 2 and 32 weeks. Although the 2-week data point is likely an outlier, the 32-week data suggests that significant degradation is occurring after 16 weeks. It is also apparent that the ultimate stress and yield stress are converging until 16 weeks, after which they are equivalent. This demonstrates that there is an elimination of the plastic region of the stress-strain curve over time.
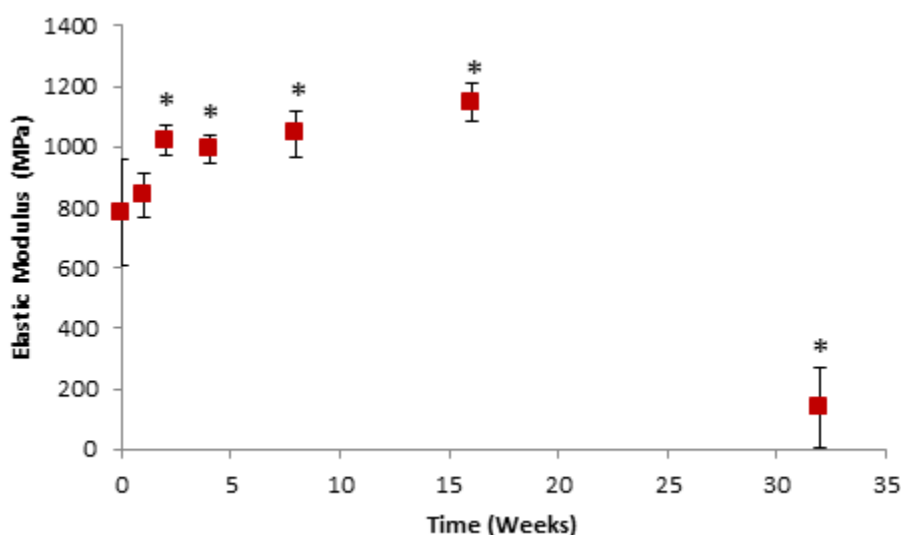
Figure 54 Elastic modulus of poly(DTD DD) non-drawn fibers at 1 day (n=7), 1 week (n=6), 2 week (n=7), 4 week (n=8), 8 week (n=7), and 16 week (n=4). * denotes statistical difference from t=1 day control.
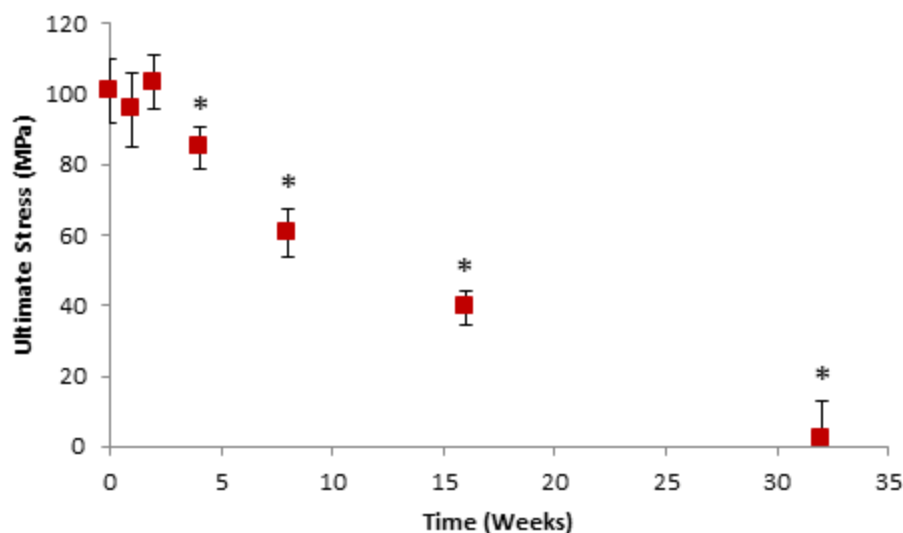
Figure 55 Ultimate stress of poly(DTD DD) non-drawn fibers at 1 day (n=7), 1 week (n=6), 2 week (n=7), 4 week (n=8), 8 week (n=7), and 16 week (n=4). * denotes statistical difference from t=1 day control.
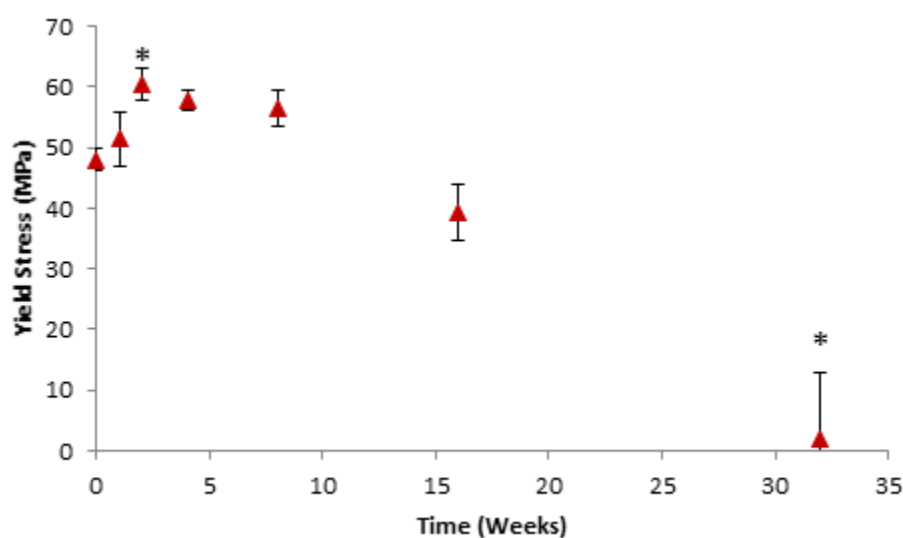
Figure 56 Yield stress of poly(DTD DD) non-drawn fibers at 1 day (n=7), 1 week (n=6), 2 week (n=7), 4 week (n=8), 8 week (n=7), and 16 week (n=4). * denotes statistical difference from t=1 day control.

The relative ultimate load and stiffness of extruded and 3D printed poly(DTD DD) can be seen in Figure 57 and Figure 58. There was no significant difference in the slope of the regression of the ultimate load between 3D printed and extruded fibers (p=0.34) but there was a difference in the slope of the relative stiffness (p<0.01). The data suggests that 3D printing is

not adversely affecting the degradation profile of poly(DTD DD) and, perhaps, the larger

thickness of the 3D printed fibers may actually delay the degradation of the material.
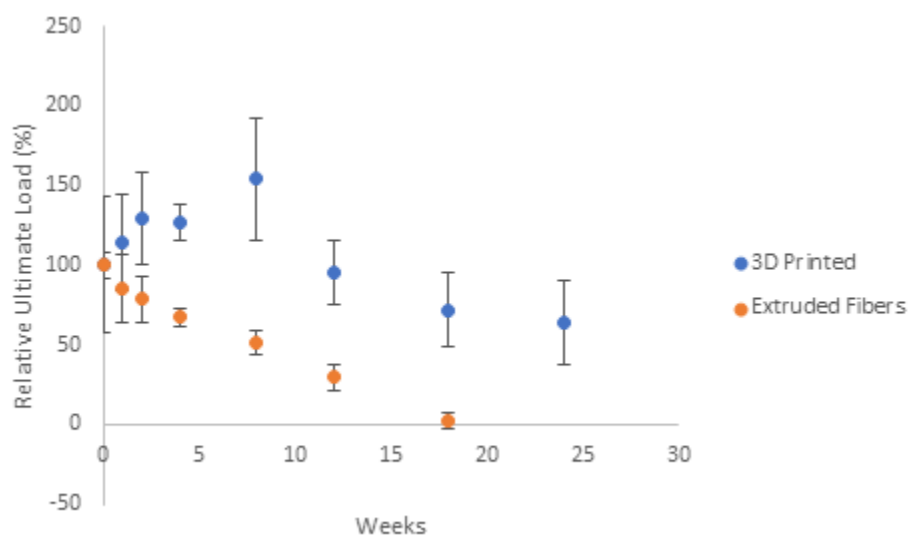
Figure 57 Relative Ultimate Load of extruded fibers and 3D printed strips of poly(DTD DD).
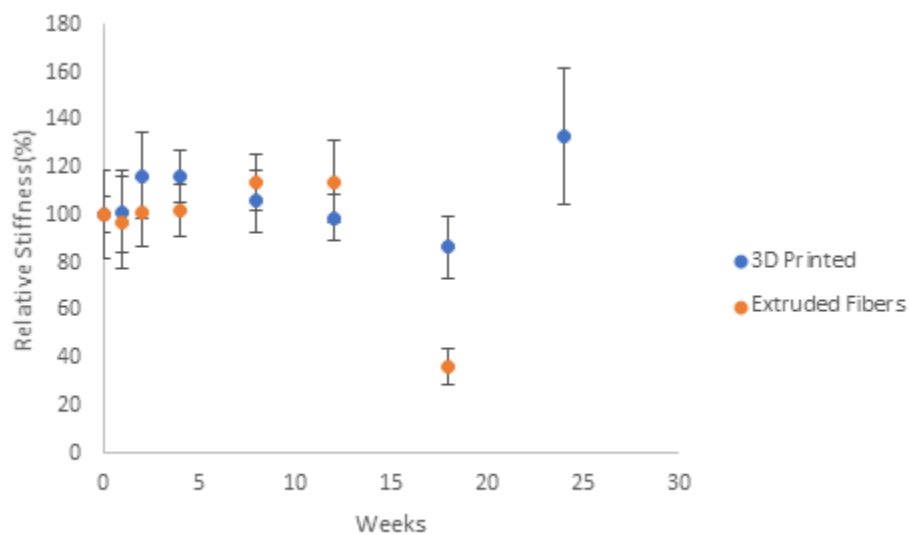
Figure 58 Relative Stiffness of extruded fibers and 3D printed strips of poly(DTD DD).

5.3   Scaffold Physical Properties
Rationale

The scaffold's physical properties were quantified to understand its proportions of

polymer, collagen, and porous volume.

Methods

The 3D printed polymer network was weighed after printing (polymer weight). The

scaffold was weighed after all fabrication steps (scaffold weight). The percent polymer and

percent collagen were calculated from these values. The dry scaffolds were weighed, hydrated

in phosphate buffered saline (PBS) for at least one hour, and weighed again. Swelling ratio was

calculated as the ratio of the hydrated mass to the dry mass (n=6).

Scaffold porosity was determined through an ethanol infiltration assay[59]. A 4 mm

diameter biopsy punch was removed from dry scaffolds (n=6) and trimmed to obtain a

cylindrical sample. The height was measured using Vernier calipers and the dry mass was

measured (m_{dry}). The samples were soaked in 100% ethanol for one hour, superficially dried,

and the mass was immediately measured (m_e). The porosity was found by dividing the pore

volume by the total volume, as demonstrated by the following equation:

$$\% \; porosity = \frac{m_e - m_{dry}}{\rho V} \times 100\%$$

where, ρ represents the density of ethanol (0.789 mg/ml) and V represents the volume of the

sample.

Results

The average print time was 142 ± 3 min. The total scaffold mass was 541 ± 70 mg with a

polymer mass of 499 ± 59 mg and a collagen mass of 42 ± 22 mg. This corresponds to an average

of 92% polymer and 8% collagen. The scaffold swelling ratio was 364 ± 58%, and the scaffold

porosity was 69.9 ± 8.0%.

5.4   Scaffold Confined Compression Creep

Rationale

The purpose of this test is to evaluate the instantaneous and time-dependent biphasic

compressive properties of the scaffold and native meniscus.

Methods

Four mm diameter x 3mm height cylindrical plugs were taken from the anterior, body, and posterior regions of scaffolds and native menisci (n = 12, 4x3 regions) (Figure 59). The hydrated plugs were placed in a 4 mm diameter cylindrical chamber with a unidirectional fluid flow filter. A 1 N load was applied for 3600 seconds (model 5542; Instron, Canton, MA). The instantaneous compressive modulus was calculated from the initial loading phase from 0.5 N to 1 N. The aggregate moduli and permeability of the samples were calculated according to Mow's biphasic theory [92]. A two-tailed, Student's t-test provided statistical comparisons between groups (α=0.05).
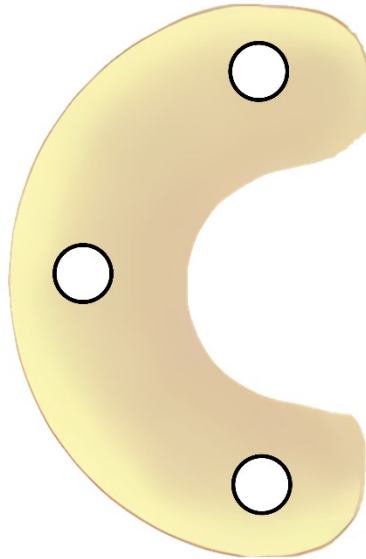
Figure 59 Three plugs were removed from the anterior, body, and posterior regions of the meniscus for confined compression creep testing.

Results

The scaffold matched both the instantaneous and time-dependent compressive properties of the native meniscus (Figure 60). The instantaneous compressive modulus of the scaffold (1.66 ± 0.44 MPa) and native meniscus (1.52 ± 0.59 MPa) were comparable (p=0.26). The aggregate modulus of the scaffold (1.33 ± 0.51 MPa) was within 2% of the native meniscus (1.31 ± 0.36 MPa) and not significantly different (p=0.93). The permeability was not significantly

different (p=0.075). The tensile stiffness of the scaffold (127.6 ± 47.6 N/mm) was 31.4% greater

(p = 0.953) than the native ovine meniscus (97.1 ± 40.3 N/mm). The ultimate tensile load of the

scaffold was 33% of that of the native meniscus (p<0.01).
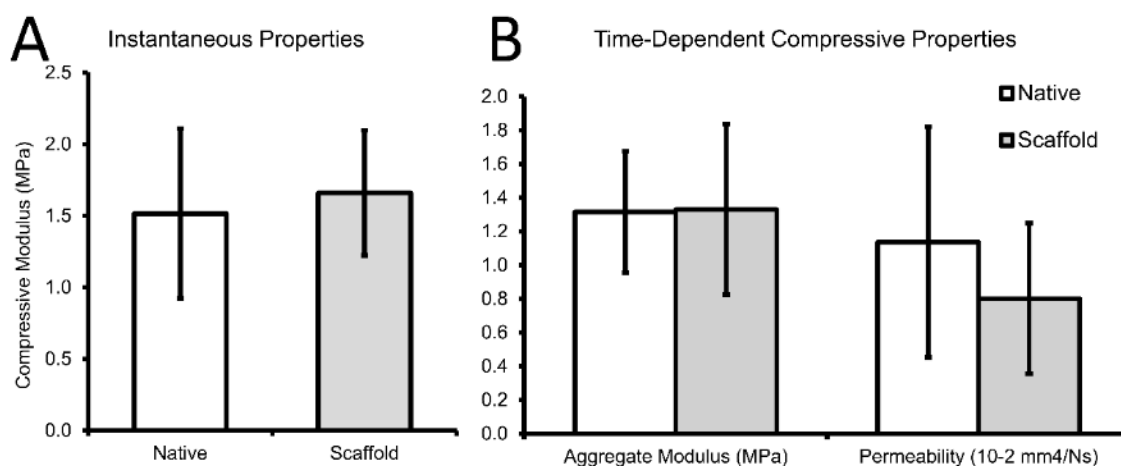
Figure 60 A) Instantaneous compressive modulus and B) aggregate modulus and permeability of native ovine meniscus and scaffold (n=4 from the anterior, body, and posterior regions). The values indicated represent mean ± SD.

5.5   Scaffold Circumferential Tensile Testing
Rationale

The purpose of this assay is to characterized the tensile properties of the partial

meniscus scaffold and compare them to the native meniscus.

Methods

Scaffolds (n=6) and native menisci (n=6) were hydrated in PBS for at least 60 minutes.

Native menisci were cut with an 80% radial width, longitudinal incision throughout the body of

the meniscus. This was done to compare a similar cross-section as the partial meniscus scaffold

which was designed with only 80% of the radial width of the native meniscus (Figure 61).

Specimens were loaded into Bose ElectroForce Cryo-clamps with an 8 mm gage length. Once

specimens within the grips are sufficiently frozen, the specimens are tested at 10 mm/min to

failure. The tensile stiffness in the elastic region and the ultimate load at failure are calculated.

Statistical comparisons were made between the inner margin, outer margin, and scaffold groups

with a one-way ANOVA with a post-hoc Bonferroni method (p=0.05).
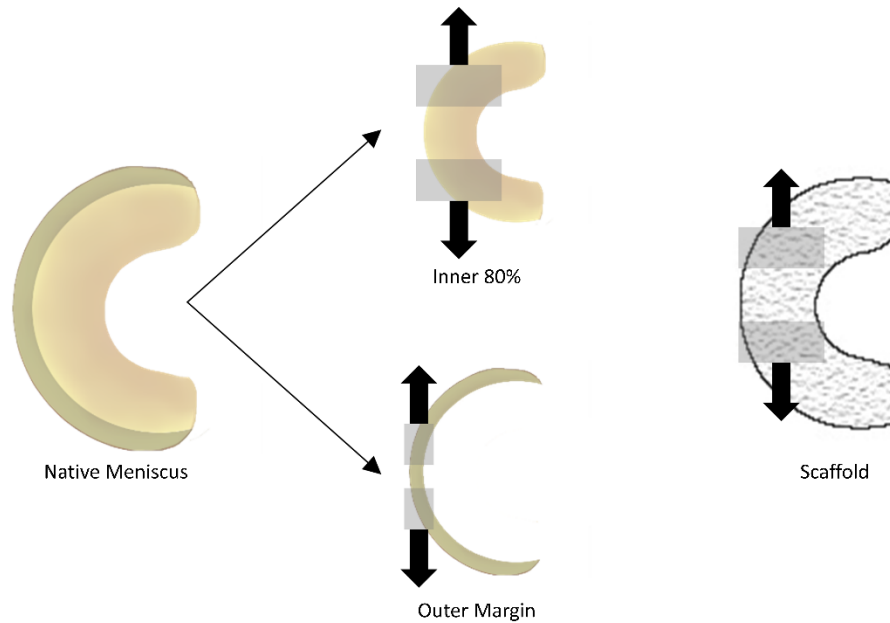
Figure 61 For uniaxial tensile testing, native menisci were transected with an 80% longitudinal tear. Each was pulled to failure and compared to the same testing for the partial meniscus scaffold.

Results

The scaffold mimicked the circumferential stiffness of the native meniscus inner 80% (p=0.953) and outer margin (p=0.522). The scaffold had an average stiffness of 127.6 N/mm, the native meniscus inner margin had a stiffness of 97.1 N/mm, and the outer margin had a stiffness of 128 N/mm. However, the ultimate load of the scaffold was only 33% of that of the native meniscus inner 80% and 25% of the native outer margin (Figure 62).
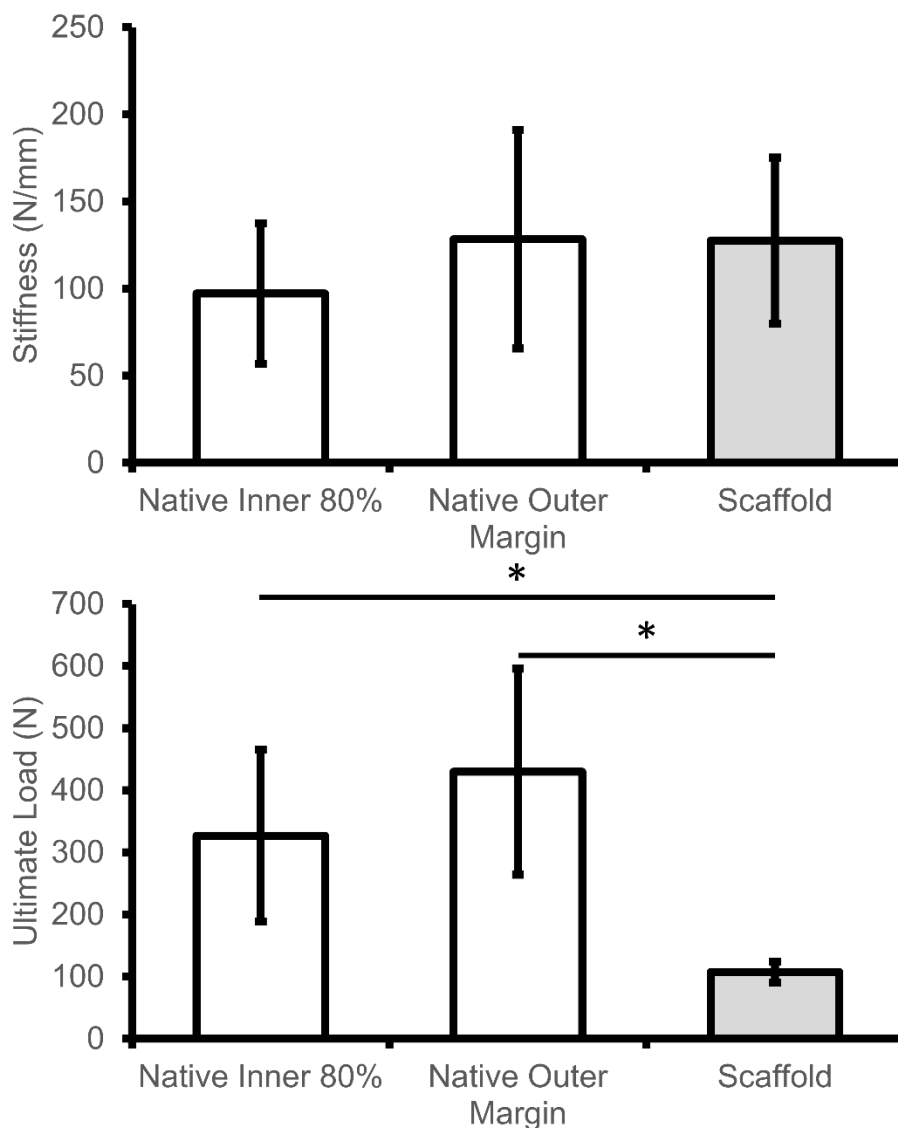
Figure 62 Ultimate load (N) and Stiffness (N/mm) of native meniscus inner 80% and outer 20% and partial meniscus scaffold. * denotes significant differences (p<0.05).

5.6   Scaffold Single Suture Pull-out Study

Rationale

The purpose of this study was to assess the suture retention properties of the scaffold.

Methods

Suture retention testing was performed on scaffolds and native menisci (n=6 each). A 2-0 Ethibond suture was placed radially in a vertical mattress fashion, 2 mm from the outer margin of samples. Two gripping sutures were placed through the sample on either side of the Ethibond suture, reinforced with cardiovascular pledgets (Ethicon, Somerville, NJ), and looped around the

outer margin (Figure 5A). The Ethibond suture was loaded in tension at 50 mm/min until failure[39, 112]. Mode of failure was recorded, and the fixation stiffness and pull-out load were calculated. A two-tailed, Student's t-test provided statistical comparisons between groups (α=0.05).
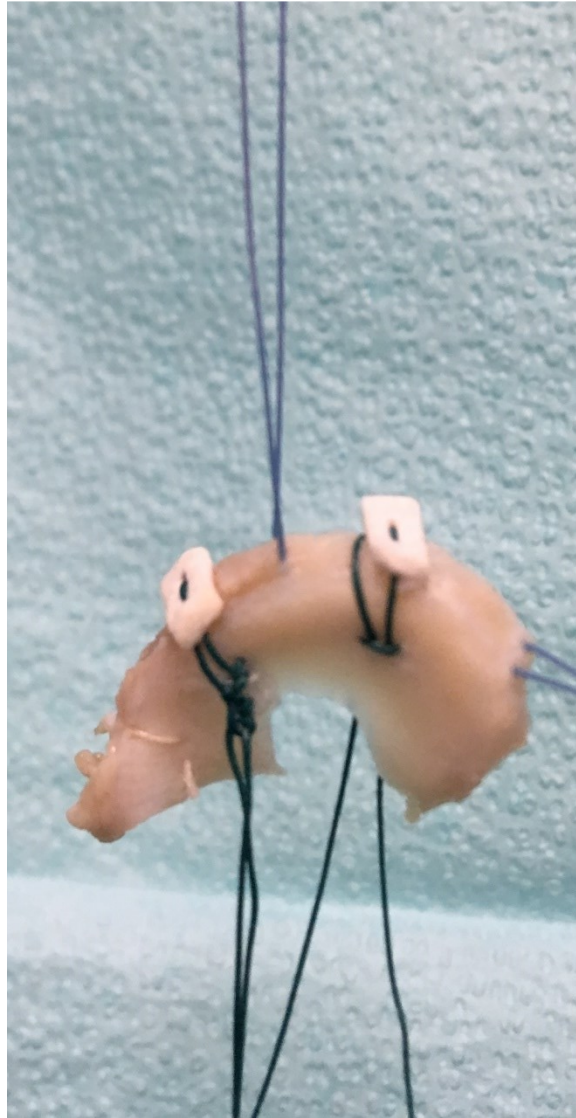
Figure 63 Suture pull-out testing set-up.

Results

the suture pulled out of the scaffold 6 out of 6 samples, whereas for the native condition, the suture failed in 4 samples and the suture pulled out of 2. The scaffold (83.1 ± 10.0

N) possessed a similar ultimate pull-out load (p=0.25) to the native meniscus (91.5 ± 15.4 N).

The stiffness of the scaffold fixation was 30% less than that of the native meniscus.
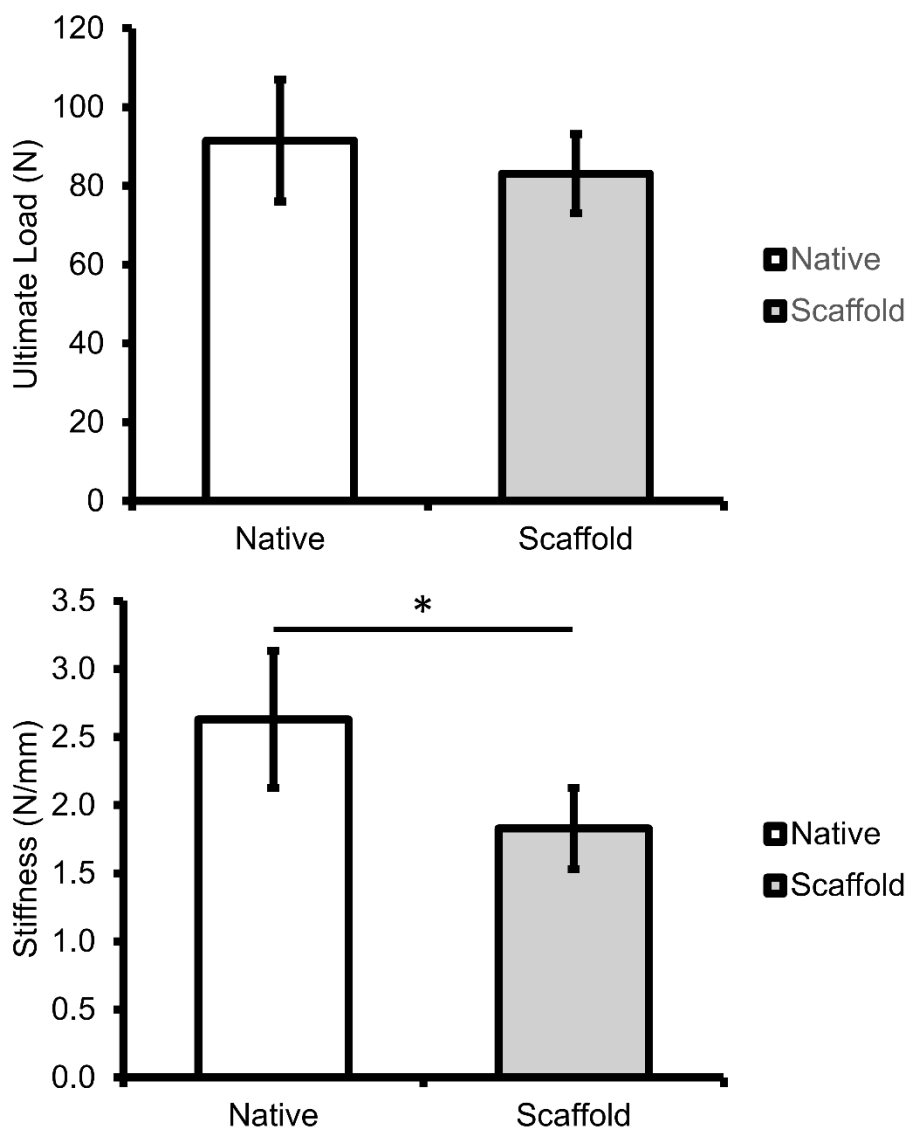
Figure 64 Ultimate load (N) and Stiffness (N/mm) of a pull-out test. * denotes significant differences (p<0.05).

5.7 Scaffold Fixation Strength
Rationale

The purpose of this study is to assess the fixation strength of the entire native meniscus-scaffold construct.

Methods

An 80% radial width, posterior meniscectomy model was produced using a 11 blade scalpel. The scaffold was sutured to the native meniscus using 4, 2-0 ethibond sutures. Two of the sutures were placed radially in a vertical mattress fashion. The other two sutures were placed circumferentially. A bone tunnel was placed through the tibia to allow for the tibia to be gripped using a custom made jig (Figure 65). The scaffold was gripped using a surgical clamp with a screw and bolt for added compression. The samples were pulled in tension laterally at 50 mm/s to failure (n=5). Maximum load and type of failure (pull-out, suture failure, etc.) were recorded. A two-tail, Student's t-test provided statistical comparisons between groups (p=0.05).
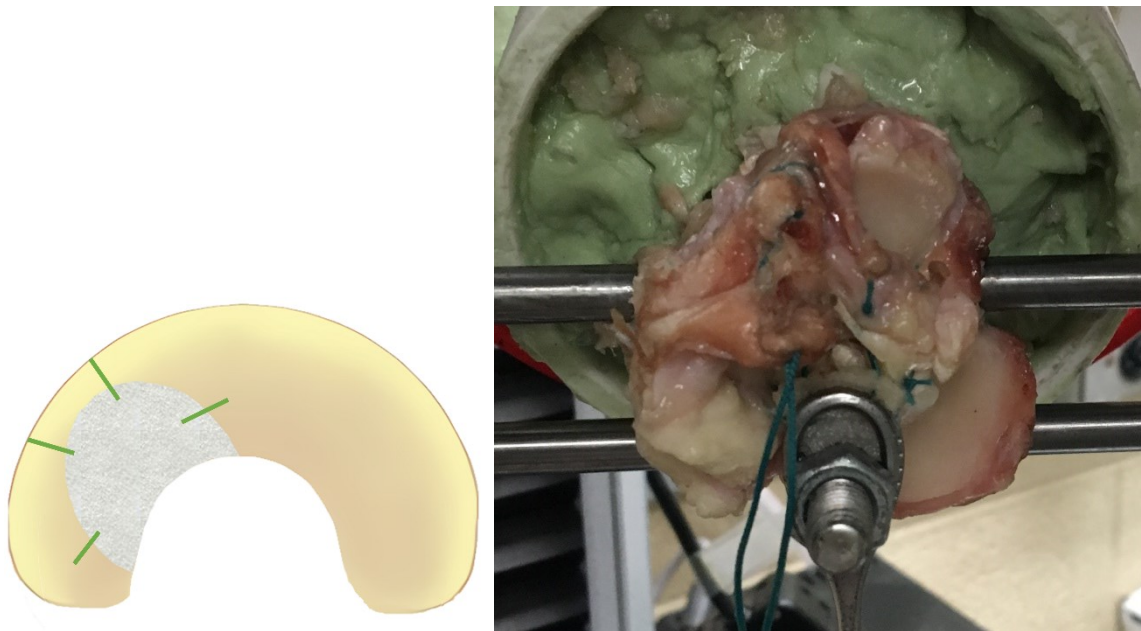
Figure 65 (Left) Schematic of fixation strength test. (Right) Example of fixation testing gripping with surgical clamp.

Results

The ultimate load of the fixation of the scaffold was 89.05 ± 13.64 N and the stiffness was 10.23 ± 1.22 N/mm (Figure 66). The sutures pulled out 4 out of 5 times.
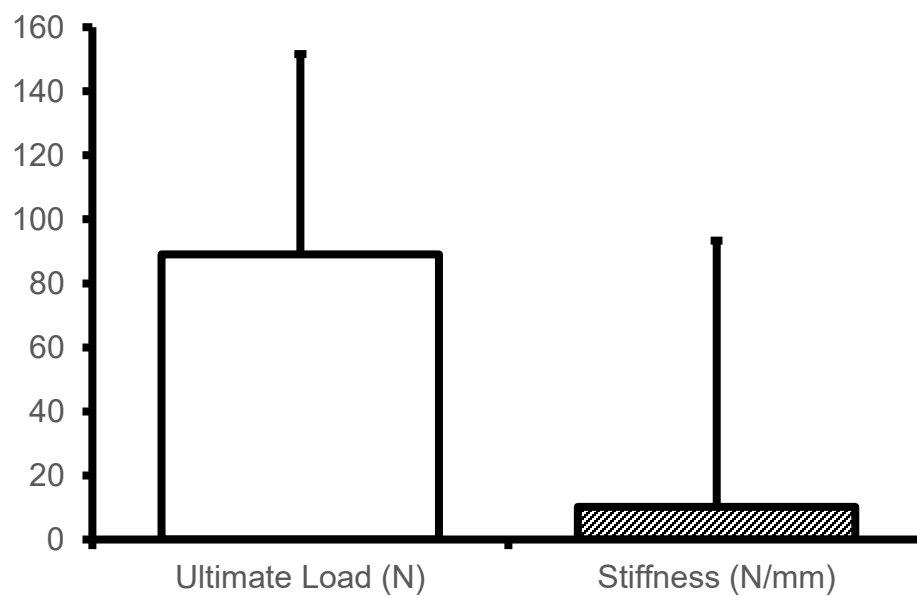
Figure 66 The Ultimate load (N) and Stiffness (N/mm) of the fixation of the partial meniscus scaffold.

5.8   *In Situ* Scaffold Contact Stress Study

Rationale

The purpose of this study is to simulate the contact stresses imposed by the ovine femoral condyle onto the tibial plateau with an intact meniscus, partial meniscectomy, implanted partial meniscus scaffold, and total meniscectomy.   Each condition is tested in 6 ovine knee joints and 2 tests are performed for each condition per knee. This provides a crucial metric for *in vivo* performance of a partial meniscus scaffold, as high peak contact stresses and reduced contact areas have been shown to cause the onset of osteoarthritis[36, 37].

Methods

Fresh frozen ovine hind limb (4-8 years old, Colorado State University) were defrosted at room temperature. The skin, subcutaneous fat, muscle, and patella were removed but the cruciate ligaments, collateral ligaments, and capsule were left intact[70]. The tibia and femur were transected about 10 cm below and above the joint line, respectively. The tibia was potted in polymethylmethacrylate. Several bone tunnels were drilled in the femur to allow for the joint to be held at 0° and 30° flexion. The joint was then covered in PBS saturated gauze and frozen until the day of testing.

On the day of testing, the joint was defrosted at room temperature. A slit was cut into the capsule beneath the medial meniscus to allow for the placement of a Tekscan piezoelectric pressure sensor (K-Scan #4000 9000 psi, Tekscan Inc.) The Tekscan strip was trimmed to the width of the medial compartment and covered in Tegaderm Transparent Film three times (3M, St. Paul, Minnesota) to protect the sensor from water damage. The strip was then covered in petroleum jelly, a suture was placed through the leading edge of the strip, and the suture was pulled to place the strip underneath the medial meniscus[143].

Prior to testing, the Tekscan strip was preconditioned five times at 1500N, and calibrated at 250 N and 1000 N. The strip was covered in petroleum jelly, a suture was placed through the leading edge of the strip, and the suture was pulled to place the strip under the medial meniscus[143]. The MCL was released at the femoral attachment and reattached with the suture endobutton technique (Smith and Nephew, Andover, MA) (Figure 67).
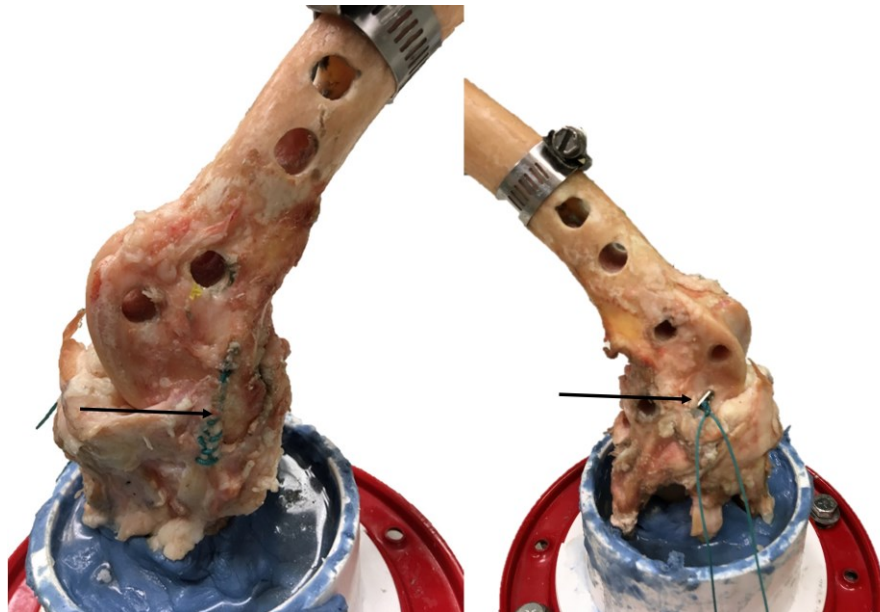
Figure 67 (Left) Sutured MCL attachment and (Right) Endobutton fixation of MCL for Contact Stress Testing.

The knee was loaded into a custom jig in an Instron 5592. The knee was slowly lowered and washers were placed beneath the base plate to ensure natural alignment of the joint. The

base plate was then screwed into place. The joint was thoroughly hydrated before each test

and during each test. A load was applied at 30 mm/min until 200 N was read on the medial

compartment for 5 cycles of preconditioning then 15 cycles of testing. The peak contact

pressure, mean contact pressure, and contact area were calculated for each cycle and averaged

for each knee in MATLAB.

The knee was tested intact, autograph, scaffold, and 80% posterior partial

meniscectomy in 6 cadaveric ovine hind limbs (Figure 68). Autograft was the implantation of

the meniscectomized tissue. The autograft and scaffold were sutured using the same technique

with 4, 2-0 Ethibond sutures (Ethicon, Somerville, NJ).

Results

Angle of flexion did not affect the contact mechanics of the ovine stifle joint for any

condition (p=0.988). The scaffold performed equivalently to autograft for mean contact stress

(p=0.079), peak contact stress (p=0.103), but differed in contact area (p=0.001). Relative to

meniscectomy, the scaffold reduced peak contact stress by 60-67% and increased contact area

by 138% (Figure 6 and 7). Partial meniscectomy demonstrated significantly greater peak and

mean contact stress and significantly less contact area than all other conditions. Compared to

the intact condition, the joint experienced progressive increases in peak contact stresses of 20%,

45%, and 130% and mean contact stress of 7%, 18%, and 167%, for autograft, scaffold, and

meniscectomy, respectively. Likewise, the contact area successively decreased by 6%, 16%, and

40%, respectively.
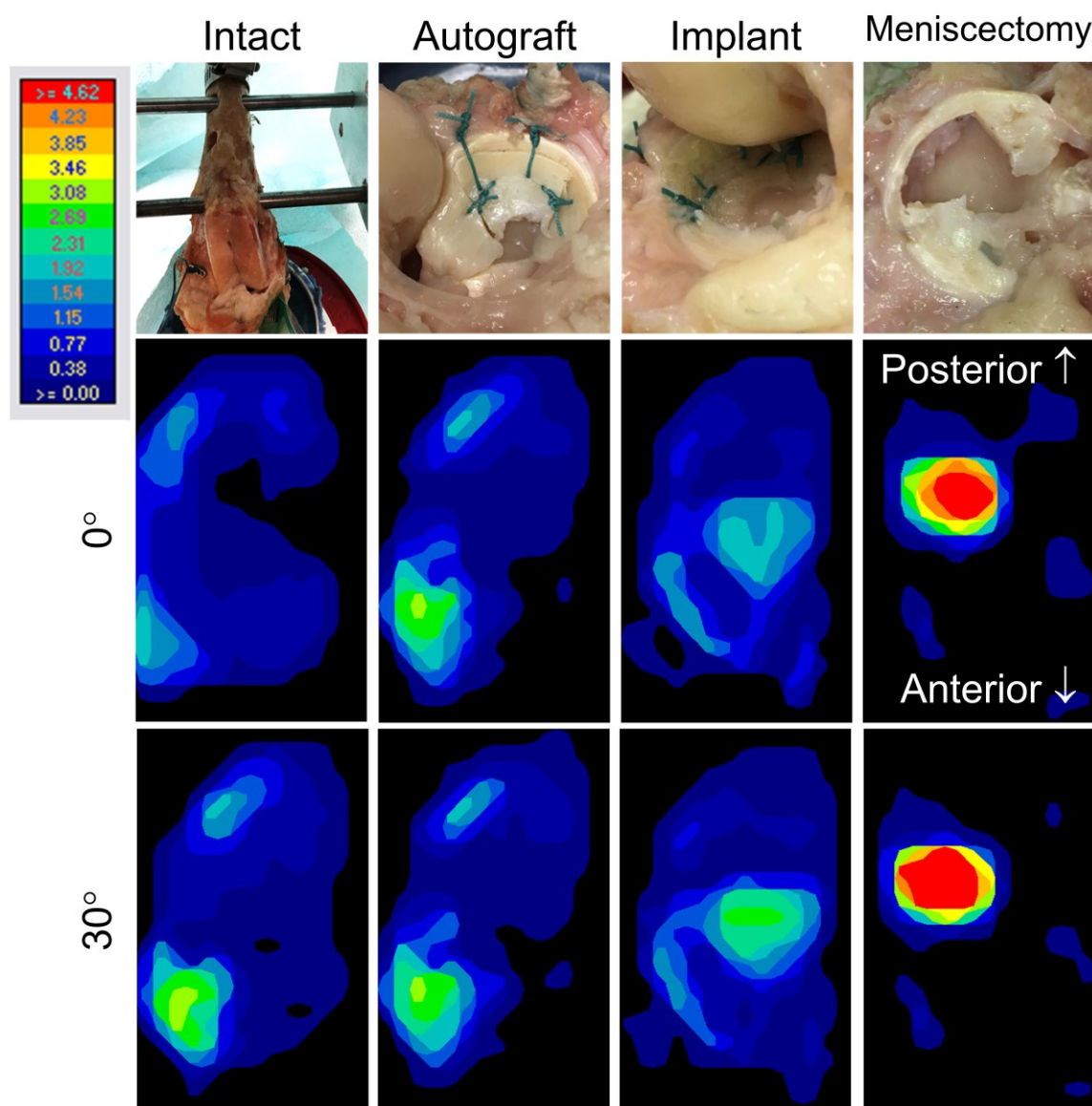
Figure 68 Representative images of intact, autograft, scaffold, and partial meniscectomy conditions. Pressure maps for each condition at 0° and 30° , scaled from 0 to 4.62 MPa.
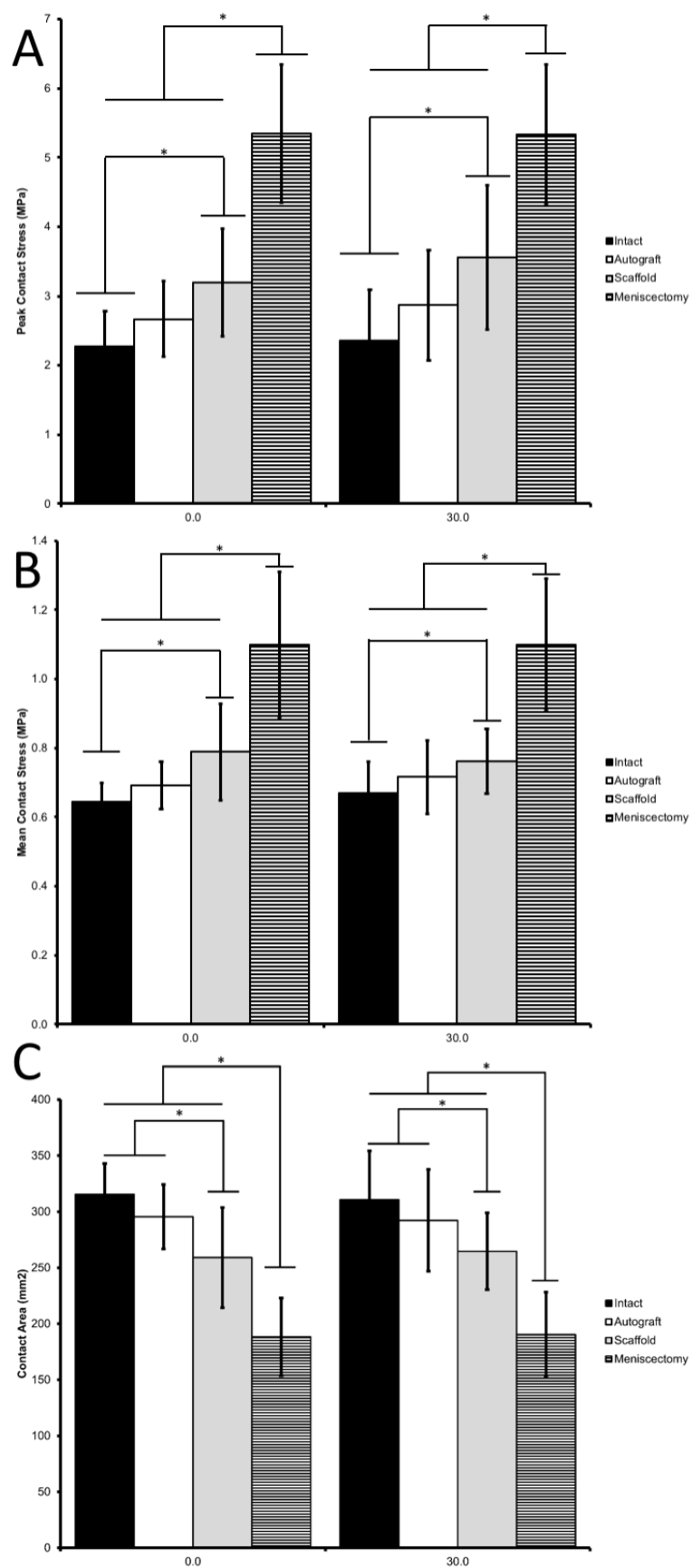
Figure 69 A) Peak contact stress, B) mean contact stress, and C) contact area for intact, autograph, scaffold, and partial meniscectomy conditions. The values indicated represent mean ± SD. *Denotes statistically significant difference (p<0.05).

5.9 Aim 2 Discussion

The primary mechanical function of the meniscus is to transmit and distribute joint loads to protect the underlying articular cartilage. The meniscus is capable of performing this function due to its complex microstructure and resulting anisotropic mechanical properties. The present study demonstrated an acellular, off-the-shelf, 3D printed collagen infused polymeric scaffold could approximate the structural properties of the native ovine meniscus and restore the load-distributing properties following partial meniscectomy of the ovine knee joint. This scaffold has the potential to delay, or possibly prevent, the onset of osteoarthritis caused by partial meniscectomy.

Compressive properties are integral to the load-sharing properties of meniscus devices. An overly stiff device will be overloaded, causing stress concentrations on the underlying cartilage. A device which is not stiff enough may not be adequately loaded or may potentially collapse or shrink, as is suspected of CMI[148]. In addition, scaffolds with compressive moduli that closely match those of the native meniscus induce greater fibrocartilage formation[32]. To our knowledge, this is the first meniscus device to successfully replicate the compressive properties of the native ovine meniscus. Others have achieved less than half of the compressive properties of the native meniscus[50, 69]. CMI and Actifit possess compressive properties of about 25% of ovine meniscus[118].

Tensile mechanics are also integral to the load-sharing properties. Our 3D-printed scaffold demonstrated a similar circumferential stiffness of the native meniscus (131.3%) but failed to reach the ultimate load (32.9%). However, the ultimate load is not of critical concern considering the indication for a partial meniscus scaffold includes an intact peripheral rim, which performs the majority of the circumferential tensile function of the native meniscus[14, 70], and the

maximum expected circumferential load experienced by an ovine meniscus would be only about

120 N[8, 23, 111]. There are no partial meniscal devices that have tensile properties that even

approach native values. Tensile stiffness values in the literature range from 25-47% of native

values using a variety of fabrication techniques[69, 118]. For example, the tensile stiffness of CMI

and Actifit are 42% and 25% that of native ovine values, respectively[118]. Lee et al reported a 3D

printed PCL scaffold that possessed a tensile modulus of 47% and an ultimate strength of 57% of

the native meniscus[69].

With compressive properties and tensile stiffness similar to native tissue, the suture

retention properties of our scaffold was established to validate implantation of the device. The

pull-out strength is important for surgeon handling and positioning of the scaffold during

implantation. The vertical mattress suture has been well documented as the strongest suturing

repair technique[13, 66, 113] and thus was used in our suture retention study. Pull-out load and

stiffness of our scaffold were 90.8% and 69.5% of native, respectively. Similarly, Lee et al found

the pull-out load of their 3D-printed scaffold was comparable to that of the native meniscus[69].

Interestingly, the pull-out strength of CMI is only approximately 20 N[73] and that of Actifit is 50

N[52], with no major indications of suture pull-out reported, suggesting that the pull-out strength

of our scaffold is more than sufficient.

The aforementioned mechanical parameters all contribute to the device's ability to

distribute loads in the joint. In this study, we were able to demonstrate restoration of contact

area and reduction of contact stresses following partial meniscectomy. An 80% partial

meniscectomy resulted in a 40% decrease in contact area and a 130% increase in peak contact

stress. The observed change in contact area was in agreement with previous contact stress

analyses of meniscectomized knees (i.e. 34-58% decrease in contact area)[14, 17, 28, 70, 119, 142, 143].

However, these studies observed peak contact stress increases of only 58%-77%, which may be

a result of the extensiveness of our 80% partial meniscectomy model. Moreover, peak contact stresses with the implanted scaffold were only 22% greater than autograft, indicating that our scaffold performs comparably to native meniscal tissue sutured back to the outer rim.

To our knowledge, the only previous assessment a scaffold's chondroprotective ability involved Actifit[17, 80]. In these studies, Actifit restored mean contact pressure to intact levels, but peak contact pressure increased 36% and contact area decreased 20%, relative to the intact knee, similar to the results with our scaffold. Unlike these previous studies, the present study used a posterior partial meniscectomy, which represents the most clinically relevant model[117, 124]. Moreover, this is the first study to assess the chondroprotective ability of an autograft to provide a positive control for comparison to a partial meniscus scaffold.

This study was not without limitations. Material properties were not calculated for the tensile properties due to difficulties measuring the cross-sectional area of native specimens. However, it may be more appropriate to compare the structural properties, considering the initially oversized scaffold is compressed to conform to the remaining meniscus. For the contact stress analysis, 60° flexion was not tested due to limitations with the testing jig; nonetheless, no effect was found regarding flexion angle.

In conclusion, we developed a polymer reinforced collagenous scaffold which replicates both the axial compressive properties and circumferential tensile stiffness of the native ovine meniscus and demonstrated that the scaffold could retain sutures to significant loads. Furthermore, by scaffolding this scaffold into an 80% partial resection model, we demonstrated the chondroprotective ability of this scaffold. The implanted scaffold successfully reduced peak contact stresses, mean contact stresses, and increased contact area relative to partial meniscectomy. These results suggest the need to further investigate the chondroprotective abilities *in vivo* in a large animal study.

6 Specific Aim 3

The purpose of this aim was to evaluate this scaffold as a partial meniscus replacement in an ovine model. We hypothesized that the partial meniscus scaffold could generate functional meniscal tissue without adversely affecting the surrounding articular surfaces. To test this hypothesis, we evaluated if the scaffold could encourage cell infiltration, extracellular matrix production, and organized tissue deposition and integrate robustly to the surrounding native meniscal tissue without adverse effect on the articular cartilage.

6.1 Study Design

Due to the anatomical similarity between ovine and human knees[18, 23], this study was performed on 24 skeletally mature male Dorset Finn Cross Sheep (2-3 years, 49-80 kg), under an approved Institutional Animal Care and Use Committee protocol (#I13-043). Eighteen sheep received an 80% posterior meniscectomy, representing a clinically relevant defect model[117, 124], followed by the implantation of the partial meniscus scaffold (n=9 at 12 and 24 weeks), fabricated according to Scaffold Fabrication). Four sheep acted as 80% meniscectomy controls (n=2 per time point). Two sheep acted as a 24-week sham control to determine the effect of the surgical procedure alone.

The evaluations methods utilized here were adapted from those established in a series of studies chronically the development of a total meniscus scaffold[87, 104, 106]. At sacrifice, synovium was assessed grossly for synovitis and articular surfaces were assessed grossly for damage and osteophyte formation. Explants were analyzed grossly for size, shape, geometry, intactness, location, and integration. Explant samples were harvested for histology, immunofluorescence, and biochemical analysis and the femoral articular surfaces were evaluated histologically.

Surgical Procedure

Animals were induced with a ketamine-xylazine-midazolam cocktail, intubated, and the right hind leg was prepared for surgery. A modified medial parapatellar arthrotomy and epicondylar osteotomy were performed to provide access to the medial compartment. The medial meniscus was exposed, and an 80% posterior meniscectomy was performed with care taken to maintain the integrity of the peripheral rim (Figure 70).   Using the excised tissue as a template, the scaffold was trimmed to the correct shape, hydrated in saline, and reduced. The scaffold was sutured with two radial 2-0 Ethibond Sutures (Ethicon, Somerville, NJ) and two circumferential 3-0 PDS sutures (Ethicon, Somerville, NJ) (Figure 70). The meniscus was restored to the proper position and the osteotomy was fixed using a 3.5 mm cortical screw (Synthes Monument, CO). The capsule, fascia, and skin were closed. Animals were recovered in cages without limitations on movement. Antibiotics (Cefazolin: 5mg/kg) and anti-inflammatory medication (Rimadyl-carprofen: 1-2 mg/kg) were administered for at least 3 days post-operatively. Animals were sent to a farm facility approximately 10 days post-operatively, and were sacrificed at 12 or 24 weeks.
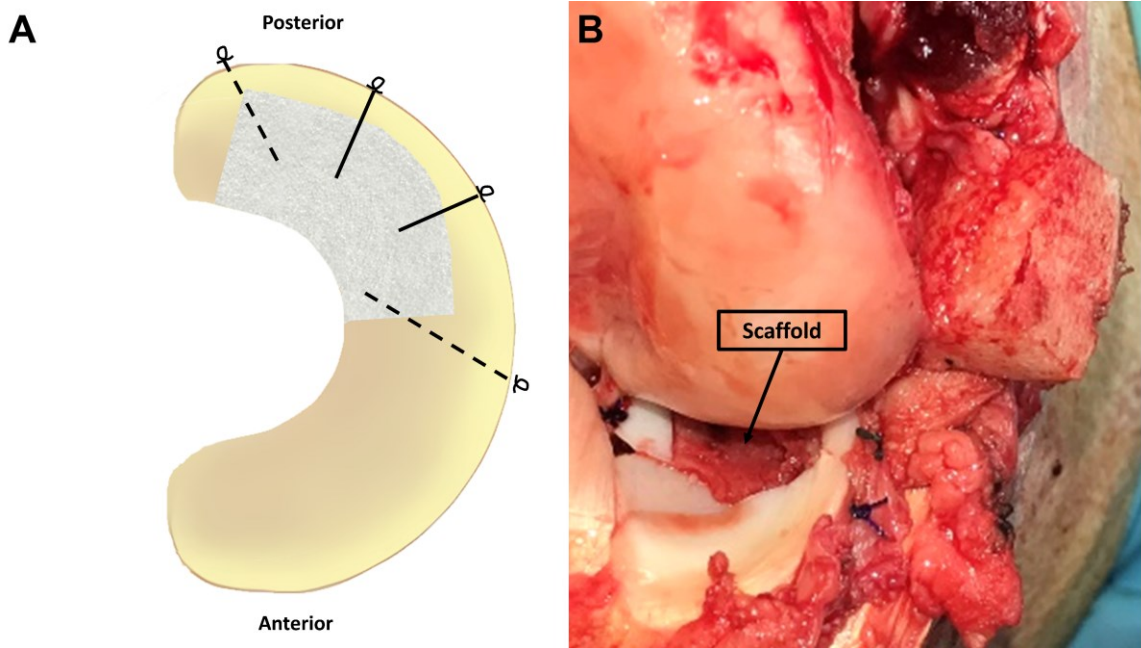
Figure 70 (A) Scaffold fixation scheme. Green lines represent 2-0 Ethibond sutures and purple lines represent 3-0 PDS sutures. (B) Implanted scaffold after meniscus is restored to the proper position.

6.2   Macroscopic Observations
Rationale

At sacrifice, the synovium was assessed grossly for synovitis and articular surfaces were

assessed grossly for damage and osteophyte formation.   Explants were analyzed grossly for size,

shape, geometry, intactness, location, and integration.

Methods

Upon sacrifice, the joint capsule was dissected and the synovium was graded using a

modified system developed for the canine model (Table 4) and imaged[76]. The joint was

disarticulated and the medial meniscus was transected at the anterior and posterior horn

attachments. The implant was evaluated for intactness, thinning, height, color, relative

stiffness, integration, location, morphology, etc. The femoral and tibial cartilage were assessed

for gross damage (Table 5) and osteophyte development (Table 6) using the OARSI

recommended scoring system for goat and sheep and imaged[76]. Cartilage hardness was

measured using a durometer on the surgical and contralateral of the femoral condyle (note: this

could not be performed on the tibial plateau due to the concave nature of the surface) in each

of nine regions as defined by the International Cartilage Repair Society (ICRS) mapping scheme

(Figure 71) [16].

Table 4 Macroscopic scoring system of Synovium [76]

Gross Characteristics	Score
Normal — opal white, semitranslucent, smooth, with sparse well defined blood vessels	0
Slight — focal involvement, slight discoloration, visible fibrillation/thickening, notable increase in vascularity	1
Mild — diffuse involvement, slight discoloration, visible fibrillation/thickening, notable increase in vascularity	2
Moderate — diffuse involvement, severe discoloration, consistent notable fibrillation/thickening, moderate vascularity	3
Marked — diffuse involvement, severe discoloration, consistent and marked fibrillation/thickening, marked synovial proliferation with diffuse hypervascularity	4
Severe — diffuse involvement, severe discoloration, consistent and severe fibrillation, thickening to the point of fibrosis, severe proliferation and hypervascularity	5

Table 5 Cartilage Damage Scoring System [76]

Gross articular damage — score each area separately		Score
Assessment of central cartilage of	Medial tibial condyle Lateral tibial condyle MFC LFC	
Normal		0
Surface roughening		1
Fibrillation and fissures		2
Small erosions down to subchondral bone (<5 mm diameter)		3
Larger erosions down to subchondral bone (>5 mm diameter)		4
Add to give lesion score		0−16

Table 6 Osteophyte Development Scoring System [76]

Osteophyte development – score each area separately		Score
Assessment of joint margin of	Medial tibial condyle Lateral tibial condyle MFC LFC	
Normal		0
Mild osteophyte development (<2 mm outgrowth or < 20% of joint margin)		1
Moderate osteophyte development (2–4 mm outgrowth or 20–50% of joint margin)		2
Large osteophyte development (>4 mm outgrowth or >50% of joint margin)		3
Add to give osteophyte score		0–12
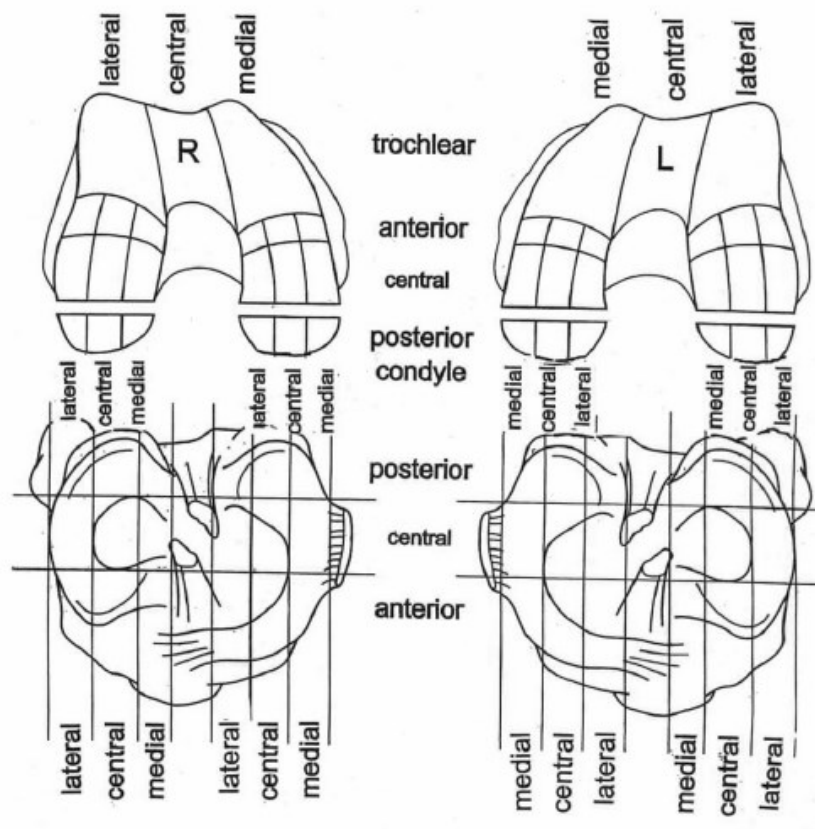
Figure 71 ICRS Mapping Scheme [16]

Results

All animals returned to an unrestricted, standing position within 4 hours postoperatively and achieved normal weight bearing by 8 weeks. The animals experienced an average of 5.6% weight gain by the conclusion of the study. One animal from the 12-week experimental group expired 4 days post-operation due to gastrointestinal complications.

At sacrifice, some discoloration and thickening of the synovium was observed in both experimental and sham joints. At 12-week sacrifice, three scaffolds were completely displaced from the joint into the knee capsule and five had partially displaced from the implantation site but remained within the joint. The completely displaced scaffolds appeared to have overturned, rotating about the outer meniscal rim. The partially displaced scaffolds were extruded underneath the native meniscus and, to varying extents, migrated posteriorly. At 24-week sacrifice, three scaffolds had successfully remained anatomically placed, four were partially displaced, and two completely displaced (Figure 72). We used the three outcomes of the scaffold as an opportunity to understand the effect of the correct biomechanical environment on the development of this scaffold. Therefore, from this point forward, we analyzed the scaffolds according to the three subgroups: anatomically placed, partially displaced, and completely displaced.

| Anatomical | Partially Displaced | Completely Displaced | Meniscectomy | Sham |
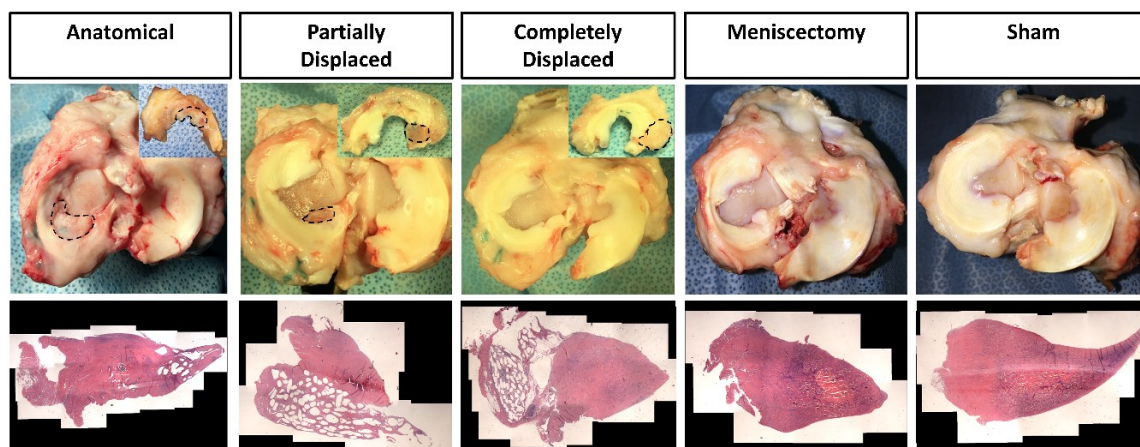
Figure 72 Representative gross appearance from top and bottom view of meniscus. Scaffolds are circled with black dotted line. H&E mosaic image (20x) from each outcome are below gross images.

Scores of synovial changes were not significantly different from 12 to 24 weeks (p=0.29). Excluding the partially displaced condition, there was no significantly differences relative to the contralateral condition in any of the surgical legs (Figure 73). The partially displaced condition significant increased (p=0.016) to 1.65, corresponding to slight to mild synovial changes. Overall, the implant and surgical procedure appears to be well tolerated.
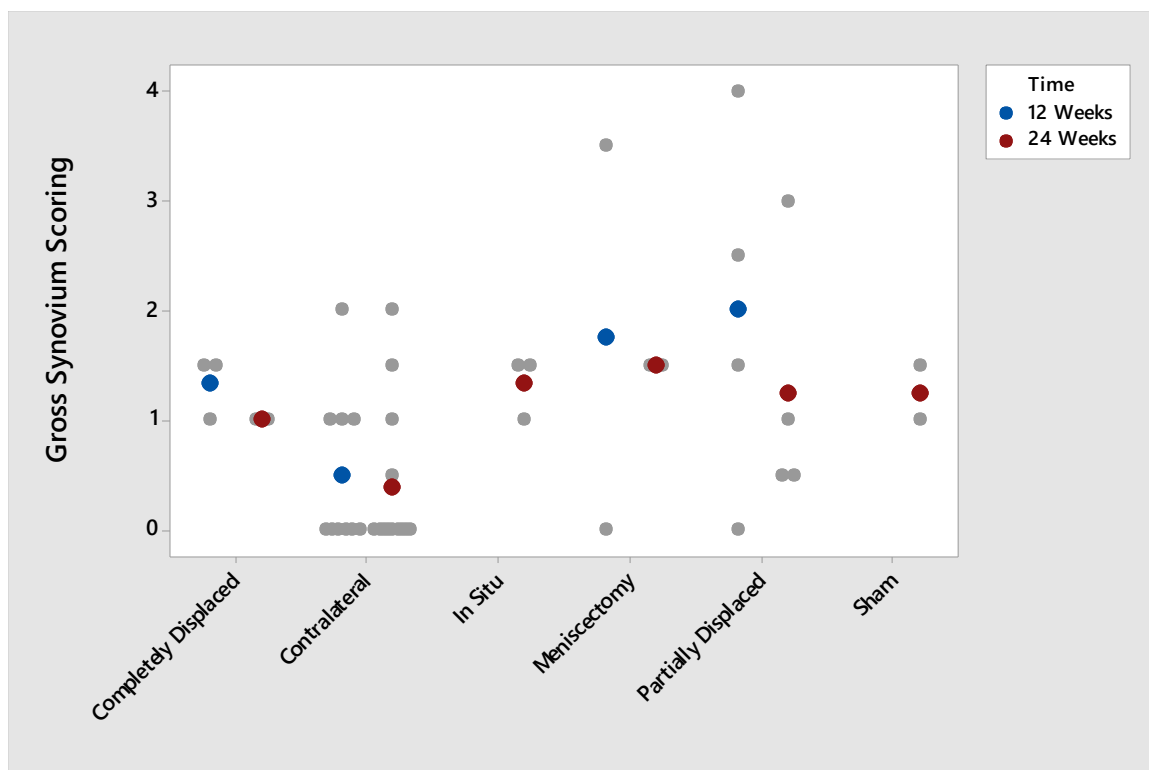
Figure 73 Individual value plot of gross synovial changes scoring. Colored points indicate the mean. Gray points indicate individual values.

All anatomical and partially displaced scaffolds experienced significant tissue infiltration, exhibited the texture of a meniscus reinforced with stiff polymer when compressed, and appeared whiter in color than the native meniscus. There was robust tissue integration with the remaining host tissue in the red-red and red-white zones. No decrease in scaffold volume from time of implantation to sacrifice was observed. At 12 weeks, two partially displaced scaffolds and one completely displaced scaffold had fragmented into two parts. This was not observed at 24 weeks. The completely displaced scaffolds exhibited more signs of wear, some tissue ingrowth, and integrated strongly to the capsule. In the meniscectomy controls, the remaining meniscal tissue deformed into a triangular shape with a thin, translucent tip towards the inner margin. However, this did not correspond to an increase in meniscal volume.

Articular surfaces from the contralateral knee exhibited mild surface roughening without any osteophytes (Figure 74). The joints from the sham subjects had similar surface roughing and

mild osteophyte development. All surgical knees demonstrated slightly increased surface roughening, relative to the sham, with some fibrillation and fissures observed. There was no macroscopic difference in cartilage health between the 12 and 24-week time points. Osteophyte formation was similar between all surgical joints, including the 24-week sham, 12-week scaffolds, and the anatomical 24-week scaffolds. Moderate osteophyte development was observed in knees corresponding to the 24-week partially and completely displaced scaffolds.
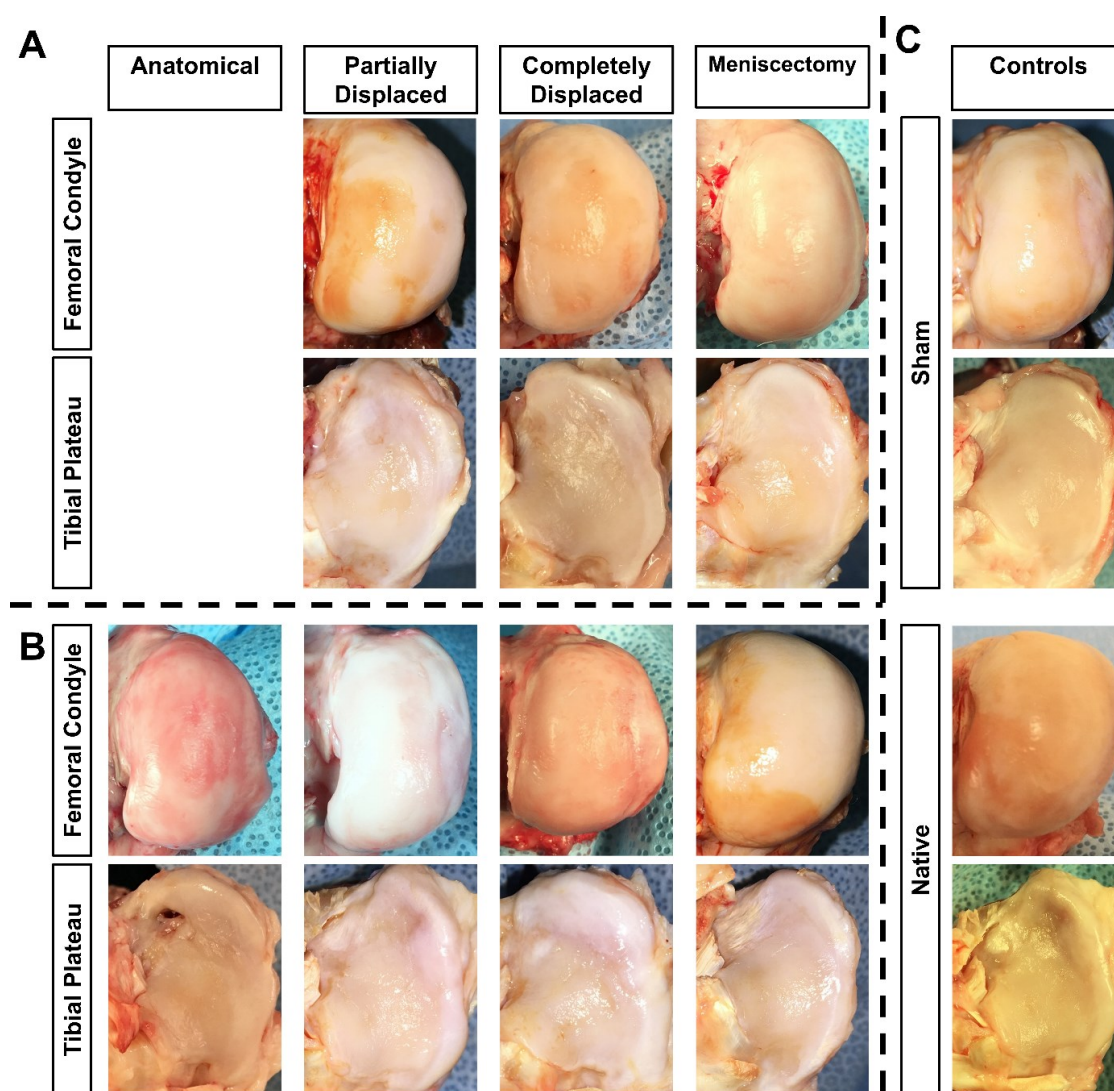
Figure 74 Representative gross appearance of femoral condyle and tibial plateau articular surfaces from each outcome at (A) 12 and (B) 24 weeks, and (C) for sham and native controls.

The cartilage indentation hardness score did not change with time (p=0.99) but were dependent on condition (p<0.001) (Figure 75). Although contralateral cartilage was scored significantly greater, there were no differences between the sham control, meniscectomies, or scaffolds. Meniscectomy did possess the lowest mean hardness of 80.8 and the contralateral had the greatest of 89.5. The scaffold and sham conditions possess hardness within 2% of each other.
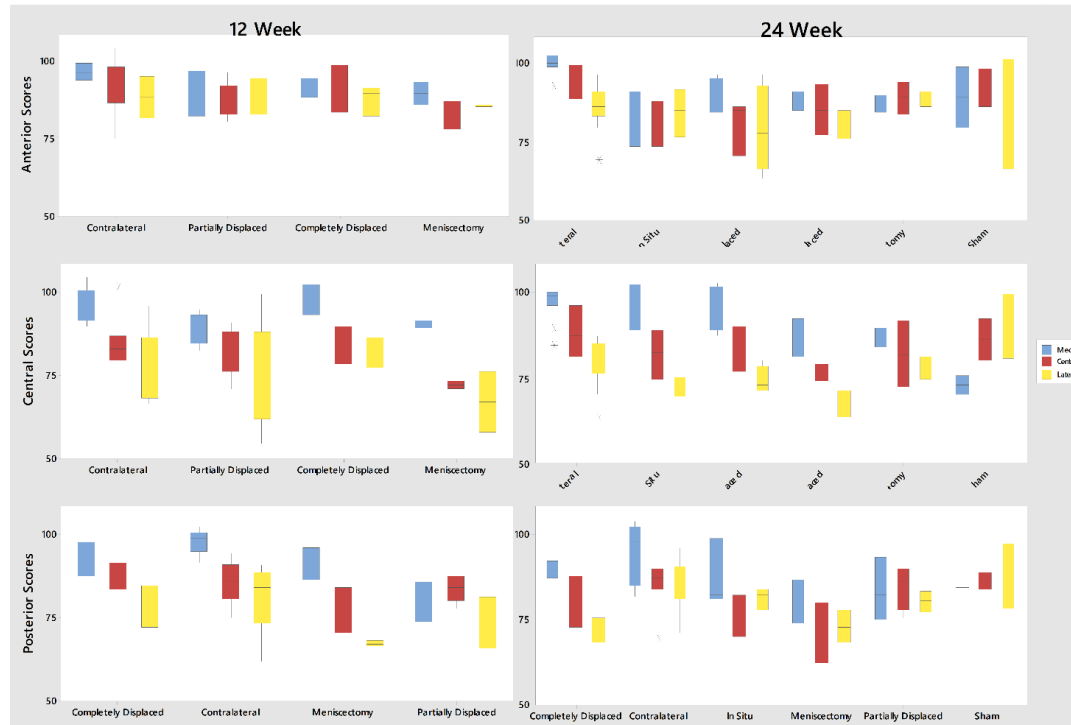
Figure 75 Cartilage hardness from each group as a function of location (3x3 grid).

There was no significant difference in OARSI gross cartilage damage and osteophyte formation scoring from 12 to 24 weeks except for femoral osteophyte formation (p=0.025) (Figure 76 and Figure 77). However, this difference corresponded to less than half a point. On average, no surgical group had a high degree of cartilage damage with the highest femoral and tibial damage observed being 2.3 and 1.87, respectively. On average, there was very mild osteophyte formation observed for all groups (<1.02).

The contralateral articular surfaces had very little cartilage damage or osteophyte formation at either time point. The surgical procedure does not adversely affect the tibial

cartilage but causes mild femoral cartilage damage and some osteophyte development, as demonstrated by the sham condition. Anatomical scaffold knees had significantly greater scores than the contralateral for femoral and tibial damage and tibial osteophyte. However, there were only 3 implants that remained anatomical and 1 of the 3 exhibited a high degree of damage. If the outlier was excluded, the anatomical implants protected the cartilage to a similar degree as the sham. Unsurprisingly, the displaced implants caused large osteophytes to develop.
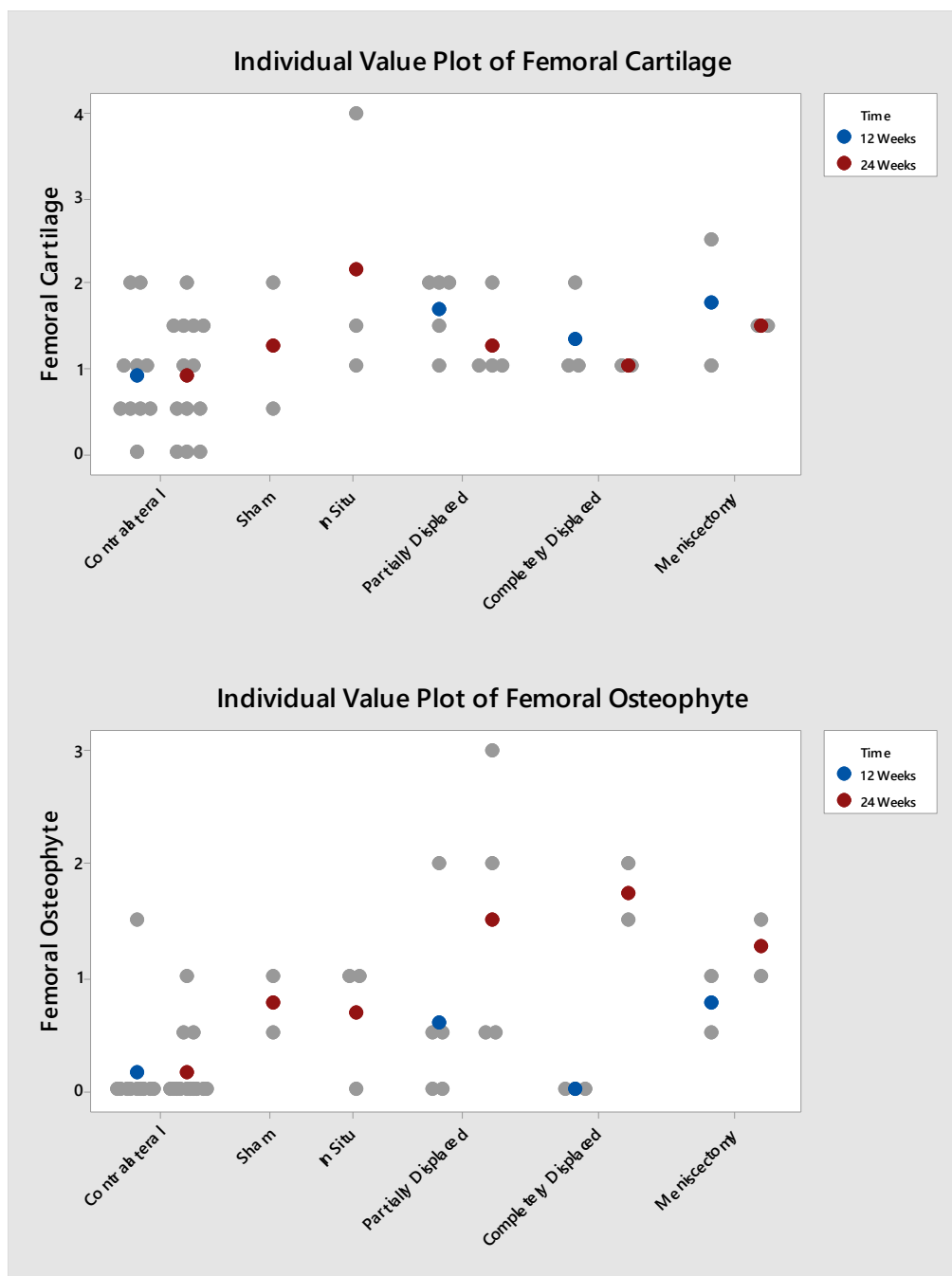
Figure 76 Individual value plots of gross femoral cartilage damage and osteophyte scoring based off of OARSI recommendations. Colored points indicate the mean. Gray points indicate individual values.
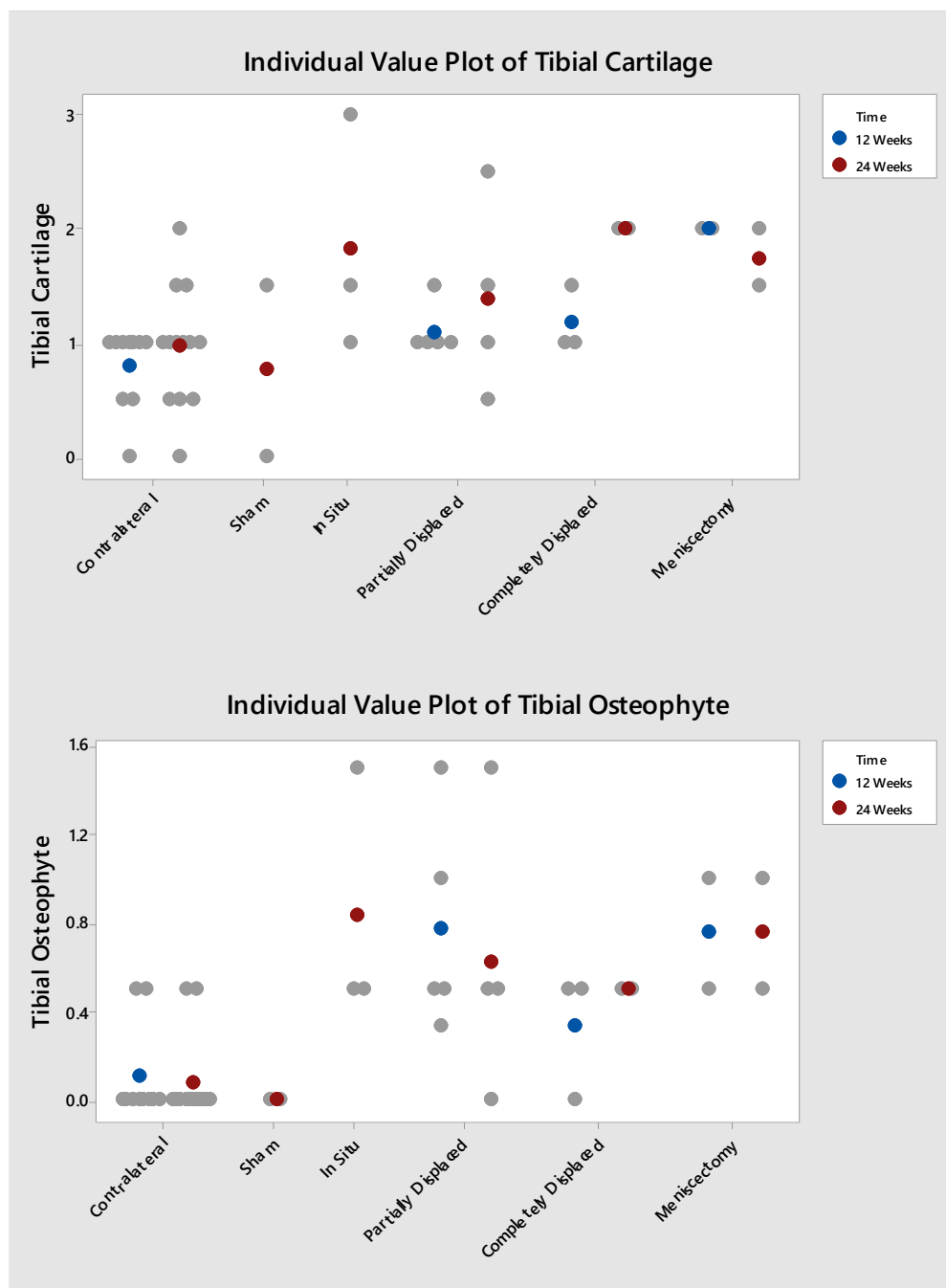
Figure 77 Individual value plots of gross tibial cartilage damage and osteophyte scoring based off of OARSI recommendations. Colored points indicate the mean. Gray points indicate individual values.

6.3 Histology of the Synovium
Rationale

The purpose of this study was to evaluate synovial changes resulting from the implant.

Methods

Synovium from the suprapatellar fold were fixed immediately in 10% Carson's buffered formalin, paraffin-embedded, sliced into 8 μm sections, and stained with H&E. The synovium was evaluated semi-quantitatively by three blinded scorers using the OARSI semi-quantitative scoring system (Table 7)[76].

Table 7 Semi-quantitative scoring of synovium changes [76].

Criteria	Score	Observation
Intimal hyperplasia	0	Normal (one cell deep only)
	1	Mild, focal (2—4 cells deep, and <20% area)
	2	Mild diffuse (2—4 cells deep, and >20% area) or Moderate focal (five or more cells deep, and <20% area)
	3	Moderate diffuse (five or more cells deep, and >20% area)
Inflammatory cell (lymphocytic/ plasmocytic) infiltration	0	Normal (occasional cell)
	1	Mild — focal infiltration, no lymphoid aggregates
	2	Moderate — diffuse infiltration, no lymphoid aggregates
	3	Marked — discreet lymphoid aggregates
Sub-intimal fibrosis (loose connective tissue areas only)	0	None
	1	Light, focal (<20% area) collagen staining
	2	Heavy focal (<20% area) or slight diffuse collagen staining
	3	Heavy diffuse collagenous staining
Vascularity	0	0—2 vascular elements per 100× field
	1	3—4 vascular elements per 100× field
	2	5—8 vascular elements per 100× field
	3	More than eight vascular elements per 100× field
Aggregate score (joint)	0—12	Sum of the scores obtained for the four criteria above

Results

There were no significant differences in synovial change scores in regards to time (p=0.947) nor condition (p=0.19) (Figure 78).
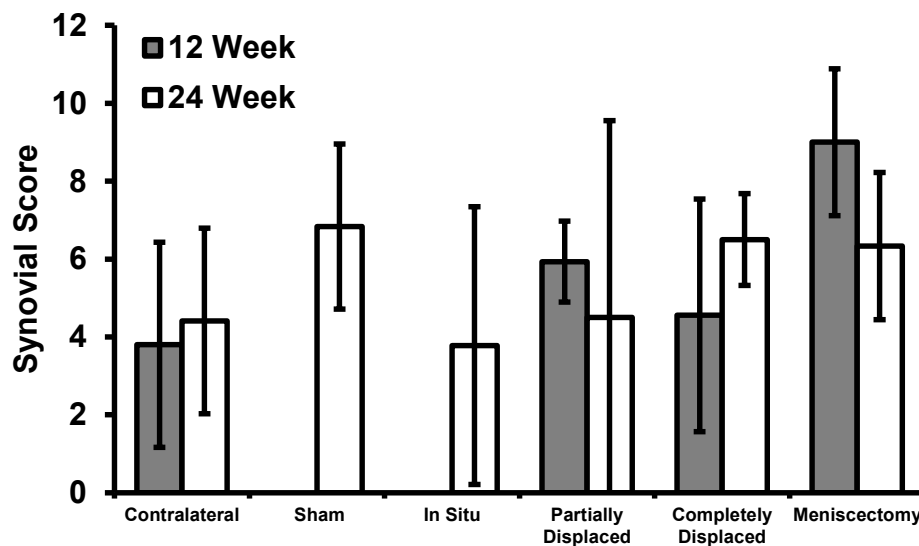
Figure 78 Macroscopic synovial changes observed after 12 and 24 weeks.

6.4 Histology of the Scaffold

Rationale

The purpose of histological analysis of the explants is to study the microarchitecture of the explant with regards to cell concentration and phenotype, extracellular organization and maturity, relative concentration of proteoglycans, integration, and inflammatory reaction.

Method

Immediately after dissection, the medial menisci were severed at the roots, the explant was located, and a cross-section was taking through the width of the explant and native outer rim. The section was fixed in 10% Carson buffered formalin, embedded in paraffin, and sliced into 8-mm cross sections. The sections were stained with hematoxylin and eosin (H&E), Safranin-O, or Picrosirius Red (AML Laboratory, Saint Augustine, FL). Slides were evaluated blindly for the magnitude and type of tissue ingrowth, tissue thickness and integrity, surface, cell density, vascularization, and inflammatory response using modified Schreiber scoring [150].

Results

Scaffold histological scoring can be found in

Appendix 3. Scaffold Histological Scoring. Histological evaluation revealed all scaffolds maintained their original thickness, did not adversely affect adjacent tissue, and experienced tissue ingrowth throughout without any large pores or gaps. Anatomical and partially displaced scaffolds exhibited dense tissue infiltration and growth at both 12 and 24 weeks with hypercellularity relative to native tissue. A mixed population of elongated and round cells were observed with a larger proportion of round cells at 24 weeks. The cells exhibited a normal cell morphology with some instances of cell clustering which were associated with a deeper Safranin-O staining. Vascularization was found throughout scaffolds at 12 and 24 week, and only in the outer margin of native menisci. Focal clusters of lymphocytes and relatively few multinucleated giant cells were observed at both time points. The tissue developed large collagenous bundles running radially with larger bundles at 24 weeks. Some Safranin-O staining was observed in all scaffolds within the joint with a slight increase observed between 12 and 24 weeks.
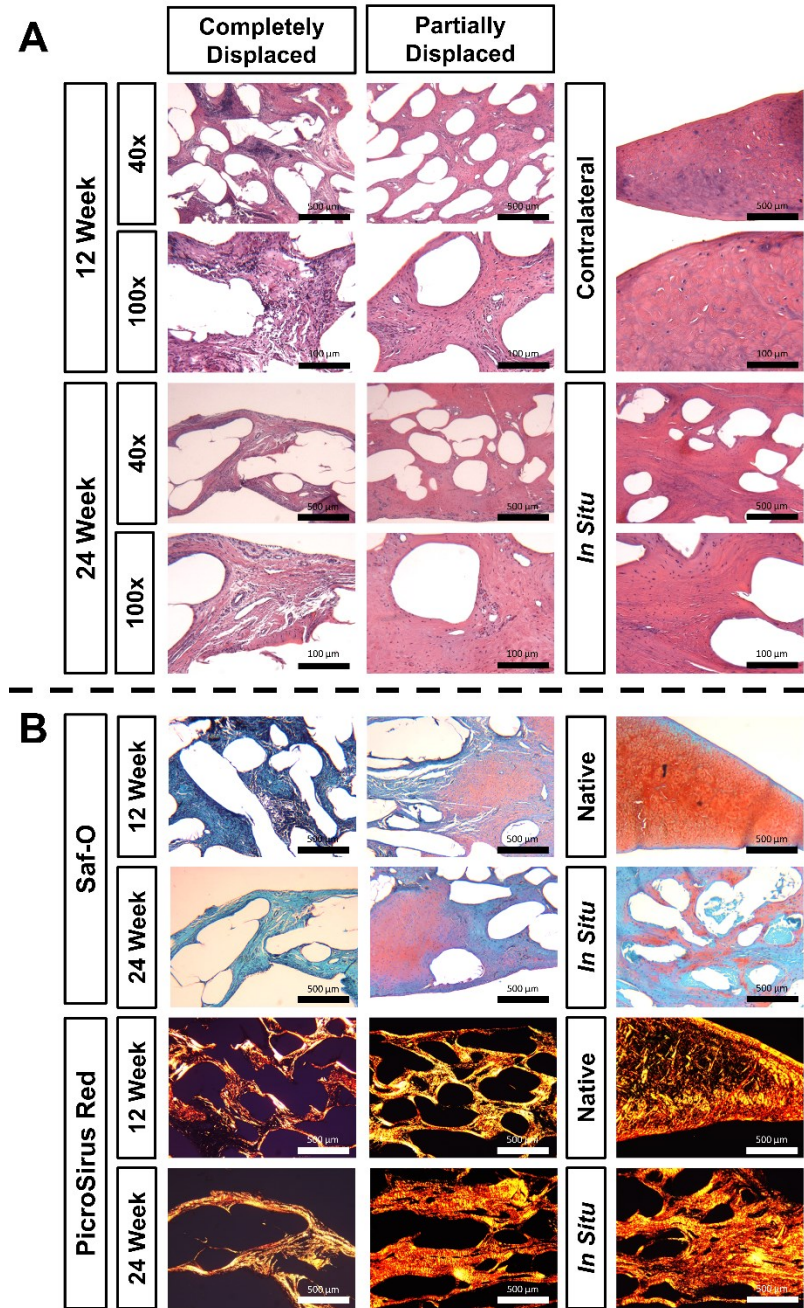
Figure 79 (A) H&E images of scaffolds and contralateral controls. Image magnification: 40x and 100x. Scale bars: 500 μm and 100 μm. **(B)** Safranin-O/Fast Green and Picrosirus Red images of scaffolds and contralateral controls. Image magnification: 40x. Scale bars: 500 μm.

On the other hand, completely displaced explants exhibited a heavy chronic inflammatory response with loose, unorganized fibrous tissue ingrowth. These explants lacked fibrochondrocytes and the predominant cell type was typically inflammatory. There were few, if

any, collagenous bundles observed and no significant Safranin-O staining. Interestingly, when a portion of these explants had remained within the joint, the portion in the joint had fibrous ingrowth and loose fibrous connective tissue ingrowth in the portion outside of the joint.

6.5   Immunofluorescence of the Scaffold
Rationale

The purpose of immuno-histochemical evaluation of the neo-tissue is to analyze the collagen content (type I and II) to further characterize the phenotypes of the present cells.

Methods

1 mm thick cross-sections were taken from the explant and the posterior region of the contralateral meniscus. The sections were embedded in Optimal Cutting Temperature compound (Tissue-Tek, Sakura, Torrance, CA), chilled on ice, flash frozen in liquid nitrogen, and stored at -80°C. 10 μm slices were cut using a cryostat, placed on microscope slides, and dried at room temperature. Rabbit Type I Collagen (AB745, Millipore, Billerica MA) with a 1:300 dilution and Rabbit Type II Collagen (AB34712, Abcam Inc., Cambridge MA) with a dilution of 1:200 were applied to the tissue. The secondary Antibody was Donkey-anti-rabbit AlexaFluor 594 Texas Red (Invitrogen) with a dilution of 1:1000. Samples were mounted with Anti-Fade ProLong Gold with DAPI for nucleus visualization and imaged with a Leica fluorescent microscope with a ProgRes camera and CapturePro imaging software (Jenoptik Laser, Jena, Germany).

Results

Immunofluorescence staining showed COL-I was throughout the scaffolds with a greater intensity on the surface and surrounding large fibers (dark voids). Cell nuclei found near COL-I staining were typically more elongated than cells found near COL-II staining (Figure 80). COL-I was observed to a much greater extent in completely displaced scaffolds. Anatomical scaffolds exhibited the least staining, relative to other scaffolds, but more than native controls. In partially displaced and anatomical scaffolds, COL-I organization typically ran concentrically around the

polymer fibers and intensity decreased from 12 and 24 weeks. Native samples only exhibited minor COL-I staining at the tissue surface.

COL-II was found throughout all anatomical and partially displaced scaffolds with round cell nuclei adjacent to the intense staining. At 24 weeks, anatomical scaffolds exhibited higher staining intensity relative to partially displaced scaffolds at equivalent time points. A small increase in intensity was observed from 12 and 24 weeks for all scaffold groups. Negligible staining was detected in completely displaced scaffolds.
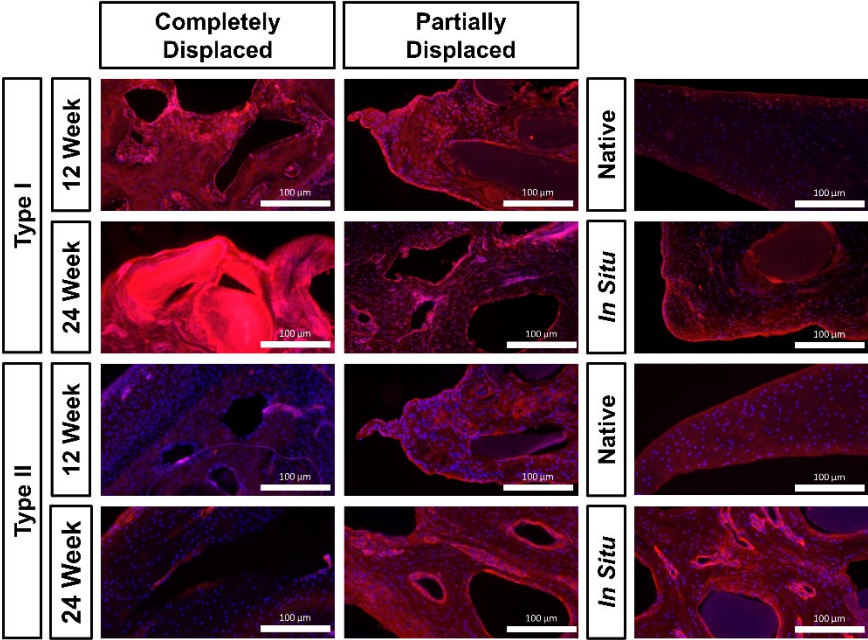
Figure 80 Type I and II collagen immunofluorescence at 100x. Red indicates collagen presence and blue indicates cell nuclei. Scale bar: 100 μm

6.6   Biochemical Analysis of the Scaffold
Rationale

The purpose of this study was to quantify the progression of collagen and sulfated glycosaminoglycans content of the neo-tissue over time and to compare to the contralateral controls.

Methods

Collagen and sulfated-glycosaminoglycans (S-GAGs) were quantified via biochemical assays. One mm cross-sections were taken from the scaffold or inner margin of native tissues at sacrifice were fresh frozen. On the day of testing, the samples were thawed and hydrated in phosphate-buffed saline (PBS). The samples were superficially dried, weighed (hydrated mass), lyophilized, and weighed (dry weight). Samples were digested in papain solution (1 mg tissue/100 μL solution; 125 mg/mL papain, 5 mM L-cysteine-HCl, 5 mM ethylenediaminetetraacetic acid disodium in PBS (pH=7.4) for 24 hours at 37°C. A portion of the sample homogenate was set aside and a portion was diluted 1:2 in 12 M HCl at 120°C for 24 hours to hydrolyze the sample. The hydrolyzed samples were diluted 1:3 in 6 M HCl and the homogenates were diluted 1:4 to bring the concentrations to an appropriate range for each assay.

Water content was defined as the ratio of the hydrated weight to total weight. Collagen content was assessed using a hydroxyproline assay kit (Chondrex, Inc., Cat #: 6017) on the hydrolyzed samples and s-GAG content was assessed using a glycosaminoglycan assay kit (Chondrex, Inc., Cat #: 6022) on the sample homogenates, according to the manufacturer's instructions. For collagen content, hydroxyproline content was converted to collagen content using a scale factor of 7.46[94]. A two-way ANOVA with a post-hoc Tukey test was performed to determine statistical differences between groups (α=0.05).

Results

There were no significant differences in water content between each condition (p=0.59) or time points (p=0.72) (Figure 81A). Native controls had significantly greater collagen and GAG content than all scaffold groups (Figure 81B and Figure 81C). The outcome of the scaffold had a direct effect on the collagen and GAG content of the scaffold. Anatomical scaffolds possessed nearly identical collagen content at 24 weeks as partially displaced scaffolds, corresponding to more than a third of contralateral controls. On the other hand, the anatomical scaffolds

developed nearly 40% more GAGs than the partially displaced scaffolds at 24 weeks. Partially

displaced scaffolds developed 15.5 ± 7.7 % collagen content at 12 weeks and continued to

increase to 22 ± 0.7 % at 24 weeks. The partially displaced and anatomical scaffolds achieved 53%

and 74% of the GAG concentration of contralateral menisci, respectively. For completely displaced

scaffolds, collagen content was 12.8 ± 4.9 % at 12 weeks and did not increase further at 24 weeks

(11.4 ± 0.1 %). GAG content demonstrated a similar trend with a content less than 40% of the

contralateral control at 12 weeks with no increase from 12 to 24 weeks.
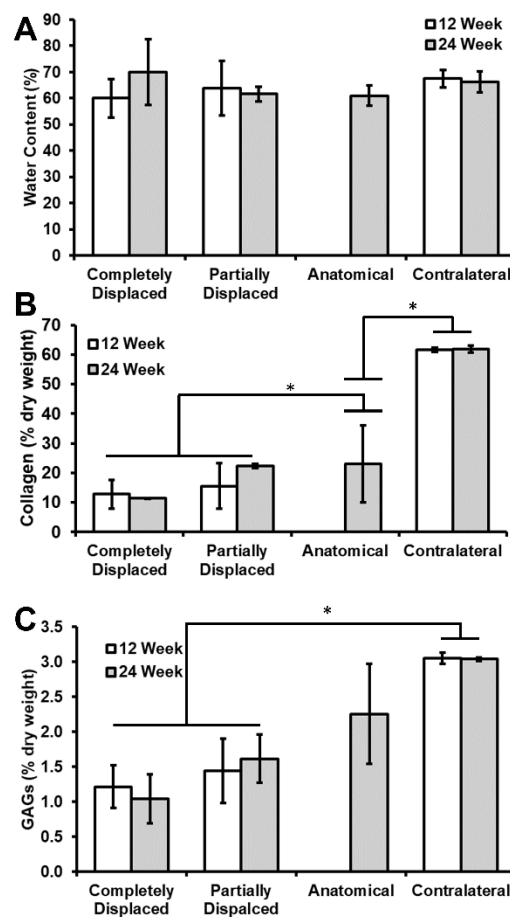
Figure 81 Biochemistry of scaffolds and contralateral controls. (A) Water content, (B) collagen content, and (C) sulfated-GAGs. Collagen and sulfated-GAGs expressed a percentage of dry weight tissue. Values indicated are mean ± S.D. Asterisk denotes statistically significant differences (p<0.05).

6.7   Histology of the Articular Cartilage
Rationale

The purpose of this study was to evaluate the underlying articular cartilage for severity of damage in order to determine if the implant had a chondroprotective effect.

Methods

Femoral condyles were evaluated histologically. Three mediolateral slices were taken from the anterior, central, and posterior regions of the surgical and contralateral joints. The slices were fixed in 10% Carson's buffered formalin, decalcified with acid-EDTA solution, paraffin-embedded, sectioned to 8µm, and stained with Safranin O/Fast Green (AML Laboratories). Each section was further divided into three regions (medial, central, and lateral) to obtain 9 regions per medial femoral condyle according to the ICRS mapping scheme. Sections were graded blindly using a modified microscopic scoring system from OARSI (Table 8)[76] by three independent observers (SAG, AB, JMP). The OARSI system includes weighted scoring for structure, chondrocyte density, cell cloning, Safranin O retention, and tidemark integrity with a maximum score of 25.

Table 8 Semi-quantitative scoring system of microscopic cartilage damage [76].

Structure (score the worst area in field of view)	
Normal	0
Slight surface irregularities (surface barely disturbed)	1
Moderate surface irregularities (surface roughened)	2
Severe surface irregularities (disruption, fissuring/fibrillation to <10% depth)	3
Fissures to transitional zone (1/3 depth)	4
Fissures to radial zone (2/3 depth)	5
Fissures to calcified zone (full depth)	6
Erosion or severe fibrillation to mid zone (1/3 depth)	7
Erosion or severe fibrillation to deep zone (2/3 depth)	8
Erosion or severe fibrillation to calcified zone (full depth)	9
Erosion or severe fibrillation to subchondral bone	10
Chondrocyte density ("average" score for whole field of view in non-calcified cartilage)	
Normal	0
Increase or slight decrease	1
Moderate decrease	2
Severe decrease	3
No cells	4
Cell cloning (score the whole field of view)	
Normal	0
Several doublets	1
Many doublets	2
Doublets and triplets	3
Multiple cell nests or no cells in section	4
Interterritorial Toluidine blue (score the worst area in field of view working from AC surface down)	
Normal	0
Decreased staining to mid zone (1/3 depth)	1
Decreased staining to deep zone (2/3 depth)	2
Decreased staining to calcified zone (full depth)	3
No staining	4
Tidemark/calcified cartilage/subchondral bone (score the worst area in field of view)	
Intact subchondral bone plate + single tidemark	0
Intact subchondral bone plate + duplicated tidemark	1
Blood vessels penetrate through subchondral bone plate to calcified cartilage	2
Tidemark penetrated by blood vessels	3

Results

The contralateral femoral surfaces experienced minor surface disruptions, normal Safranin-O staining, normal cell density and cloning, and an uninterrupted tidemark (Figure 82). The sham surfaces exhibited moderate surface irregularities and very mild cell cloning. The 12 and 24 week meniscectomy surfaces had severe surface irregularities, a slight decrease in cell density, moderate cell cloning, and normal Safranin-O staining.

The cartilage damage was least for the joints corresponding to anatomical scaffolds, followed by partially displaced, and completely displaced experienced the most damage. Articular surfaces from anatomical scaffolds typically exhibited mild surface disruption, normal cell density, Safranin-O staining, mild cell cloning, and an uninterrupted tidemark (Figure 82). Joints with partially displaced scaffolds were slightly hypocellular and had mild cell cloning at both time

points but advanced from moderate to severe surface irregularities with some fissures to the transitional zone from 12 to 24 weeks. The cartilage from joints with completely displaced scaffolds experienced severe surface irregularities at 12 weeks and fissures down to the transitional zone at 24 weeks, in addition to a hypocellularity and mild cell cloning.
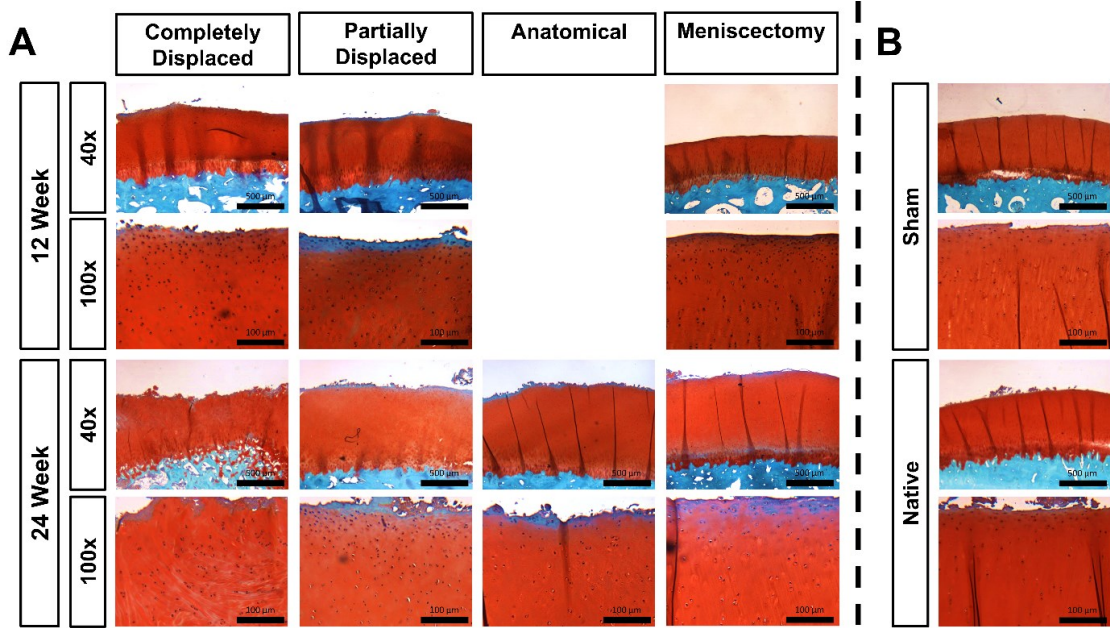
Figure 82 Representative cartilage histology. Femoral condyle cartilage stained with Safranin-O/Fast Green from knees with (A) scaffolds and (B) controls. Image magnification: 40x and 100x. Scale bars: 500 μm and 100 μm.

OARSI cartilage damage scores did not show large differences between groups. The score did not significantly increase (p=0.056) from 12 to 24 weeks and there was not a significant difference in average damage between the anatomical scaffolds, meniscectomy, sham, and contralateral conditions with averages ranging from 6.2 to 7.7. The partially and completely displaced scaffolds resulted in significantly increased cartilage damage relative to the contralateral controls with averages of 8.3 and 8.8, respectively.
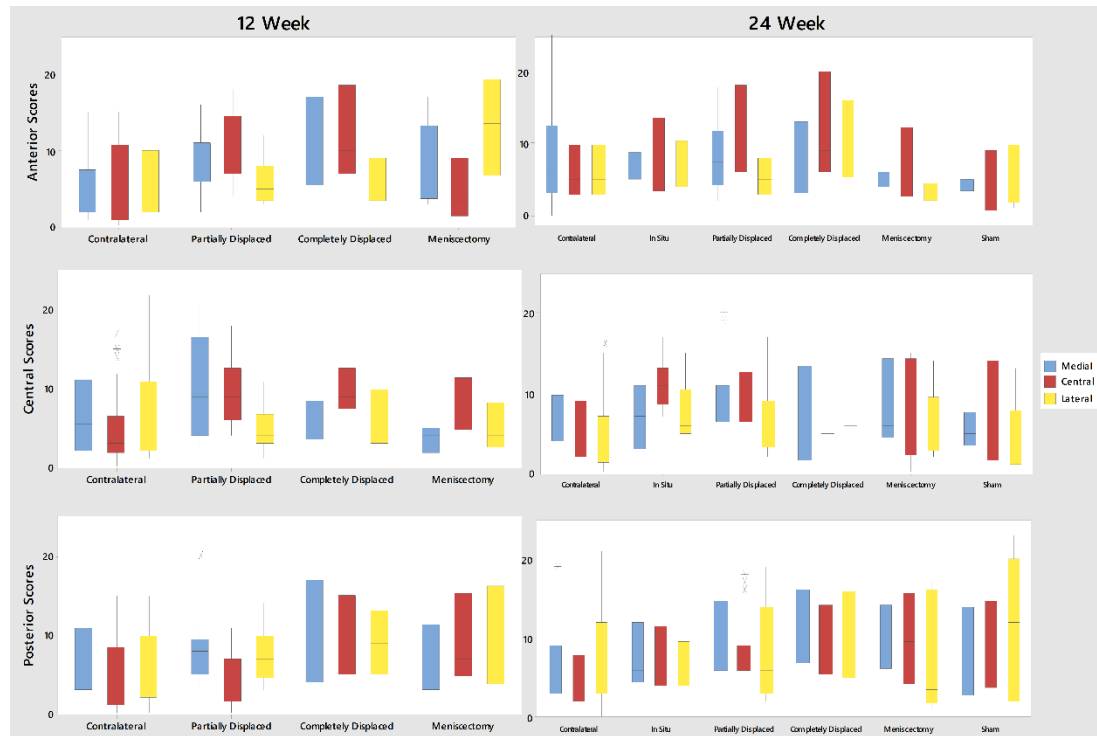
Figure 83 Box and whisper plot of OARSI histological cartilage damage scoring for native, in situ, partially displaced, completely displaced, meniscectomy, and sham conditions. Maximum score: 25.

6.8 Aim 3 Discussion

The purpose of this study was to assess the functionality of a novel 3D printed, mechanically functional, polymeric scaffold in a short term, clinically relevant *in vivo* model. We unexpectedly observed three different outcomes for the scaffold; however, this provided a unique insight into the performance of this device. We observed differences in the three outcomes in regards to tissue ingrowth, type, organization, and density, and biochemical composition. The anatomical scaffold induced significant tissue ingrowth, remodeled into neo-meniscal tissue, integrated robustly to the host meniscal tissue, and continually improved in these characteristics with time. The scaffold also did not adversely affect the articular cartilage of the joint.

Significant tissue ingrowth was found within all scaffolds. The original porous collagen matrix was completely remodeled into a dense extracellular matrix with cells exhibiting both a fibroblastic and fibrochondrocytic morphology. Interestingly, the type of tissue ingrowth was

directly dependent on the location of the scaffold. Those scaffolds that had remained in place and were exposed to the appropriate biochemical and mechanical stimuli, revealed a fibrocartilage-like tissue, partially displaced scaffolds exhibited a range of fibrous to fibrocartilage-like tissue, and completely displaced scaffolds had developed loose, fibrous connective tissue.

The quality of tissue observed in the scaffolds were typically denser and more organized than tissue generated from previous scaffolds lacking biological enhancement at equivalent time points [50, 69, 78, 128]. CMI exhibited bands of unorganized connective tissue with fibroblasts, capillaries, and fine collagen fibers in mixed breed dogs at 12 weeks. At 24 weeks, the collagen fibers had grown in diameter and became more organized but islands of the crosslinked collagen scaffold material remained[128]. At 12 weeks, Actifit remained relatively porous and lacked any clear organization[78]. Gruchenberg et al observed pores up to 10 µm in diameter that were empty or filled with amorphous material in a silk fibroin scaffold at 12 and 24 weeks[50]. A 3D printed PCL scaffold, when growth factors were not added, only developed an amorphous fibrous tissue at 12 weeks resembling the tissue quality of the completely displaced scaffolds in this study[69]. The relatively dense and organized tissue observed in this study without the addition of any biological factors is most like the result of the similarity of the mechanics of the scaffold relative to the native meniscal tissue.

The ability of a scaffold to integrate to the remaining meniscal tissue is essential for the success of a partial meniscus scaffold and may be enhanced with ECM-derived materials. The integration observed in this study was quite robust as early as 12 weeks with little distinguishable interface between the neo- and host tissue. In CMI, integration does not occur up to 6 weeks but is robust by 52 weeks[51]. PCL hyaluronan scaffolds resulted in some fibrous ingrowth in 2 out of 3 cases in a partial, segmental defect but the interface was noticeably less dense than the rest of the generated tissue[24]. Actifit, a synthetic scaffold, integrates less reliably with only 4 out of 7

scaffolds well-integrated as late as 52 weeks in one study[78] and silk fibroin scaffolds left a large gap between the scaffold and host tissue with no signs of fibrous adhesion as late as 24 weeks[50].

The scaffold demonstrated a weak foreign body response but a stronger lymphocytic response, similar to other collagenous scaffolds[27, 128]. Relatively few multinucleated giant cells were observed relative to other synthetic meniscal scaffolds developed in the past[67, 132, 133], suggesting the scaffold material was well tolerated. The clusters of cartilaginous differentiation have been observed in PCL-hyaluronan scaffolds but only when seeded with cells[67], indicating the correct mechanical environment of our scaffold enhances the cellular response, as supported by *in vitro*[9] and *in vivo*[32] studies. Vascularization was observed throughout the scaffold similar to our laboratory's total meniscus device at similar time points[87].

The biochemical composition of the native meniscus dictates its biomechanical function. The collagen provides the tensile properties and the GAGs increase the ability of the tissue to absorb and retain water, improving the viscoelastic compressive properties[92]. The outcome of each scaffold had a direct effect on the biochemical development of the scaffold with the anatomical scaffolds achieving the best biochemical composition. The biochemical data in this study further confirmed that the anatomical scaffolds are maturing towards a fibrocartilaginous tissue up to 24 weeks. The contralateral controls agreed with the previous values from the literature of 68% water content[18] and 60-70% collagen[85]; however, the GAG content in this study (3%) was greater than previous values 1-2% GAGs[41, 105], perhaps because samples were taken exclusively from the inner margin and those values were an average of the whole tissue.

We characterized the gross and histological changes of the articular surfaces to show the scaffold does not adversely affect the surround cartilage. Although a small increase in the OARSI scale was found in the partially and completely displaced animals, there was no significant change between the contralateral, sham, meniscectomy, and in place scaffolds and no change from 12 to

24 weeks. This is consistent with findings in the literature that used similar defect models[50, 78].

Gruchenberg et al found, when excluding outliers, there was little change in the macroscopic area

of cartilage damage and the mechanics of the cartilage did not change in the region underneath

a silk fibroin scaffold[50]. However, they did observe some degenerative changes via histology

including some fibrillation, a reduction in Safranin-O staining, and cell cloning in the experimental

joints. Maher et al also did not observe adverse changes in cartilage histological scoring between

12 and 24 weeks[78].

The geometry of our defect model proved to be a shortcoming of this study with the

majority of the scaffolds displaced. In an effort for a highly reproducible defect model, we chose

a model with right angles and predefined dimensions; however, this may have resulted in the

native meniscal tissue deforming due to stress concentrations. We recommend changing the size

and shape of the defect in future studies to avoid these problems.

The animal model simulates a worst-case scenario in rehabilitation protocol. The animals

were standing four hours post-operatively, potentially leading to early displacement of the

scaffold. In humans, a strict toe-touch weight bearing protocol would be in place for four weeks

before returning to weight bearing. This allows for early tissue infiltration and integration to occur

before subjecting the scaffold to significant loads. Considering our small number in each group

and the observation that all anatomical scaffolds were harvested at the longer time point suggests

there is a critical early time frame which the scaffold must remain in place for long term success.

We hypothesize the fixation failure begins with the failure of the anterior circumferential

suture from the shear force as a result flexion/extension, causing a tendency to separate the

scaffold from the anterior portion of the meniscus. This allows the scaffold to move more freely

in the joint resulting in either the extrusion of the scaffold underneath the host tissue (as in the

case of the partially displaced scaffolds) or rotation of the entire scaffold over the meniscal rim

and into the knee capsule (completely displaced scaffolds). The fixation can be improved by performing a subtotal implantation as this would allow for exclusively radial sutures that are not susceptible to the same phenomenon.

This was a first-in-animal, feasibility study which suffered from a few limitations. First, due to ethical and financial limitations, this study was performed with a relatively small sample size. Additionally, the time points were too short to assess the chondroprotective abilities of our scaffold. Finally, no biomechanical testing was performed as the amount of tissue available per animal was extremely limited.

This study demonstrated a biomechanically functional, collagen-hyaluronan infused 3D-printed polymeric scaffold could induce significant fibrochondrocytic tissue ingrowth, integrate robustly, and continue to mature as late as 24 weeks without adversely affecting the articular cartilage of the joint. However, we failed to reproducibly fix the scaffold to the remaining native meniscal rim. Future work will explore a modified fixation method for longer time points in order to assess the continued remodeling of the tissue and the scaffold's ability to protect the underlying articular cartilage.

7   Specific Aim 4

The purpose of this aim is to enhance the tensile mechanics of the scaffold by introducing molecular orientation in the scaffold fibers by optimizing the 3D printing parameters. Highly oriented polymer fibers are typically produced by drawing a melt-spun fiber. Examples include polyethylene [5, 6], poly(ethylene terephthalate)[7], nylon 6 [8], polypropylene[9], polyoxymethylene[10], and poly(vinylidene fluoride)[11]. In this method, the mechanical properties are enhanced by increasing the draw ratio, defined as the ratio of the final length to the initial length of the fiber [4].   There is a relatively small temperature range at which this drawing can be accomplished efficiently. As the temperature of the fibers approaches the melting temperature of the polymer, the force required for mechanical deformation decreases, but the polymer molecules relax freely back to the randomly oriented state.

In this study, we demonstrate that a high degree of orientation can be obtained using 3D printers by translating the print head at sufficiently high speeds while the polymer is kept in a semi-solid state as it is being cooled from the fluid state at the tip of the nozzle. We achieved molecular orientation comparable to drawn fibers by 3D printing with a critical combination of print speed, nozzle diameter, the extrusion pressure and polymer melt and platform temperature that allowed for the drawing process to occur before the polymer has had sufficient time to cool into a solid.   The method was illustrated with poly(DTD DD). Poly(L, lactic acid), PLLA, was processed under similar conditions to determine if these results could be generalized to other materials.

A series of experiments were performed with poly(DTD DD) which systematically varied the 3D printing processing parameters to determine the extent of polymer orientation. These parameters include temperature, pressure, nozzle diameter, platform temperature, and print

platform temperature. After a successful set of parameters were discovered, PLLA was tested under similar conditions to determine if these results could be generalized to other materials. Finally, a meniscus scaffold was 3D printed under conditions that produce molecular orientation to determine whether the tensile mechanics of the scaffold are enhanced with molecular orientation.

7.1   Methods
Materials

High molecular weight poly(DTD DD) powder was synthesized at the New Jersey Center for Biomaterials with an average molecular weight of 108 kDa. Drawn poly(DTD DD) 100 μm fibers were produced as a positive control for orientation, as previously described[136]. Medical grade PLLA, Purasorb PL 18, was purchased from Corbion Biomedical. 1-ethyl-3-(3-dimethaylaminopropyl)carbodiimide hydrochloride (EDC) and N-hydroxysuccinimide (NHS) were purchased from Sigma-Aldrich. Lyophilized bovine Achilles tendon collagen was purchased from Worthington Biochemical Corporation (Lakewood, NJ).

Rheology

Rheology measurements were performed in a capillary rheometer (Malvern RH 2000) with a 0.5 mm diameter die. Poly(DTD DD) and PLLA were desiccated overnight. Approximately 15 g of poly(DTD DD) or PLLA were packed into the chamber and allowed to reach the test temperature. The polymers were tested at shear rates of 10/s to 5000/s in five logarithmic steps, tested in duplicate. Poly(DTD DD) was tested at 140°C, 150°C, and 160°C. PLLA was tested at 160°C, 170°C, 180°C, 190°C, and 200°C.

Fiber Drawing

Fibers that were used for comparison were produced by conventional spinning-drawing methods. The fibers were extruded on a three-quarter inch single screw extruder (Alex James &

Associates, Inc., Greenville, SC). Polymer of molecular weight 108 kDa was extruded through a 1mm diameter at 140 °C to a diameter of 170 μm, and then drawn at 55°C 2.5 X to a final diameter of 100 μm.

3D Printing

3D printing was performed using a pneumatic extrusion-based 3D Bioplotter (EnvisionTEC, Dearborn, MI). Unless otherwise specified, strips of polymer were directly printed on Kapton tape with a platform at room temperature. The extrusion pressure, polymer melt temperature, nozzle inner diameter, and printing speed were controlled.

A part of this study was performed using "mid-air printing" in which the print head was positioned at a large vertical distance from the printing platform (Figure 84). Although printing at these speeds is not practical, this allowed for printing of a continuous stream of polymer at very fast print head speeds. 3D printing directly on the platform at similar speeds would lead to fiber breakages.
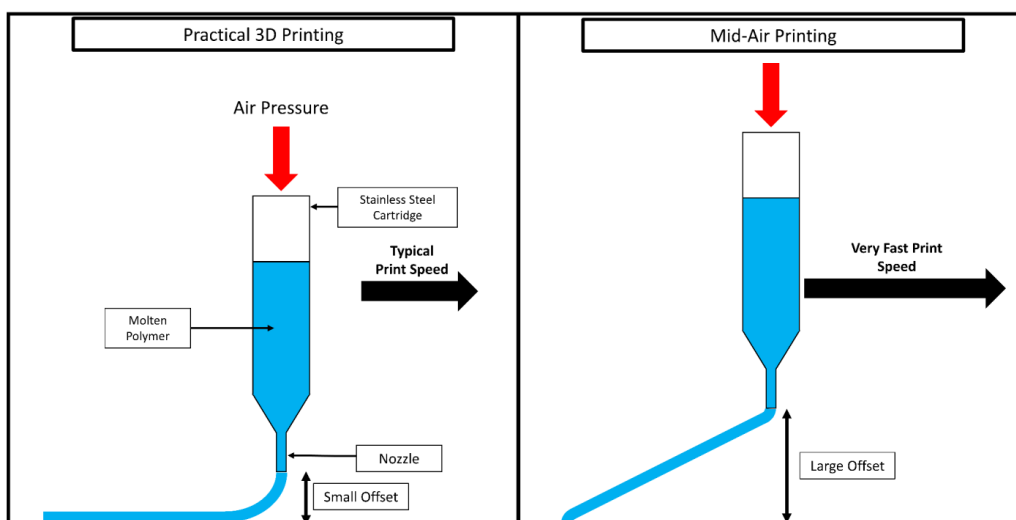

Figure 84 A diagram of the practical 3D printing process and the mid-air printing process.

Orientation Characterization

The degree of polymer chain orientation (molecular orientation) of the fibers and 3D printed strips was measured using x-ray diffraction (XRD). 2D XRD patterns were recorded with

Mo Kα radiation (λ = 0.709 Å) using a Smart APEX detector mounted on a Bruker AXS

diffractometer. The 2D patterns were used to obtain the azimuthal intensity distribution of the

main equatorial reflection at a scattering angle (2θ) ~ 9.3 °, corresponding to ~ 4.4 Å interchain

distance. The scan was fit to a Gaussian model in MATLAB (Mathworks) to obtain the full width

at half maximum (FWHM) calculated using the following equation:

$$Y = Offset + e^{-\ln(2)*\frac{x-x_0}{(\frac{FWHM}{2})^2}}$$

where Y is the observed intensity, x is the azimuthal angle, and offset is an arbitrary offset[93].

The degree of orientation was further evaluated by measuring the thermal shrinkage,

which was calculated as the ratio of the length of the fiber before and after immersion in water

at 65°C water for 0.5-1 minute. Immersion was performed at 65°C so the polymer was exposed

to temperatures above the first thermal transition event of 55°C but below its final melting

point of 100°C[15].

Partial Meniscus Scaffold Mechanical Testing

Poly(DTD DD) scaffolds were printed at 160°C and 9 bar with a 500 µm inner diameter

nozzle. The scaffolds were printed at two printing speeds: 2 and 4.5 mm/s. 20 g/L lyophilized

bovine Achilles tendon collagen was ground and swollen in dilute hydrochloric acid (pH 2.35).

The scaffolds were infused with collagen, frozen, and lyophilized. Scaffolds were cross-linked

with 10 mM EDC and 5 mM NHS for 5 hours. Scaffolds were rinsed three times for 10 minutes in

DI water, one time for 3 hours in 100 mM sodium phosphate, and rinsed for 24 hours in DI

water.

Scaffolds (n=4/group) were hydrated in PBS at room temperature for at least one hour.

Each scaffold was loaded into cryogenic freeze clamps (TA Instruments, New Castle, DE) with an

8 mm gage length encompassing the central region. The samples were loaded in tension at a

rate of 10 mm/min to failure (model 5592; Instron, Canton, MA). Circumferential tensile

stiffness and ultimate tensile load were calculated for each sample.

7.2   Results

7.2.1   Rheological Characterization

The viscosity of poly(DTD DD) decreased markedly as the temperature was increased

from 140°C to 160°C (Figure 85). At low shear rates, the viscosity decreased by approximately

30-40% and 70-80% from 140°C to 150°C and 160°C, respectively. Considering the 3D printing

process occurs at very low shear rates, poly(DTD DD) must be printed at the highest possible

temperature to allow for significant print speeds regardless of the thermal instability observed

(Poly(DTD DD) Thermal Degradation Rates).

The behavior of PLLA could not be tested at 160°C, 170°C, and 180°C because the

pressures required to cause the flow were too high. When the temperature of PLLA was

increased from 190°C to 200°C, the shear viscosity decreased by about a third at low shear rates

(Figure 85). PLLA at 200°C most closely matched the shear viscosity of poly(DTD DD) at low

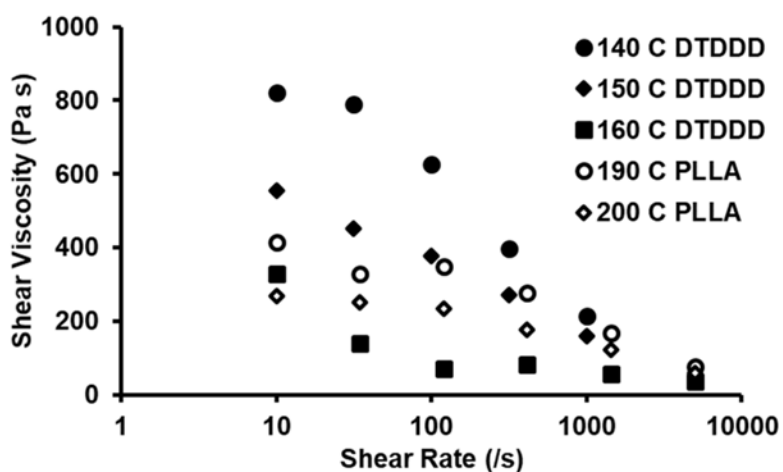shear rates and, therefore, should be 3D printable at this temperature.

Figure 85 Shear viscosity as a function of shear rate for poly(DTD DD) and PLLA at various temperatures.

7.2.2 Effect of Platform Temperature

Poly(DTD DD) was 3D printed at 150°C and 6.5 bar, with a 400 μm inner diameter nozzle directly onto the printing platform. The speeds tested ranged from 0.5 to 1 mm/s and the platform temperature was tested at room temperature and 8°C. This was performed to understand how the printing process can be modulated in order to achieve orientation.

Although negligible orientation (>94°) was achieved with the platform at 8°C, the orientation improved from 114° to 69° with increasing printing speed at 25°C (Figure 1). These results were further verified by low values for thermal shrinkage in all conditions (Figure 86). There were no significant differences between any of the conditions tested (one-way ANOVA, p=0.18). These results suggest that greater orientation can be achieved with a room temperature platform, most likely due to a slower cooling rate.
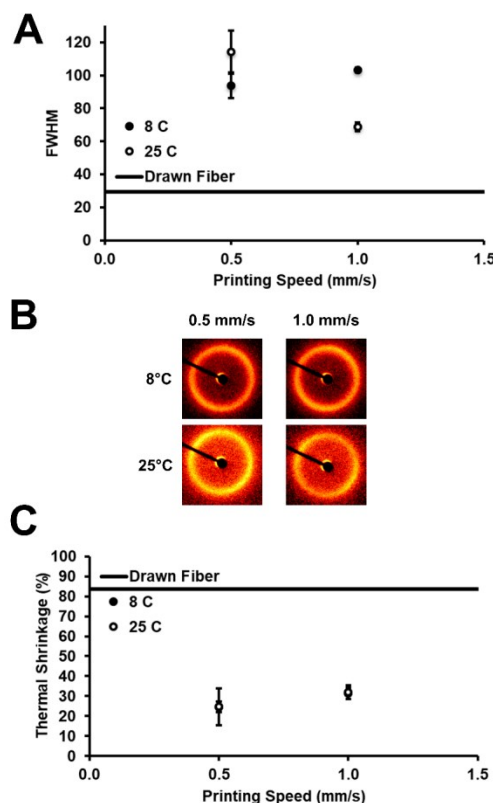
Figure 86 (A) Full width at half maximum (n=1) and (B) corresponding WAXS images. (C) Thermal shrinkage (n=4) of poly(DTD DD) printed on the printing platform at 8°C and 25°C.

7.2.3 Effect of Extrusion Temperature on Strips Produced in Mid-Air

Poly(DTD DD) was 3D printed at 9 bar with a 400 μm inner diameter nozzle in midair to allow for testing very high print speeds. It was expected that lower printing temperatures should result in a greater degree of orientation. Poly(DTD DD) was printed at 140°C and 160°C to the maximum achievable speed resulting in a continuous fiber which was 2 and 10 mm/s, respectively. The higher temperature was tested because the polymer had improved adherence to the platform or previously printed polymer layers.

The degree of orientation increased significantly as the speed was increased at both temperatures (Figure 87). Higher speeds were necessary to achieve the same orientation at a higher temperature as at the lower temperature. The orientation achieved was better than that routinely achieved by fiber drawing (Figure 87). It should be emphasized that this was achieved

by printing in a straight line midair and therefore is not practically useful. It was empirically

determined that at 140°C the maximum speed is 0.5 mm/s and at 160°C is 1.7 mm/s.

Thermal shrinkage results confirmed a high degree of orientation of the strips; however,

the shrinkage values were 7% and 4% less than those measured in drawn fibers for 140°C and

160°C, respectively (Figure 87). The shrinkage did demonstrate a significant increasing linear

trend at both 140°C and 160°C (regression analysis, $p<0.001$).

Figure 87 (A) Full width at half maximum (n=1) and (B) corresponding WAXS images. (C) Thermal shrinkage (n=4) of poly(DTD DD) printed at 140°C and 160°C with a 400 μm nozzle directly on the printing platform.

7.2.4   Orientation at Practical Printing Speeds at 150°C

Poly(DTD DD) was 3D printed at 150°C and 9 bar with a 400 μm inner diameter nozzle

directly on the printing platform to test polymer orientation at practical printing speeds. The

speeds tested ranged from 1 mm/s to 2.5 mm/s. No significant orientation was observed with

FWHM corresponding to values above 75 (Figure 88). However, thermal shrinkage did

demonstrate a significant increasing linear trend (regression analysis, $p < 0.001$) of polymer

orientation, albeit only moderate values were observed. These results suggest that if the

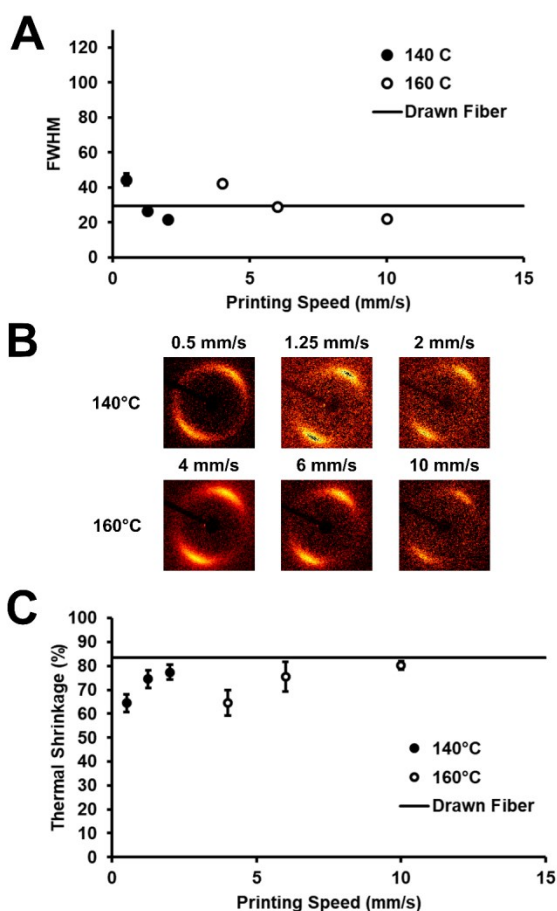printing speed could be increased further, significant polymer orientation could be achieved.
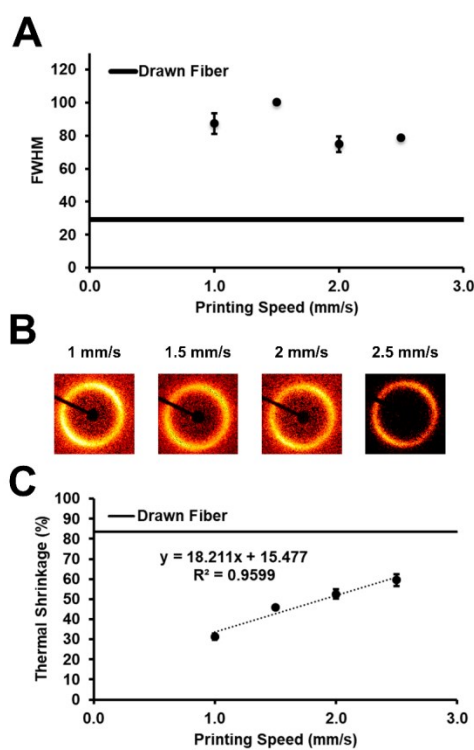

Figure 88 (A) Full width at half maximum (n=1) and (B) corresponding WAXS images. (C) Thermal shrinkage (n=3) of poly(DTD DD) printed at 150°C and a 400 μm nozzle directly on the printing platform.

7.2.5 Effect of Nozzle Diameter

At higher temperatures, a larger diameter nozzle (600 um), allowing for a higher flow

rate, was tested to allow for higher practical printing speeds. Poly(DTD DD) was 3D printed at

160°C and 9 bar with a 600 μm inner diameter nozzle directly on the printing platform to test

faster printing speeds. At the speeds tested, a moderate increase in orientation was observed

from 2 mm/s to 4 mm/s but no significant increase was observed as print head speed was

increased further to 10 mm/s.

Therefore, a second study was performed in which the print head speed was increased

up to 50 mm/s. From 10 to 50 mm/s, a linear correlation was observed between printing speed

and FWHM (Figure 89). These results were confirmed by thermal shrinkage values which

demonstrated a highly significant linear response (regression analysis, p<0.001).

It should be noted that the speeds which approached the orientation of drawn fiber

could be only used to print rectilinear geometries. If the user is attempting more complicated

curvilinear geometries, we observed that high quality printing could only be achieved between

10 and 20 mm/s.
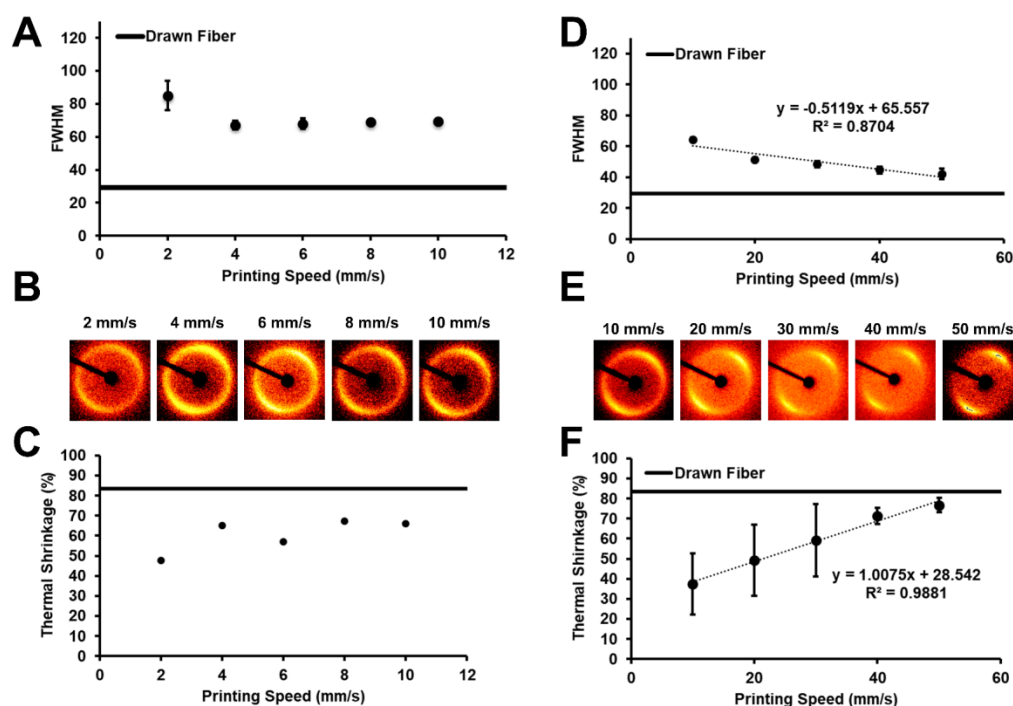

Figure 89 (A and D) Full width at half maximum (n=1) and (B and E) corresponding WAXS images. (C) Thermal shrinkage (n=1) and (F) thermal shrinkage (n=4) of poly(DTD DD) printed at 160°C and a 600 μm nozzle on the printing platform.

To determine if there is design space where sufficiently high print speeds for orientation could be achieved at practical speeds, which was not observed for the 400 μm and 600 μm diameters nozzles, an intermediate diameter nozzle (500 μm inner diameter) was tested. Strips were printed at 160°C and 9 bar directly on the printing platform from 2 to 12 mm/s. A linear relationship was observed between orientation and printing speed, as measured by X-Ray diffraction and thermal shrinkage (Figure 90). The orientation approached but did not match the orientation achieved in drawn poly(DTD DD) fiber. The minimum FWHM achieved was 39° and the greatest thermal shrinkage reached was 78%. The speeds tested all represent practical speeds for rectilinear geometries, with more complicated curvilinear geometries printable from 4-8 mm/s. Therefore, a design space of parameters was found which included practical printing parameters with significant polymer orientation.
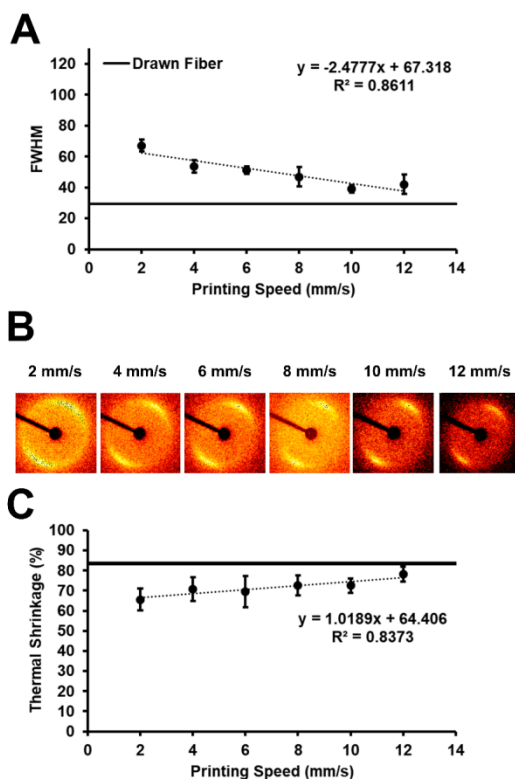

Figure 90 (A) Full width at half maximum (n=1) and (B) corresponding WAXS images. (C) Thermal shrinkage (n=4) of poly(DTD DD) printed at 160°C and a 500 μm nozzle on the printing platform.

7.2.6   Translation to Other Polymers: PLLA

We desired to determine if the orientation achieved in 3D printed poly(DTD DD) could

be implemented more broadly. Therefore, PLLA was investigated as well. Rheological

measurements were taken to determine the viscosities at which polymer orientation was

successfully achieved for poly(DTD DD). Then the rheological properties of PLLLA were measured

to determine the temperature at which the viscosity profile matched that of poly(DTD DD). We

hypothesized that matching the shear viscosity at low shear rates were crucial due to the low

shear rates polymers are exposed to during 3D printing.   Once the appropriate temperature

was determined for PLLA, PLLLA was 3D printed at the same processing parameters at which

poly(DTD DD) was successfully oriented.

PLLA was 3D printed at 200°C and 9 bar with a 500 μm inner diameter nozzle directly on

the printing platform from 2 to 12 mm/s. Visual analysis of the WAXS images revealed no

orientation from 2 to 12 mm/s (Figure 91) and, therefore, numerical quantification of FWHM
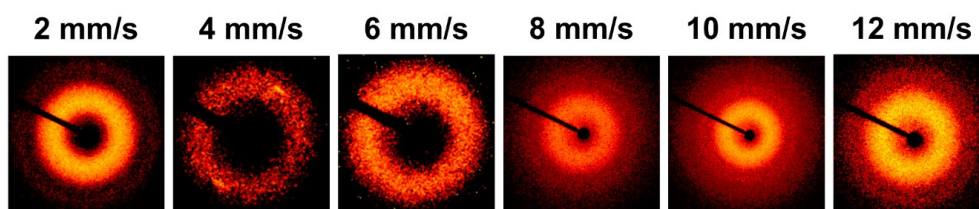
was not performed.

Figure 91 WAXS images of PLLA printed at 200°C, 9 bar, and a 500 μm nozzle on the printing platform.

7.2.7   Printing and Mechanical Characterization of Enhanced Meniscus Scaffold

Meniscus scaffolds were printed with a minor change from previous designs to allow for

continuous extrusion in the radial struts rather than in many discrete segments (Figure 92). This

allowed for improved print quality at higher speeds. Scaffolds were reproducibly printed at

speeds of 2 and 4.5 mm/s with high quality (Figure 93A). The FWHM was reduced by 52% from

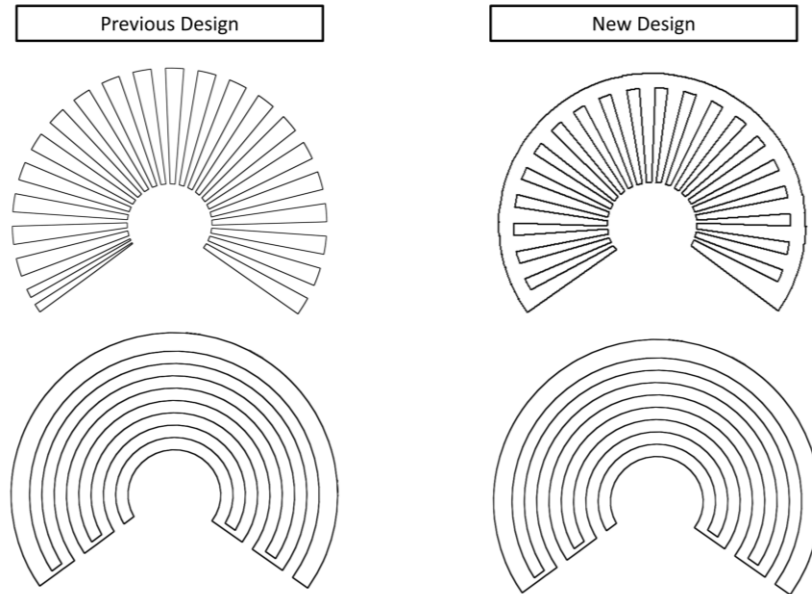72° to 34° by increasing the speed from 2 to 4.5 mm/s.

Figure 92 Previous and new modified design for high speed 3D printing.

The 4.5 mm/s meniscus scaffolds (142.29 ± 48.78 N/mm) exhibited a significantly

increased tensile modulus (p=0.03) of 2.2-fold relative to the 2 mm/s scaffolds (142.29 ± 48.78

N/mm) (Figure 93B). On the other hand, the ultimate load did not significantly increase due to

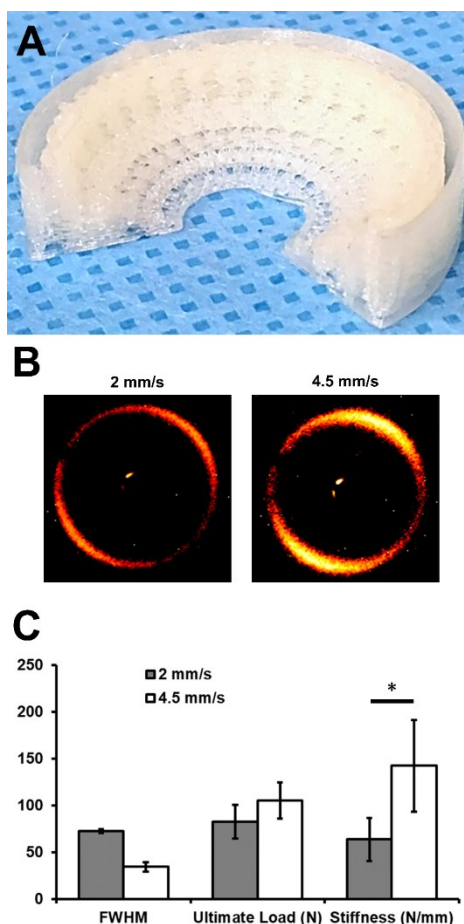printing speed (p=0.14) but the average did increase 27% from 82 N to 105 N (Figure 93C).

Figure 93 (A) Meniscus scaffold, (B) corresponding WAXS images, (C) Full width at half maximum (n=1) and tensile mechanics of poly(DTD DD) scaffolds printed at 160°C with a 500 μm nozzle at 2 and 4.5 mm/s. *denotes significant differences.

7.3 Aim 4 Discussion

In thermal extrusion-based printing, polymers are extruded from the molten state and solidify once cooled. The molecular orientation, the orientation of the molecules and polymer chains within these printed filaments, is an important parameter that determines the mechanical properties of the printed object. This study represents, as best as we can tell, the first time polymer orientation has been achieved and measured in objects manufactured via 3D printing. Furthermore, the practicality of this phenomenon was demonstrated by improving the mechanical properties of a partial meniscus scaffold by simply altering the processing parameters, and consequentially, the polymer orientation within the scaffold. This has the

potential to improve the mechanics of any 3D printed polymeric load bearing scaffold in the biomedical field.

However, we were not able to demonstrate that this can be realized in any biopolymer. PLLA proved to be less susceptible to orientation. This may be a result of the sharper thermal transition of PLLA relative to poly(DTD DD)[136]. For a polymer to be successfully oriented, there needs to be an appropriate window of time for the polymer to be adequately sheared [30]. This window may be too narrow for PLLA to orient under the processing limitations used in this setup.

On the other hand, poly(DTD DD) proved to be relatively easily oriented via 3D printing; however, the challenge was determining processing conditions that attained orientation while maintaining print quality. In fact, orientation greater than that achieved via fiber drawing was obtained but these conditions proved to sacrifice print quality. But rectilinear scaffolds could be printed with orientations which nearly matched those of drawn fibers and more complicated geometries, such as the meniscus scaffold, could be printed with FWHMs as low as 55°.

It should be noted that the orientations in this study do not represent the maximum achievable orientations via 3D printing. The results in this study were fundamentally limited by the flow rate of poly(DTD DD). The flow rate could be increased using an external lubricant such as zinc stearate[127], which would allow for faster print speeds and, therefore, greater orientation under similar conditions. In addition, by replacing the pneumatic extruder with a screw based extruder of the 3D printer, the polymer flow rate could be significantly increased without any additives [108].

Molecular orientation can be achieved in 3D printed filaments. This was demonstrated with a poly(ester amide), which was successfully oriented to a greater extent than

conventionally drawn fibers using a pneumatic extrusion based 3D printer. However, the

printing parameters need to be optimized for each polymer based on the rheological properties

of the polymer and may be more difficult for materials with a sharp thermal transition such as

PLLA. The practical utility of this technique was illustrated by fabricating mechanically superior

biomedical scaffolds for meniscus regeneration. The knowledge gained from this study has the

potential to combine the advantages of 3D printing with the superior mechanics of conventional

manufacturing techniques.

8 Summary and Future Directions

This dissertation was aimed to translate the successful technology from the total meniscus scaffold, developed in the Orthopaedic Research lab, for a partial meniscus indication. The two main differences between the applications are a scaffold must be cut to each patients defect in the operating room and the scaffold must be fixed to the remaining host tissue, not the tibia. However, as we furthered our understanding, it became clear that the mechanical requirements were different as well.

In the total meniscus scaffold, the most essential requirements are the tensile mechanics. This allows the scaffold to convert axial compressive loads into circumferential hoop stresses and transfer it to the tibia via the bone tunnel fixation. On the other hand, the partial meniscus scaffold does not need to tolerate large tensile loads as the remaining host tissue still possesses the majority of its tensile mechanics when the outer rim is intact. Therefore, we needed to optimize the compressive properties of the scaffold in order to allow for the scaffold to load share with the host tissue.

As a result, we reconsidered the fiber based manufacturing of the total meniscus scaffold and developed a collagen-hyaluronan infused 3D-printed polymeric scaffold with the objective to satisfy the following requirements: 1) mimic the mechanical properties of the native meniscus, 2) be successfully sutured to the remaining native meniscal rim, 3) increase the contact area and reduce peak stresses relative to partial meniscectomy, 4) encourage cell infiltration, extracellular matrix production, and organized tissue deposition, 5) integrate robustly to the surrounding native meniscal tissue, and 6) protect the articular surfaces to prevent or delay degenerative changes in the underlying cartilage.

We assessed these objectives via 3 specific aims. In aim 1, we performed a comparative study on insoluble collagen derived from three species: bovine, ovine, and porcine. This was

essentially a sourcing study to understand the implications of changing from bovine sources to other species. We learned that there were not large functional differences between species that would alter the performance of a meniscal scaffold.

In aim 2, we characterized the optimal 3D printed design *in vitro*. We performed a series of benchtop mechanical tests including axial confined compression, circumferential tension, a suture retention test, and an ovine cadaveric knee contact stress study. Here, we demonstrated that the scaffold was biomechanically functional and potentially had chondroprotective abilities. This motivated the next aim in which the scaffold was tested *in vivo*.

In aim 3, we tested the optimized meniscal scaffold in an 80% posterior meniscectomy model for 12 and 24 weeks. In the anatomical and partially displaced scaffolds, we observed significant tissue infiltration, ingrowth, and integration, a strong collagen type II signal, a tissue composition approaching that of the native meniscus, and no adverse effect on the synovium and articular surfaces but we failed to properly secure the scaffold to the host tissue.

In aim 4, we sought to improve the circumferential tensile mechanics of the meniscus scaffold by orienting the molecular structure of the polymer fibers of the implant. This was completed by finding a critical combination of the 3D printing parameters and resulted in a doubling of the tensile stiffness.

Future work will have to address the shortcomings of the research of this dissertation. Improvements can be made at many steps of the fabrication and implantation protocols in order to improve the clinical outcomes of this device. The most significant problem to address is the fixation technique utilized in the *in vivo* study.

The fabrication of this device has many ways that can be optimized to improve the meniscal scaffold. The scaffold design utilized in aims 2 and 3 consisted of a continuous

circumferential layer and discrete pairs of radial segments (Figure 21). In aim 4, the radial layer

had to be altered to allow for very fast printing speeds (Figure 92). This innovation should be

incorporated into the next generation design.

The polymer extrusion during 3D printing can be optimized in multiple ways to facilitate

and improve the printing process. The thermal degradation that occurs during the printing

process is a result of free radial generation. This degradation meant that there was a finite

printing time from beginning of heating which limited the complexity of the scaffold design.

Additionally, we suspect gas is generated from this process and intermittently would cause the

3D printing to fail due to the formation of an air channel throughout the molten polymer to the

extrusion needle, resulting in having to start the printing process over. This degradation can be

retarded by utilizing nitrogen as the pneumatic fluid instead of air and incorporating an

antioxidant into the polymer formulation.

The 3D printing process could be accelerated if the extrusion flow rate is increased. This

could be accomplished by the addition of external lubricants into the polymer formulation such

as zinc stearate[83]. Additionally, a plunger was not utilized in this dissertation to allow for a

greater maximum extrusion flow rate but due to a parabolic laminar flow profile this

necessitated the nearly twice as much polymer to be loaded into the extruder to complete a

scaffold. If the flow rate can be increased and the thermal degeneration retarded, the addition

of a plunger to the 3D printing system could greatly reduce polymer waste, therefore,

decreasing the cost of a scaffold significantly.

The tribology of the scaffold was not investigated in this dissertation due to a lack of

facilities necessary for such work. There were three scaffolds that remained anatomically

placed for 24 weeks *in vivo*. In two of those animals, the cartilage did not show a difference

relative to the sham but in one of the animals significant degeneration was observed. This may

suggest that the large fibers of the scaffold have resulted in a rough scaffold surface and the tribology needs to be improved in the next generation design. This could be accomplished by electrospinning a randomly organized layer of poly(DTD DD) nanofibers after the 3D printing process to produce a smoother surface.

The fixation method was the most significant shortcoming of this dissertation. The initial fixation must be improved in order to tolerate the large shear forces experienced by the meniscal scaffold. This can be addressed by using a defect model with rounded corners and performing a subtotal implantation to allow for exclusively radial sutures that are not susceptible to the same phenomenon.

An acellular scaffold was investigated in this dissertation without any biological augmentation. Future work could study the improvement caused by the addition of various biological additives such as platelet rich plasma or bone marrow aspirate. These treatments could be added at the point of use without the need of solving challenges surrounding biological treatments such as sourcing, storage, disease transmission, and shelf-life.

The work in this dissertation represents the first time a meniscal scaffold achieved the biomechanical properties of the native ovine meniscus. We achieved both the axial compressive properties and circumferential tensile stiffness of the native ovine meniscus and demonstrated that the scaffold could retain sutures to significant loads. Furthermore, by implanting this scaffold into an 80% partial resection model, we demonstrated the chondroprotective ability of this scaffold. When implanted, the scaffold induces significant fibrochondrocytic tissue ingrowth, integrates robustly, and continues to mature as late as 24 weeks without adversely affecting the articular cartilage of the joint. A scaffold possessing these characteristics has the potential to transform the standard of care following meniscal injury, thereby preventing osteoarthritis in millions of patients each year.

9 References

1. USDA Long-Term Agricultural Projection Tables In: Agriculture USDo, ed. February 2015 ed; 2015.
2. Abat F, Gelber PE, Erquicia JI, Tey M, Gonzalez-Lucena G, Monllau JC. Prospective comparative study between two different fixation techniques in meniscal allograft transplantation. *Knee Surgery Sports Traumatology Arthroscopy.* 2013;21(7):1516-1522.
3. Alhalki MM, Howell SM, Hull ML. How three methods for fixing a medial meniscal autograft affect tibial contact mechanics. *The American Journal of Sports Medicine.* 1999;27(3):320-328.
4. Altman GH, Horan RL, Martin I, et al. Cell differentiation by mechanical stress. *FASEB J.* 2002;16(2):270-272.
5. Angele P, Abke J, Kujat R, et al. Influence of different collagen species on physico-chemical properties of crosslinked collagen matrices. *Biomaterials.* 2004;25(14):2831-2841.
6. Armstrong CG, Mow VC. Variations in the intrinsic mechanical properties of human articular cartilage with age, degeneration, and water content. *J Bone Joint Surg Am.* 1982;64(1):88-94.
7. Arnoczky SP. Building a Meniscus: Biologic Considerations. *Clinical orthopaedics and related research.* 1999;367:S244-S253.
8. Arnoczky SP, Warren RF. Microvasculature of the human meniscus. *Am J Sports Med.* 1982;10(2):90-95.
9. Baker BM, Mauck RL. The effect of nanofiber alignment on the maturation of engineered meniscus constructs. *Biomaterials.* 2007;28(11):1967-1977.
10. Balint E, Gatt CJ, Jr., Dunn MG. Design and mechanical evaluation of a novel fiber-reinforced scaffold for meniscus replacement. *J Biomed Mater Res A.* 2012;100(1):195-202.
11. Balint EA. *Development of a fiber-reinforced meniscus scaffold*: RUTGERS THE STATE UNIVERSITY OF NEW JERSEY-NEW BRUNSWICK; 2009.
12. Barber FA, Schroeder FA, Oro FB, Beavis RC. FasT-Fix meniscal repair: mid-term results. *Arthroscopy.* 2008;24(12):1342-1348.
13. Beamer BS, Masoudi A, Walley KC, et al. Analysis of a new all-inside versus inside-out technique for repairing radial meniscal tears. *Arthroscopy.* 2015;31(2):293-298.
14. Bedi A, Kelly NH, Baad M, et al. Dynamic Contact Mechanics of the Medial Meniscus as a Function of Radial Tear, Repair, and Partial Meniscectomy. *Journal of Bone and Joint Surgery-American Volume.* 2010;92A(6):1398-1408.
15. Bedoui F, Murthy N, Kohn J. Structure and Thermal Transitions in a Biomedically Relevant Liquid Crystalline Poly (ester amide). *Macromolecules.* 2017;50(6):2257-2266.
16. Brittberg M, Winalski CS. Evaluation of cartilage injuries and repair. *J Bone Joint Surg Am.* 2003;85-A Suppl 2:58-69.

17.   Brophy RH, Cottrell J, Rodeo SA, Wright TM, Warren RF, Maher SA. Implantation of a synthetic meniscal scaffold improves joint contact mechanics in a partial meniscectomy cadaver model. *Journal of Biomedical Materials Research Part A.* 2010;92(3):1154-1161.

18.   Brzezinski A, Ghodbane SA, Patel JM, Perry BA, Gatt CJ, Dunn MG. The Ovine Model for Meniscus Tissue Engineering: Considerations of Anatomy, Function, Implantation, and Evaluation. *Tissue Eng Part C Methods.* 2017;23(12):829-841.

19.   Buckwalter JA, Einhorn TA, Simon SR. *Orthopaedic basic science: biology and biomechanics of the musculoskeletal system.* Vol 1: Amer Academy of Orthopaedic; 2000.

20.   Buma P, Ramrattan N, van Tienen TG, Veth RP. Tissue engineering of the meniscus. *Biomaterials.* 2004;25(9):1523-1532.

21.   Burks RT, Metcalf MH, Metcalf RW. Fifteen-year follow-up of arthroscopic partial meniscectomy. *Arthroscopy.* 1997;13(6):673-679.

22.   Chen MI, Branch TP, Hutton WC. Is it important to secure the horns during lateral meniscal transplantation? A cadaveric study. *Arthroscopy: The Journal of Arthroscopic & Related Surgery.* 1996;12(2):174-181.

23.   Chevrier A, Nelea M, Hurtig MB, Hoemann CD, Buschmann MD. Meniscus structure in human, sheep, and rabbit for animal models of meniscus repair. *J Orthop Res.* 2009;27(9):1197-1203.

24.   Chiari C, Koller U, Dorotka R, et al. A tissue engineering approach to meniscus regeneration in a sheep model. *Osteoarthritis Cartilage.* 2006;14(10):1056-1065.

25.   Chien S. Molecular basis of rheological modulation of endothelial functions: importance of stress direction. *Biorheology.* 2006;43(2):95-116.

26.   Chivers MD, Howitt SD. Anatomy and physical examination of the knee menisci: a narrative review of the orthopedic literature. *J Can Chiropr Assoc.* 2009;53(4):319-333.

27.   Cook JL, Tomlinson JL, Arnoczky SP, Fox DB, Reeves Cook C, Kreeger JM. Kinetic study of the replacement of porcine small intestinal submucosa grafts and the regeneration of meniscal-like tissue in large avascular meniscal defects in dogs. *Tissue Eng.* 2001;7(3):321-334.

28.   Cottrell JM, Scholten P, Wanich T, Warren RF, Wright TM, Maher SA. A new technique to measure the dynamic contact pressures on the Tibial Plateau. *J Biomech.* 2008;41(10):2324-2329.

29.   Cullen KA, Hall MJ, Golosinskiy A, Statistics NCfH. *Ambulatory surgery in the United States, 2006*: US Department of Health and Human Services, Centers for Disease Control and Prevention, National Center for Health Statistics; 2009.

30.   D'Haese M, Mykhaylyk OO, Van Puyvelde P. On the Onset of Oriented Structures in Flow-Induced Crystallization of Polymers: A Comparison of Experimental Techniques. *Macromolecules.* 2011;44(7):1783-1787.

31.   de Groot J. Actifit, Polyurethane Meniscus Implant: Basic Science. *Meniscus.* 2010:383-387.

32. De Groot J, Zijlstra F, Kuipers H, et al. Meniscal tissue regeneration in porous 50/50 copoly (L-lactide/ε-caprolactone) implants. *Biomaterials.* 1997;18(8):613-622.

33. De Groot J, Zijlstra F, Kuipers H, et al. Meniscal tissue regeneration in porous 5050 copoly (l-lactide/ε-caprolactone) implants. *Biomaterials.* 1997;18(8):613-622.

34. DeHaven K. Meniscectomy versus repair: clinical experience. *Knee Meniscus: Basic and Clinical Foundations.* 1992:131-140.

35. Elema H, De Groot J, Nijenhuis A, et al. Use of porous biodegradable polymer implants in meniscus reconstruction. 2) Biological evaluation of porous biodegradable polymer implants in menisci. *Colloid and polymer science.* 1990;268(12):1082-1088.

36. Englund M, Lohmander L. Risk factors for symptomatic knee osteoarthritis fifteen to twenty-two years after meniscectomy. *Arthritis & Rheumatism.* 2004;50(9):2811-2819.

37. Englund M, Roos EM, Roos HP, Lohmander LS. Patient-relevant outcomes fourteen years after meniscectomy: influence of type of meniscal tear and size of resection. *Rheumatology (Oxford).* 2001;40(6):631-639.

38. Fairbank T. Knee joint changes after meniscectomy. *Journal of Bone & Joint Surgery, British Volume.* 1948;30(4):664-670.

39. Fisher SR, Markel DC, Koman JD, Atkinson TS. Pull-out and shear failure strengths of arthroscopic meniscal repair systems. *Knee Surg Sports Traumatol Arthrosc.* 2002;10(5):294-299.

40. Fithian DC, Kelly MA, Mow VC. Material properties and structure-function relationships in the menisci. *Clin Orthop Relat Res.* 1990(252):19-31.

41. Fox AJ, Bedi A, Rodeo SA. The basic science of human knee menisci: structure, composition, and function. *Sports Health.* 2012;4(4):340-351.

42. Freyman TM. *Development of an in vitro model of contraction by fibroblasts*, Massachusetts Institute of Technology; 2001.

43. Friess W. Collagen--biomaterial for drug delivery. *Eur J Pharm Biopharm.* 1998;45(2):113-136.

44. Gatt CJ, Merriam AS, Dunn MG. Implantable device and method to replace the meniscus of the knee and other body structures: Google Patents; 2013.

45. Gelinsky M, Welzel PB, Simon P, Bernhardt A, Konig U. Porous three-dimensional scaffolds made of mineralised collagen: Preparation and properties of a biomimetic nanocomposite material for tissue engineering of bone. *Chemical Engineering Journal.* 2008;137(1):84-96.

46. Gibson I, Rosen DW, Stucker B. Additive Manufacturing Technologies: Rapid Prototyping to Direct Digital Manufacturing. *Additive Manufacturing Technologies: Rapid Prototyping to Direct Digital Manufacturing.* 2010:1-459.

47. Gibson LJ, Ashby MF. *Cellular solids: structure and properties*. Cambridge: Cambridge university press; 1997.

48. Grant JA, Wilde J, Miller BS, Bedi A. Comparison of inside-out and all-inside techniques for the repair of isolated meniscal tears: a systematic review. *Am J Sports Med.* 2012;40(2):459-468.

49. Grayson WL, Frohlich M, Yeager K, et al. Engineering anatomically shaped human bone grafts. *Proc Natl Acad Sci U S A.* 2010;107(8):3299-3304.

50. Gruchenberg K, Ignatius A, Friemert B, et al. In vivo performance of a novel silk fibroin scaffold for partial meniscal replacement in a sheep model. *Knee Surg Sports Traumatol Arthrosc.* 2015;23(8):2218-2229.

51. Hansen R, Bryk E, Vigorita V. Collagen scaffold meniscus implant integration in a canine model: a histological analysis. *J Orthop Res.* 2013;31(12):1914-1919.

52. Hardeman F, Corten K, Mylle M, et al. What is the best way to fix a polyurethane meniscal scaffold? A biomechanical evaluation of different fixation modes. *Knee Surgery, Sports Traumatology, Arthroscopy.* 2015;23(1):59-64.

53. Haugh MG, Jaasma MJ, O'Brien FJ. The effect of dehydrothermal treatment on the mechanical and structural properties of collagen-GAG scaffolds. *J Biomed Mater Res A.* 2009;89(2):363-369.

54. Hede A, Jensen DB, Blyme P, Sonne-Holm S. Epidemiology of meniscal lesions in the knee. 1,215 open operations in Copenhagen 1982-84. *Acta Orthop Scand.* 1990;61(5):435-437.

55. Houck DA, Kraeutler MJ, Belk JW, McCarty EC, Bravman JT. Similar clinical outcomes following collagen or polyurethane meniscal scaffold implantation: a systematic review. *Knee Surg Sports Traumatol Arthrosc.* 2018.

56. Jaureguito JW, Elliot JS, Lietner T, Dixon LB, Reider B. The effects of arthroscopic partial lateral meniscectomy in an otherwise normal knee: a retrospective review of functional, clinical, and radiographic results. *Arthroscopy.* 1995;11(1):29-36.

57. Jeong HJ, Lee SH, Ko CS. Meniscectomy. *Knee Surg Relat Res.* 2012;24(3):129-136.

58. Jorgensen U, Sonne-Holm S, Lauridsen F, Rosenklint A. Long-term follow-up of meniscectomy in athletes. A prospective longitudinal study. *J Bone Joint Surg Br.* 1987;69(1):80-83.

59. Kakkar P, Verma S, Manjubala I, Madhan B. Development of keratin-chitosan-gelatin composite scaffold for soft tissue engineering. *Mater Sci Eng C Mater Biol Appl.* 2014;45:343-347.

60. Kane RJ, Roeder RK. Effects of hydroxyapatite reinforcement on the architecture and mechanical properties of freeze-dried collagen scaffolds. *J Mech Behav Biomed Mater.* 2012;7:41-49.

61. Kang SW, Son SM, Lee JS, et al. Regeneration of whole meniscus using meniscal cells and polymer scaffolds in a rabbit total meniscectomy model. *Journal of Biomedical Materials Research Part A.* 2006;77a(4):659-671.

62. Kim Y, Nowzari H, Rich SK. Risk of Prion Disease Transmission through Bovine-Derived Bone Substitutes: A Systematic Review. *Clinical Implant Dentistry and Related Research.* 2013;15(5):645-653.

63. Klompmaker J, Jansen HW, Veth RP, de Groot JH, Nijenhuis AJ, Pennings AJ. Porous polymer implant for repair of meniscal lesions: a preliminary study in dogs. *Biomaterials.* 1991;12(9):810-816.

64. Klompmaker J, Veth R, Jansen H, et al. Meniscal repair by fibrocartilage in the dog: characterization of the repair tissue and the role of vascularity. *Biomaterials.* 1996;17(17):1685-1691.

65. Kobayashi M, Chang YS, Oka M. A two year in vivo study of polyvinyl alcohol-hydrogel (PVA-H) artificial meniscus. *Biomaterials.* 2005;26(16):3243-3248.

66. Kohn D, Siebert W. Meniscus suture techniques: a comparative biomechanical cadaver study. *Arthroscopy.* 1989;5(4):324-327.

67. Kon E, Chiari C, Marcacci M, et al. Tissue engineering for total meniscal substitution: animal study in sheep model. *Tissue Eng Part A.* 2008;14(6):1067-1080.

68. Kon E, Filardo G, Tschon M, et al. Tissue engineering for total meniscal substitution: animal study in sheep model--results at 12 months. *Tissue Eng Part A.* 2012;18(15-16):1573-1582.

69. Lee CH, Rodeo SA, Fortier LA, Lu C, Erisken C, Mao JJ. Protein-releasing polymeric scaffolds induce fibrochondrocytic differentiation of endogenous cells for knee meniscus regeneration in sheep. *Sci Transl Med.* 2014;6(266):266ra171.

70. Lee SJ, Aadalen KJ, Malaviya P, et al. Tibiofemoral contact mechanics after serial medial meniscectomies in the human cadaveric knee. *Am J Sports Med.* 2006;34(8):1334-1344.

71. Lee SR, Kim JG, Nam SW. The tips and pitfalls of meniscus allograft transplantation. *Knee Surg Relat Res.* 2012;24(3):137-145.

72. Li H, Liu BL, Gao LZ, Chen HL. Studies on bullfrog skin collagen. *Food Chemistry.* 2004;84(1):65-69.

73. Li S-T, Rodkey WG, Yuen D, Hansen P, Steadman JR. Type I collagen-based template for meniscus regeneration. *Tissue Engineering and Biodegradable Equivalents. Scientific and Clinical Applications.* 2002:237-266.

74. Li YJ, Batra NN, You L, et al. Oscillatory fluid flow affects human marrow stromal cell proliferation and differentiation. *J Orthop Res.* 2004;22(6):1283-1289.

75. Lin YK, Liu DC. Comparison of physical–chemical properties of type I collagen from different species. *Food Chemistry.* 2006;99(2):244-251.

76. Little CB, Smith MM, Cake MA, Read RA, Murphy MJ, Barry FP. The OARSI histopathology initiative - recommendations for histological assessments of osteoarthritis in sheep and goats. *Osteoarthritis Cartilage.* 2010;18 Suppl 3:S80-92.

77. Maffulli N, Longo UG, Campi S, Denaro V. Meniscal Tears (Meniscectomy, Meniscopexy, Meniscal Transplants/Scaffolds). *Evidence-Based Orthopedics.* 2012:803-811.

78. Maher SA, Rodeo SA, Doty SB, et al. Evaluation of a porous polyurethane scaffold in a partial meniscal defect ovine model. *Arthroscopy.* 2010;26(11):1510-1519.

79. Maher SA, Rodeo SA, Doty SB, et al. Evaluation of a Porous Polyurethane Scaffold in a Partial Meniscal Defect Ovine Model. *Arthroscopy-the Journal of Arthroscopic and Related Surgery.* 2010;26(11):1510-1519.

80. Maher SA, Rodeo SA, Potter HG, Bonassar LJ, Wright TM, Warren RF. A pre-clinical test platform for the functional evaluation of scaffolds for musculoskeletal defects: the meniscus. *HSS J.* 2011;7(2):157-163.

81. Mandal BB, Park SH, Gil ES, Kaplan DL. Multilayered silk scaffolds for meniscus tissue engineering. *Biomaterials.* 2011;32(2):639-651.

82. Martinek V, Ueblacker P, Braun K, et al. Second generation of meniscus transplantation: in-vivo study with tissue engineered meniscus replacement. *Arch Orthop Trauma Surg.* 2006;126(4):228-234.

83. Matyjaszewski K, Möller M, Müllen K, Ober CK. *Polymers for Advanced Functional Materials*: Elsevier; 2012.

84. McCarty EC, Marx RG, DeHaven KE. Meniscus repair: considerations in treatment and update of clinical results. *Clin Orthop Relat Res.* 2002(402):122-134.

85. McDevitt CA, Webber RJ. The ultrastructure and biochemistry of meniscal cartilage. *Clin Orthop Relat Res.* 1990(252):8-18.

86. Merriam A. *Development of a Hybrid Polymer Fiber/Collagen Sponge Meniscus Scaffold*: Department of Orthopaedic Surgery, Rutgers, The State University of New Jersey; 2013.

87. Merriam AR, Patel JM, Culp BM, Gatt CJ, Dunn MG. Successful Total Meniscus Reconstruction Using a Novel Fiber-Reinforced Scaffold: A 16-and 32-Week Study in an Ovine Model. *American Journal of Sports Medicine.* 2015;43(10):2528-2537.

88. Messner K. The concept of a permanent sythetic meniscus prothesis: a critical discussion after 5 years of experimental investigation using Decron and Teflon implants. *Biomaterials.* 1994;15(4):243-250.

89. Miller MD, Kline AJ, Gonzales J, Beach WR. Pitfalls associated with FasT-Fix meniscal repair. *Arthroscopy.* 2002;18(8):939-943.

90. Mordecai SC, Al-Hadithy N, Ware HE, Gupte CM. Treatment of meniscal tears: An evidence based approach. *World J Orthop.* 2014;5(3):233-241.

91. Mow V, Hayes W. Basic orthopaedic biomechanics, 1997: Raven Press, New York.

92. Mow VC, Kuei SC, Lai WM, Armstrong CG. Biphasic creep and stress relaxation of articular cartilage in compression? Theory and experiments. *J Biomech Eng.* 1980;102(1):73-84.

93. Murthy NS. X-ray Diffraction from Polymers. *Polymer Morphology: Principles, Characterization, and Processing.* 2016:14-36.

94. Neuman RE, Logan MA. The determination of hydroxyproline. *J Biol Chem.* 1950;184(1):299-306.

95. Nielsen AB, Yde J. Epidemiology of acute knee injuries: a prospective hospital investigation. *J Trauma.* 1991;31(12):1644-1648.

96. Nomura Y, Sakai H, Ishii Y, Shirai K. Preparation and some properties of type I collagen from fish scales. *Bioscience Biotechnology and Biochemistry.* 1996;60(12):2092-2094.

97. Northmore-Ball MD, Dandy DJ, Jackson RW. Arthroscopic, open partial, and total meniscectomy. A comparative study. *J Bone Joint Surg Br.* 1983;65(4):400-404.

98. Noyes FR, Barber-Westin SD. Long-term Survivorship and Function of Meniscus Transplantation. *Am J Sports Med.* 2016;44(9):2330-2338.

99. O'Brien FJ, Harley BA, Yannas IV, Gibson L. Influence of freezing rate on pore structure in freeze-dried collagen-GAG scaffolds. *Biomaterials.* 2004;25(6):1077-1086.

100. Ohan MP, Dunn MG. Glucose stabilizes collagen sterilized with gamma irradiation. *J Biomed Mater Res A.* 2003;67(4):1188-1195.

101. Olde Damink LH, Dijkstra PJ, Van Luyn MJ, Van Wachem PB, Nieuwenhuis P, Feijen J. Changes in the mechanical properties of dermal sheep collagen during in vitro degradation. *J Biomed Mater Res.* 1995;29(2):139-147.

102. Papageorgiou CD, Gil JE, Kanamori A, Fenwick JA, Woo SL, Fu FH. The biomechanical interdependence between the anterior cruciate ligament replacement graft and the medial meniscus. *The American journal of sports medicine.* 2001;29(2):226-231.

103. Parenteau-Bareil R, Gauvin R, Cliche S, Gariepy C, Germain L, Berthod F. Comparative study of bovine, porcine and avian collagens for the production of a tissue engineered dermis. *Acta Biomater.* 2011;7(10):3757-3765.

104. Patel JM, Merriam AR, Culp BM, Gatt CJ, Dunn MG. One-Year Outcomes of Total Meniscus Reconstruction Using a Novel Fiber-Reinforced Scaffold in an Ovine Model. *The American journal of sports medicine.* 2016:0363546515624913.

105. Patel JM, Merriam AR, Culp BM, Gatt CJ, Dunn MG. One-Year Outcomes of Total Meniscus Reconstruction Using a Novel Fiber-Reinforced Scaffold in an Ovine Model. *American Journal of Sports Medicine.* 2016;44(4):898-907.

106. Patel JM, Merriam AR, Kohn J, Gatt CJ, Jr., Dunn MG. Negative Outcomes of Poly(l-Lactic Acid) Fiber-Reinforced Scaffolds in an Ovine Total Meniscus Replacement Model. *Tissue Eng Part A.* 2016;22(17-18):1116-1125.

107. Petersen W, Tillmann B. Collagenous fibril texture of the human knee joint menisci. *Anat Embryol (Berl).* 1998;197(4):317-324.

108. Ragaert K, Cardon L, Dekeyser A, Degrieck J. Machine design and processing considerations for the 3D plotting of thermoplastic scaffolds. *Biofabrication.* 2010;2(1).

109. Resnick N, Gimbrone MA, Jr. Hemodynamic forces are complex regulators of endothelial gene expression. *FASEB J.* 1995;9(10):874-882.

110. Ricard-Blum S. The collagen family. *Cold Spring Harb Perspect Biol.* 2011;3(1):a004978.

111. Richards C, Gatt C, Langrana N, Calderon R. Quantitative measurement of human meniscal strain.

112. Rimmer MG, Nawana NS, Keene GC, Pearcy MJ. Failure strengths of different meniscal suturing techniques. *Arthroscopy.* 1995;11(2):146-150.

113. Rimmer MG, Nawana NS, Keene GC, Pearcy MJ. Failure strengths of different meniscal suturing techniques. *Arthroscopy: The Journal of Arthroscopic & Related Surgery.* 1995;11(2):146-150.

114. Robinson JJ. Comparative biochemical analysis of sea urchin peristome and rat tail tendon collagen. *Comp Biochem Physiol B Biochem Mol Biol.* 1997;117(2):307-313.

115. Rodeo SA. Meniscal allografts - Where do we stand? *American Journal of Sports Medicine.* 2001;29(2):246-261.

116. Rodkey WG. Menaflex (TM) Collagen Meniscus Implant: Basic Science. *Meniscus.* 2010:367-371.

117. Roos H, Laurén M, Adalberth T, Roos EM, Jonsson K, Lohmander LS. Knee osteoarthritis after meniscectomy: prevalence of radiographic changes after twenty-one years, compared with matched controls. *Arthritis & Rheumatism.* 1998;41(4):687-693.

118. Sandmann GH, Adamczyk C, Grande Garcia E, et al. Biomechanical comparison of menisci from different species and artificial constructs. *BMC Musculoskelet Disord.* 2013;14:324.

119. Seitz AM, Lubomierski A, Friemert B, Ignatius A, Dürselen L. Effect of partial meniscectomy at the medial posterior horn on tibiofemoral contact mechanics and meniscal hoop strains in human knees. *Journal of Orthopaedic Research.* 2012;30(6):934-942.

120. Sgaglione NA, Steadman JR, Shaffer B, Miller MD, Fu FH. Current concepts in meniscus surgery: resection to replacement. *Arthroscopy.* 2003;19 Suppl 1:161-188.

121. Shaffer B, Kennedy S, Klimkiewicz J, Yao L. Preoperative sizing of meniscal allografts in meniscus transplantation. *Am J Sports Med.* 2000;28(4):524-533.

122. Shrive NG, O'Connor JJ, Goodfellow JW. Load-bearing in the knee joint. *Clin Orthop Relat Res.* 1978(131):279-287.

123. Sihvonen R, Paavola M, Malmivaara A, et al. Arthroscopic partial meniscectomy versus sham surgery for a degenerative meniscal tear. *N Engl J Med.* 2013;369(26):2515-2524.

124. Smith JP, 3rd, Barrett GR. Medial and lateral meniscal tear patterns in anterior cruciate ligament-deficient knees. A prospective analysis of 575 tears. *Am J Sports Med.* 2001;29(4):415-419.

125. Sommerlath K, Gillquist J. The effect of a meniscal prosthesis on knee biomechanics and cartilage. An experimental study in rabbits. *Am J Sports Med.* 1992;20(1):73-81.

126. Song E, Kim SY, Chun T, Byun HJ, Lee YM. Collagen scaffolds derived from a marine source and their biocompatibility. *Biomaterials.* 2006;27(15):2951-2961.

127. Stepek J, Daoust H. *Additives for plastics.* Vol 5: Springer Science & Business Media; 2012.

128. Stone KR, Rodkey WG, Webber R, McKinney L, Steadman JR. Meniscal regeneration with copolymeric collagen scaffolds. In vitro and in vivo studies evaluated clinically, histologically, and biochemically. *Am J Sports Med.* 1992;20(2):104-111.

129. Stone KR, Steadman JR, Rodkey WG, Li S-T. Regeneration of Meniscal Cartilage with Use of a Collagen Scaffold. Analysis of Preliminary Data*. *J Bone Joint Surg Am.* 1997;79(12):1770-1777.

130. Subramony SD, Dargis BR, Castillo M, et al. The guidance of stem cell differentiation by substrate alignment and mechanical stimulation. *Biomaterials.* 2013;34(8):1942-1953.

131. Terraciano V, Hwang N, Moroni L, et al. Differential response of adult and embryonic mesenchymal progenitor cells to mechanical compression in hydrogels. *Stem Cells.* 2007;25(11):2730-2738.

132. Tienen TG, Heijkants RG, Buma P, De Groot JH, Pennings AJ, Veth RP. A porous polymer scaffold for meniscal lesion repair--a study in dogs. *Biomaterials.* 2003;24(14):2541-2548.

133. Tienen TG, Heijkants RG, de Groot JH, et al. Replacement of the knee meniscus by a porous polymer implant: a study in dogs. *Am J Sports Med.* 2006;34(1):64-71.

134. Tienen TG, Heijkants RG, de Groot JH, et al. Meniscal replacement in dogs. Tissue regeneration in two different materials with similar properties. *J Biomed Mater Res B Appl Biomater.* 2006;76(2):389-396.

135. Tissakht M, Ahmed AM. Tensile stress-strain characteristics of the human meniscal material. *J Biomech.* 1995;28(4):411-422.

136. Tovar N, Bourke S, Jaffe M, et al. A comparison of degradable synthetic polymer fibers for anterior cruciate ligament reconstruction. *J Biomed Mater Res A.* 2010;93(2):738-747.

137. Toyonaga T, Uezaki N, Chikama H. Substitute meniscus of Teflon-net for the knee joint of dogs. *Clin Orthop Relat Res.* 1983(179):291-297.

138. Tucker B, Khan W, Al-Rashid M, Al-Khateeb H. Tissue Engineering for the Meniscus: A Review of the Literature. *The open orthopaedics journal.* 2012;6:348.

139. Van Der Straeten C, Doyen B, Dutordoir C, Goedertier W, Pirard S, Victor J. SHORT- AND MEDIUM-TERM RESULTS OF ARTIFICIAL MENISCAL IMPLANTS. *Bone & Joint Journal Orthopaedic Proceedings Supplement.* 2016;98-B(SUPP 4):91-91.

140. Vangsness CT, Jr., Garcia IA, Mills CR, Kainer MA, Roberts MR, Moore TM. Allograft transplantation in the knee: tissue regulation, procurement, processing, and sterilization. *Am J Sports Med.* 2003;31(3):474-481.

141. Verdonk R, Verdonk P, Huysse W, Forsyth R, Heinrichs EL. Tissue ingrowth after implantation of a novel, biodegradable polyurethane scaffold for treatment of partial meniscal lesions. *Am J Sports Med.* 2011;39(4):774-782.

142. Verma NN, Kolb E, Cole BJ, et al. The effects of medial meniscal transplantation techniques on intra-articular contact pressures. *J Knee Surg.* 2008;21(1):20-26.

143. Von Lewinski G, Stukenborg-Colsman C, Ostermeier S, Hurschler C. Experimental measurement of tibiofemoral contact area in a meniscectomized ovine model using a resistive pressure measuring sensor. *Annals of biomedical engineering.* 2006;34(10):1607-1614.

144. Weiss CB, Lundberg M, Hamberg P, DeHaven KE, Gillquist J. Non-operative treatment of meniscal tears. *J Bone Joint Surg Am.* 1989;71(6):811-822.

145. Welsing RT, van Tienen TG, Ramrattan N, et al. Effect on tissue differentiation and articular cartilage degradation of a polymer meniscus implant: A 2-year follow-up study in dogs. *Am J Sports Med.* 2008;36(10):1978-1989.

146. White RA, Hirose FM, Sproat RW, Lawrence RS, Nelson RJ. Histopathologic observations after short-term implantation of two porous elastomers in dogs. *Biomaterials.* 1981;2(3):171-176.

147. Wood DJ, Minns RJ, Strover A. Replacement of the rabbit medial meniscus with a polyester-carbon fibre bioprosthesis. *Biomaterials.* 1990;11(1):13-16.

148. Zaffagnini S, Grassi A, Marcheggiani Muccioli GM, et al. MRI evaluation of a collagen meniscus implant: a systematic review. *Knee Surg Sports Traumatol Arthrosc.* 2015;23(11):3228-3237.

149. Zein I, Hutmacher DW, Tan KC, Teoh SH. Fused deposition modeling of novel scaffold architectures for tissue engineering applications. *Biomaterials.* 2002;23(4):1169-1185.

150. Zhang H, Leng P, Zhang J. Enhanced meniscal repair by overexpression of hIGF-1 in a full-thickness model. *Clin Orthop Relat Res.* 2009;467(12):3165-3174.

10 Appendix 1. Protocols

10.1 Collagen Extraction Protocol
1. Dissect tendon and remove from any other debris.
2. Cut the tendon into 1 cm pieces and freeze dry overnight.
3. Shred dry using large blender
    a. NOTE: For each extraction, spin down sample at 800 g for 15 minutes, drain solution using aspirator, fill with 500 mL ultrapure DI water, place on oscillator for 10 minutes, centrifuge at 800 g for 15 minutes, fill with fresh solution, place on oscillator for ten minutes, and return to fridge
    b. 4.0 g of tendon and 650 mL of solution go into each centrifuge bottle
4. 6, 24 hour extractions of basic proteins using 0.211 M sodium phosphate solution. Change daily.
    a. For 4 L Sodium Phosphate solution
        i. 120g NaH_2PO_4 into 4 L Ultrapure DI water
5. 2, 24 hour extractions of using 0.48 M NaCl solution buffered to pH 7.4 using Sodium phosphate.
    a. For 4 L NaCl solution
        i. 112.2 g NaCl in 4 L Ultrapure DI water
6. 2, 24 hour extractions of using 0.225 M citrate buffer solution (pH 3.7).
    a. For 4 L citrate buffer
        i. Stock solution of sodium citrate
            1. 90 g Sodium Citrate in 1360 mL Ultrapure DI water
        ii. Stock solution of citric acid
            1. 125 g Citric Acid in 2640 mL Ultrapure DI water
        iii. Mix together and pH to 3.7.
7. 4, 24 hour extractions of using 0.175 M acetic acid solution
    a. For 4 L acetic acid solution
        i. Dilute 53 mL glacial acetic acid to 4 L Ultrapure DI water
8. Wash several time with Ultrapure DI water, soak 4 times for 24 hours.
9. Freeze in freezer.
10. Lyophilize until complete

10.2 Collagen Sponge Tensile Testing Fabrication Protocol

1. Make 100 mL of 1% (w/v) with 1 g collagen and 100 mL of dilute HCl
    a. Place ground collagen in desiccator for 10 minutes
    b. Use dilute HCl (pH 2.35)
        i. Make with ultrapure DI water
    c. Pulse blend until viscous
    d. If using hyaluronic acid, mix the night before
2. Add magnetic stirrer and use vacuum pump in Room 429
3. Suck in solution with large syringe and apply to mold
    a. Use another 5 mL syringe with needle to suck up bubbles
    b. Use rubber band to hold mold closed
4. Freeze on dry ice/ethanol for 30 minutes
5. Put in freeze dryer until completion

6. Cross-linking (for 2 sponges)
    a. Desiccate EDC for 10 minutes
    b. Make 534 mL of Solution
        i. 1.024 g EDC
        ii. 0.307 g NHS
        iii. 534 mL ultrapure DI water
    c. Place TWO sponges in solution in pyrex glass pan for 5 hours
        i. Use perforated molds without polyester mesh and secure using ONE rubber band
    d. Place in fresh DI water for 10 minutes, 3 times
    e. Place in 100 mM Sodium phosphate monohydrate for 2 hours
        i. 500 mL DI water
        ii. 6.8995 g Sodium phosphate monobasic monohydrate
    f. Rinse overnight in DI water
7. Freeze using dry ice/ethanol bath for 30 minutes
8. Freeze dry until completion

10.3 Collagen Sponge Uniaxial Tensile Testing

1. Cut sponge into 1.5 cm strips
2. Use parallel razor apparatus to cut 56 mm gage length
3. Use 6 mm biopsy punch to cut filet at each end of gage length
4. Weigh each sample
5. Hydrate in PBS at 37°C overnight.
6. Weigh each sample
7. Take 3 thickness measurements using Z-mike.
8. Use camera to take picture of samples, ensuring the samples are placed as straight as possible
    a. Take picture with ruler in frame in macro setting
9. Test using small Instron at 14 mm/min to failure with freeze clamps.
10. Data Analysis
    a. Determine width of gage length using Collagen_Sample_Image_processing.m
    b. Analyze stress-strain curve using Collagen_Sponge_Tensile.m

10.4 Collagen Sponge Compression Fabrication Protocol

Note: This protocol makes 6 sponges in a full 6-well cell culture mold.

1. Make 180 mL of 1% (w/v) collagen dispersion
   a. 1.8 g Collagen
   b. 180 mL Ultrapure DI Water
2. Degas under high vacuum
3. Transfer to 6 well plate perforated mold with mesh.
4. Cover with perforated top with mesh and use to rubber bands to keep closed. When placing top try to push out any excess collagen to have uniform amount in each.
5. Freeze in dry ice/ethanol for 30 minutes.
6. Freeze dry overnight.
7. Crosslink in EDC/NHS solution per syringe for 5 hours with perforate flat tops and rubber band to keep uniform.
   a. 0.981 g EDC
   b. 0.294 g NHS
   c. 512 mL Ultrapure DI Water
8. Place in fresh DI water for 10 minutes, 3 times
9. Place in 100 mM Sodium phosphate monohydrate for 2 hours per syringe
   a. 480 mL DI water
   b. 6.612 g Sodium phosphate anhydrous

10.5 Collagen Sponge Compression Testing Protocol
1. Use 1 cm biopsy punch to form 10 mm diameter cylinders. Super glue each sample to a penny and let dry overnight.
2. Hydrate samples for at least 30 minutes.
3. Use metallic basin
   a. The basin was previously used for some sort of ACL tests. It has two basins one of which has 4 pegs at the bottom. I removed the sides of the basin without the pegs and filled the hole on the side with a screw with plumbing tape.
   b. Use clamp to keep basin fixed.
4. Use the small aluminum compression head on the Instron #5542.
5. Fill basin with PBS so the compression head is submerged initially.
6. Strain at 0.01 mm/s (0.001/s) to 75% strain.
7. Modulus is the linear fit from 2 to 5% strain and report the compressive strength at 20, 40, and 75%.
   a. Analyze with Collagen_Sponge_Compression

10.6 Collagen Sponge Confined Compression Protocol

1. Take 4 mm biopsy punch of sponge and trim to about 4 mm
2. Set up confined compression jig and add 5 mm extension to zero-gauge length
3. Balance load at zero-gauge length and allow test to run
4. Ensure test has significant initial linear extension (this is necessary for correct calculation).
5. Calculate properties with Collagen_Compression_Creep.m

10.7 Collagen Sponge Degradation Protocol (Collagenase Resistance Time)

1. Cut n=8 squares for each source with samples =2.0±0.2 mg.
2. Insert each sponge into a labeled fulcon test tube
    a. 5 for collagenase +3 control per source
3. Prepare enzyme solution
    a. 5 mL Collagenase 1000 U/mL in 1x Tris (pH 7.4)
        i. 20.41 mg Collagenase
        ii. 5 mL 1x Tris
    b. 2 mL Trypsin 16000 U/mL in PBS
        i. 2.35 mg Trypsin
        ii. 2 mL PBS
4. Prepare plastic basin heated with water bath
    a. Use pump to keep water flowing
    b. Adjust flow rate and temperature to matintain 37 C
5. Put samples in solution WITHOUT enzyme to incubate for 1 hour
    a. 6 samples in 1 mL 1x Tris
    b. 2 samples in 1 mL PBS
    c. Place enzyme solutions to incubate as well
6. Use pipette to put 1 mL of solution into each sample
    a. Control gets 1 mL of tris
    b. PBS samples get 1 mL trypsin
    c. Rest of samples get 1 mL collagenase
7. Check every 5 minutes and record time that the sponge entirely dissolves.

Collagenase mass was calculated with 244.9 U/mg Collagenase
Trypsin mass was calculated with 13600 U/mg Collagenase

10.8 Partial Meniscus Fabrication Protocol

1. Add 1.1 g Poly(DTD DD) to metallic cartridge with 400 micron inner diameter needle and push polymer into bottom using plunger. Ensure that polymer covers entire opening so when it melts it will create a seal.
2. Place Poly(DTD DD) at 160C in high temperature head for 10 min.
3. Set platform temperature to 27 C.
4. Purge at 4 bar for 1 min. Slowly increase pressure to 8 bar to test needle connection.
5. Calibrate needle.
6. Purge at 8 bar for 1 min.
7. Print at 160C, 8.3 bar, 1.2 mm/s, 1.3 s pre-flow, -0.60 s post-flow, 27 C platform temperature, 0.20 mm offset.
8. When two hours of printing has occurred, prepare next cartridge.
9. Once complete, immediately place next cartridge on heater.
10. Disassemble cartridge and clean out molten polymer. Use allen wrench to push all polymer out of lower cartridge attachment. Place needle and lower portion in THF immediately with stirring. Let cylinder cool then place in THF.

Collagen Procedures

1. Prepare 4 grams of 2% collagen, 1.25 % (w/w) hyaluronic acid dispersion.
   a. NIGHT BEFORE: Add 50 mg sodium hyaluronate to 200 mL dilute HCl (pH=2.35).
   b. Add 4 gram ground collagen and whip using magic bullet.
2. Place scaffold into negative mold in centrifuge cover and fill hole with collagen.
3. Spin at 600g for 15 minutes.
4. Freeze scaffold in mold for 15 minutes.
5. Pop out scaffold and leave in freezer.
6. When all scaffold are collagened, freeze dry overnight.
7. Use spatula to cover articulating surfaces with extra layer of collagen.
8. Label each scaffold using a suture with varying number of knots.
9. Prepare crosslinking solution (all values per scaffold)
   a. Add 0.0499 g EDC, 0.0144 g NHS to 25 mL Ultrapure DI Water
10. Soak scaffolds in crosslinking solution for 6 hours with very low agitation.
11. Wash 3x 10 minutes.
12. Prepare sodium phosphate solution
    a. Add 0.3549 g Sodium Phosphate anhydrous to 25 mL Ultrapure DI water.
13. Wash in Ultrapure DI water for 24 hours using several washes, including one long wash overnight.
14. Freeze and freeze dry overnight.
15. Sterilize using gamma radiation at Sterigenics with dose as close to 25 kGy as possible

10.9 Partial Meniscus Scaffold Uniaxial Tension Protocol
1. Thaw native menisci at room temperature.
2. Cut 80% radial width longitudinal cut through each of the native menisci.
   a. The outer margins will be utilized for construct pull-out assessment later.
   b. DO NOT CUT scaffold at all.
3. Hydrate 4 native menisci and 4 scaffolds for 30 minutes in PBS.
4. Fill cooler with ice and water and use pump to pump water to clamps.
5. Attach Bose system wires to clamps.
6. Load specimen in cryo-clamps and lightly tighten with 8 mm gage length.
7. Turn on electrical component of clamps and wait a few minutes.
8. When specimen begins freezing, tighten clamps further and wait 2 minutes
9. Tighten well once more and begin test immediately.
10. Test specimen at 10 mm/min to failure.
11. Use Scaffold_Tensile.m to analyze for ultimate load and tensile stiffness.

10.10 Meniscus Pull-out Test
1. Defrost meniscus.

2. Place dots 4.6 mm apart measured circumferentially. Makes 3 tests per meniscus (one per region).
3. Measure 2 mm inward from each dot and mark.
4. Place 2-0 Ethibond vertical mattress suture at each mark. Make a loop and tie.
    a. For scaffold, engage the bulk of the fibers of the implant.
5. The knot was super glued and wrapped in tape.
6. For gripping, place sutures 5 mm in circumferential direction from each testing suture. This suture (with pledgets) is placed evenly with the tested sutures in the radial direction. The suture goes through the meniscus, around the outer margin (with the pledgets reinforcing the outer margin), back through the meniscus, and then the 2 ends are tied in a loop.
7. Place both gripping loops into the lower pin of the intron. The knots were super glued.
8. Grip testing suture with pneumatic grip.
9. Test at 50 mm/min to failure.

10.11 Scaffold-Native Meniscus Construct Pull-out Protocol
1. Thaw full native menisci (for control group) and outer 20% from tensile tests overnight in fridge.
2. Using 4 2-0 Ethibond sutures about 1 centimeter apart in vertical mattress suture fashion, attach scaffold to outer 20% specimens from tensile tests
3. Cut 80% radial width longitudinal tear throughout meniscus and then using same suture technique as scaffold group attach the meniscus segments back together.
4. Using 2-0 stainless steel sutures
    a. For outer 20%, about 15 mm apart suture in and out twice and then tie suture around large pin on upper grip.
    b. For inner 80%, with point of entry and exit lining up with outer 20% stainless steel suture, suture in and out 4 times avoiding the points sutured with Ethibond. Tie this suture around large pin in lower grip
5. Test at 0.5 mm/s to pull-out, record maximum load and type of failure (pull-out suture failure).
6. Omit results if stainless steel sutures fail.

10.12 Contact Stress Study Protocol
Knee Preparation
1. Thaw ovine knees for 3 days in a fridge.
2. Remove skin, subcutaneous fat, muscle, and patella leaving joint capsule intact except for anterior portion.
3. Cut the bones 15 cm from the joint line.
4. Pot the tibia in a PVC pipe with PMMA ensuring that the medial plateau remains level. Let cure for half an hour.
5. Drill 2 sets of holes for 30 and 60 degrees using template.

Contact Stress Testing
1. Use a fresh strip for each knee.
2. Cut strip to 12 vertical pixels.
3. Cut leading tab triangular and reinforce with a plastic sheet.
4. Tegaderm 3 times with a plastic support tab on leading tab.
5. Precondition to 1500 N using silicone mold material on both strips.
6. Calibrate at 250 N, 1000 N using long silicone strip.
7. Cut anterior and posterior capsule just under meniscus to provide a place to put the strip.
8. Cut MCL attachment on femur. Drill K wire through this location. (This will be used to fixed the MCL after preparation.)
9. Coat the strip with Vaseline and put suture through leading tab .
10. Pull sutures through using suture puller.
11. While pulling on sutures, guide strip so the non-sensing part folds up against MCL.
    a. NOTE: this should go through relatively easily. If significant resistance, the leading tab may be bunching up as its pulled through.
12. Tie suture to something to fix strip in place.
13. Suture end of MCL with #5 ethibond suture, pull through k wire hole using suture passers and fix using endobutton.
14. Balance jig with pins on instron and place plastic base plate on bottom of instron.
15. Hang knee on jig and slowly lower so its just touching the plastic base plate.
16. Mark locations for screws to fix the knee pot to base plate.
17. Drill locations with 1/4 " drill bit then use threader to thread holes.
18. Return base plate to instron. Lower knee so its just touching the base plate. Place washers where needed to maintain this angle. Screw pot to base plate.
19. Check that the force on the strip is about 10-40 N when instron reads no load. If not adjust varus valgus by adding washers under pot.
20. Manually apply load until 200 N is read on strip and note load on instron
21. At 30 degrees, cycle the load 20 times (1st 5 are preconditioning) to load needed for 200 N +50 N safety factor.
22. Hydrate tissue.
23. Run test.
24. Remove knee from jig. Remove tekscan strip. Untied suture holding endobutton. Perform sham surgery. Return tekscan strip. Fix MCL with Endobutton. Return to jig. Test force necessary. Run test at 30 and 60.
25. Repeat for meniscectomy and scaffold.
26. Output variables analyzed in Contact_Stress_Analysis.m
    a. Average contact area
    b. Average contact stress

        c.   Peak contact stress

        d.   Area at peak contact stress

10.13 Fixation Strength Testing

1. Once contact stress testing is complete, cut all ligaments.
2. Drill bone tunnel in anterior-medial plane about 2 cm below joint line on tibia.
3. Place knee into jig with one rod in bone tunnel and one rod preventing rotation of knee.
4. Grip the scaffold using a surgical clamp with a screw and bolt for added gripping strength.
5. Grip surgical clamp using large pneumatic clamps.
6. Test in tension at 50 mm/min to failure.
7. Output variables analyzed in Scaffold_Tensile.m
   a. Maximum fixation strength (N)
   b. Stiffness (N/mm)

10.14 Immunofluorescence Embedding and Staining Protocol
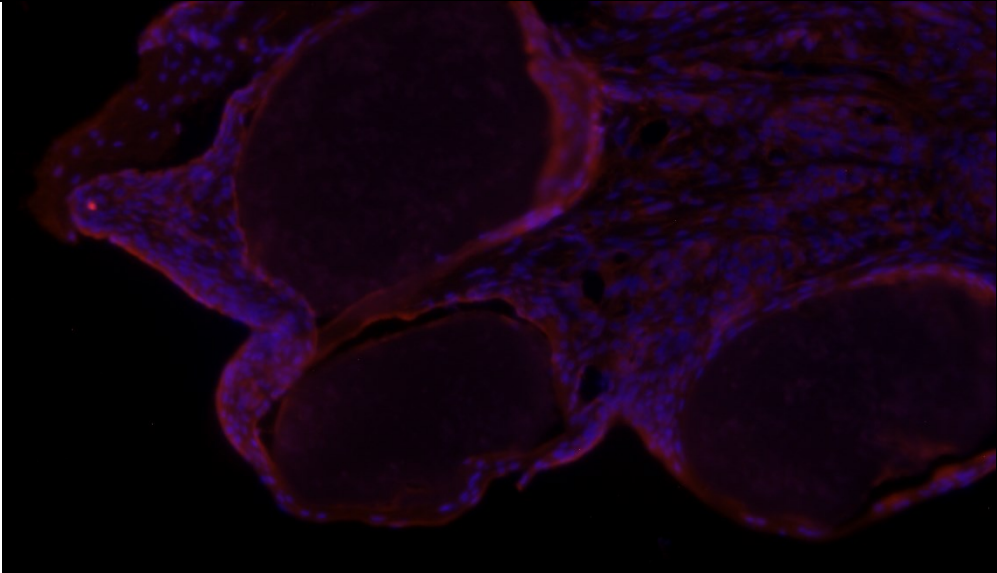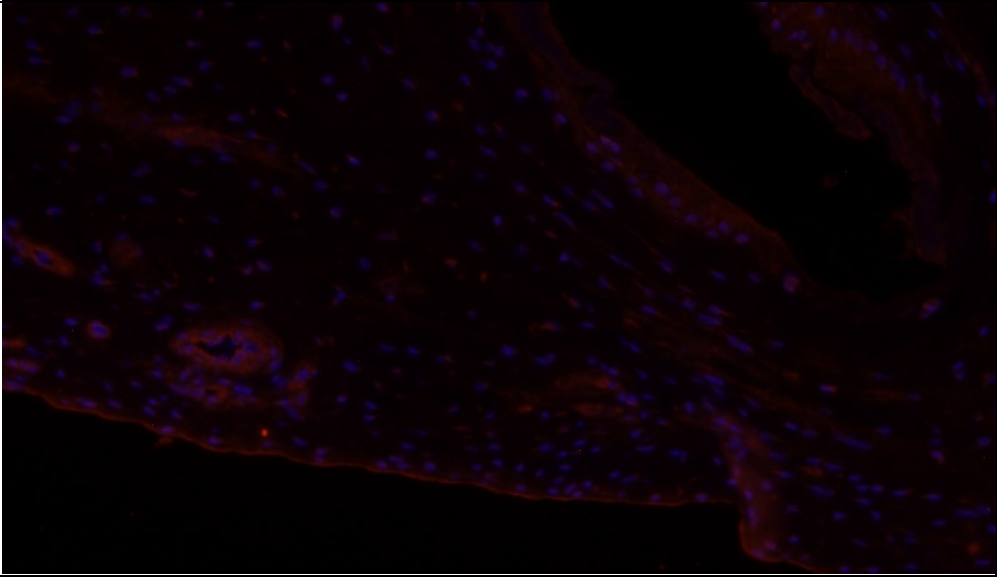
1. Fixation in 100% methanol at -20°C, 3min
2. Rehydration in PBS, 2x5min
3. Blocking with 5% Normal Donkey Serum in PBS/Tween-20 at 21°C, 60min
4. Primary antibody (listed below) in PBS/Tween-20 at 4°C, 60min
5. Rinse with PBS/Tween-20, 3x10min
6. Secondary antibody (listed below) in PBS/Tween-20 at 21°C in dark, 60min
7. Rinse with PBS/Tween-20, 3x10min
8. Dark incubation with DAPI (0.4ug/mL) at 21°C, 5min
9. Rinse with PBS/Tween-20, 1x5min
10. Mounting with Prolong Gold Antifade Reagent and coverslip
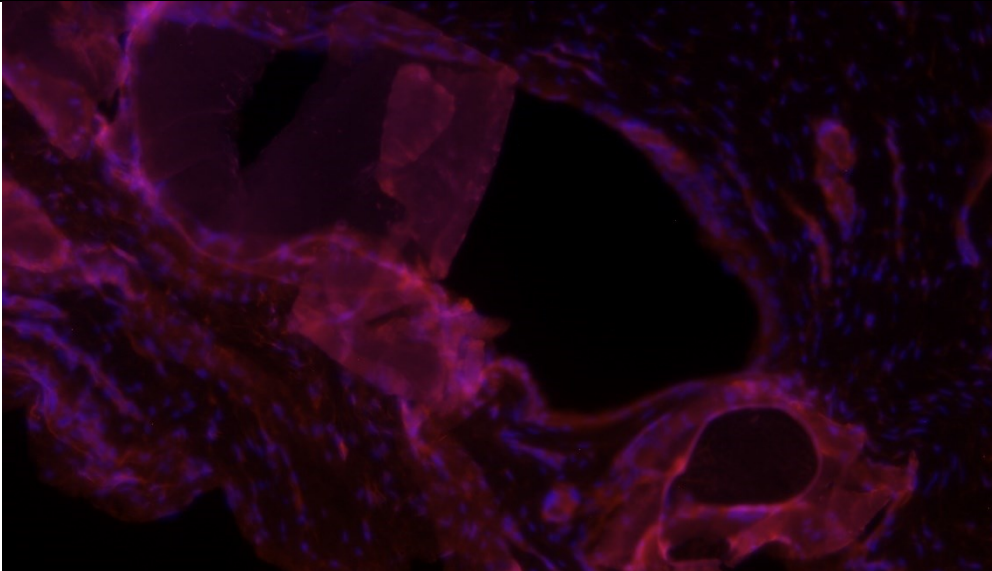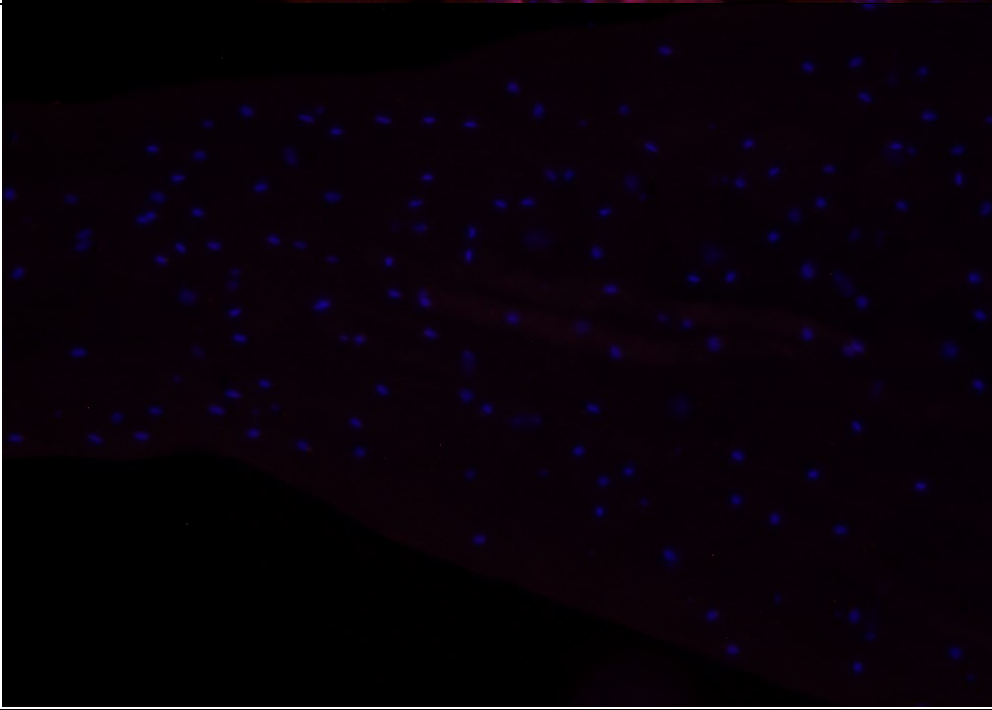
The following antibodies are used:
- Primary Antibody – Type I Collagen (AB745, Millipore, Billerica MA)
o Host – rabbit
o Dilution – 1:300
- Primary Antibody – Type II Collagen (AB34712, Abcam Inc, Cambridge MA)
o Host – rabbit
o Dilution – 1:200
- Secondary Antibody – AlexaFluor 594 Texas Red (Invitrogen)
o Donkey-anti-rabbit
o Dilution – 1:1000
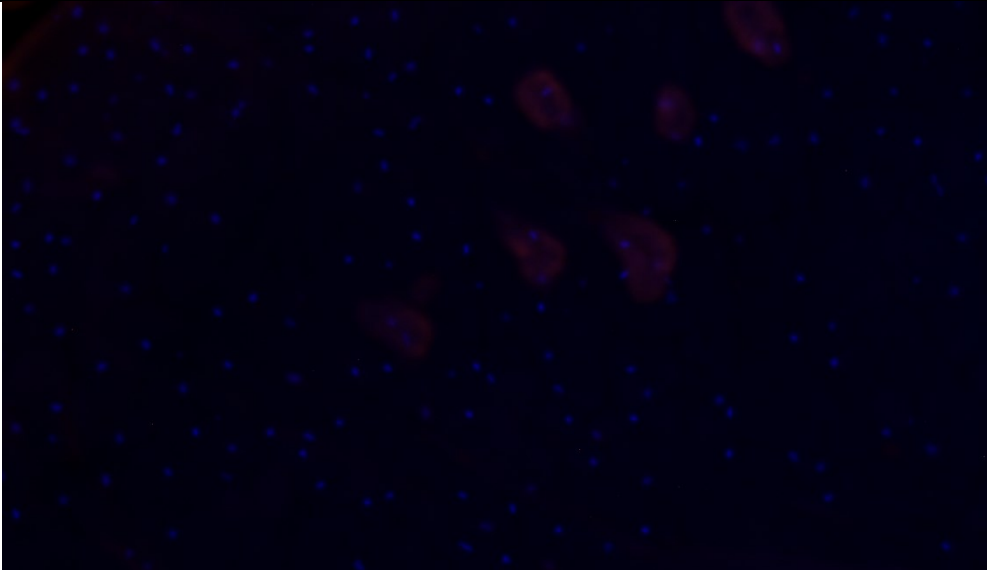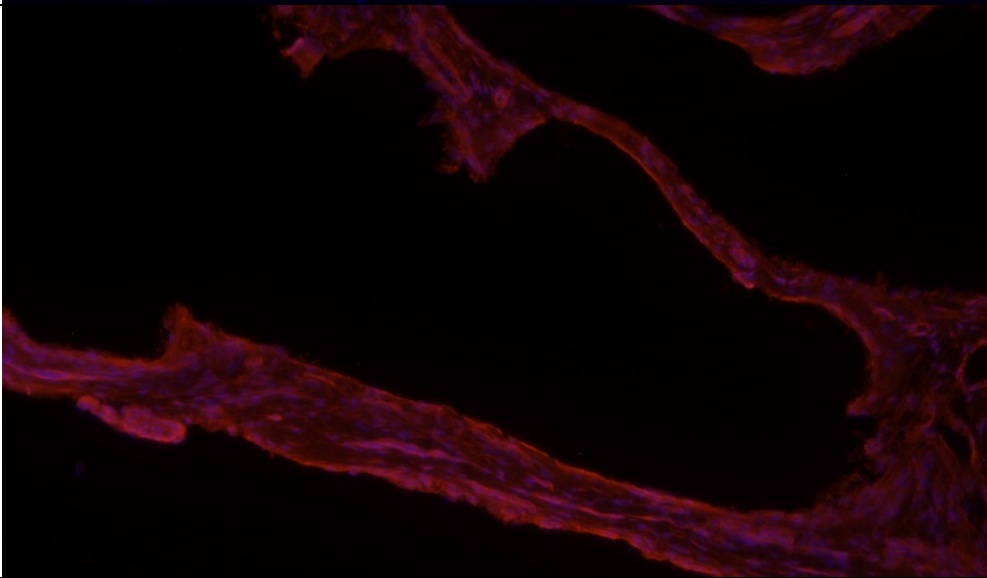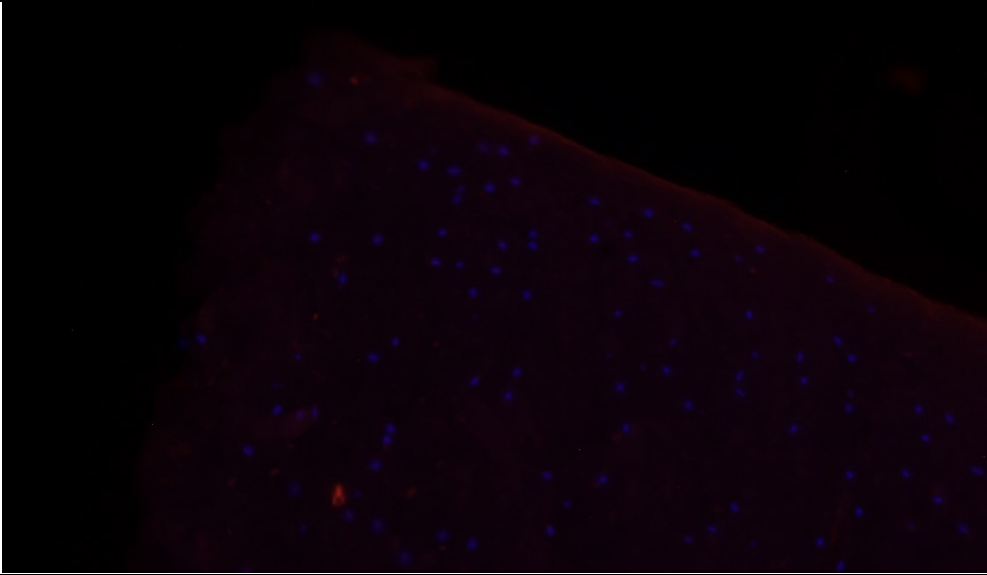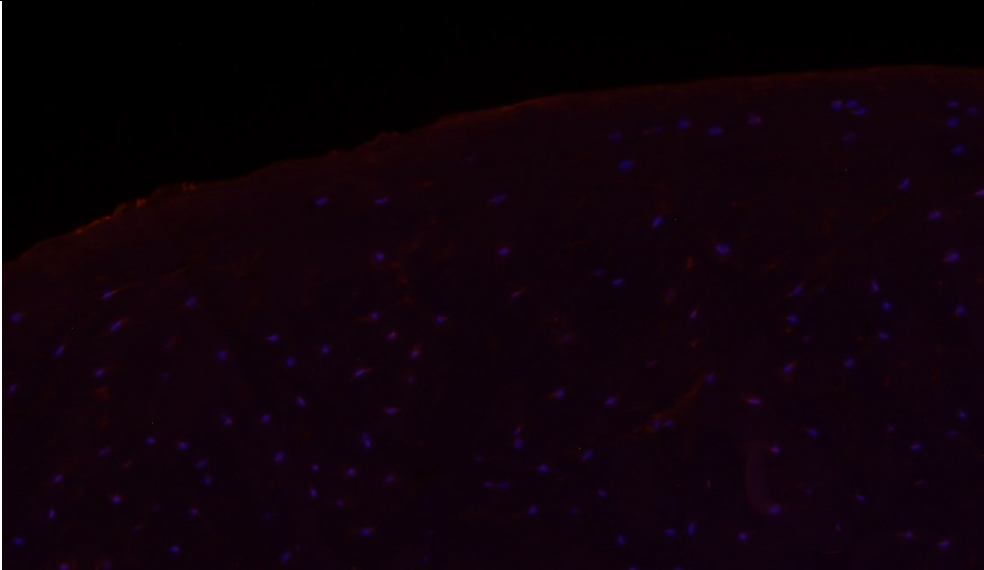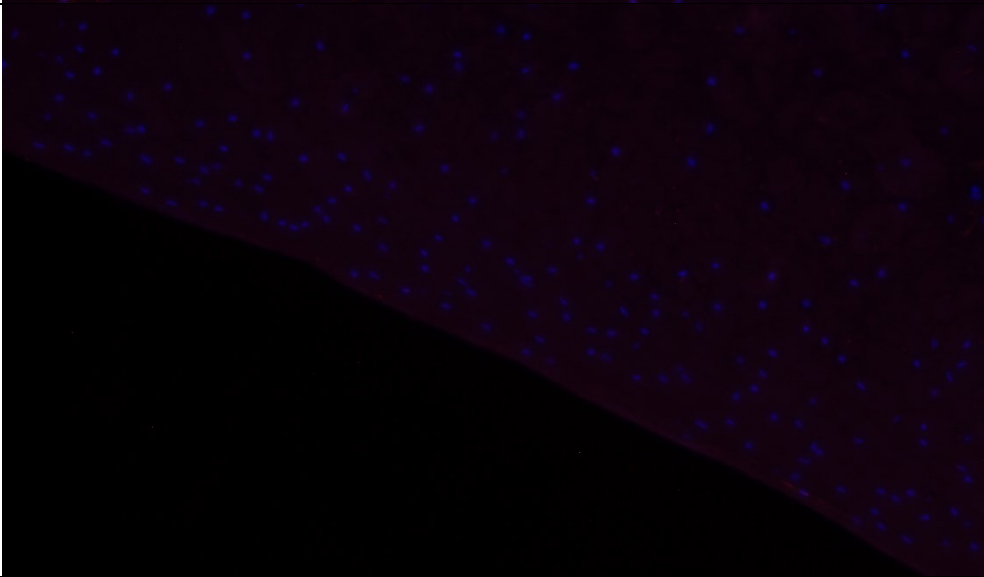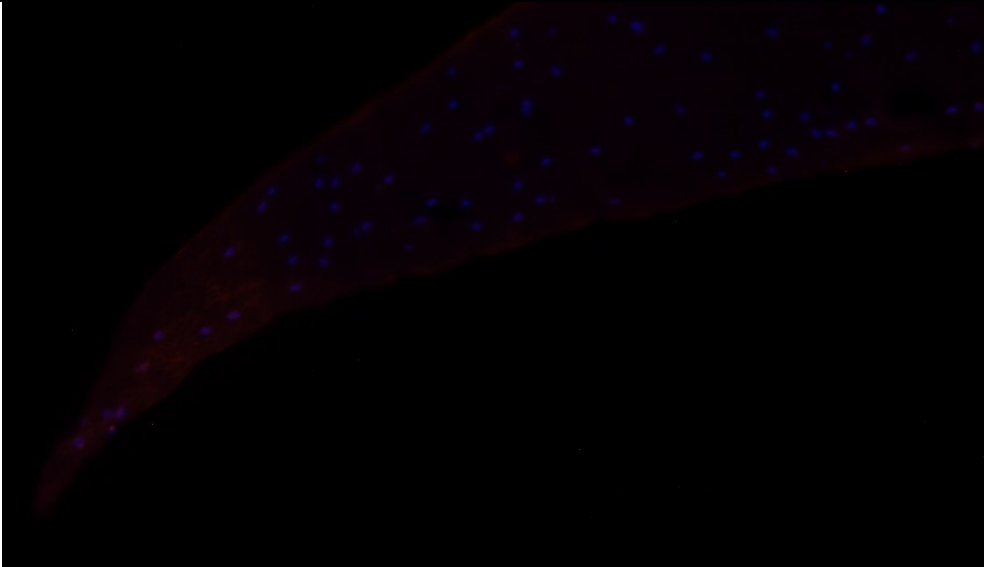
11 Appendix 2. Immunofluorescence Images from Individual Animals
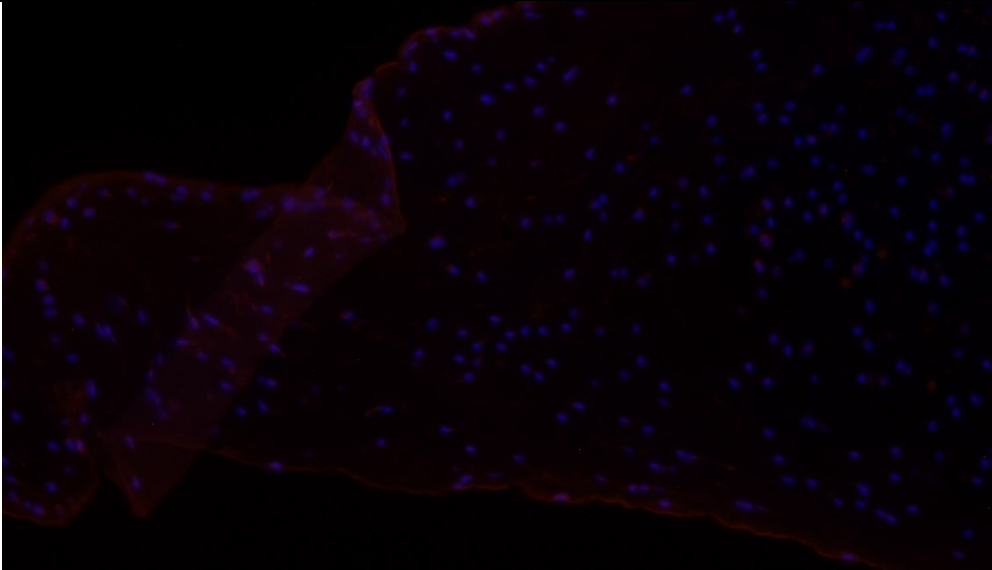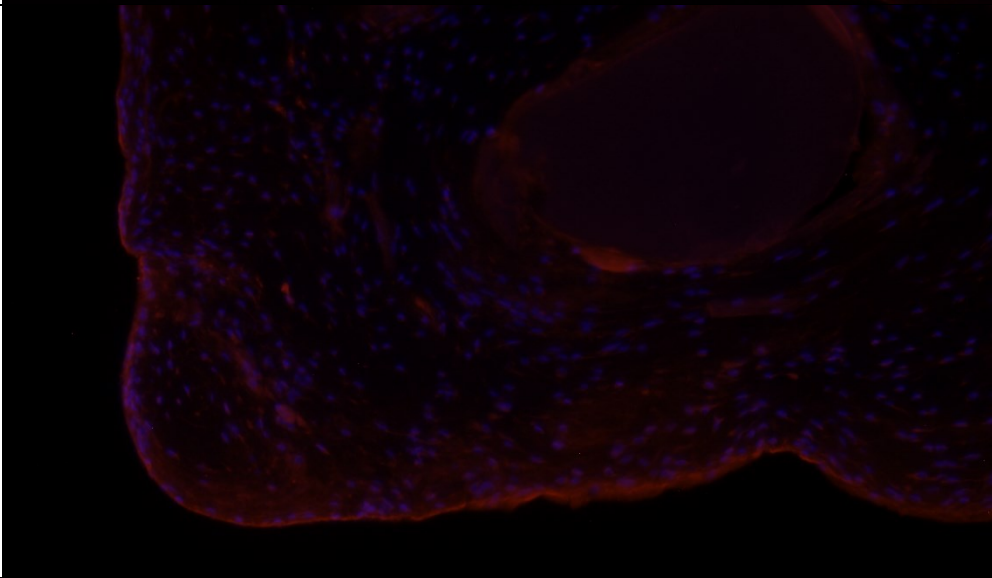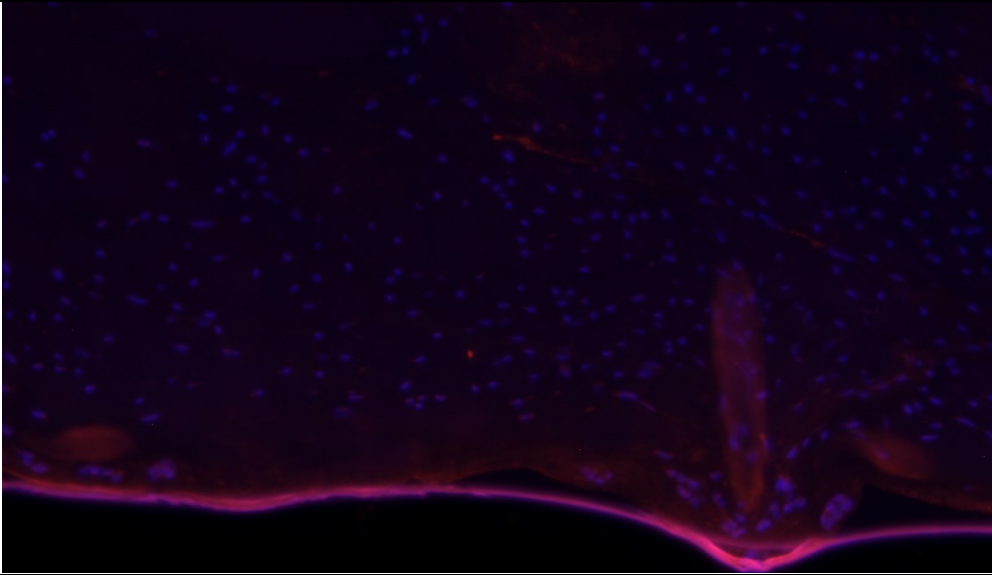
11.1 Type I Collagen

1R3	
2R3	

3R1	
4R1	
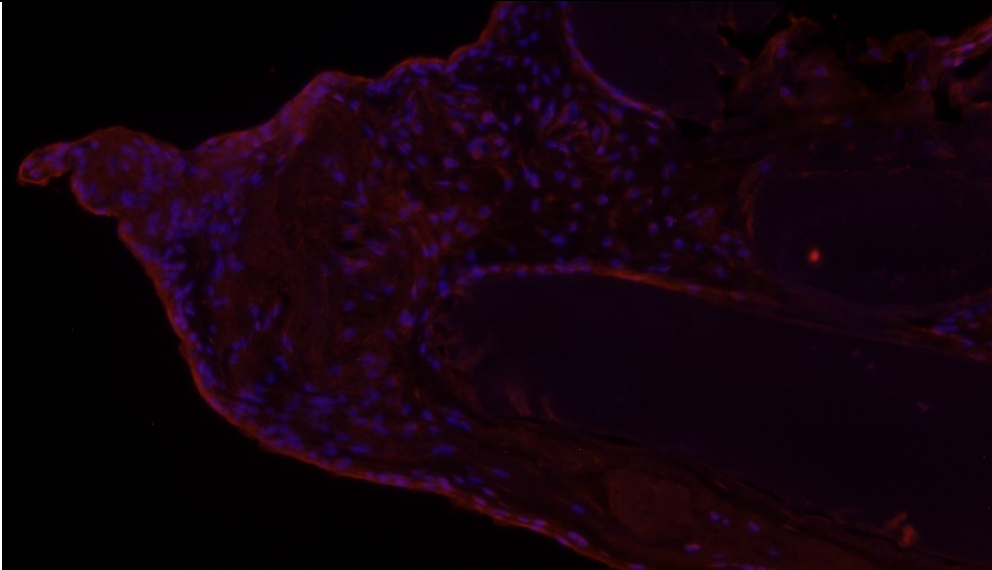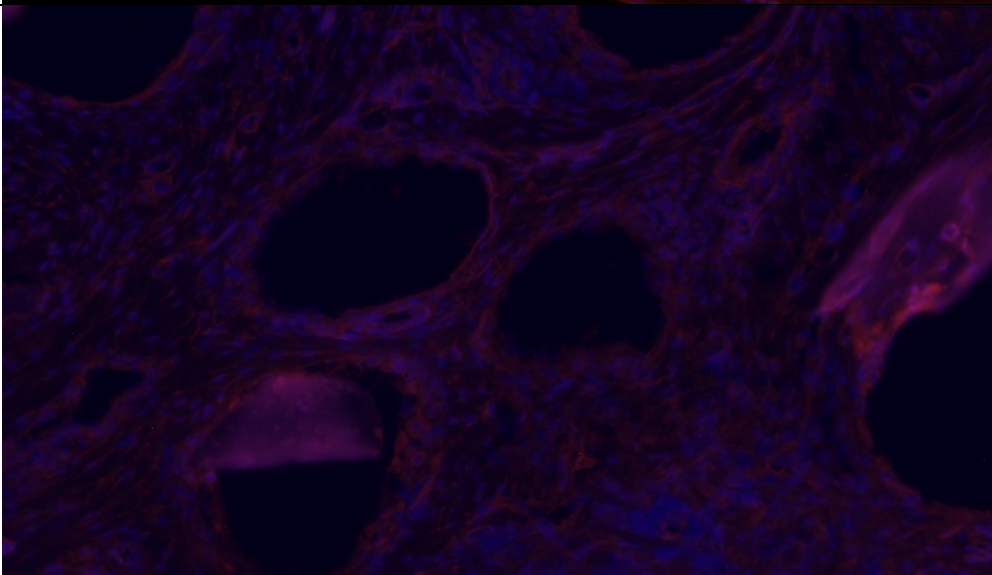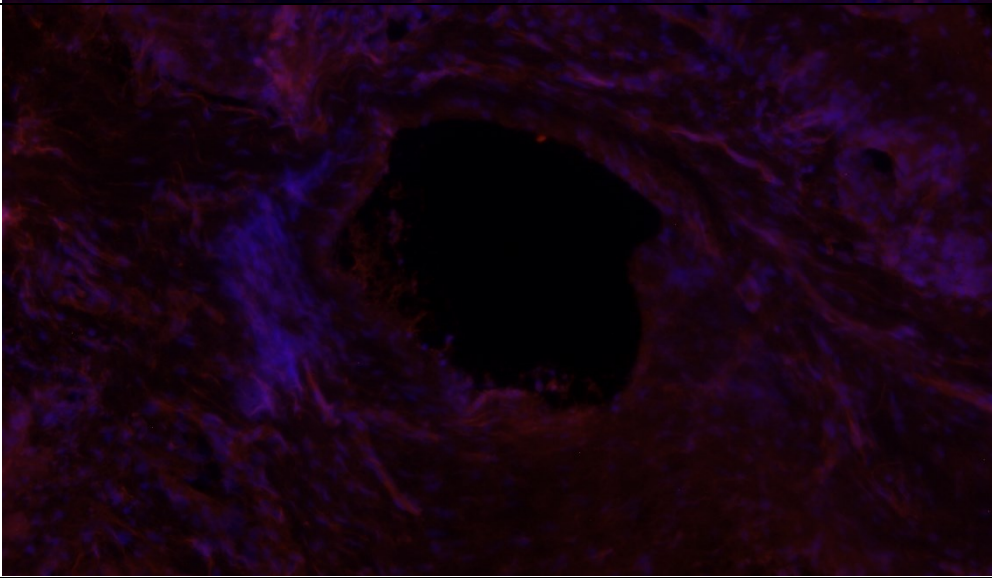
4R-OUTER	
5R1	
6L1*	

6R1	
7L1	
7R1	

8R1	
9R1*	
10R1*	

11R1 *	
13R2	
14R1 *	

15R2 *	
16L2	
16R2 *	

17R4	
19R4	
20R3 *	

21R1 *	
22R5	
23R1	

| 24L1* | |
| 24R1 | |
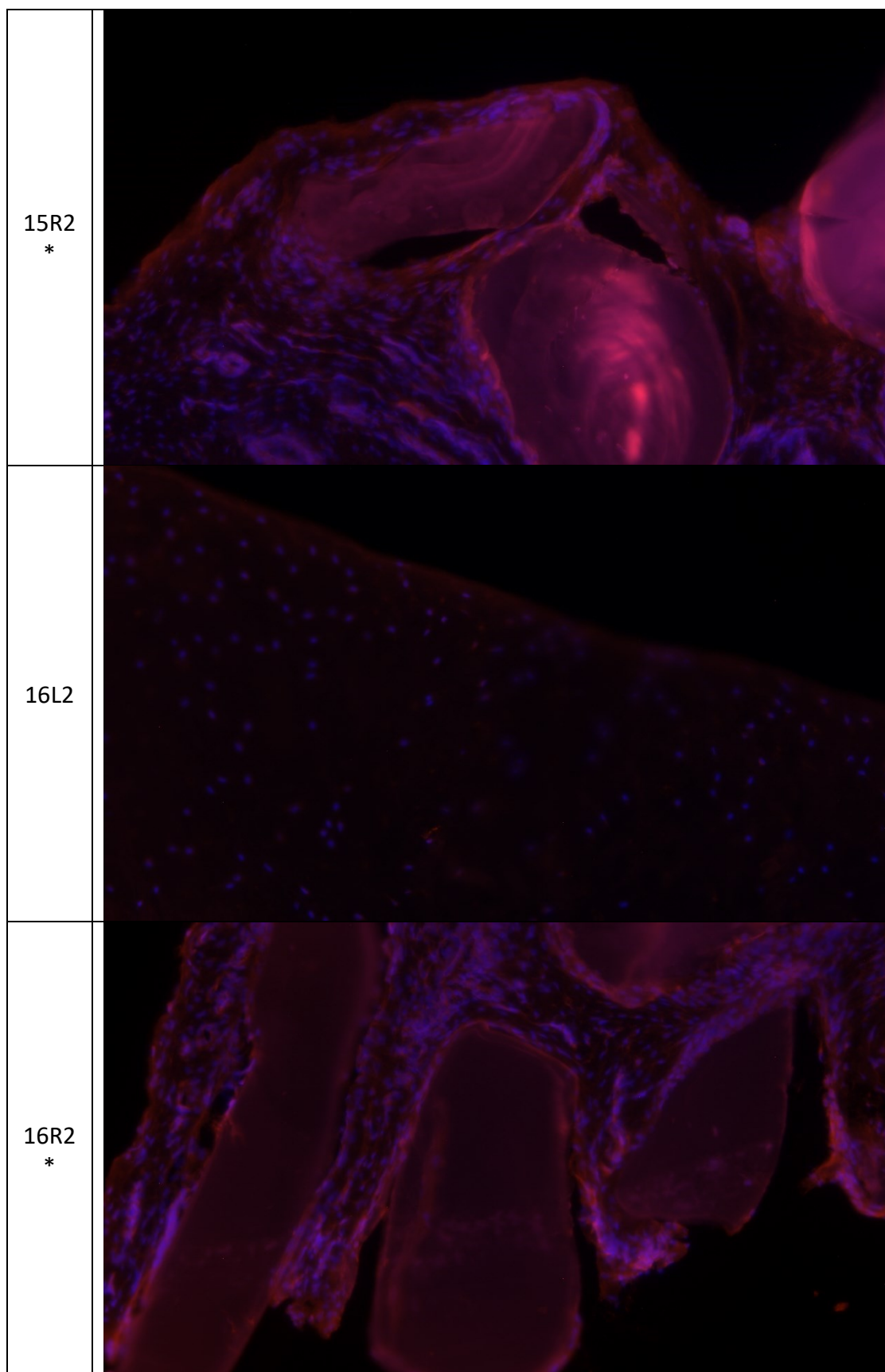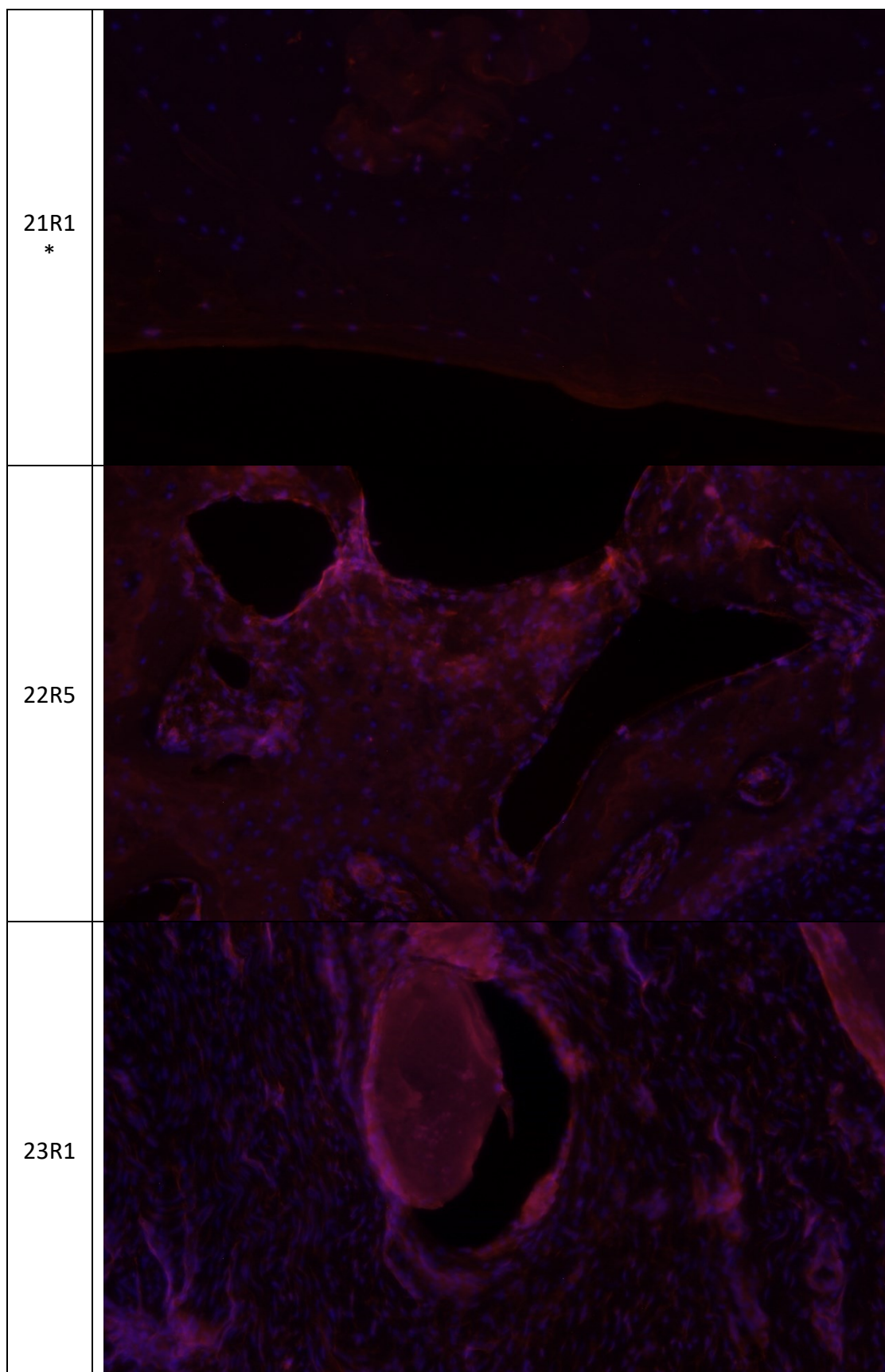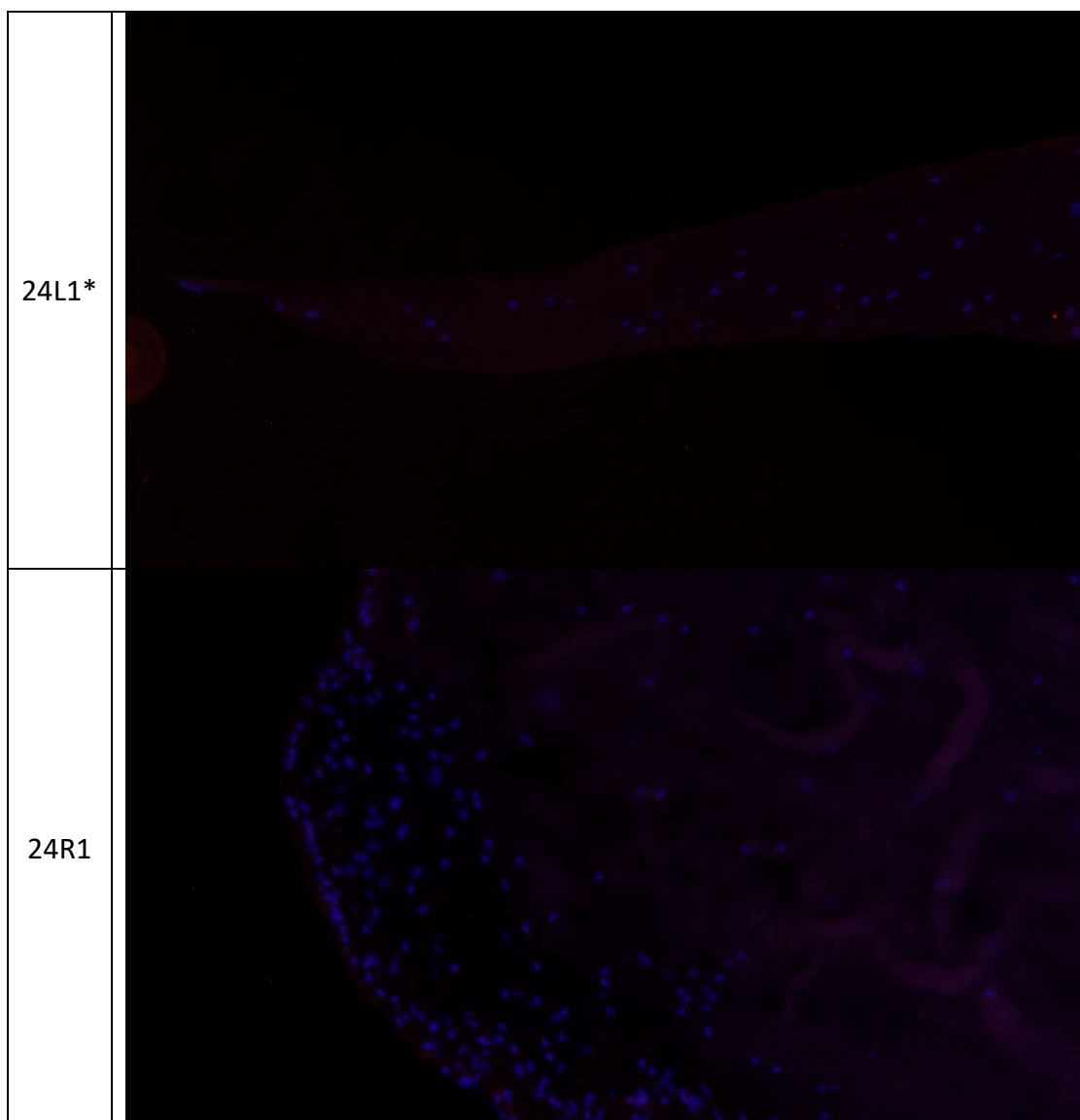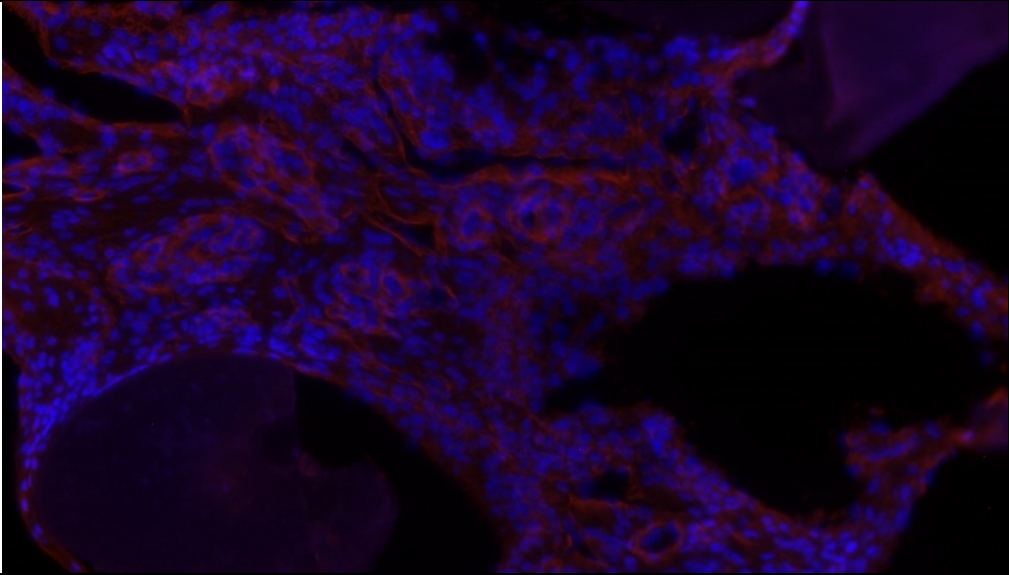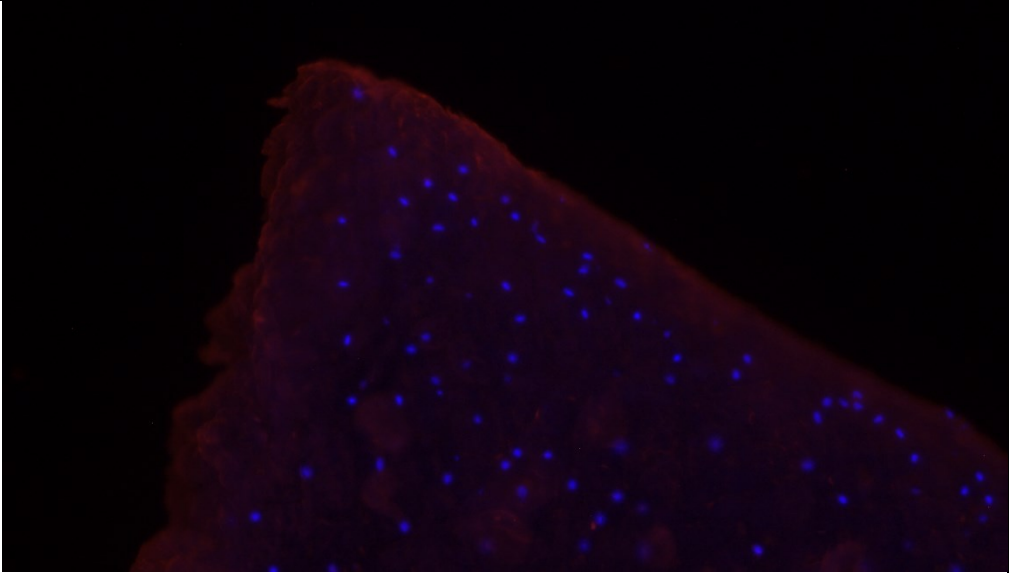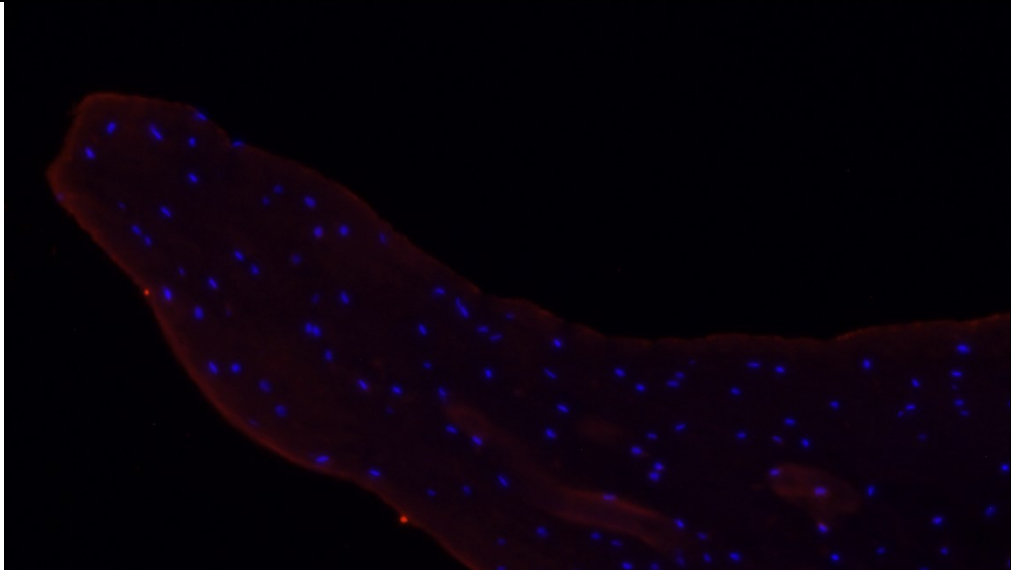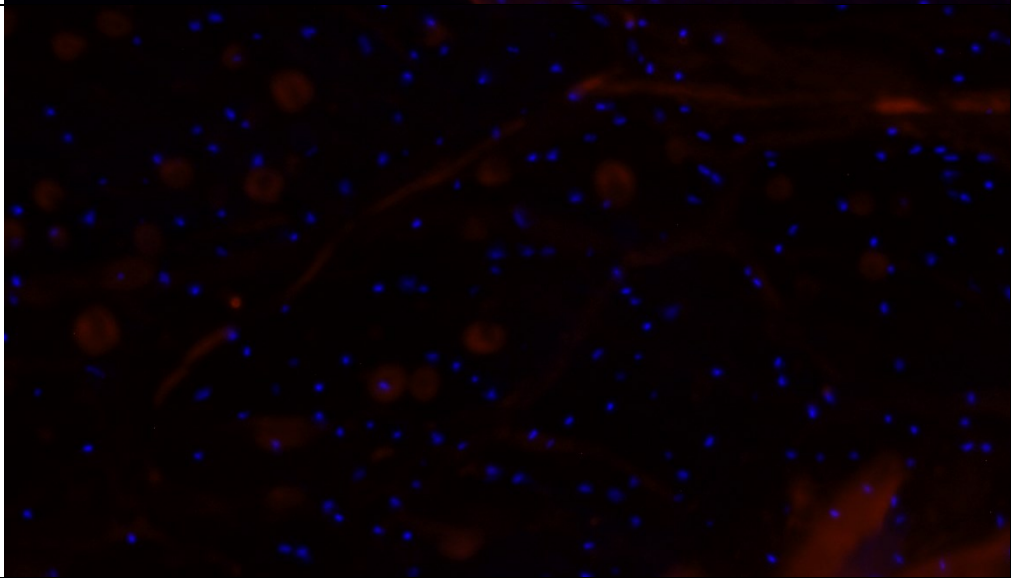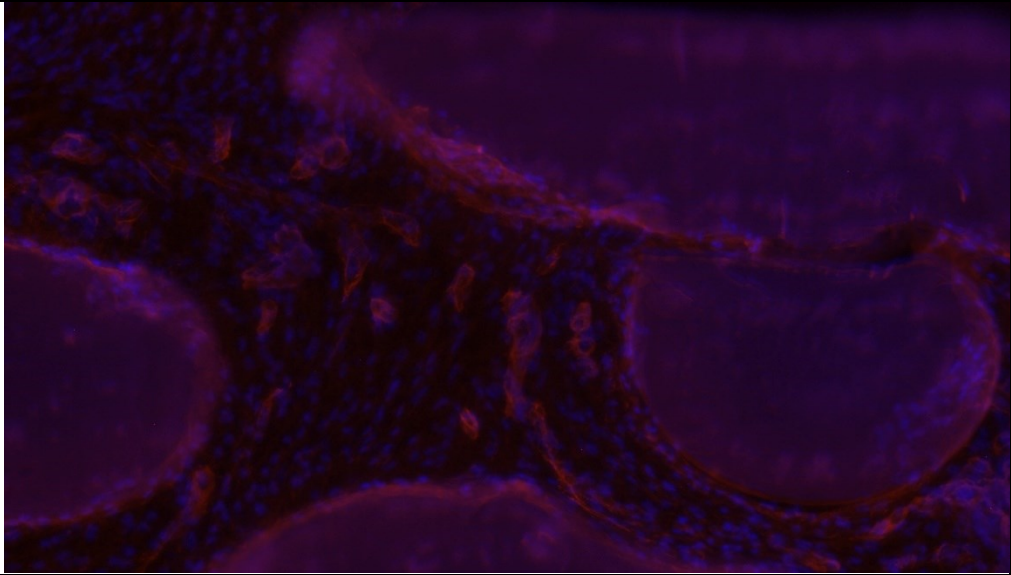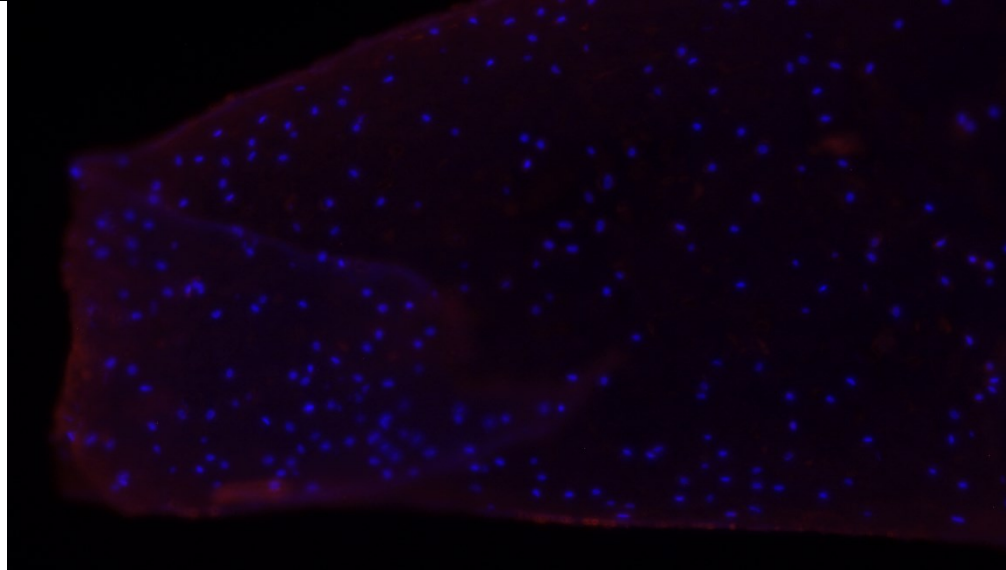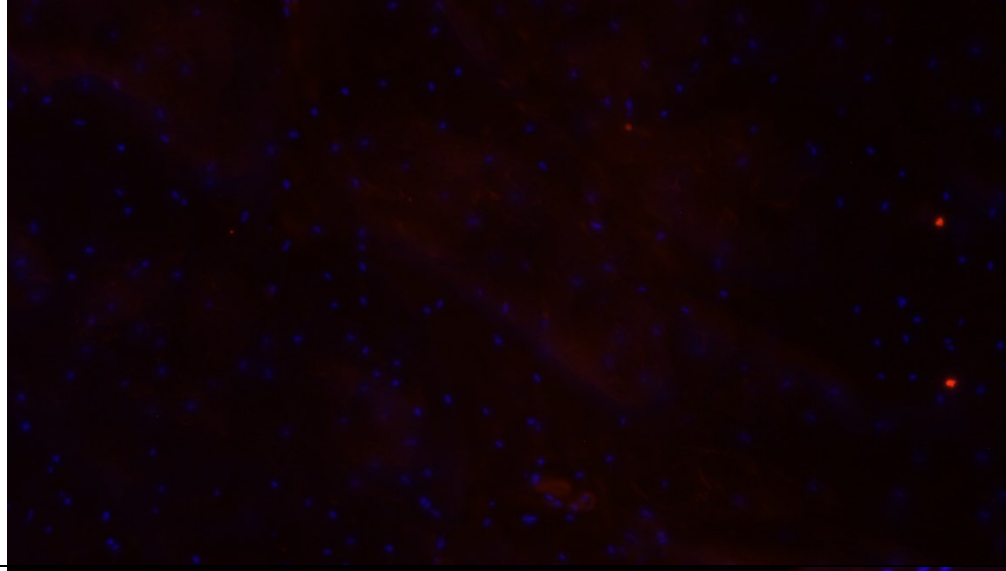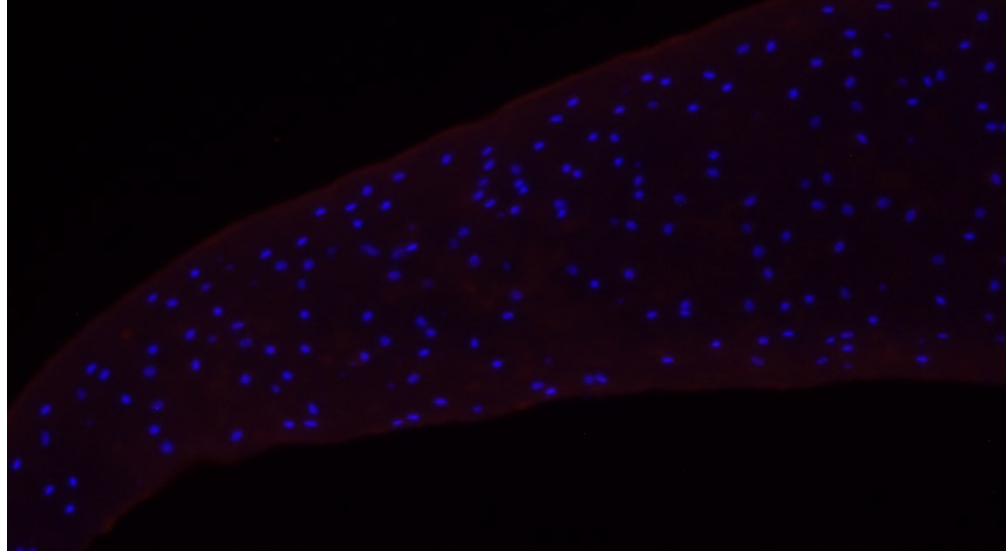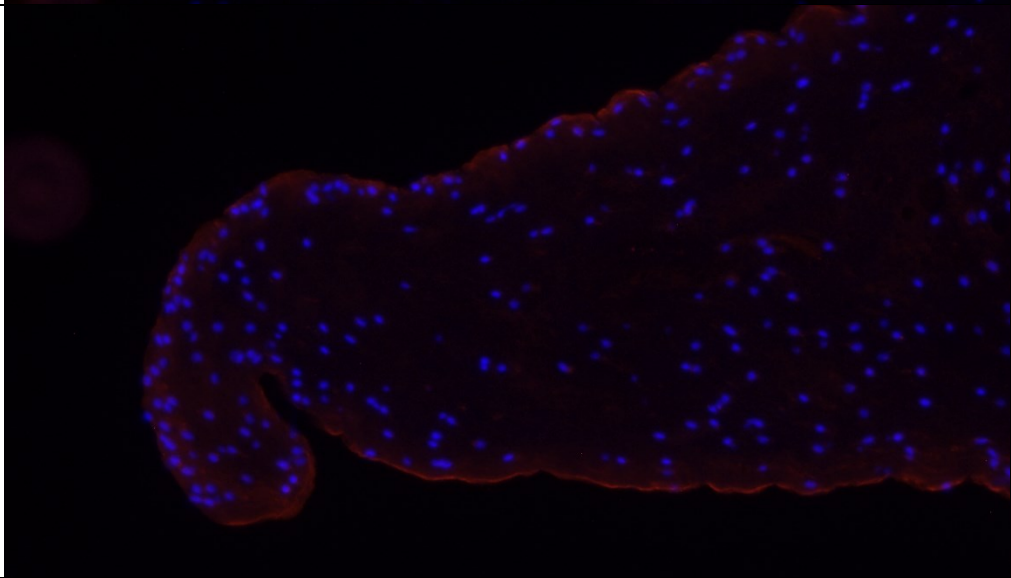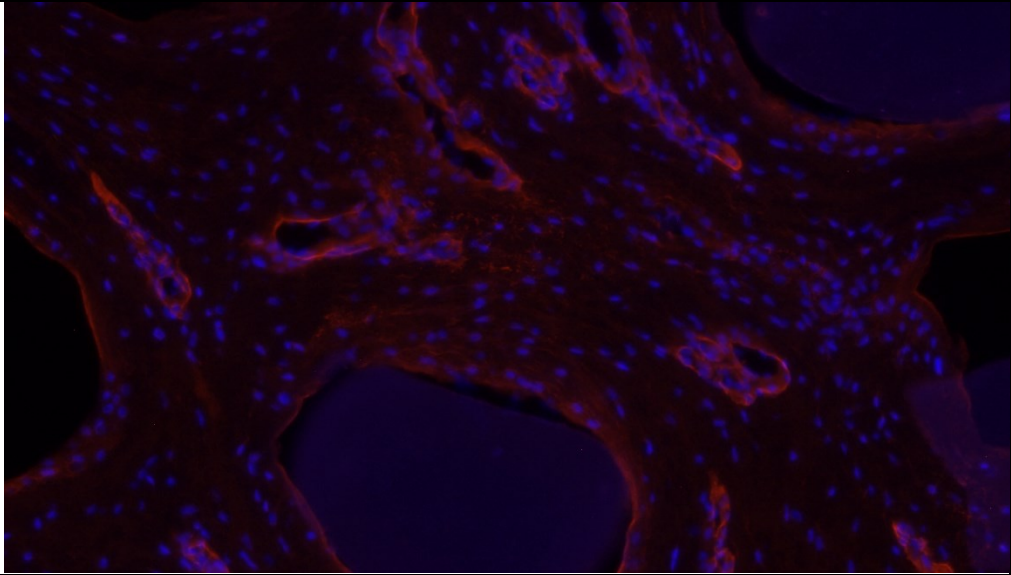
11.2 Type II Collagen

1R1	
2L1	

2R4	
3R1	
4L1	

4R1	
4R-OUTER	
5R3*	

7L1	
7L-OUTER	
7R2	

7R-OUTER	
8R1	
9R3*	

10R 5*	
11R 1*	
12R 1	

13R 2*	
14R 3*	
17R 4*	

19R 1*	
20R 3*	
21R 2*	

23R 4*	
24L 3*	
24L - OU TER	

24R3

12 Appendix 3. Scaffold Histological Scoring

			Matrix Morphology Staining	Safranin-O Surface	Integrity	Thickness	Bonding to host tissue	Repair tissue in defect	Adjacent host tissue	Cartilage Cell Number	Matrix Porosity
12 Week	Partially Displaced	1R3	2	0	2	2	2	1	2	1	5
		5R2	5	1	2	2	1	2	3	3	5
		16R2	0	0	3	2	2	0	3	0	4
		17R1	4	1	3	2	2	2	3	2	5
	Completely Displaced	19R1	4	1	2	2	2	3	3	2	5
		20R2	0	0	2	2	2	0	0	0	5
		22R1	0	0	2	2	1	1	1	1	5
		23R1	4	0	3	2	2	3	3	2	5
	In Situ	2R2	5	1	3	2	2	3	3	3	5
		2R3	5	1	3	2	2	3	3	3	5
		9R2	5	1	3	2	2	3	3	3	5
		9R4	5	2	2	2	2	2	2	3	5
		3R1	5	1	3	2	2	3	3	3	5
		11R1	4	0	2	2	2	2	3	3	5
		13R2	5	0	2	2	2	2	3	3	5
24 Week	Partially Displaced	14R1	4	2	2	2	2	0	3	3	5
	Completely Displaced	12R4	2	0	2	2	2	1	3	1	5
		15R1	2	1	1	1	2	1	3	2	4